ANTENNAS AND COMPONENTS FOR MODERN TELECOMMUNICATION SYSTEMS INCLUDING WIRELESS BODY AREA NETWORKS

by

Syed Muzahir Abbas

Dissertation submitted in fulfilment of the requirements

for the degree of

DOCTOR OF PHILOSOPHY

Department of Engineering
Faculty of Science and Engineering
Macquarie University
Sydney, Australia

December 2015

MACQUARIE UNIVERSITY

GRADUATE COMMITTEE APPROVAL

of a Dissertation submitted by

Syed Muzahir Abbas

This dissertation has been read by each member of the following graduate committee and by majority vote has been found to be satisfactory.

_____   _____

Date   Professor Karu P. Esselle, Chair

_____   _____

Date   Committee Member A

_____   _____

Date   Committee Member B

_____   _____

Date   Committee Member C

_____   _____

Date   Committee Member D

MACQUARIE UNIVERSITY

As chair of the candidate's graduate committee, I have read the dissertation of Syed Muzahir Abbas in its final form and have found that (1) its format, citations, and bibliographical style are consistent and acceptable and fulfill university and department style requirements; (2) its illustrative materials including figures, tables, and charts are in place; and (3) the final manuscript is satisfactory to the graduate committee and is ready for submission to the university library.

_____

Date

_____

Professor Karu P. Esselle
Chair, Graduate Committee

Accepted for the Department

_____

Department Chair Name, Chair
Department of Engineering

Accepted for the Division

_____

Dean Name, Associate Dean
Faculty of Science and Engineering

ABSTRACT

With the advancements in wireless communications, there is a constant need to develop novel antennas and components to support modern communication systems. These systems are targeted for applications in medical, defence, healthcare, public security, communications. The antenna is a vital front end component in any wireless system. Although many narrow- and wide-band antennas have been designed over past decades, still there are several challenges when designing such antennas for modern systems. These challenges include compactness, space constraints, desired radiation characteristics, low cost, light weight, multi-band operation, interference mitigation, reconfigurability, and stable performance under varying conditions. Motivated by the increasing demand for modern telecommunication systems including wireless body area networks (WBAN), this thesis addresses such challenges and presents several solutions.

In this thesis, in addition to characterization of carbon nanotube yarns, several antennas are designed and investigated. The designed antennas are broadly classified into narrow-band antennas, wide-band antennas, embroidered antennas on polymer composites, wide-band antennas with notching, antennas with Frequency Selective Surface (FSS) and High Impedance Surface (HIS) reflectors, and reconfigurable antennas.

The narrow-band antennas provide single- and dual-band operation for the 2.45GHz industrial, scientific and medical (ISM) band and for 4.9GHz public safety wireless local area network (WLAN)/5GHz IEEE 802.11 WLAN. These an-

tennas have significant advantages of compactness (only 14mm wide), full ground plane to minimize radiation towards the body, a wide radiation pattern over the body surface to provide maximum coverage, and less sensitivity to the variation of the gap between the antenna and the human body. These advantages make them suitable for on-body communications and wearable applications.

The wide-band antennas target ultra-wideband (UWB) systems. One such antenna is fabricated using conductive fibres on polymer composite substrate (PDMS) that is flexible and semi-transparent. A UWB antenna with a notch band provides design flexibility to reject a desired frequency band. A mathematical expression is presented to predict initial design parameters of these antennas and to avoid excessive numerical computations required otherwise. These antennas are compact, have stable wide radiation patterns and provide band rejection with a high VSWR.

FSSs are employed with UWB antennas to achieve a uni-directional pattern by reflecting the radiation from the lower hemisphere to the upper hemisphere. The presented design has a stable radiation pattern over a wide bandwidth and is suitable for applications using uni-directional beam. It also helps to save and use the power that otherwise could propagate into the human body, thus are suitable for off-body communications. Periodic and quasi-periodic sequences of modulated line based HIS are also investigated and is used to achieve controlled radiation patterns.

Reconfigurable antennas are designed for the 2.45GHz ISM band and 5GHz WLAN to operate in close proximity of the human body. They have same advantages as narrow-band antennas mentioned above. A reconfigurable antenna to provide UWB operation in one mode and a narrow-band operation in another mode is presented. It is designed using a low cost substrate, has planer configu-

ration, avoids the need of vias and has a fully printed bias circuit.

Theoretical and experimental characterization of Carbon Nanotubes (CNT) yarns is a valuable contribution that opens new paths of research related to CNT. Electrical properties of CNT yarns were known for Direct Current (DC), however they were not available at RF and microwave frequencies. In this thesis, CNT yarns are modelled as transmission lines and are characterized for a frequency range from 500MHz to 20GHz. Results show that the yarns exhibit a frequency independent resistive behaviour and are suitable for wide-band applications including wireless body area networks.

STATEMENT OF CANDIDATE

I certify that the work in this thesis has not previously been submitted for a degree nor has it been submitted as part of the requirements for a degree to any other university or institution other than Macquarie University.

I also certify that the thesis is an original piece of research and it has been written by me.

In addition, I certify that all information sources and literature used are indicated in the thesis.

. . . .

Syed Muzahir Abbas

ACKNOWLEDGMENTS

I would like to express my deepest and sincerest gratitude to my principal supervisor, Professor Karu P. Esselle, for his expert and quality supervision during this research work. I highly acknowledge his invaluable guidance, consistent support and encouragement for successful and timely completion of this milestone.

I would also like to express my profound gratitude to my adjunct supervisor, Dr. Stuart G. Hay (from CSIRO, Australia), for his guidance and support during this research.

I am grateful to Prof. Anand K. Verma, Prof. Michael Heimlich, Dr. Ladislau Matekovits (Politecnico di Torino, Italy), Dr. Yogeshwar Ranga (IP, Australia), Dr. Javad Foroughi (University of Wollongong, Australia) and Dr. Peiyuan Qin (U) for their continuous support, guidance, encouragement and valuable feedback during this research that up-lifted the quality of work.

I am thankful to Prof. John L. Volakis (ElectroScience Lab, the Ohio State University, Columbus, Ohio, USA) for his guidance, feedback and for providing me with the opportunity to visit and work with his research group. I extend my gratitude to Safa Salman, Dr. Konstantinos Karathanasis, Dr. Sharvil C. Desai and Dr. Asimina Kiourti for their support and facilitation during my visit and research.

I would like to thank Dr. Akram Alomainy (Queen Mary, University of London, UK) for his guidance, support and, for providing me with the opportunity to visit and work with his research group. I extend my gratitude to Syeda Fizzah

To my son, wife, brothers and parents for their love, care, encouragement and support.

Contents

List of Figures

List of Tables

Chapter 1

Introduction

Wireless communication has revolutionized the world with its traits and developments over the past decades. Technology has transformed the way we communicate with our sorroundings. Distances are not an issue anymore and the world has become a global village. This requires increased mobility, better and expanded coverage, ease of use and cost effective solutions at high speed connectivity. With the advancements in wireless communications, there is a constant need to develop novel antennas and components to support modern communication systems. These systems are targeted for applications in medical, defence, healthcare, and public security. Antennas serve as a vital front end component in any wireless system. Although many antennas have been designed over past decades, still there are several challenges when designing such antennas for modern systems. These challenges include compactness, space constraints, desired radiation characteristics, low cost, light weight, multi-band operation, interference mitigation, reconfigurability, and stable performance under varying conditions. This thesis presents novel antennas and components by addressing these challenges for applications in modern telecommunication systems including wireless body area networks.

1.1   Challenges and Objectives

Motivated by the increasing demand for modern telecommunication systems including wireless body area networks (WBAN), this thesis addresses such challenges and presents several solutions. The main challenges considered during this research are;

- For the narrow-band antennas presented in chapter 3, the challenge is to achieve wide coverage over the body and around it, and to achieve stable antenna performance when placed closed to human body. Furthermore, with the changing gap between the antenna and the body, the performance of antenna should have minimum variations (i.e. should be less sensitive to the gap variations). The other challenges are compactness and narrow slit in design to achieve electromagnetically-coupled feed. Stable performance and less sensitivity to gap variation under conformal bending conditions are additional challenges.

- Accurate fabrication of embroidered antenna having an ultra-wide bandwidth, fabricated on polydimethylsiloxane (PDMS) composite substrate using conductive fibers.

- High band rejection, wide radiation patterns and compactness for UWB printed monopole antenna were difficult to obtain in one design. Also achieving tunability over a broad range of frequencies from 3.55GHz to 6.8GHz, is challenging. Furthermore, obtaining the piece-wise analytical expressions that give sufficiently accurate first estimate of the required stub length, avoiding excessive trail-and-error full-wave simulations is also a significant contribution.

- Use of wideband FSS to obtain stable uni-directional radiations with higher gain.

- Control of dispersion characteristics mainly in the band-gap region for novel printed microstrip HIS. Moreover, using HIS to obtain omni-directional or controlled radiations.

- Reconfigurable antenna with narrow band operations focusing on ISM band at 2.45GHz and WLAN band at 5GHz in a single design when it need to operate in close proximity of human body. wide beam radiations along with compactness are also challenging to achieve.

- To design an antenna that operates in ISM band at 2.45GHz in one mode and in another mode it provides UWB operation. The antenna is required to have simple design with single side printed geometry and provide low-cost solution.

- Obtaining Carbon Nanotube (CNT) yarns and their fixturing on test structures. Their modeling and comparison of data to make a conclusion due to this research's significance.

1.2   Organization of Thesis

Chapter 2 presents literature review focusing on wireless body centric communication and its different types. Narrow- and ultra wide-band antennas are discussed. Research work carried on embroidered and wearable antennas, sensors and transmission line structures for potential usage in wireless body area networks is highlighted. Discussion on ultra wideband antennas is focused on their use to reject interference by band notching, and increase in gain and radiation pattern controlling using reflectors such as frequency selective surfaces and high impedance surfaces. Research work on reconfigurable antennas is also presented. Carbon nanotubes and carbon nanotube yarns are discussed in detail along with their potential applications and usage to highlight the significance to this new research dimensions.

Chapter 3 presents novel narrow band antennas. Single- and dual-band antennas are presented for wireless body area network devices operating in the industrial, scientific, and medical (ISM) band at 2.45GHz and 4.9GHz public safety Wireless Local Area Net-

works (WLAN) band. Performance of the designed antennas has been analyzed for near body scenarios and in close proximity to the human arm models. These antennas have significant advantages of compactness (only 14mm wide), full ground plane to minimize radiation towards the body, a wide radiation pattern over the body surface to provide maximum coverage, and less sensitivity to the variation of the gap between the antenna and the human body. These advantages make them suitable for on-body communications and wearable applications. Furthermore, performance of these antennas has been analyzed in close proximity of different body models. To assess their real-time performance, they have been evaluated with gel based tissue equivalent layer models and over a female body phantom. They show good performance and are suitable for on-body communications.

In Chapter 4, a flexible embroidered antenna having an ultra-wide bandwidth, fabricated on polydimethylsiloxane (PDMS) composite substrate using conductive fibers, is presented. Another antenna was fabricated using Rogers material and copper, and is compared with embroidered version of the same design fabricated using conductive fibers on PDMS composite. Measured results show the similarity between the two prototypes. The embroidered antenna fabricated using conductive fibers on PDMS composite substrate also provides ultra-wide band operation. It is water resistant, flexible, compact, semi-transparent and is easy to integrate in clothing without being prominent. These traits make it suitable for wearable systems.

In chapter 5, a compact UWB printed monopole antenna with high band rejection (up to VSWR > 25), tunable over a broad range of frequencies from 3.55GHz to 6.8GHz, is presented. The piece-wise analytical expressions give sufficiently accurate first estimate of the required stub length, avoiding excessive trail-and-error full-wave simulations. The new antenna has additional advantages of smaller size and wide radiation patterns. To demonstrate its practical usage, as examples, design parameters are presented to reject two different interfering frequency bands.

In Chapter 6, the use of wideband FSS to obtain uni-directional radiations is presented. By use of in-phase reflection over a wideband, the backward radiation are reduced and a stable radiation pattern with higher gain is obtained. Moreover, investigation focusing on control of dispersion characteristics mainly in the band-gap region are presented for novel printed microstrip HIS. By placing these HIS in a cylindrical shape and feeding it using a dipole from inside, omni-directional or controlled radiations can be obtained depending upon selected modulated width for the HIS.

In Chapter 7, reconfigurable antenna with narrow band operations focusing on ISM band at 2.45GHz and WLAN band at 5GHz is presented. The design has narrow width which makes it feasible for integration in wearable applications. Another design that operates in ISM band at 2.45GHz in one mode and in another mode it provides UWB operation has been presented. This antenna has simple design with single side printed geometry and provides low-cost solution.

Chapter 8 presents a novel work on Carbon Nanotube (CNT) yarns. Theoretical and experimental characterization of CNT yarns is a valuable contribution that opens new paths of research related to CNT. Electrical properties on CNT yarns were known for Direct Current (DC), however they were not available at RF and microwave frequencies. CNT yarns are modelled as transmission lines and are characterized. They were measured at RF/microwave frequencies in a microstrip configuration to ascertain their material properties for UWB WBAN system components as EM surfaces, dielectrics, and conductors. In this first such test for CNT yarns, the data suggests that the CNT yarn performs very much like the underlying multi-walled CNT bundles. Contact resistance is relatively high, but good conduction is found within the yarn itself. After accounting for the contact and an effective sheet resistance, the yarn presents a characteristic impedance that is well approximated through measurement and modeling by a copper wire of similar diameter and attachment method. These models for the CNT yarn give very good

agreement to both the transmitted and reflected S-parameters. The observed frequency-independent resistive behavior of the CNT yarn is a very promising indicator that when the conductivity is improved as a result of ongoing research, this material, with its added values of mechanical resilience and thermal conductivity, could be invaluable for a range of applications such as body area network (BAN). These results suggest that the CNT yarn can be used in microwave applications in a manner similar to resistive materials, such as NiCr or doped polysilicon. In this configuration, the CNT yarn could act as a probe or conductive structure that is acceptable to biological tissue.

Finally, Chapter 9 presents the conclusion with future work. This chapter discusses the overall achievements and contributions made towards the research carried out in the thesis. It also highlights the signicance of my research and its impacts. At the end of this chapter, the new research directions are indicated as future work.

1.3 List of Publications

1.3.1 Journal Papers

Published

[J1] S. M. Abbas, Y. Ranga, A. K. Verma, and K. P. Esselle, "A Simple Ultra Wideband Printed Monopole Antenna With High Band Rejection and Wide Radiation Patterns," *IEEE Transactions on Antennas and Propagation*, vol. 62, pp. 4816-4820, 2014.

[J2] S. M. Abbas, O. Sevimli, M. C. Heimlich, K. P. Esselle, B. Kimiaghalam, J. Foroughi, and F. Safaei, "Microwave Characterization of Carbon Nanotube Yarns For UWB Medical Wireless Body Area Networks," *IEEE Transactions on Microwave Theory and Techniques*, vol. 61, pp. 3625-3631, 2013.

In-progress

[J3] Syed Muzahir Abbas, Sharvil C. Desai, Karu P. Esselle, John L. Volakis, "Flexible Embroidered Antenna on Polydimethylsiloxane (PDMS) Composite using Conductive Fibers for Wideband Applications,".

[J4] Syed Muzahir Abbas, Safa Salman, Yogesh Ranga, Karu P. Esselle, John L. Volakis, "A Printed Antenna with Wide Radiation Pattern along the Human Body Surface for On-body Communications,".

[J5] Syed Muzahir Abbas, Yogesh Ranga, Karu P. Esselle, Ladislau Matekovits, Stuart G. Hay, "Ultra-Wideband Low Profile CPW-fed Slot Antenna Loaded with Dual-layer Frequency Selective Surface for Stable Directional Patterns Over a Broad-Bandwidth,".

[J6] Syed Muzahir Abbas, Yogesh Ranga, Pei-Yuan Qin, Karu P. Esselle, "A Simple Coplanar-Strip-Fed Switchable Antenna for 2.45 GHz ISM and UWB Systems,".

1.3.2   Invited Papers

[I1] Syed Muzahir Abbas, Yogesh Ranga, Karu P. Esselle, Stuart G. Hay, "Recent Developments in Antennas with Full Ground Plane for Wireless Body Area Networks," *International Symposium on Antennas and Propagation (ISAP 2015)*, November 9-12, 2015, in Hobart, Tasmania, Australia. (Invited Paper)

[I2] Syed Muzahir Abbas, Jawad Foroughi, Yogesh Ranga, Ladislau Matekovits, Karu P. Esselle, Stuart G. Hay, "Stretchable and Highly Conductive Carbon Nanotube-Graphene Hybrid Yarns for Wearable Systems," *10th International Conference on Body Area Networks (BodyNets 2015)*, September 28-30, 2015 in Sydney, Australia. (Invited Paper)

[I3] Roy B. V. B. Simorangkir, Syed Muzahir Abbas, Karu P. Esselle, "Robust Wideband Printed Antennas for Body-Centric Communications," *10th International Conference on Body Area Networks (BodyNets 2015)*, September 28-30, 2015 in Sydney, Australia. (Invited Paper: The Keynote Speech of UWBAN-2015)

[I4] Syed Muzahir Abbas, Karu P. Esselle, Yogesh Ranga, Pei-Yuan Qin, "Reconfigurable Antennas with Narrowband and Ultra Wideband Modes," *IEEE MTT-S International Microwave Workshop Series on RF and Wireless Technologies for Biomedical and Healthcare Applications (IMWS-Bio 2015)*, September 21-23, 2015 in Taipei, Taiwan. (Invited Paper)

[I5] Syed Muzahir Abbas, Yogesh Ranga, Karu P. Esselle, "Reconfigurable Antenna Options for 2.45/5 GHz Wireless Body Area Networks in Healthcare Applications," *37th Annual International Conference of the IEEE Engineering in Medicine and Biology Society (EMBC)*, August 25-29, 2015 in Milano, Italy. (Invited Paper)

[I6] Syed Muzahir Abbas, Yogesh Ranga, Karu P. Esselle, "A Switchable Printed Antenna with a Ground Plane for 2.45/5 GHz Wireless Body Area Networks," *International Workshop on Antenna Technology (iWAT 2015)*, March 4-6, 2015, Seoul, Korea. (Invited Paper)

[I7] Syed Muzahir Abbas, Yogesh Ranga, Karu P. Esselle, "An Armband-Wearable Printed Antenna with a Full Ground Plane for Body Area Networks," *IEEE Antennas and Propagation Symposium*, July 6-12, 2014 in Memphis, Tennessee, USA. (Invited Paper)

1.3.3 Conference Papers

[C1] Syed Muzahir Abbas, Syeda Fizzah Jilani, Akram Alomainy, Karu P. Esselle, Stuart G. Hay, "A Frequency Switchable Printed Antenna for 2.4/5GHz WLAN," *International Symposium on Antennas and Propagation (ISAP)*, November 9-12, 2015 in Hobart, Tasmania, Australia.

[C2] H. Zahra, Syed Muzahir Abbas, M. Farhan Shafique, Karu P. Esselle, "A Switchable FSS based on Modified Jerusalem-Cross Unit Cell with Extended Top Loading," *International Symposium on Antennas and Propagation (ISAP)*, November 9-12, 2015 in Hobart, Tasmania, Australia.

[C3] Syeda Fizzah Jilani, Syed Muzahir Abbas, Karu P. Esselle, Akram Alomainy, "Millimeter-Wave Frequency Reconfigurable T-shaped Antenna for 5G Networks," *IEEE Workshop on Advances in Body-Centric Wireless Communications and Networks and Their Applications (BCWNets)*, October 19-21, 2015 in Abu Dhabi, UAE.

[C4] Syed Muzahir Abbas, Yogesh Ranga, and Karu P. Esselle, "Sensitivity of a Wearable Printed Antenna with a Full Ground Plane in Close Proximity to Human Arm," *9th European Conference on Antennas and Propagation (EuCAP 2015)*, April 12-17, 2015 in Lisbon, Portugal.

[C5] Syed Muzahir Abbas, Yogesh Ranga, Karu P. Esselle, Stuart G. Hay, "Conformal Antenna for Wireless Body Area Network Systems Operating in 2.45 GHz Industrial, Scientific and Medical Band," *Fourteenth Australian Symposium on Antennas*, February 18-19, 2015 in Sydney, Australia.

[C6] Syed Muzahir Abbas, Ladislau Matekovits, Yogesh Ranga, Karu P. Esselle, "Controlling the Band-Gap of a High Impedance Surface of Quasi-Periodic Sequences

using Cascade Arrangement," *8th European Conference on Antennas and Propagation (EuCAP 2014)*, April 6-11, 2014, Hague, Netherlands.

[C7] Syed Muzahir Abbas, Yogesh Ranga, Karu P. Esselle, "A Printed Dual Band Antenna with a Ground Plane and Electromagnetically-Coupled Feed for Wireless Body Area Networks," *International Workshop on Antenna Technology (iWAT 2014)*, March 4-6, 2014, Sydney, Australia.

[C8] Syed Muzahir Abbas, Yogesh Ranga, Karu P. Esselle, "Stub- Loaded Printed Antenna with a Ground Plane and Electromagnetically Coupled Feed for 2.45GHz Body Area Networks," *IEEE MTT-S International Microwave Workshop Series on RF and Wireless Technologies for Biomedical and Healthcare Applications (IMWS-Bio 2013)*, December 9-11, 2013, Singapore.

[C9] Syed Muzahir Abbas, Yogesh Ranga, Karu P. Esselle, "A Printed Antenna with a Ground Plane and Electromagnetically Coupled Feed for 2.45GHz Body Area Networks," *IEEE Antennas and Propagation Symposium*, July 7- 13, 2013 in Orlando, Florida, USA.

[C10] Syed Muzahir Abbas, Michael Heimlich, Karu P. Esselle, "Microwave Characterization of Carbon Nanotubes Yarns for UWB Medical WBAN," *Thirteen Australian Symposium on Antennas*, February 13- 14, 2013 in Sydney, Australia.

Chapter 2

Background and Related Work

In this chapter we present an overview and related work for the topics covered in this thesis. This will enable the reader to quickly refresh on the relevant topics. These topics include wireless body centric communication and its different communication types. Reported work carried out in studies on narrow band antennas for wireless body area networks include embroidered and wearable antennas. Discussion on ultra wideband antennas addresses their being used to reject interference through band notching, and increase in gain and radiation pattern controlling using reflectors such as frequency selective surfaces and high impedance surfaces. Research work on reconfigurable antennas is highlighted. Carbon nanotubes and carbon nanotube yarns are discussed in detail along with their potential applications and usage to highlight the significance to this new research dimensions.

2.1   Wireless Body Centric Communication

Wireless body centric communication is an emerging technology of fourth and fifth generation mobile technology. One of the research topics in antennas for this type of communication is body worn antennas. In recent years, textile and polymer composite have been

used as antenna substrates. In future complete body worn antennas will be developed that might be integrated into clothing called smart clothes. These smart clothes will be used in sports outfits, military, medical, space applications, etc. The research conducted on wearable antenna designs in the previous years used conventional antenna design methods such as monopoles, dipoles and planar printed shapes. Microstrip patch antennas can be constructed using printed circuit fabrication techniques. Due to their advantages such as light weight, low profile and ease of fabrication they have become popular and are now mostly used for wearable antennas. Employing carbon nanotubes (CNTs) in place of conventional metals is expected to improve antenna performance along with size reduction and weight reduction.

Body centric communication includes Personal Area Network (PAN) and Body Area Network (BAN). A typical Body Area Network (BAN) consists of several communication/sensing nodes placed over the body. They constitute the first level of BAN. These nodes communicate with each other and transfer the data to a main personal server (cell phones or PDAs). The last level is the main remote server, in which the remote application is working and to which the data is transferred. Fig. 2.1 shows a typical Body Area Network connected to the internet. Body Area Networks can be classified into three categories on the basis of placement of devices [14].

2.1.1   Off-body Communication

Off-body communication is defined as communication from off-body (i.e. from point away from the body) to an on-body device or system. For example, a device placed over the body is communicating with some access point or base station that is at a distance from the body.

---

[1]http://www.jneuroengrehab.com/content/2/1/6/figure/F1?highres=y
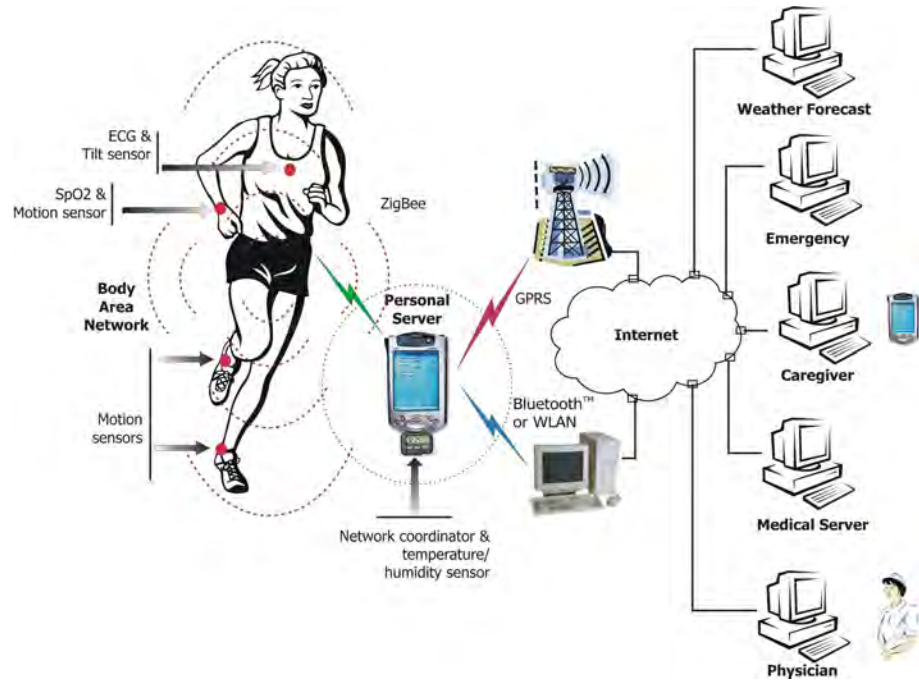
Figure 2.1: Typical Body Area Network.[1]

2.1.2   On-body Communication

Communication between on-body networks and wearable systems is termed as on-body communication. In this category the channel is the surface of the body and both antennas in the link are placed on the body. On-body communication is influenced by dielectric properties of the body which vary with change of frequency [15]. Fig. 2.2 describes a simple human body model along with antenna placement over the body.

2.1.3   In-body Communication

Communication to medical implants and sensors (i.e. system that is planted inside the body) is known as in-body communication. Since we are communicating through the body we have to take SAR into consideration because exposure to and absorption of electromagnetic radiation is harmful for human body. It is used for communication at a very short distance since the signal is highly degraded due to greater lossy nature of
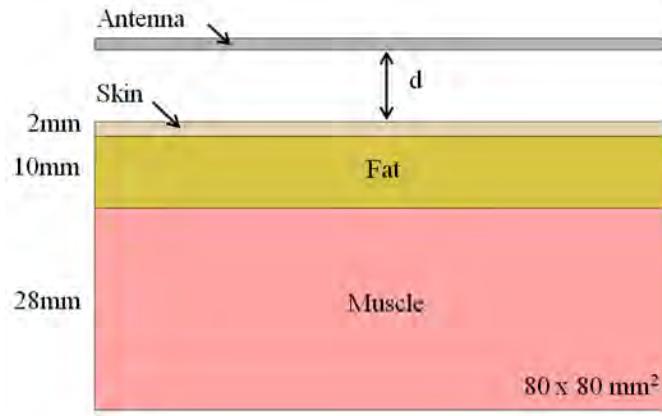
Figure 2.2: Antenna placement over a simplified body model with three tissue layers.

human body.

2.2 Narrow Band Antennas

Body Centric Wireless Communication (BCWC) is a rapidly growing research area targeted for applications in healthcare, public safety and defense [14]. In medical and healthcare systems, wireless communication is used for monitoring patients, telemedicine and elderly healthcare. Sensors can collect data on respiratory rate, ECG (electrocardiogram), EEG (Electroencephalography), blood pressure and flow, nerve potentials, EMG (Electromyogram), SGR (Galvanic Skin Reflex), temperature, etc. This data needs to be communicated from one location to another location, either over the body or away from the body. Antennas play a vital role in BCWC (i.e. on-body, in-body and off-body). Significant changes in antennas' properties have been reported when placed close to a human body. The challenge here is to achieve a wide coverage over the body and around it, and to make the return loss less sensitive to the gap between the antenna and the human body [16]. Compact antennas with full ground planes and electromagnetically coupled feeds, designed for body area network devices operating in the ISM band at 2.45 GHz,

have been reported previously [17,18]. An electromagnetically coupled feed was employed to partially fill a null that was otherwise present in the direction opposite to the feed. In [18] stub loading has been used to achieve better impedance matching. A dual-band antenna with a full ground plane and an electromagnetically coupled feed, operating in both the ISM band at 2.45 GHz and the public safety Wireless Local Area Network (WLAN) band at 4.9 GHz (4.9404.990 GHz) has also been reported [19]. A printed antenna described in [20] has a flexible substrate. With a full ground plane and electromagnetically coupled feed, it is suitable for arm-band wearable applications in the 2.45 GHz ISM band. These antennas exhibit wide radiation patterns along the body's surface to provide wider coverage. The narrow gap between metal strips in these antennas, required for electromagnetically coupled feeding, is difficult to fabricate. A reconfigurable antenna with a full ground plane for 2.45/5 GHz has been presented in [21]. This design does not require such a small gap and is easy to fabricate. It also exhibits a wide radiation pattern along the body's surface to provide wide coverage. By introducing switching to the design, the operating band can be reconfigured between 2.45 GHz and 5 GHz bands. [22] presents a comparison between reconfigurable antenna with a partial ground and a full ground plane. This analysis helps a biomedical device designer to choose an appropriate antenna design for a given application, considering trade-offs between bandwidth, impedance matching, radiation characteristics and sensitivity of antenna to the gap between the antenna and the human body.

2.3 Embroidered and Wearable Antennas

Wireless body area networks (WBAN) have attracted the attention of antenna researchers in the recent decades, as they find promising applications in healthcare, monitoring, defence, sports, rescue and public safety [14]. Wearable systems for these applications are

expected to use antennas that are light weight, integratable in clothing, conformal and flexible for ease of mobility. Traditionally, antennas are made using copper wires or by etching metal patterns on rigid substrates [1]. These rigid antennas become permanently deformed or break when stretched, folded or twisted. Furthermore, when they are large they are not convenient for mobility. Rigid antennas are not a suitable choice for wearable applications as they may require antennas to be bendable and flexible. In the literature, several flexible antennas have been reported using copper tape [6] and conductive ink [23, 24] on flexible substrates. Copper tape and conductive inks have durability issues for operating over longer periods of time as the tape peels off the substrate easily and the inks erase off. In the past, reliable fabrication and excellent performance of antennas [8], RFID tags [2] and transmission line samples [25] with conductive E-fibers on flexible substrates using embroidery technique [1] have been reported. Fig. 2.3 shows some of the selected designs for antennas, sensors and transmission lines reported using embroidery, copper fabric and copper tape.

Several embroidered antennas and wearable sensors have been reported in the literature using conductive fibers on textiles and polymer composite substrates [1, 3–5, 7, 8]. Embroidered wearable, flexible and stretchable antennas on textile and polymer composites have been reported earlier [1, 2, 26]. The performance of these antennas has been investigated and results are comparable to the standard flexible copper antennas. Though significant research has been carried out on embroidered antennas which are designed for lower frequencies or to provide narrow band operation, more investigation is needed to analyze their behavior when designed for broad band or ultra-wide band operation.

(a) (b) (c)

(d) (e)

(f) (g) (h)

(i) (j)
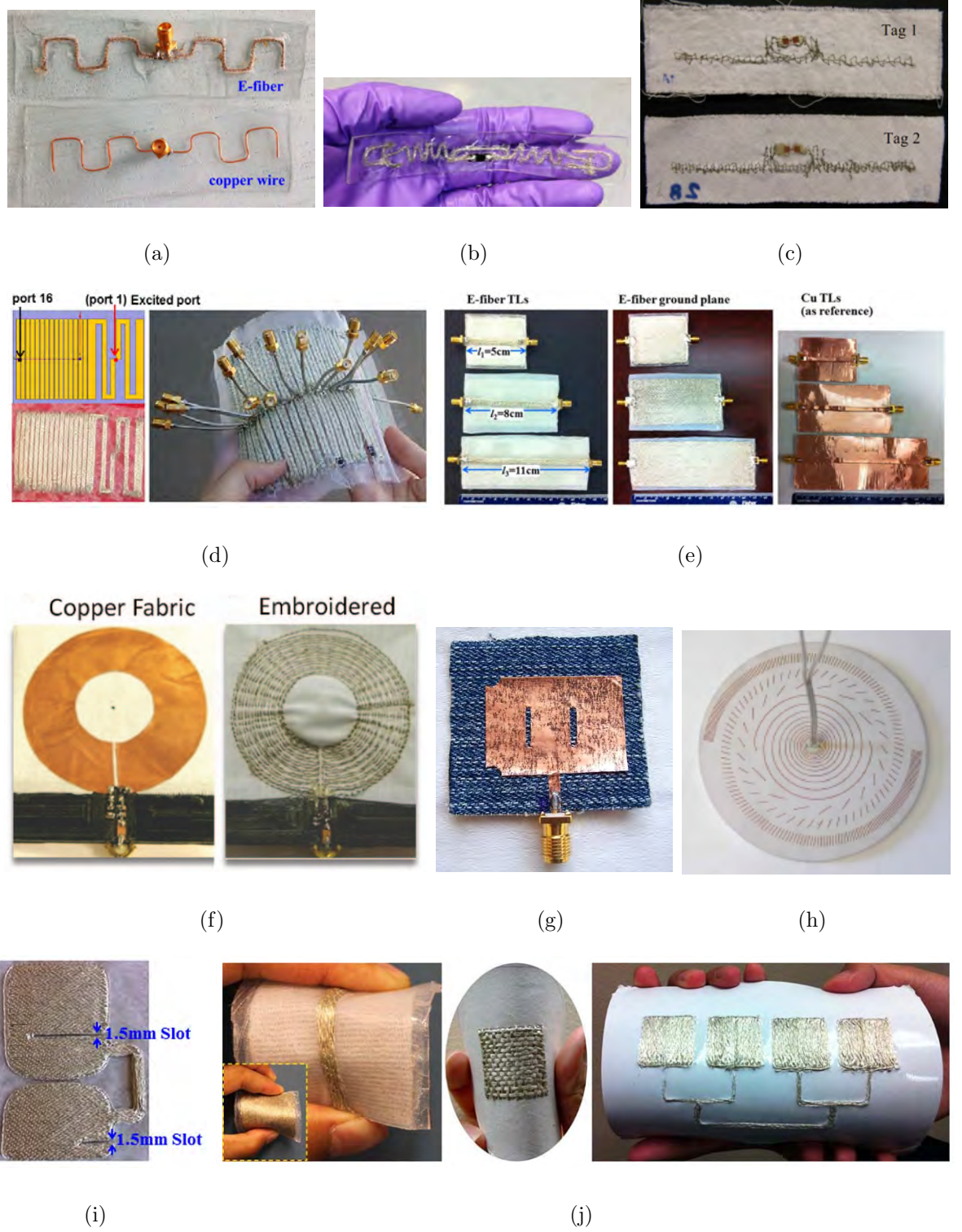
Figure 2.3: Selected designs of wearable antennas, sensors and transmission lines using embroidery, copper fabric and copper tape (a) [1] (b) [2] (c) [3] (d) [4] (e) [4] (f) [5] (g) [6] (h) [7] (i) [4] (j) [8].

2.4   Ultra Wideband Antennas

Ultra wideband (UWB) systems attract the attention of researchers due to their potential of handling communications at high data rates, accurate positioning and short pulse transmission [27, 28]. UWB systems have been considered for a range of applications such as ground penetrating radars initially targeted for detection of land-mines in military [29–31], rescue operation by detection of trapped persons [32], evaluation of concrete, pavements and walls [33], short range communications at higher data rates [34], medical and through-wall imaging [35–37], security [38, 39], and wearable devices in wireless body area network [40–43]. FCC has specified an unlicensed spectrum from 3.1 to 10.6 GHz for UWB technology, leading to more focused research in this area. Given the demand for compact and light weight UWB systems, antenna designers often face challenges such as meeting space constraints, controlled stable radiation patterns and achieving wide impedance bandwidth. Printed UWB antennas are suitable candidates in meeting these challenges due to their planar structure, size, low profile, light weight, easy fabrication and low cost.

2.4.1   Ultra Wideband Antennas with Band Notching

UWB printed antenna designers often face challenges such as meeting space constraints, achieving a wide impedance bandwidth and wide radiation patterns. In addition, the antenna may need to effectively reject potential interference from the existing narrowband systems operating at higher power levels. This particular requirement becomes more stringent as many wireless systems including 3.6GHz IEEE 802.11y Wireless Local Area Networks (WLAN) (3.6575−3.69GHz), 4.9GHz public safety WLAN (4.94−4.99GHz) and 5GHz IEEE 802.11a/h/j/n WLAN (5.15−5.35GHz, 5.25−5.35GHz, 5.47−5.725GHz, 5.725−5.825GHz) are operating within the FCC UWB band of 3.1−10.6GHz.

Several designs of planar printed UWB antennas incorporating a notch-band have been proposed to minimize this interference. The most commonly used method is inserting various shapes of slots in the radiating elements or in the ground plane [44–50]. Parasitic elements, electromagnetic-band gap (EBG) structures [51], integrated stopband filters [52], defected ground structures (DGS) [53, 54] and frequency selective surfaces (FSS) positioned above the antennas [55] have also been used to achieve band rejection.

Another popular method is to use a resonator on the other side of the substrate, such as a split ring resonator (SRR), square ring resonator [56], CPW resonator [48], composite right/left-handed (CRLH) resonator [57], capacitive loaded loop (CLL) resonator, open-loop resonator [58, 59] or a dual-gap open-loop resonator. However, only a few of these antennas have strong band rejections with VSWR above 15 [48, 51, 56, 60]. We still need more compact antennas with high band rejections and wide radiation patterns across the UWB band.

2.4.2   Ultra Wideband Antennas with Reflectors

Several designs of printed UWB antennas have been reported in literature utilizing monopole radiating structures with partial ground plane [61, 62] or with co-planer waveguide (CPW) [63–65]. Slots have also been incorporated in monopole radiators [62] or used independently as radiators [13] to achieve ultra-wide bandwidth. Typically slot antennas are printed on one side of the substrate and radiators bi-directionally [63], however, due to their planar and printed structure they constitute a suitable choice in meeting space constraints. In some UWB applications, such as point-to-point communication, imaging or body area network, a uni-directional radiation beam is desired. For slot antennas, uni-directional beam can be achieved by reflecting radiations from one hemisphere to another hemisphere using ground plane or reflector. To achieve a uni-directional pattern, an electric conducting surface has to be added at a distance of a quarter-wavelength below the

slot as a reflector. This works only for narrow-band systems, as when metallic reflectors are placed at a distance of $\lambda/4$; the electrical length of the forward and backward paths compensates the out-of-phase reflection from the metallic plate, and the entire energy is radiated in one direction due to constructive interference between the two rays. Due to wide bandwidth and size constraints this solution is not feasible in UWB systems. To obtain a uni-directional radiation pattern from the slot over a broad range of frequency, two different approaches are available in literature. The first approach involves cavity-backed slot antennas whereas the second approach uses artificial magnetic conductor (AMC) in the ground plane.

2.5 Reconfigurable Antennas

With the recent advances in modern communications, Medical Body Area Networks (MBAN) [40] and Body Centric Wireless Communication (BCWC) [14] are rapidly growing areas of research that demonstrate significant potential in healthcare, public safety, sports and defence applications. Devices used for these applications are expected to be less expensive, light weight, and supportive to long- and short-range communications. Generally, two separate antennas are required, namely a narrow-band antenna for long-range communications and a wide-band antenna for short-range communications at a higher data rate. That consumes a lot of space and restricts the compactness of the device. Also it is very challenging to design multiple antennas to fit-in and operate in a limited space. Single antenna supporting multiple frequency bands can significantly contribute towards size reduction in wireless communication systems.

In the last decade, the development of printed reconfigurable antennas helped in solving some of these challenges [66, 67]. These printed antennas have the advantages of low cost, low profile, and providing frequency, polarization and pattern reconfigurabil-

ity [68, 69]. The narrowband reconfigurable antennas exploit the potential of microstrip patches. Since the introduction of the first varactor-tuned microstrip patch [70], microstrip antennas have evolved with emerging switching technologies of PIN diodes [68, 71], varactors [72], RF microelectromechanical systems (MEMS) [73], field-effect transistors (FETs) [74] and optical switches [75]. While there have been substantial advances in the design of frequency reconfigurable antennas, most of the reported microstrip-fed antennas require vias and double-sided printing, which complicate fabrication. In addition most of the designed antennas cover sensing applications within a certain band. However, sometimes the transmission of data over a long range and the generation of remote sleep and wake signals of wearable instruments require operation in the ISM band, which needs a separate antenna [40].

Recently, a selective frequency-reconfigurable antenna [76] for cognitive radio applications demonstrated switching between a wide operating band of $2.63-3.7$GHz and four different sub-bands, which enables it to be used for sensing the entire band and then adjusting its bandwidth to select the suitable sub-band and pre-filter out the other ones. To further widen the use of bandwidth a reconfigurable slot antenna for the upper ultra-wideband frequency range is presented in [77]. The antenna can operate at any of eight adjacent sub-bands in the $6.0-10.6$GHz frequency range, and is configured by means of seven PIN diode switches. A more versatile reconfigurable antenna with frequency, pattern and polarization reconfiguration option is presented in [78]. The antenna has planar geometry and is designed for frequency, pattern and polarization reconfigurability over ultra-wide bandwidth. When the antenna is frequency reconfigured, the antenna can switch operation from Ultra-wideband mode ($2.6-11$GHz) to Narrowband mode ($4.39-5.85$GHz).

While there have been substantial advances in the design of frequency reconfigurable antennas, most of the reported microstrip-fed antennas require vias and double-sided printing, which complicate fabrication. In addition most of the designed antennas cover

the sensing application within a certain band. However, sometimes the transmission of data over a long range and the generations of remote sleep and wake signals of wearable instruments require operation in the ISM band, which need a separate antenna [40]. In chapter 7, a simple coplanar-strip-fed bandwidth reconfigurable antenna capable of switching between an ultra-wide bandwidth $(3.1-10.6\text{GHz})$ in first mode and the 2.45GHz ISM band in second state is proposed. The complete feed network and antenna is printed on a single low-cost substrate. To the best of the authors' knowledge, no such coplanar-strip-based antennas have been reported in the literature.

2.6   Carbon Nanotubes and Carbon Nanotube Yarns

Metals are commonly used as conductors to carry charge. In antenna theory, they are used as radiating elements, ground planes and feed lines [79]. Some recent studies have used various composite materials as replacement for metals like conductive inks (silver nanoparticle ink [23,80,81] and metallo-organic conductive ink), conducting polymer [82], metalized foam and advanced carbon-fiber composite (CFC) materials. There are various types of CFCs: short carbon fibers (SCF), reinforced continuous carbon fibers (RCCF), carbon black (CB) and carbon nanotube (CNT) [10,11]. Carbon nanotubes (CNTs) are drawing great attention of researchers due to their significant mechanical, electrical and thermal properties. CNT composites can be made using single-wall carbon nanotubes (SWCNTs) or multi-wall carbon nanotubes (MWCNTs). CNT yarns comprised of woven individual nanotubes can be made in greater lengths and are suitable for nanoelectronics and nanoantenna applications. Researchers have investigated electrical properties (i.e. conductivity and resistivity) for direct current (DC) but these properties need to be explored at RF/microwave frequencies.

Carbon nanotube (CNT) has emerge as a potential candidate for the replacement of

conventional metals due to their significant mechanical (high strength and load bearing), electrical (conductivity and resistivity), thermal properties (sustain at high temperatures) and non-oxidizing abilities. CNTs have been of interest in nanoelectronics and nanoantenna applications since the density of CNT composites is about five times lower than copper and around half that of aluminium. Also their thermal conductivity is about ten times that of copper. Electrical conductivity of CNT composites depends on the properties and loading of CNTs, the aspect ratio of the CNTs and the characteristics of the conductive network.

Researchers have explored use of CNTs as replacement of metals in antenna designing for multiband, wideband millimetre wave and load bearing antenna applications. In 2010, Mehdipour et al. [10] have proposed sierpinski fractal composite antenna using CNTs for multiband wireless applications covering UHF-RFID (900MHz), Bluetooth (2.4GHz) and WLAN (5.5GHz).

In 2011, CNT composites were investigated for wideband millimetre wave antenna applications [11]. By observing housing effects on the copper and CNT antennas performance, it has been proposed that at higher frequencies (i.e. above 30GHz) housing effect is significantly less, resulting in stable gain and less distortion in radiation pattern. At low frequencies both copper and CNT antennas have almost similar performance characteristics.

Yijun et al. [9] proposed polymer CNT sheets having high structural density vertically aligned carbon nanotubes within polymer composites. They also presented a circuit model to calculate CNT sheet conductivity. They achieved resistivity of 0.9 ohms/square as compared to earlier reported (i.e. 20 ohms/square) in the literature. By conducting mechanical tests for stress, strain and bending they proposed it as a suitable candidate for conformal load bearing antennas and RF circuits.

CNT yarns (fibers) and films are composed of individual CNTs. Various methods

<div align="center">(a)   (b)</div>
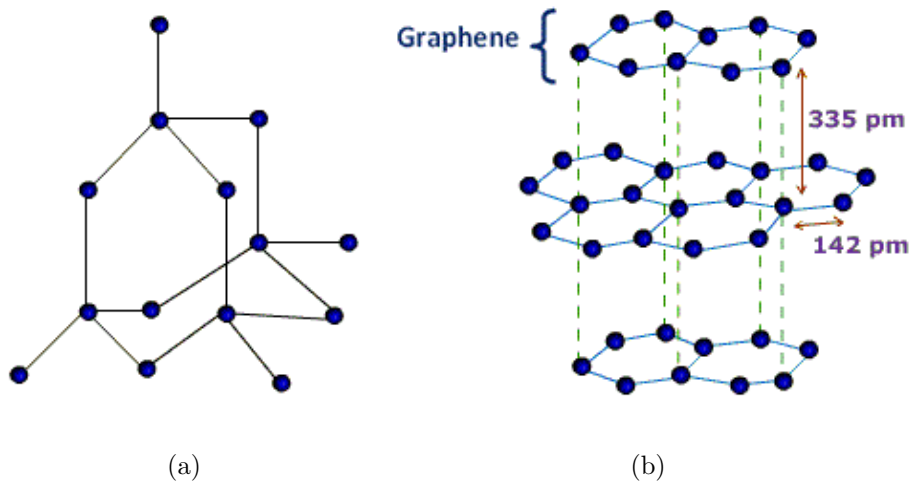
<div align="center">Figure 2.4: Atomic structure of (a) Diamond (b) Graphite.[2]</div>

have been reported for obtaining CNT yarns. CNT yarns can be spun from CNT forest by spinning as we obtain cotton yarn from cotton. CNT films can be converted to CNT fibers by passing CNT films through a drop of volatile liquid such as ethanol or methanol. As the volatile liquid evaporates, the surface tension shrinks the CNT films into densely packed CNT fibers. Diameter of CNT can be controlled by the CNT film width [12]. CNT films and CNT yarns are potential candidates for many RF applications such as aircraft and spacecraft antennas, mobile radio, satellite communications, wireless body area network (WBAN), body centric communication and biomedical. They are also becoming increasingly importance in nanoelectronics. Electrical properties such as conductivity and resistivity, and their behaviour at RF frequencies are important features that determine their use in these application. Since these properties depend on their manufacturing and various methods have been reported to obtain CNT and CNT yarn. Moreover, their electrical properties have also been explored and further improvement is desired. Their behavior at direct current (DC) has been investigated but at RF frequencies are yet to be explored.

---

[2]http://chem-guide.blogspot.com.au/2010/04/covalent-solid.html

2.6.1 Carbon Nanotubes

Diamond and graphite are two well known allotropes of carbon, and their atomic structures are shown in Fig. 2.4 (a) and (b) respectively. A layer of graphite (i.e. a single atom thick) is called graphene and is used to make carbon nanotubes. Carbon nanotubes (CNT) are allotropes of carbon and consist of nano scale tubular structures. A nanometer is one-billionth of a meter, or about one ten-thousandth of the thickness of a human hair. Depending on their structures carbon nanotubes can be categorized as:

Single-Walled Carbon Nanotubes

Single-walled carbon nanotubes (SWCNT) are tubes of graphite having a single cylindrical wall and are normally capped at the ends. The structure of a SWCNT can be visualized as a layer of graphite, a single atom thick, called graphene, which is rolled into a seamless cylinder as shown in Fig. 2.5. SWCNT typically have a diameter close to 1 nm while their length can be thousand times longer than their diameter. SWNT are expected to play a major role in the next generation of miniaturized electronics due to their unique electrical, mechanical and thermal properties.

Multi-Walled Carbon Nanotubes

Multi-walled nanotubes (MWCNT) consist of concentric tubes (i.e. multiple rolled layers) of graphene or a single sheet of graphite rolled into the shape of a scroll as shown in Fig. 2.6. The interlayer distance in MWCNT is close to the distance between the graphene layers in graphite. The diameters of MWNT are typically in the range of 5 nm to 50 nm. A multi-wall carbon nanotube is illustrated shown in Fig. 2.7.

These cylindrical carbon molecules have unusual properties, which are valuable for nanotechnology, electronics, optics and other fields of materials science and technology. In particular, they exhibit extraordinary thermal conductivity and mechanical and electrical
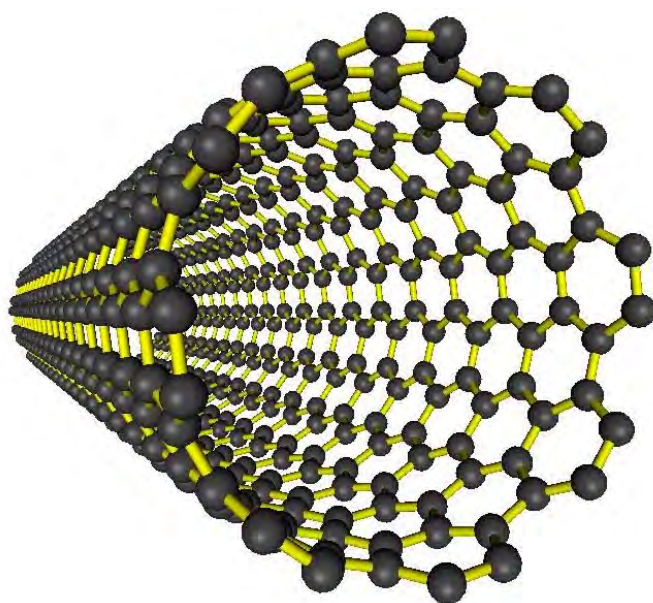
Figure 2.5: Carbon nanotube structure.[3]

properties. Fig. 2.8 presents a close-up look of carbon nanotubes and obtained CNT film.

Figure 2.6: MWCNT using graphene.[4]

---

[3]http://staff.aist.go.jp/h-kataura/Kogaku-kiji-forweb.htm

[4]http://www.nanowerk.com/spotlight/spotid=11723.php
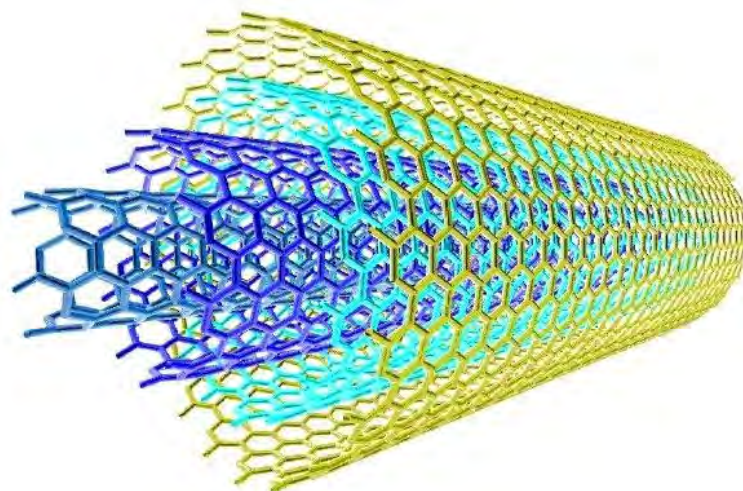
Figure 2.7: Multi-wall carbon nanotube.[5]
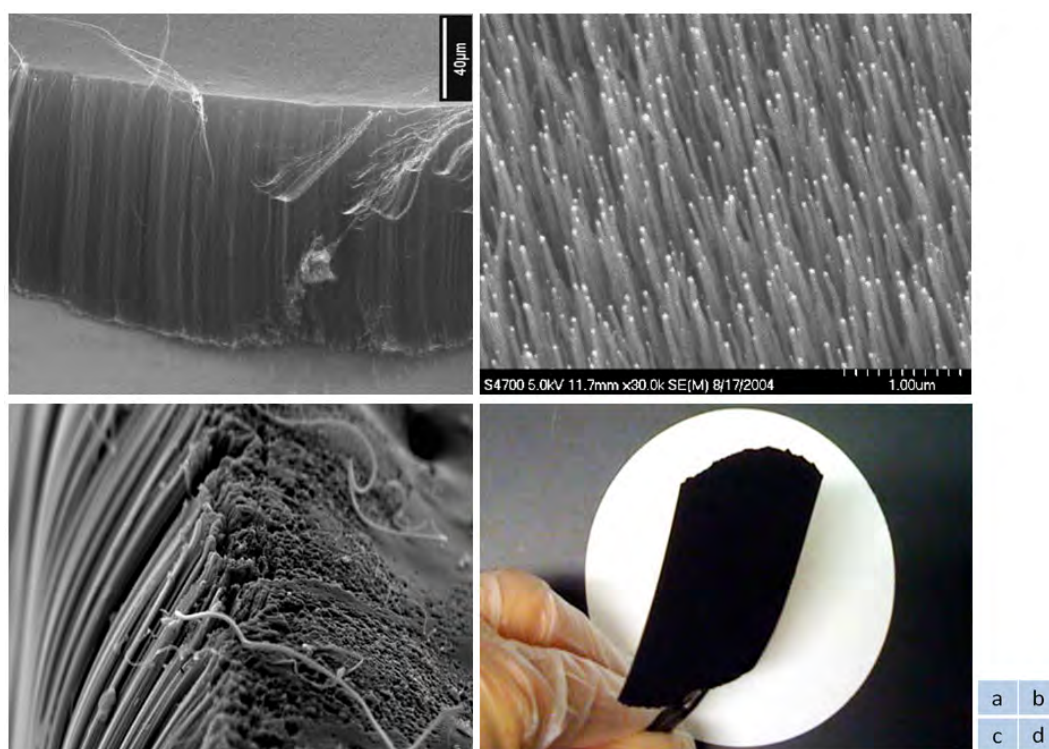
Figure 2.8: Carbon nanotube.[6] [7]

[5]http://staff.aist.go.jp/h-kataura/Kogaku-kiji-forweb.htm
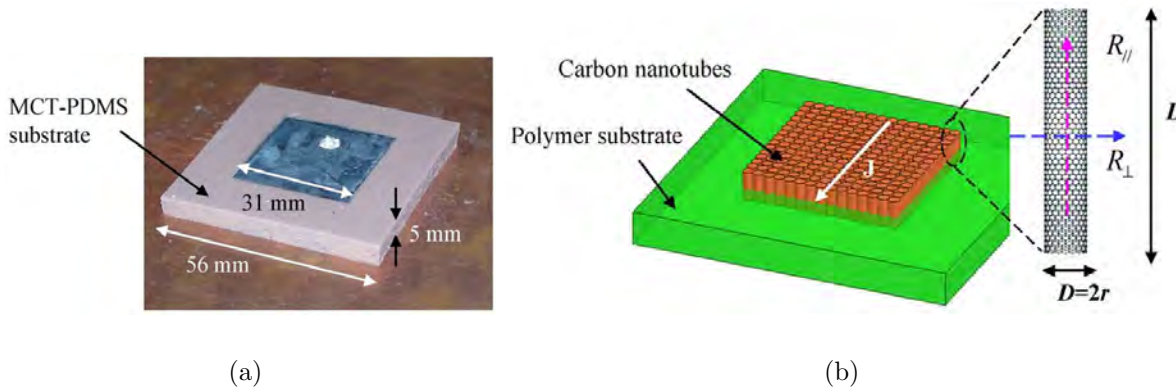
Figure 2.9: (a) Printed polymer-CNT patch antenna (b) model of vertically aligned CNTs [9].

2.6.2   Applications of Carbon Nanotubes

Carbon nanotubes have great promise for a number of applications due to their mechanical, electrical, thermal properties and non-oxidizing abilities. Their density is about five times lower than copper and around half that of aluminium. Also their thermal conductivity is about ten times that of copper. They can be flexible as well as five times stronger than steel. Electrical conductivity of CNT composites depends on the properties, loading and aspect ratio of the CNTs, and the characteristics of the conductive network. SWCNT can be used in numerous applications, such as field-emission displays, nanocomposite materials, nanosensors, and logic elements. These materials are on the leading-edge of electronic fabrication. Particularly in the domain of antenna design, they have been used for planar antennas, antenna arrays and load bearing antennas. They have also been used to design antennas for multiband wireless and wideband millimetre-wave antenna applications.

---

[7]http://explow.com/buckypaper

[7]http://www.phy.mtu.edu/yap/frontiercarbon.html
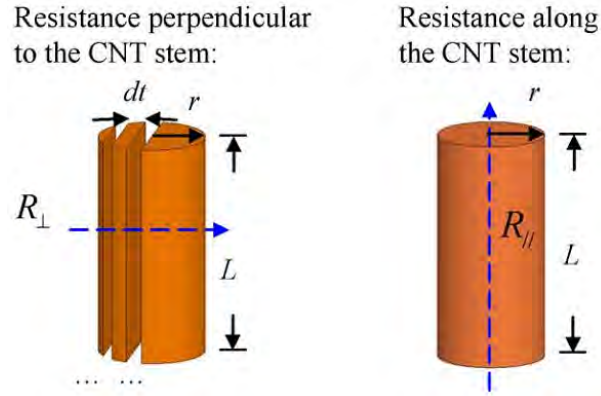
Figure 2.10: Ohm's law for a single CNT [9].

Load Bearing Antenna Applications

Yijun et al. [9] proposed polymer CNT sheets having high structural density vertically aligned carbon nanotubes within polymer composites. Fig. 2.9 shows the fabricated antenna prototype and model design.

Practically achieved resistivity for CNTs is very high and researchers are currently working to improve it. In this context, the authors have also presented a circuit model to calculate CNT sheet conductivity. On the basis of ohms law for single CNT as illustrated in Fig. 2.10, they investigated resistance for array of CNTs and proposed a circuit model which is explained in Fig. 2.11. They achieved resistivity of 0.9 ohms/square which is comparable to what has been reported in earlier studies, i.e. 20 ohms/square.

By conducting mechanical tests for stress, strain and bending as illustrated in Fig. 2.12, they proposed it as a suitable candidate for conformal load bearing antennas and RF circuits.
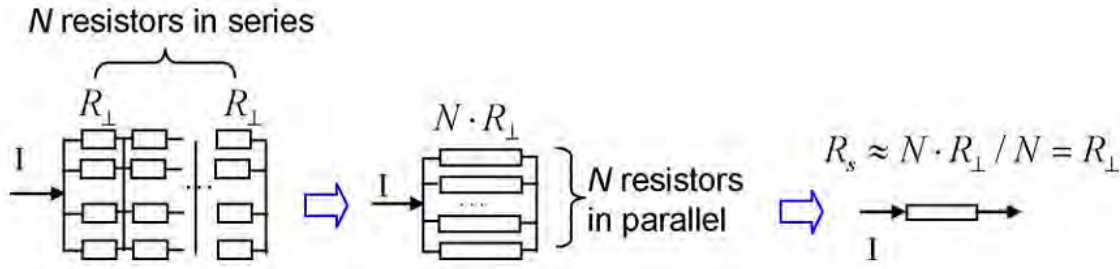
Figure 2.11: Model of the CNT array for sheet resistance calculation [9].

Multiband Wireless Applications

In 2010, Mehdipour et al. [10] proposed sierpinski fractal composite antenna (as shown in Fig. 2.13) using CNTs for multiband wireless applications covering UHF-RFID (900MHz), Bluetooth (2.4GHz) and WLAN (5.5GHz). Measured and simulated results show that the CNT composite antennas has good performance over the desired frequency bands. Based on their investigations, the authors found that antenna gain and read range can be controlled by changing the conductivity of the composite, which is not possible for materials with fixed conductivity such as copper.

Wideband Millimeter-Wave Antenna Applications

In 2011, Mehdipour et al. [11] investigated CNT composites for wideband millimetre wave antenna applications (presented in Fig. 2.14) over a frequency range of $24-34$GHz. By observing housing effects (i.e. how much the antenna is affected by the surrounding metallic objects) on the copper and CNT antenna performance, it has been proposed that at higher frequencies (i.e. above 30GHz) housing effect is significantly less, resulting in stable gain and less distortion in the radiation pattern. At low frequencies both copper and CNT antennas have almost similar performance characteristics.
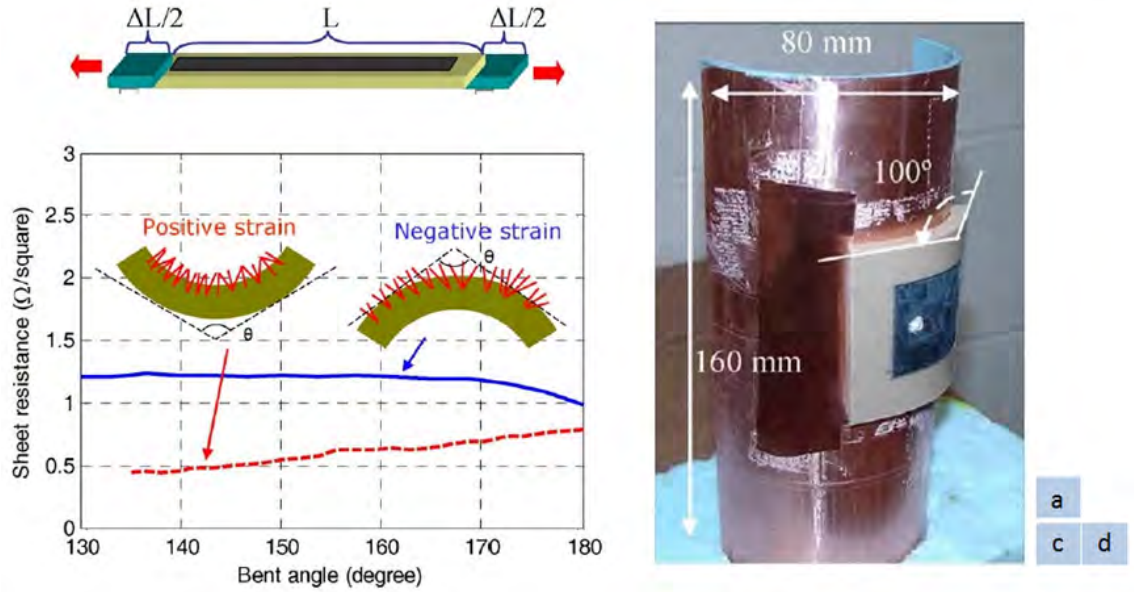
Figure 2.12: Mechanical test of proposed antenna for (a) Stress (b) Strain and (c) Bending [9].

2.6.3 Carbon Nanotube Yarns

CNT yarns (fibers) are composed of individual CNTs. They can be spun from the CNT forest using the spinning process in a similar way as we obtain cotton yarn from raw cotton. Several methods have been described in the literature to obtain CNT yarns. The yarns were drawn from the forest by pulling and twisting [83]. Fig. 2.15 describes how CNT yarn can be obtained form the CNT forest. CNT yarns can also be produced by passing CNT films through a drop of volatile liquid such as ethanol or methanol [12]. As the liquid evaporates, the surface tension of the liquid shrinks the CNT film into densely packed CNT fibers (yarns) as shown in Fig. 2.16. CNT yarn can also be produced by employing the dry spinning process [84].

---

[8]http://www.csiro.au/Outcomes/Materials-and-Manufacturing/Innovation/Carbon-Nanotubes-2.aspx
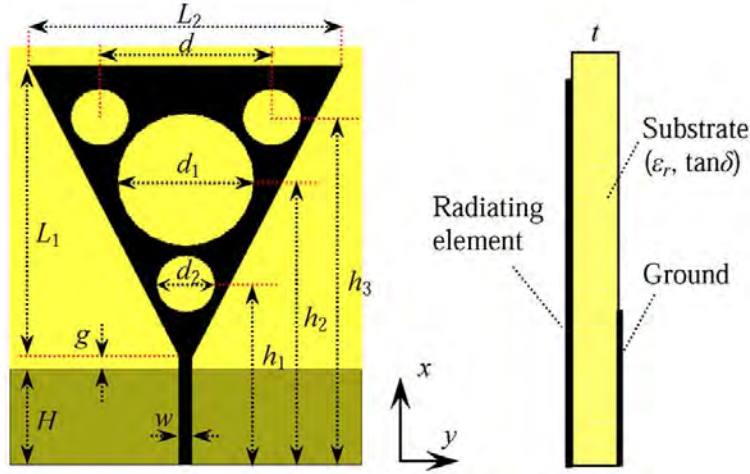
Figure 2.13: Full-composite fractal antenna using carbon nanotubes for multiband wireless applications [10].

2.6.4   Applications of CNT Yarns

CNT yarns can be used in medical applications, such as artificial muscle due to their incredible strength-to-weight ratio and can also be utilized for in-body integrated circuits. CNT yarns can also be modelled as potential data transmission lines. Due to their significant advantages they are suitable for RF/microwave dielectrics, conductors, sensors, transistors, MEMs, VLSI, EMI/EMC and electronics applications.

2.6.5   Properties of Carbon Nanotubes Yarns

Researchers have explored electrical properties of CNT yarns at DC but they have not been characterized for RF/Microwave frequencies. The properties of CNTs and CNT yarns depends on that how they are obtained. Researchers are investigating ways to determine and improve their properties because the currently achieved properties are not good and require further improvements. Determining electrical properties such as conductivity and resistivity will open new dimensions for their use in nanoantenna and nanoelectronics applications.

(a)   (b)
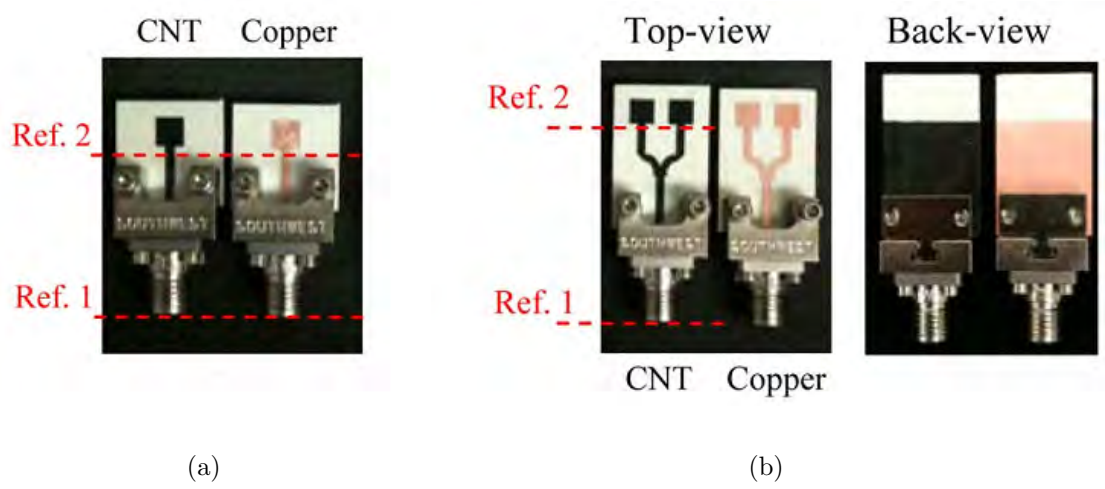
Figure 2.14: (a) Proposed antenna design (b) Antenna Array [11].
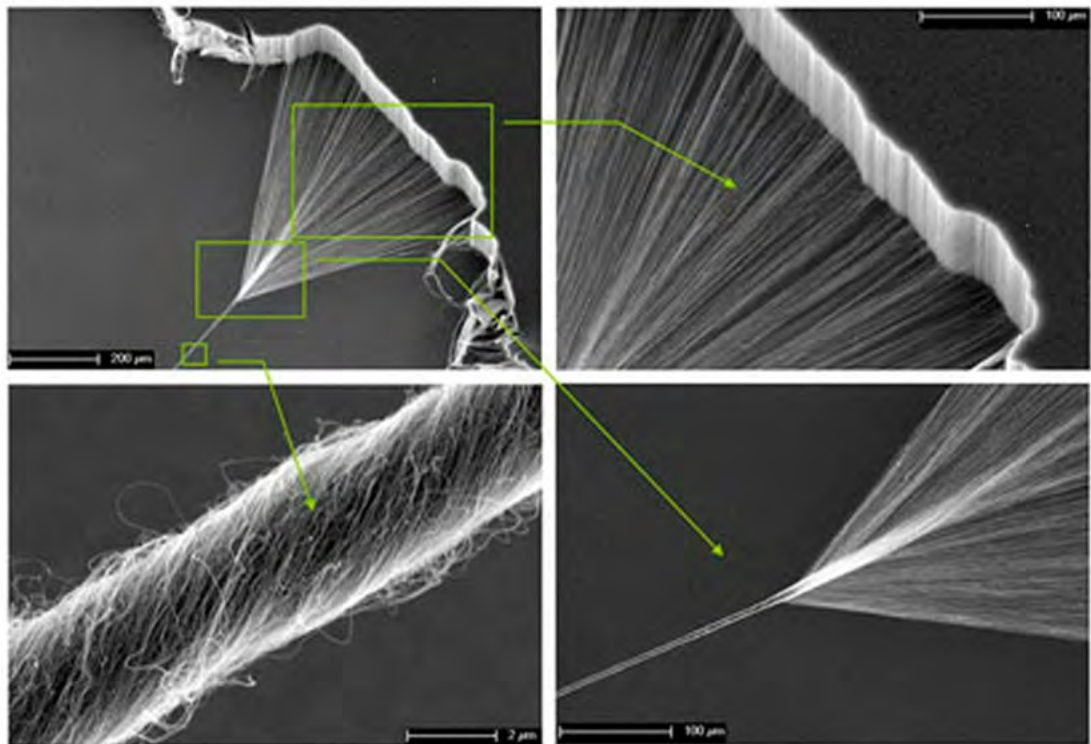
Figure 2.15: CNT yarns produced by CSIRO.[8]
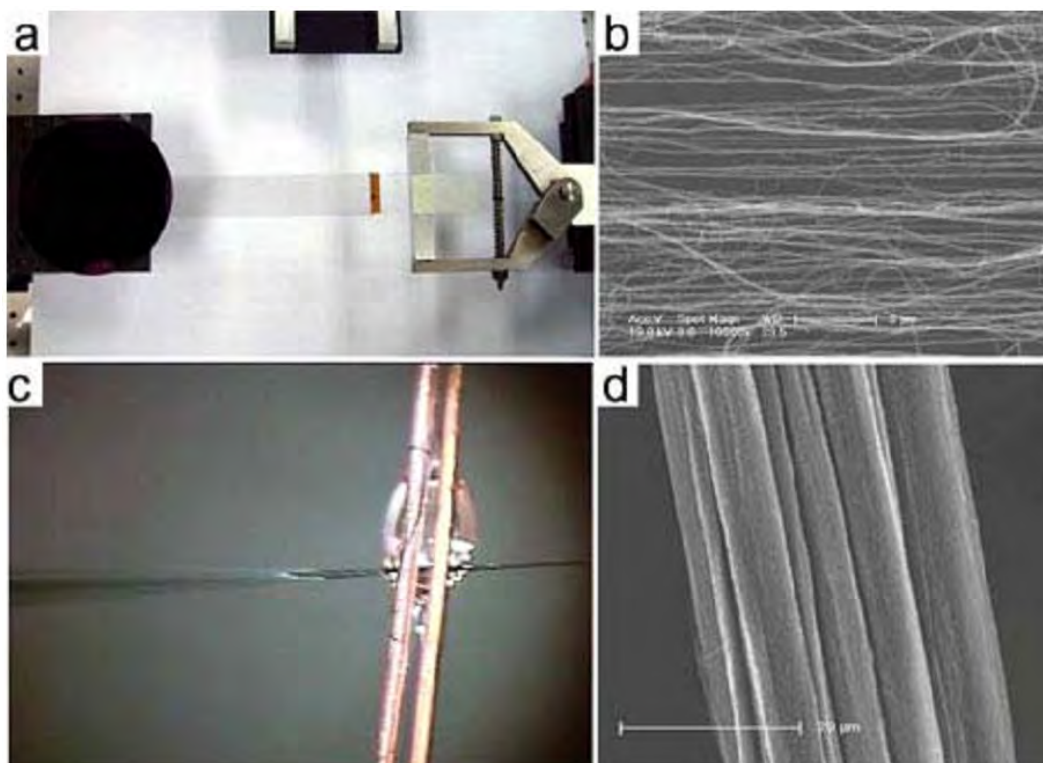
Figure 2.16: (a) Spinning CNT film (b) A SEM image of the CNT film (c) A CNT film shrinks into a fiber when passing through a drop of ethanol (d) A SEM image of the CNT fiber [12].

2.7   Conclusion

In this chapter we have discussed wireless body centric communication and its different types. Moreover, narrow- and ultra wide-band antennas are discussed. Research work carried out on embroidered and wearable antennas, sensors and transmission line structures for potential usage in wireless body area networks is highlighted. Discussion on ultra wideband antennas is focused on employing them to reject interference by band notching, and increase in gain and radiation pattern controlling using reflectors such as frequency selective surfaces and high impedance surfaces. Furthermore this chapter presents research on reconfigurable antennas. Finally, carbon nanotubes and carbon nanotube yarns are discussed in detail along with their potential applications and usage to highlight the significance towards new research dimensions.

Chapter 3

Narrow Band Antennas

Body Centric Wireless Communication (BCWC) is a rapidly growing research area targeted for application in healthcare, public safety and defence [14]. Ambitious projects like Google smart watch and curve phones promise endless possibilities for future. Their design needs to address the body transceiver specifications, the curvature of the body and the effects of body tissues on antenna performance. Significant changes in antenna performance characteristics have been reported when placed close to human body [42]. The challenge here is to achieve a wide beamwidth over the body and around, and to make the antenna return loss less sensitive to the distance between the antenna and the body [16].

In this chapter, we present novel narrow-band antennas to provide single- and dual-band operation for the 2.45GHz industrial, scientific and medical (ISM) band and for 4.9GHz public safety wireless local area network (WLAN)/5GHz IEEE 802.11 WLAN. These antennas have significant advantages of compactness (only 14mm wide), full ground plane to minimize radiation towards the body, a wide radiation pattern over the body surface to provide maximum coverage, and less sensitivity to the variation of the gap between the antenna and the human body. These advantages make them suitable for

on-body communications and wearable applications. This chapter also presents their sensitivity when placed in close proximity to the human arm.

Printed antennas are selected to achieve the desired objectives due to their significant advantages of low profile, compactness, low cost, light weight and ease of integration with communication systems. The proposed designs look like a printed dipole on one side of substrate with a full ground plane on the other side of the substrate. To achieve the desired radiation characteristics for maximum coverage, the radiating elements are fed with in-phase currents instead of out-of-phase currents. For this purpose, a printed transmission line feed is used to provide in-phase currents to both radiating elements through electromagnetic coupling. The challenge here is to tune the gap between the feed line and the radiating elements to achieve the desired capacitance to make the structure resonating at the required operating frequency. Moreover, the full ground used underneath the substrate acts as reflecting surface and helps to protect the radiations that could go into the body and can potentially be harmful.

3.1   Single Band Antennas

In this section, we present a printed antenna with a full ground plane and electromagnetically coupled feed for body area network devices operating in industrial, scientific, and medical (ISM) band at 2.45GHz. Performance characteristics along with parametric analysis are presented. Specific absorption rate (SAR) analysis is carried out to investigate its performance for body centric wireless communication. The electromagnetically-coupled feed used is tuned to fill a null in the radiation pattern and to achieve impedance matching. The proposed antenna exhibits wide radiation pattern along the body surface to provide maximum coverage and its small width (14mm) makes it suitable for on-body applications.
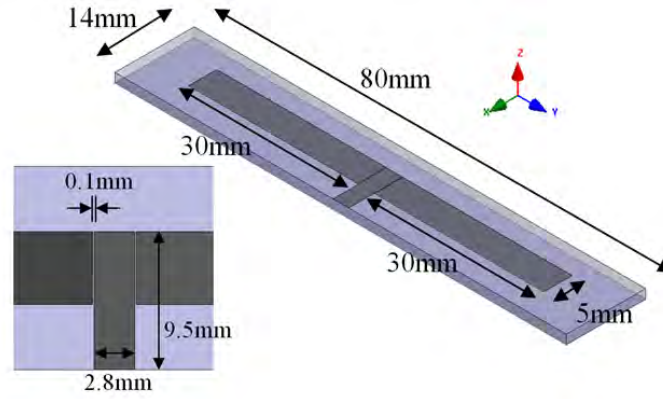
Figure 3.1: Geometry of the proposed antenna.

Figure 3.2: Prototype of the proposed antenna.

3.1.1 Antenna Design

Fig. 3.1 shows the geometry of the proposed antenna with dimensions. It is fabricated on 14 x 80 mm^2 FR-4 substrate with dielectric constant 4.4 and height of 1.6mm. Fig. 3.2 shows the antenna prototype. This Antenna consists of two radiating elements and a full ground plane. Full ground plane is considered to reduce radiation toward the body that can harm human tissues. Radiating elements consist of two rectangular strips each having length 30mm and width 5mm. They are electromagnetically coupled to a microstrip transmission line feed with dimensions 9.5mm x 2.8mm. The gap (g) between the transmission line and rectangular radiating elements is 0.1mm. The dielectric constants, conductivity and loss tangent of different body tissues have been considered while modeling the antenna operation near the human body [15].
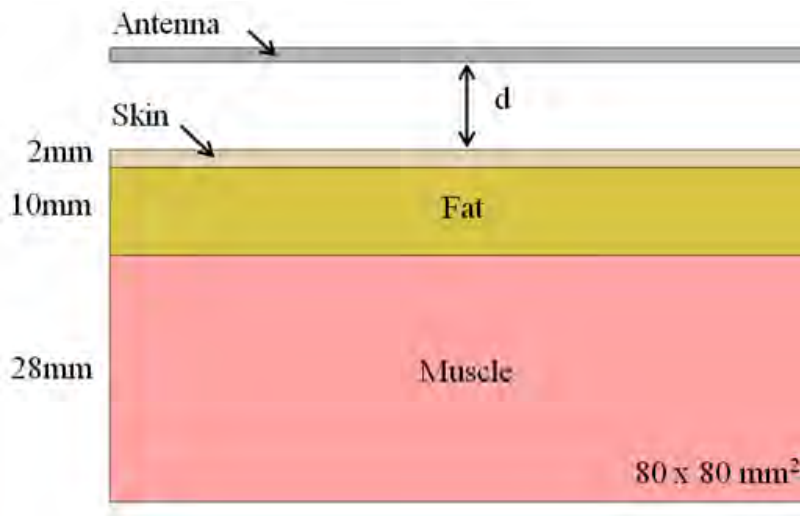
Figure 3.3: Simplified body model with three tissue layers.

Table 3.1: ELECTRICAL PROPERTIES OF TISSUES AT 2.45 GHz.

Tissues	ε_r	$\sigma\,(S/m)$	$\tan\delta$
Skin	38	1.464	0.2826
Fat	5.28	0.1045	0.1452
Muscle	52.73	1.7388	0.2419

3.1.2 Results and Analysis

Simulations of the proposed antenna are carried out using HFSS. After designing the antenna in free space, its performance is investigated in near-body environment. The average thicknesses of skin, muscle and fat tissues is considered while modeling a sample phantom for near body simulation [6, 85]. The tissue layers are shown in Fig. 3.3. The properties of the three tissue are given in Table 3.1. The properties of the tissues normally changes with frequency and thickness of the tissues [85].
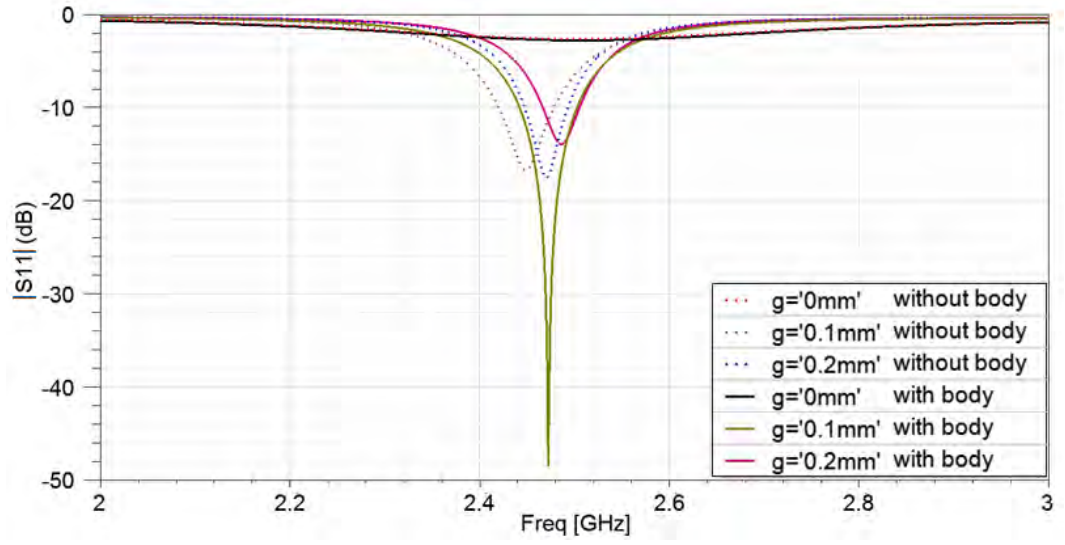
Figure 3.4: Predicted $|S_{11}|$ in free space (i.e. without body) and with body model at various values of the gap between the feed and radiating elements.

Figure 3.5: Predicted $|S_{11}|$ corresponding to distances between the antenna and the human body.
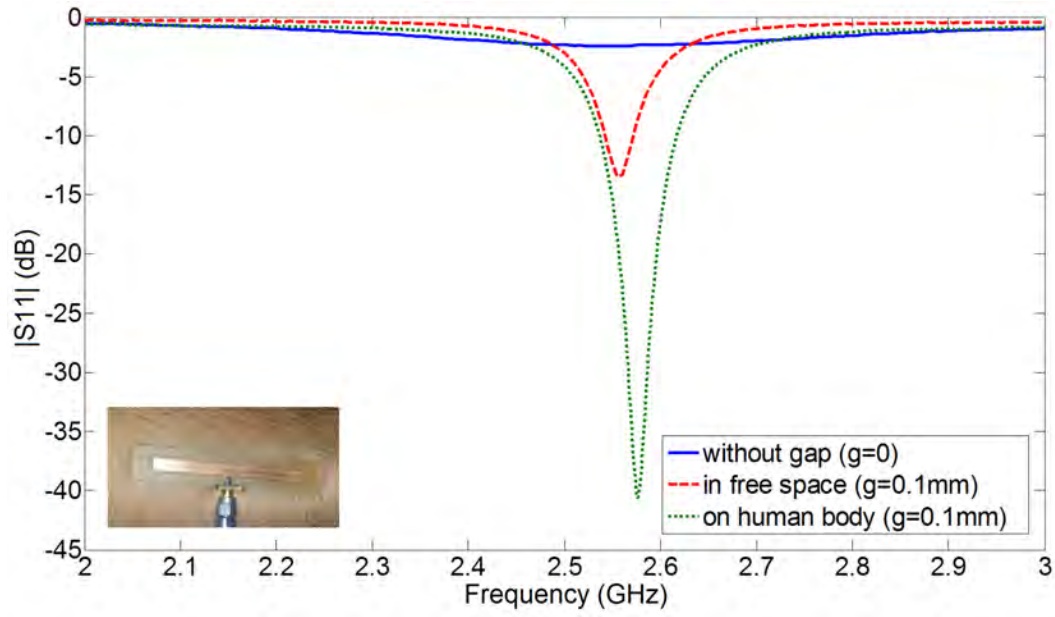
Figure 3.6: Measured $|S_{11}|$ in free space (i.e. without body) and with body.
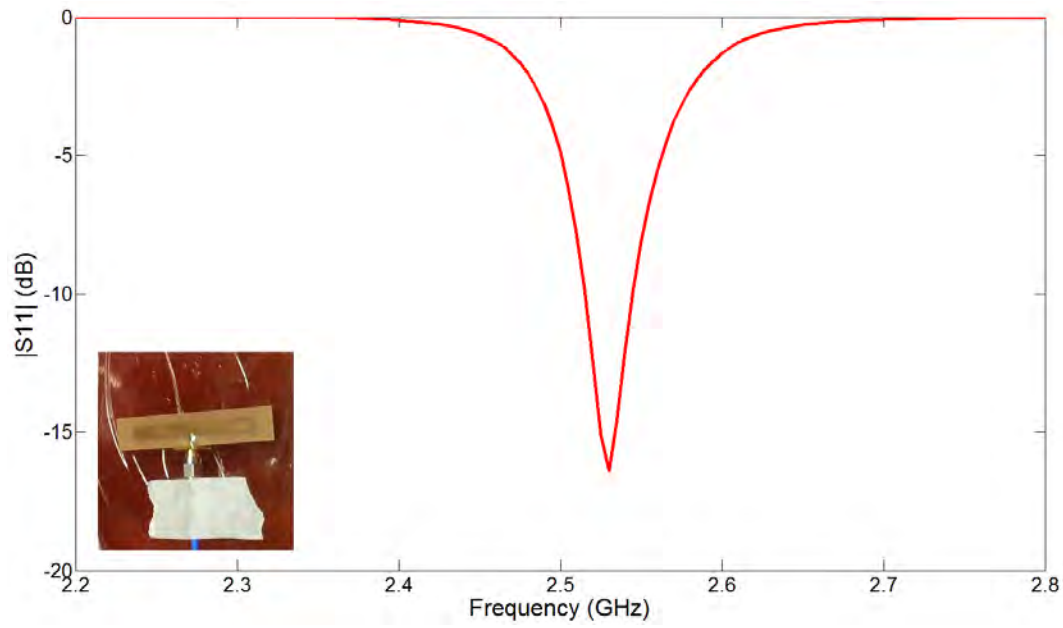
Figure 3.7: Measured $|S_{11}|$ over gel based three layer human body tissue model.
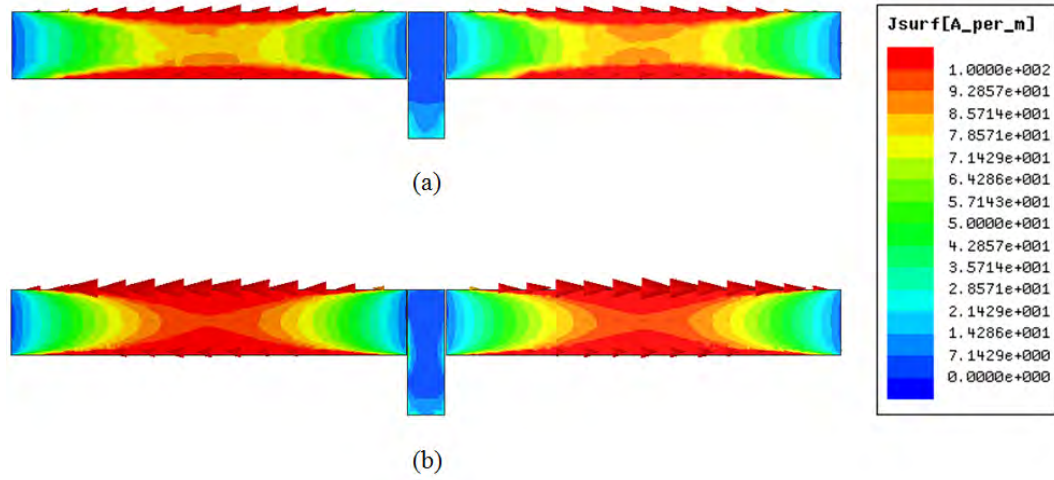
Figure 3.8: Current distribution over the antenna radiating elements in (a) free space (b) in close proximity to human tissue model.

A. *Return Loss*

Fig. 3.4 shows the simulated S-parameters of the proposed antenna along with a gap parametric analysis for free space and near-body scenarios. The antenna covers the ISM band at 2.45GHz which is suitable for body centric wireless communication. The antenna has been simulated in free space and for different distances from the human body (i.e. from 0mm to 10mm) and the return loss is as shown in Fig. 3.5. It shows that the antenna can be placed as close as 2mm from the body. This distance could not be reduced before 2mm in the simulation setup due to the space taken by the connector in the simulation model. The fabricated antenna has been measured in free space and over a male human arm and the corresponding results are shown in Fig. 3.6. It is also measured over a gel based three layer human body tissue model (described in section 3.5) and the result is presented in Fig. 3.7.

Usually, detuning occurs when an antenna is placed closed to a human body. This detuning is avoided in the proposed design by using a full ground plane but due to the small size of ground plane slight detuning is noted. In free space, this antenna

provides 10dB return loss bandwidth of 58MHz (2.420−2.478GHz) with a peak return loss of 16.7dB while near the body at 2mm bandwidth is 60MHz (2.442−2.502GHz) and the peak return loss is 48.5dB.

(a)   (b)
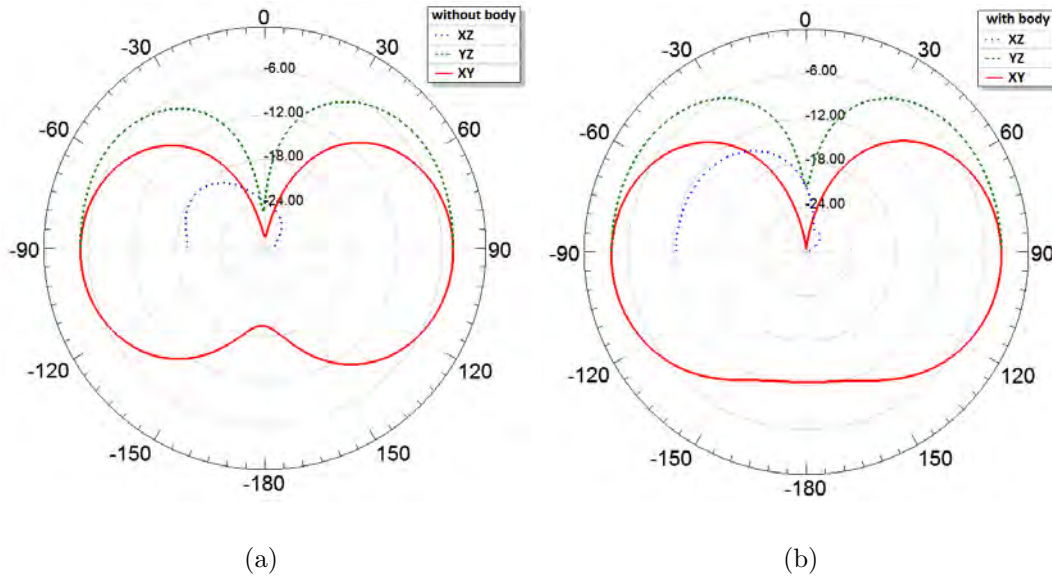
Figure 3.9: Predicted radiation patterns (a) in free space i.e. without body (b) with body.
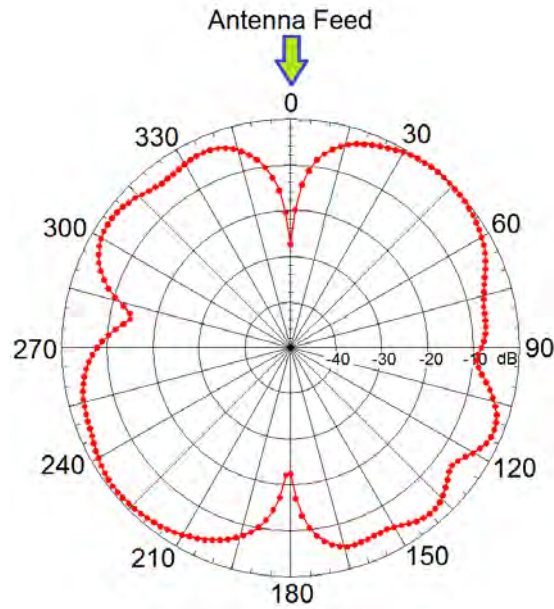
Figure 3.10: Measured radiation pattern in free space for the xy plane.

(a)   (b)
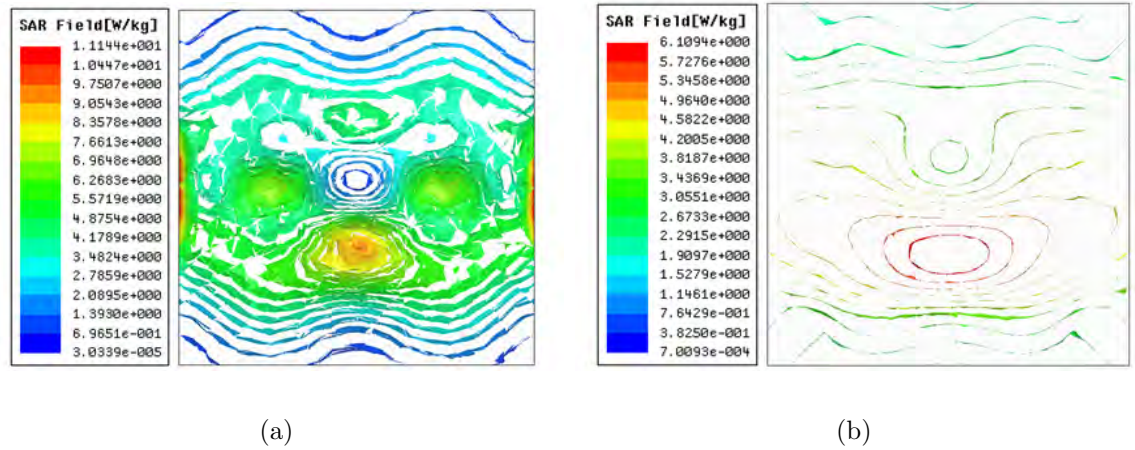
Figure 3.11: (a) local SAR (b) average SAR in the three-layer human body model.

B. *Radiation Characteristics*

Fig. 3.9 presents the predicted radiation patterns of the proposed antenna at 2.45GHz for free space and near-body scenarios. It can be depicted from current distribution presented in Fig. 3.8 that current in both radiating elements is in-phase that results in nulls along the feed and radiations from the sides. It is also noted that current becomes stronger due to full ground plane when antenna is places closer to human body. Measured radiation pattern (in the plane parallel to the human body) is presented in Fig. 3.10. Results show that near the body the antenna beam becomes wider especially in the plane of the body (xy plane) and the null along the negative x-axis is partially filled to provide maximum coverage.

C. *Specific Absorbtion Rate*

Local and average SAR has been computed considering the three-layer human body model. Fig. 3.11 presents the SAR distribution for both.

To summarize this section, a printed antenna with a wide beam radiation pattern by partially filling a null to provide maximum coverage along the body surface has been proposed. Impedance matching by tuning the gap parameters has been investigated. Vari-

ation in the distance between the antenna and the human body slightly affects the return loss but there is no significant change in bandwidth that makes it a suitable candidate for wearable devices.

3.2 Dual Band Antennas

This section presents a printed dual band antenna with a full ground plane and electromagnetically coupled feed for body area network devices operating in the industrial, scientific, and medical (ISM) band at 2.45GHz and 4.9GHz public safety Wireless Local Area Networks (WLAN) band (4.94−4.99GHz). Performance along with parametric analyses are presented. Investigations have been carried out to assess its performance for body centric wireless communication. The electromagnetically-coupled feed is tuned to fill a null in the radiation pattern and to achieve impedance matching. The proposed antenna exhibits a wide radiation pattern along the body surface to provide maximum coverage and its small width (14mm) makes it suitable for on-body applications.

In section 3.1, we have discussed a compact single band antenna with a full ground plane and electromagnetically-coupled feed designed for body area network devices operating in industrial, scientific, and medical (ISM) band at 2.45GHz [17]. It exhibit a radiation pattern that is along the body surface. An electromagnetically coupled feed was used to partially fill a null that is otherwise present towards the direction opposite to the feed. The antenna proposed in this section is dual band operating in both industrial, scientific, and medical (ISM) band at 2.45GHz and 4.9GHz public safety Wireless Local Area Networks (WLAN) band (4.940−4.990GHz). It exhibits a wide radiation pattern along the body surface to provide maximum coverage.
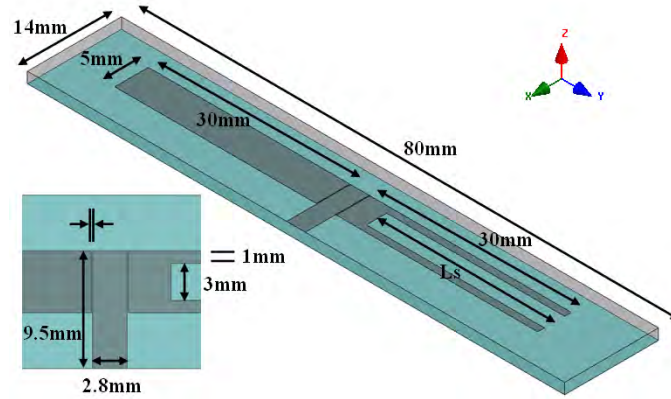
Figure 3.12: Geometry of the proposed dual band antenna.

3.2.1 Antenna Design

Fig. 3.12 shows the geometry of the proposed antenna with dimensions. It is to be fabricated on a 14mm x 80mm FR-4 substrate with a dielectric constant of 4.4 and height of 1.6mm. The fabricated antenna is shown in Fig. 3.13. This antenna consists of two radiating elements and a full ground plane. Full ground plane is considered to reduce radiation towards the body, which can harm human tissues. Radiating elements consist of a rectangular strip and a U-shaped strip, each having a length of 30mm and a width of 5mm. The U-shaped strip is implemented by removing a slit of width 3mm and length (Ls) from the far-end of one rectangular strip. Both radiating elements are electromagnetically coupled to a microstrip transmission line feed with dimensions 9.5mm x 2.8mm. The gap (g) between the transmission line and rectangular radiating elements is 0.1mm [17]. The dielectric constants, conductivity and loss tangent of different body tissues have been considered when modeling the antenna operation near a human body [15].

3.2.2 Results and Analysis

Simulations of the proposed antenna have been carried out using HFSS. After designing the antenna in free space, its performance was investigated in near-body environment.
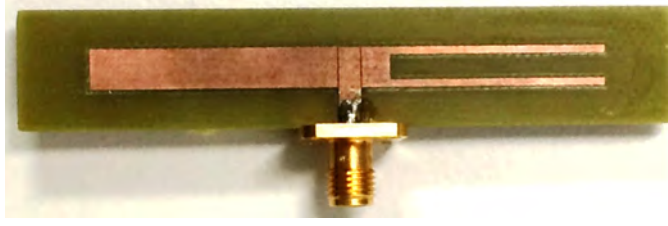
Figure 3.13: Prototype of the proposed antenna.

Table 3.2: ELECTRICAL PROPERTIES OF TISSUES AT 5.2 GHz.

Tissues	ε_r	$\sigma\,(S/m)$	$\tan\delta$
Skin	35.61	3.2185	0.3124
Fat	5.01	0.2547	0.1757
Muscle	49.28	4.2669	0.2993

The average thicknesses of skin, muscle and fat tissues were considered while modeling a sample phantom for near body simulation [6, 15, 17, 85]. The tissue layers are shown in Fig. 3.1. The properties of the three tissues at 2.45GHz and 4.9GHz are given in Table 3.1 and Table 3.2, respectively. The properties of the tissues normally change with frequency and thickness of the tissues [15, 85].

A. *Return Loss*

Fig. 3.14 shows the predicted $|S_{11}|$ of the proposed dual band antenna for free space and near-body scenarios. The antenna covers the ISM band at 2.45GHz, which is suitable for body centric wireless communication, and 4.9GHz public safety WLAN band (4.940−4.990GHz). Fig. 3.15 presents the measured $|S_{11}|$ of the proposed antenna in free space and over gel based three layer human body tissue model. The antenna has been simulated in free space as well as for different distances from the human body (i.e. from 2mm to 10mm) and the return loss is shown in Fig. 3.16 and Fig. 3.17, for 2.45GHz and 4.9GHz body models, respectively. It shows that the antenna can
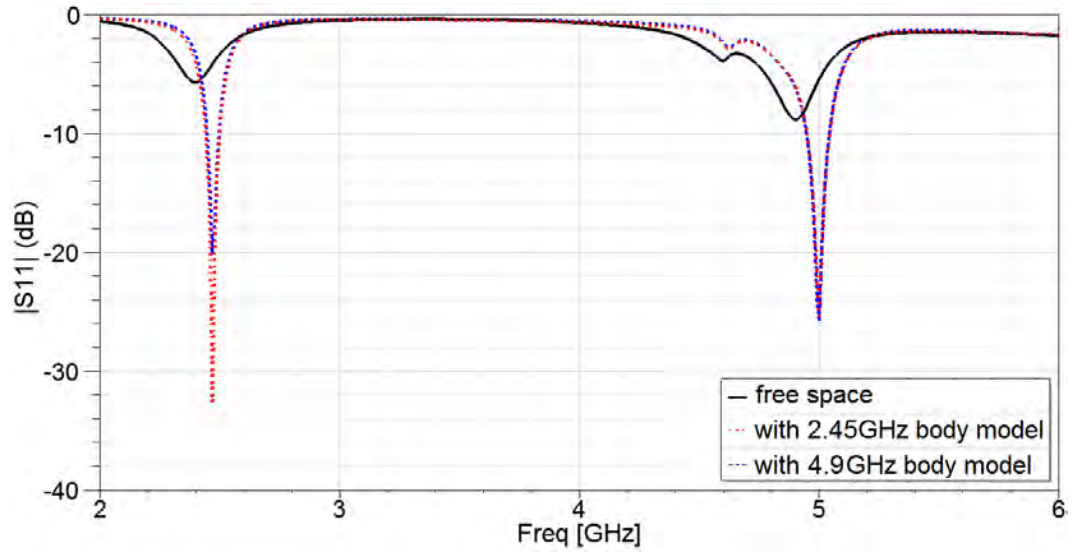
Figure 3.14: Predicted $|S_{11}|$ in free space (i.e. without body) and near the human body (i.e. 2.45GHz body model and 4.9GHz body model).

be placed as close as 2mm from the body. This distance could not be reduced below 2mm in the simulation setup due to the space taken by the connector in the simulation model.

Usually, detuning occurs when an antenna is placed closed to a human body. This detuning is reduced in the proposed design by using a full ground plane but due to the small size of ground plane slight detuning is still noted. In free space, this antenna shows resonance, without good impedance matching, around 2.4GHz and 4.9GHz. when antenna is placed near 2.45GHz body model at a distance of 2mm, it provides a 10dB return loss bandwidth of 60MHz (2.44−2.50GHz) with a peak return loss of 32dB in the ISM band and a 10MHz bandwidth (4.94−5.04GHz) with a peak return loss of 25dB in the WLAN band. When it is placed near 4.9GHz body model at distance of 2mm, it provides a bandwidth of 53MHz (2.445−2.498GHz) with a peak return loss of 20dB in the ISM band and a 10MHz (4.94−5.04GHz) with a peak return loss of 25dB in the WLAN band.
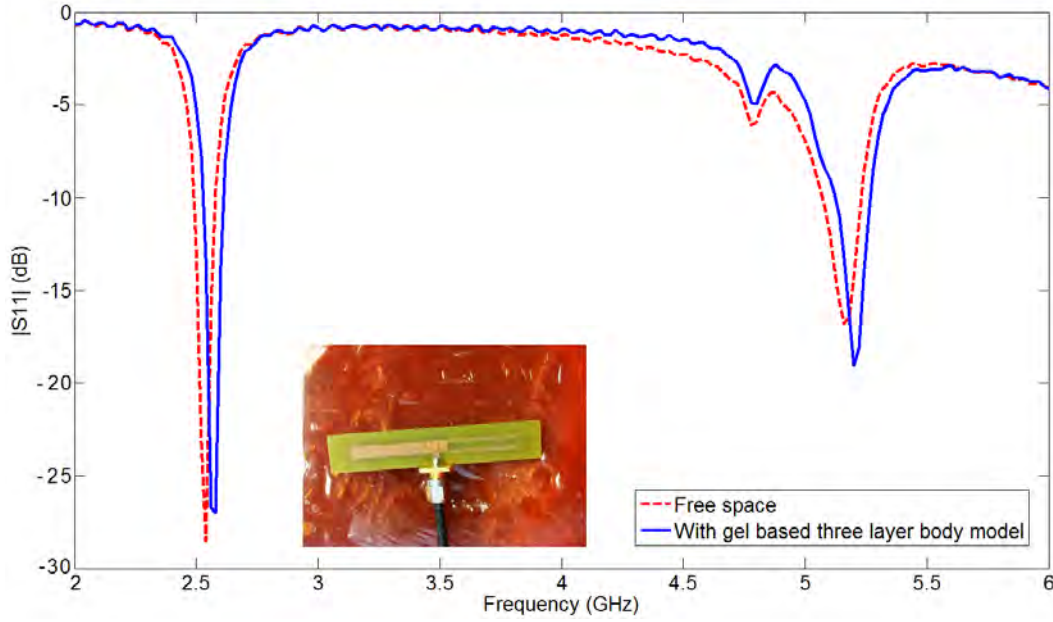
Figure 3.15: Measured $|S_{11}|$ in free space (i.e. without body) and over gel based three layer human body tissue model.

To achieve dual band operation, a slit of length Ls=26.5mm is inserted from far-end of one radiating element to obtain a U-shaped strip. Length of the slit has been varied to investigate its effects. Fig. 3.18 shows the predicted $|S_{11}|$ corresponding to various values of slit length.

B. *Radiation Characteristics*

Fig. 3.19 presents the simulated radiation patterns of the proposed antenna at 2.45GHz and 4.96GHz for free space. Radiation patterns for near-body scenarios, with 2.45GHz and 4.9GHz body models, are presented in Fig. 3.20 and Fig. 3.21, respectively, for both operating bands. They show that near the body the antenna beam becomes wider especially in the plane of the body (x-y plane) and the null along the negative x-axis is partially filled to provide maximum coverage.
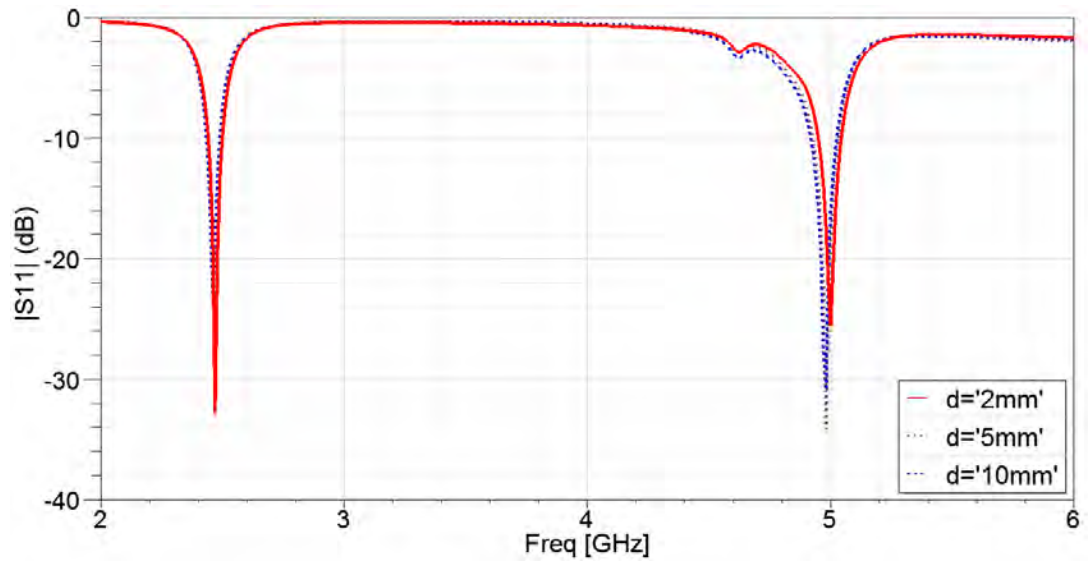
Figure 3.16: Predicted $|S_{11}|$ corresponding to distances between the antenna and the human body (i.e. 2.45GHz body model).
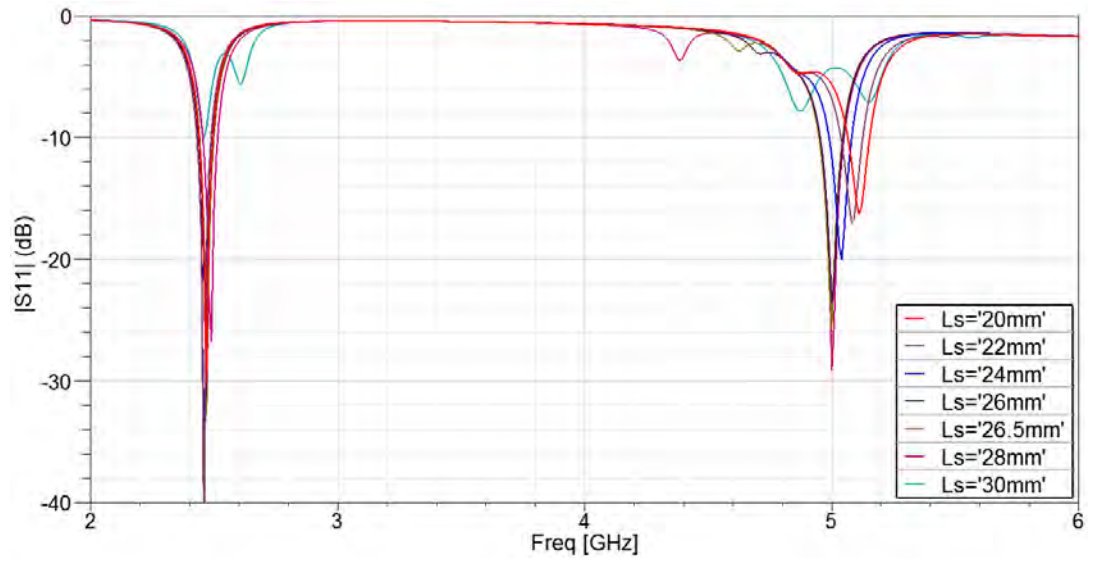
Figure 3.18: Predicted $|S_{11}|$ with 2.45GHz body model corresponding to various values of slit length (L_s).

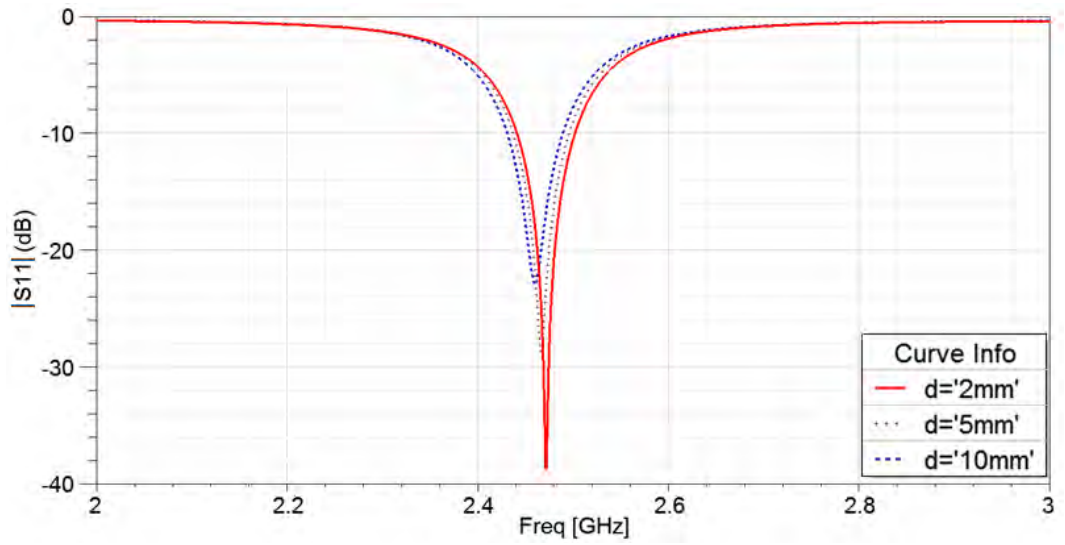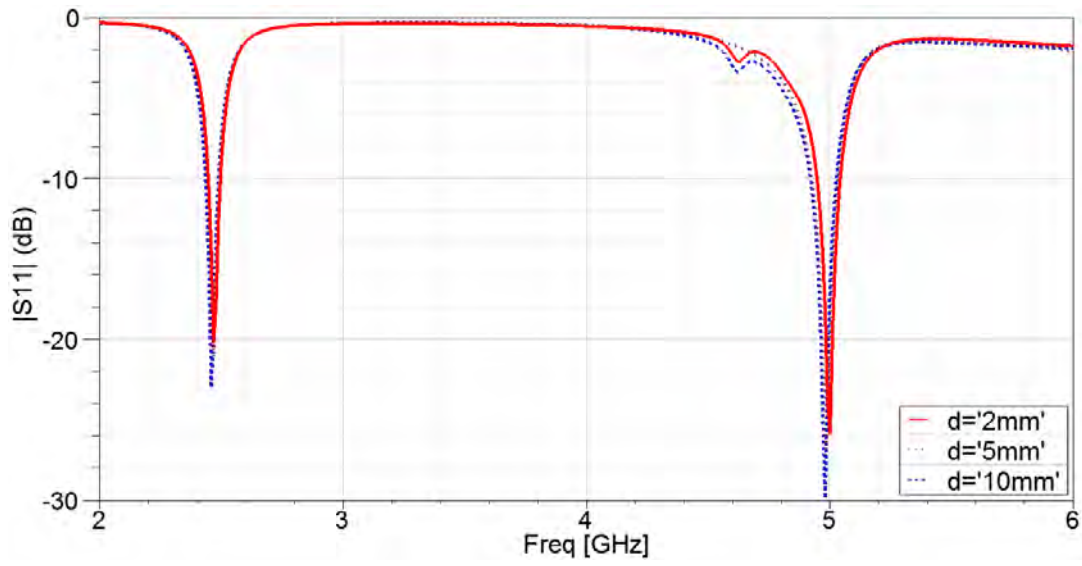Figure 3.17: Predicted $|S_{11}|$ corresponding to distances between the antenna and the human body (i.e. 4.9GHz body model).

(a)   (b)
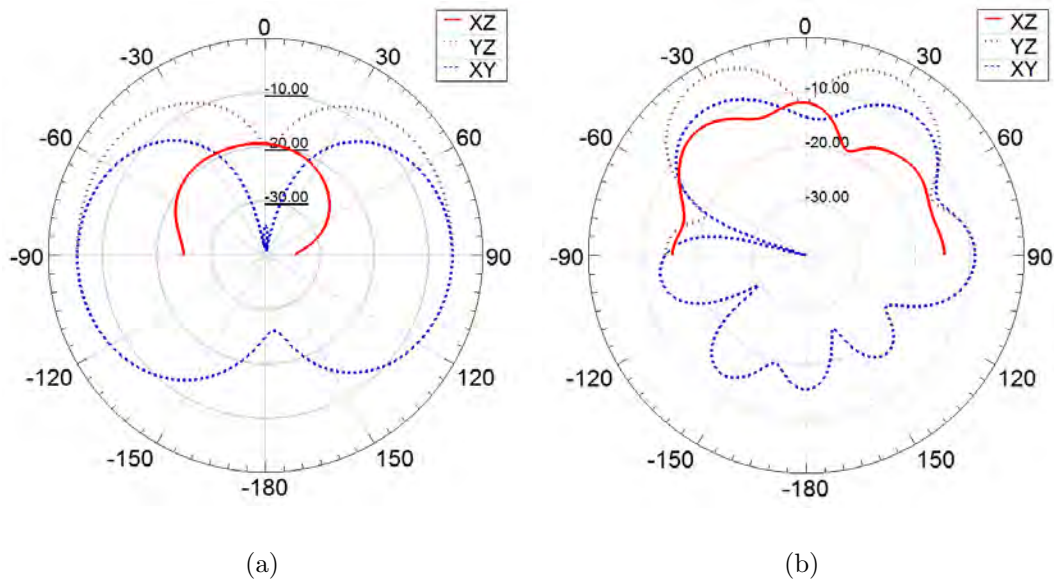
Figure 3.19: Predicted radiation patterns in free space i.e. without body at (a) 2.45GHz (b) 4.96GHz.

(a)   (b)
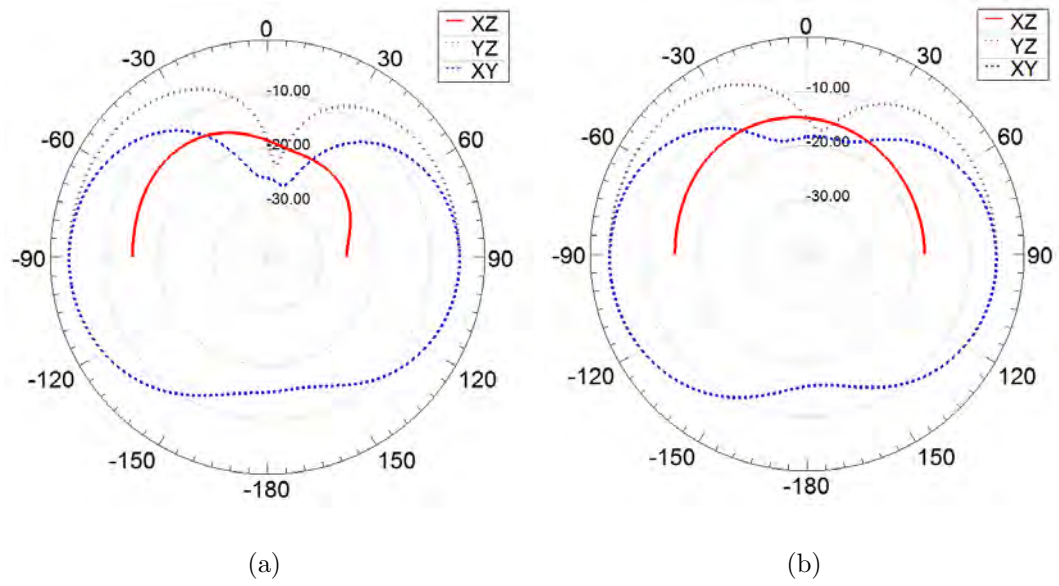
Figure 3.20: Predicted radiation patterns near 2.45GHz body model at (a) 2.45GHz (b) 4.96GHz.

(a)   (b)
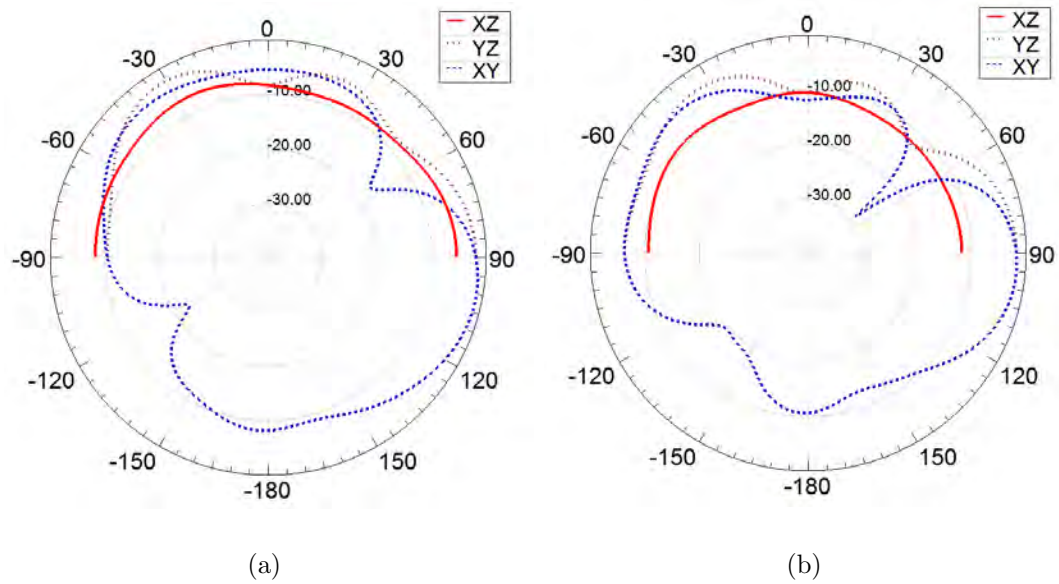
Figure 3.21: Predicted radiation patterns near 4.9GHz body model at (a) 2.45GHz (b) 4.96GHz.

To summarize this section, a printed dual band antenna with a wide beam radiation pattern, to provide maximum coverage along the body surface, has been proposed. Antenna performance characteristics near the human body models at 2.45GHz and 4.9GHz has been investigated. Variation in the distance between the antenna and the human body slightly affects the return loss but there is no significant change in bandwidth that makes it a suitable candidate for wearable devices.

3.3   Conformal Antennas

Earlier, in Section 3.2 and Section 3.2, compact antennas with a full ground plane and electromagnetically-coupled feed for body area network devices operating in industrial, scientific, and medical (ISM) band at 2.45GHz are presented. They exhibit a radiation pattern that is along the body surface. The proposed design in this section is an improved version and is suitable for wearable armbands and other such body area network devices operating in the 2.45GHz ISM band. The electromagnetically-coupled feed is tuned to partially fill a null in the radiation pattern and to achieve impedance matching, which is further fine tuned by stub loading. Initially, it is designed on FR-4 Substrate for comparison and then using flexible substrate. Performance and characteristics are presented along with parametric analyses. Antenna performance is investigated under conformal bending over human arm to assess its suitability for armband-type body centric wireless communication devices. The full ground plane makes the antenna performance highly insensitive to the gap between the antenna and the arm. It also reduces electromagnetic radiation absorption in the arm. The proposed antenna exhibits a wide radiation pattern along the body surface to provide better coverage and its small width (14mm) makes it suitable for wearable on-body applications.
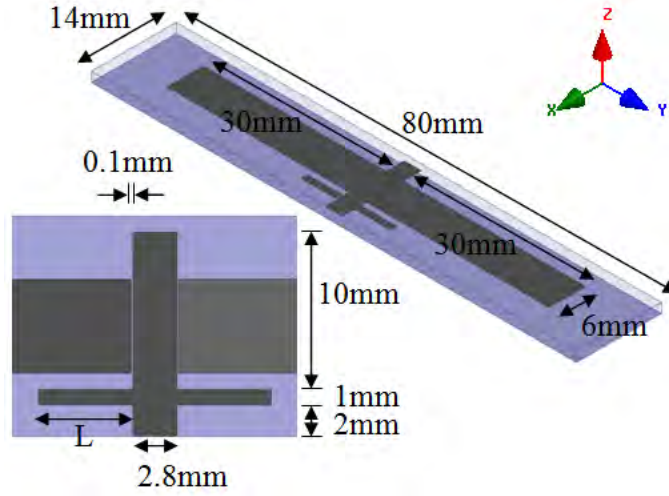
Figure 3.22: Geometry of the proposed antenna with stub loading on FR-4 substrate.

3.3.1 Antenna Design with FR-4 Substrate

Fig. 3.22 shows the geometry of the proposed antenna with dimensions. Initially, the antenna is designed on 14 x 80 mm^2 FR-4 substrate with a dielectric constant of 4.4 and a height of 1.6mm to have a better comparison with previously reported designs and then designed using flexible substrate. Fig. 3.23 shows the antenna fabricated antenna using flexible substrate. It is analyzed in close proximity to flat three layer tissue model that is shown in Fig. 3.3. This antenna also consists of two radiating elements and a full ground plane. Full ground plane is considered to reduce radiation toward the body that can potentially harm human tissues. Radiating elements consist of two rectangular strips each having a length of 30mm and a width of 6mm. They are electromagnetically coupled to a microstrip transmission line feed with dimensions of 13mm x 2.8mm. A pair of stubs with a stub width of 1mm and a length (L) is tuned to achieve impedance matching. This combination of feed and stub also help to improve null filling as compared to earlier designs discussed in earlier sections. Each gap (g) between the feed line and rectangular radiating elements is 0.1mm [17].
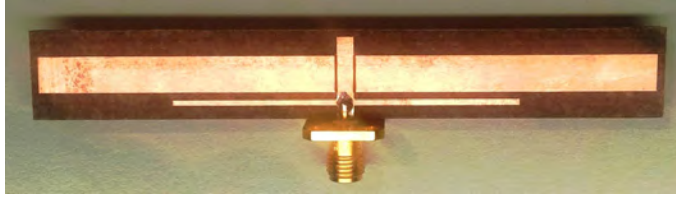
Figure 3.23: Prototype of the proposed antenna.
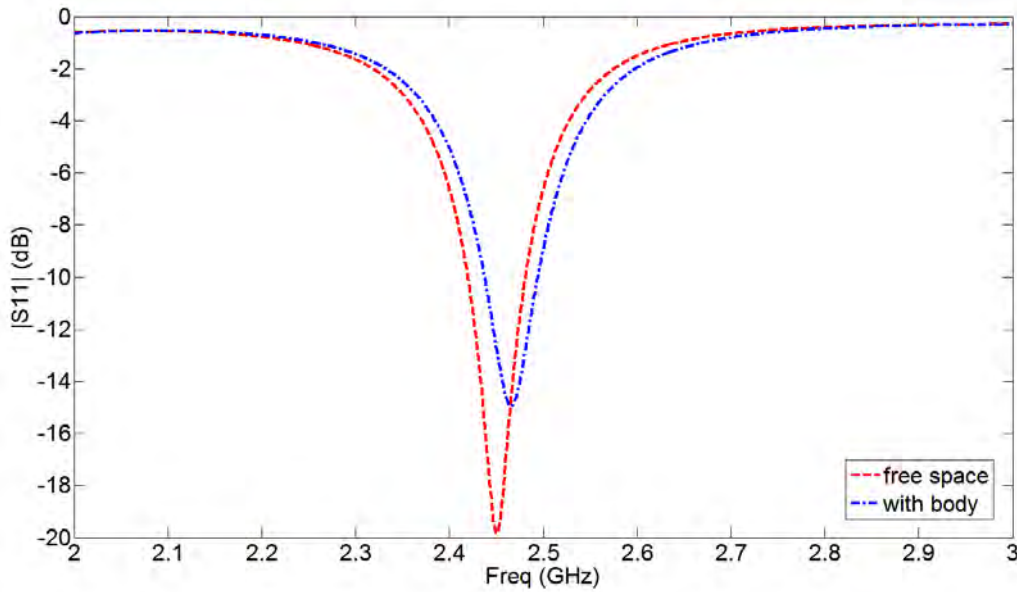
Figure 3.24: Predicted $|S_{11}|$ without bending in free space and near the human body. Stub length (L) is 18.6mm.

3.3.2   Results with Planar Three Layer Tissue Model

Simulations of the proposed antenna have been carried out using CST Microwave Studio. After designing the antenna in free space, its performance is investigated in the near-body environment. It has also been investigated under bending conditions in free space as well as near the human body model. The average thicknesses of skin, muscle and fat tissues were included while modeling a sample planar phantom. The tissue layers are shown in Fig. 3.3 and the properties of the three tissues are given in Table 3.1.
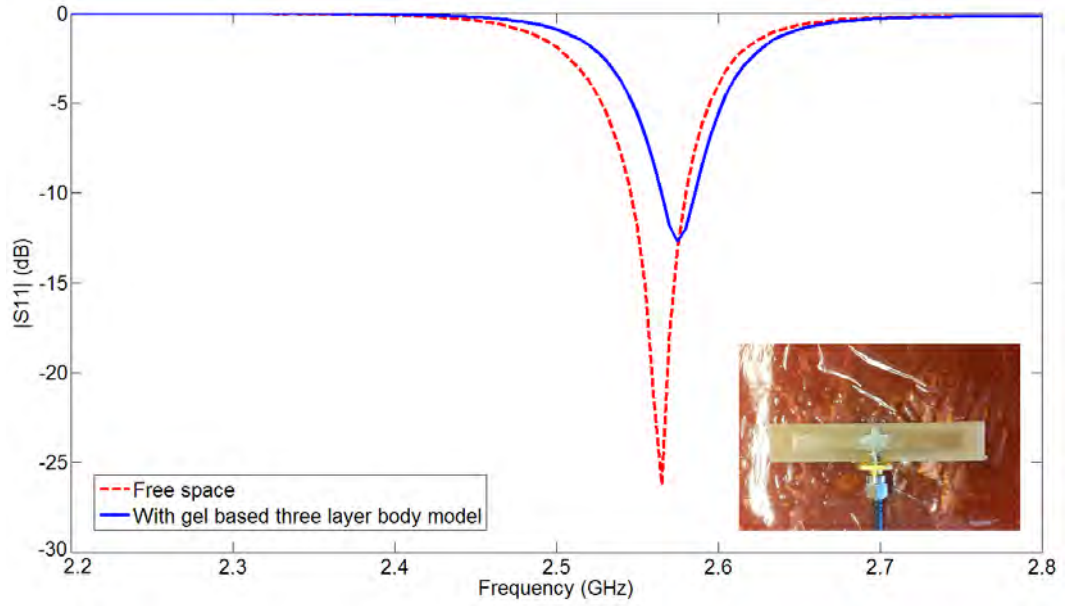
Figure 3.25: Measured $|S_{11}|$ without bending in free space and over gel based three layer human body tissue model.

A. ***Return Loss***

Fig. 3.24 shows the predicted S-parameters of the proposed antenna in free space and near-body scenarios. The distance between antenna and the human body model is considered as 5mm. The antenna covers the ISM band at 2.45GHz and hence is suitable for body centric wireless communication. In free space, this antenna provides a 10dB return loss bandwidth of 62MHz ($2.419-2.481$GHz) while near the body (at a distance of 5mm) bandwidth is 57MHz ($2.437-2.494$GHz). Usually, detuning occurs when an antenna is placed closed to a human body. This detuning is reduced in the proposed design by using a full ground plane but due to the small size of the ground plane slight detuning is noted. Fig. 3.25 shows measured results for antenna without bending in free space and when place over the gel based human body tissue model.

Simulations are carried out to investigate antenna performance under bending conditions in free space and near the human body. Proposed antenna is bent over a
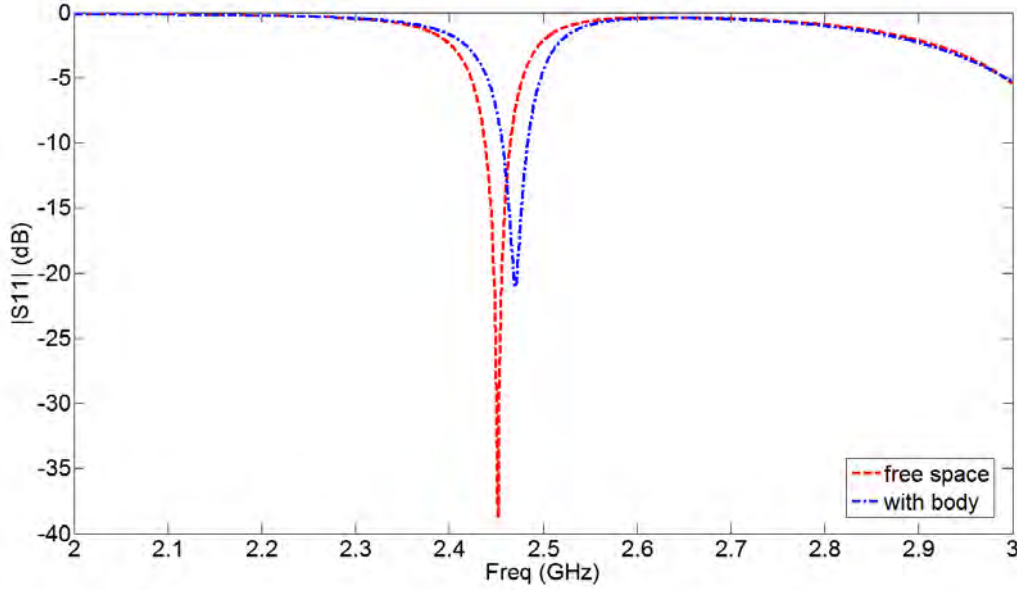
Figure 3.26: Predicted $|S_{11}|$ with bending on a cylindrical surface with a radius of 40mm, in free space and with the human body. Stub length (L) is 18.6mm.

cylindrical surface with different radius and corresponding return loss is illustrated in Fig. 3.26. Shifting in frequency band is observed with the change in bend radius. Fig. 3.27 presents antenna performance under bending (i.e. on a cylindrical surface with r=40mm) in free space and near the human body model. The human body model considered is flat (i.e. without bending). In free space, this antenna provides 10dB return loss bandwidth of 27MHz (2.438−2.465GHz) with a peak return loss of about 38dB while near the body bandwidth is 27MHz (2.456−2.483GHz) with a peak return loss of about 20dB.

B. *Radiation Characteristics*

Fig. 3.28 presents the simulated radiation patterns of the proposed antenna without bending in the plane parallel to the human body at 2.45GHz for free space and near-body scenarios. Fig. 3.29 presents the radiation patterns in the planes that are
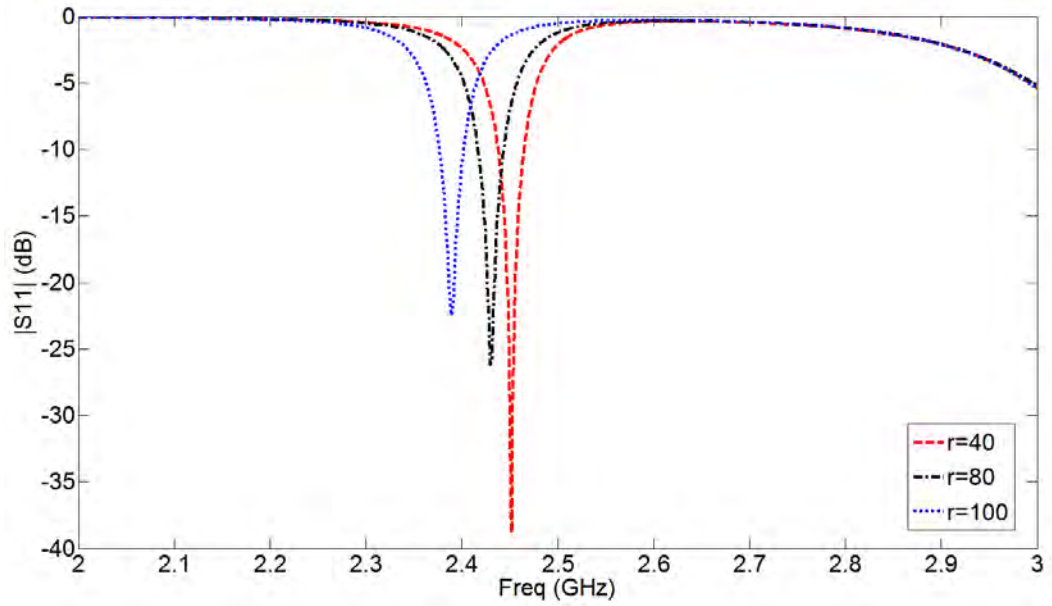
Figure 3.27: Predicted $|S_{11}|$ corresponding to different bending radii.

perpendicular to the human body surface. Proposed antenna is bend over a cylindrical surface with radius of 40mm and radiation pattern in the plane tangential to the human body are shown in Fig. 3.30 for free space and near-body scenarios. Results show that under bending the antenna beam becomes omni-directional in the plane tangential to the body and the nulls that exists in flat condition are filled to provide maximum coverage that were only partially filled in the design discussed in Section 3.1. Furthermore, Fig. 3.31 demonstrates that the antenna radiates more out of the body (as opposed to into the body) to provide better coverage. Omni-directional pattern over the body provides maximum coverage while a partial null in direction perpendicular to body surface is useful as it prevents off-body transmissions that are undesirable when antennas is to be used for on-body communication. It is also beneficial to minimize interference caused off-body communication devices.
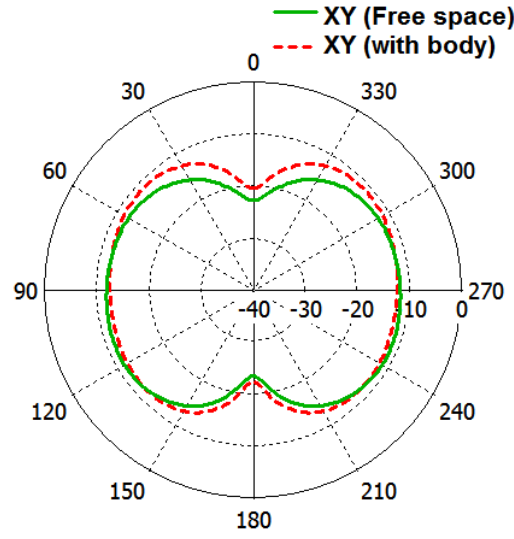
Figure 3.28: Predicted radiation pattern of proposed antenna without bending in the plane parallel to the human body.

(a)   (b)
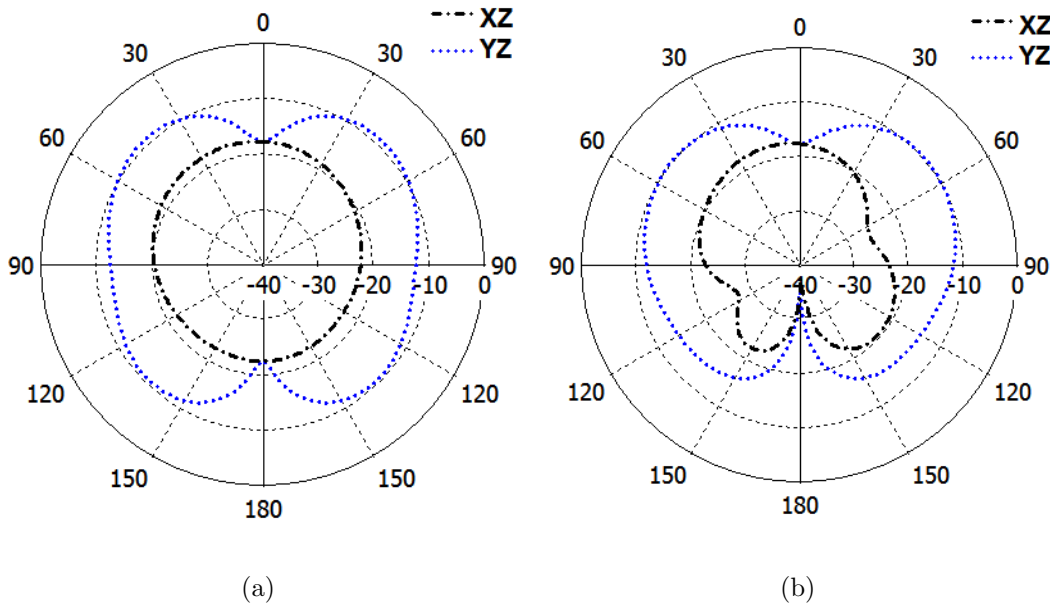
Figure 3.29: Predicted radiation patterns of proposed antenna without bending in the planes perpendicular to the human body (a) in free space (b) near the human body.
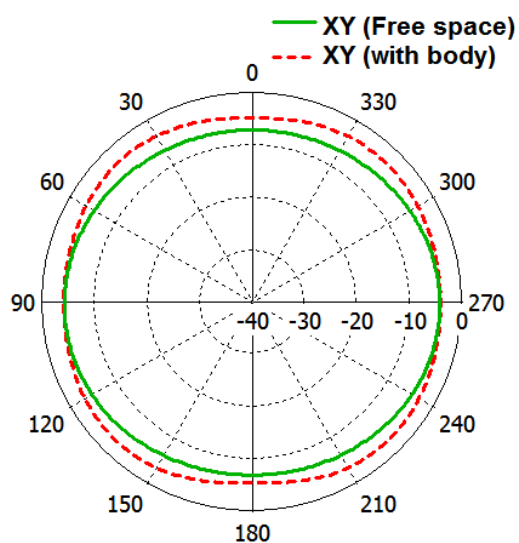
Figure 3.30: Predicted radiation pattern of proposed antenna bent over a cylindrical surface with radius (r=40 mm) in the plane tangential to the human body.

(a)   (b)
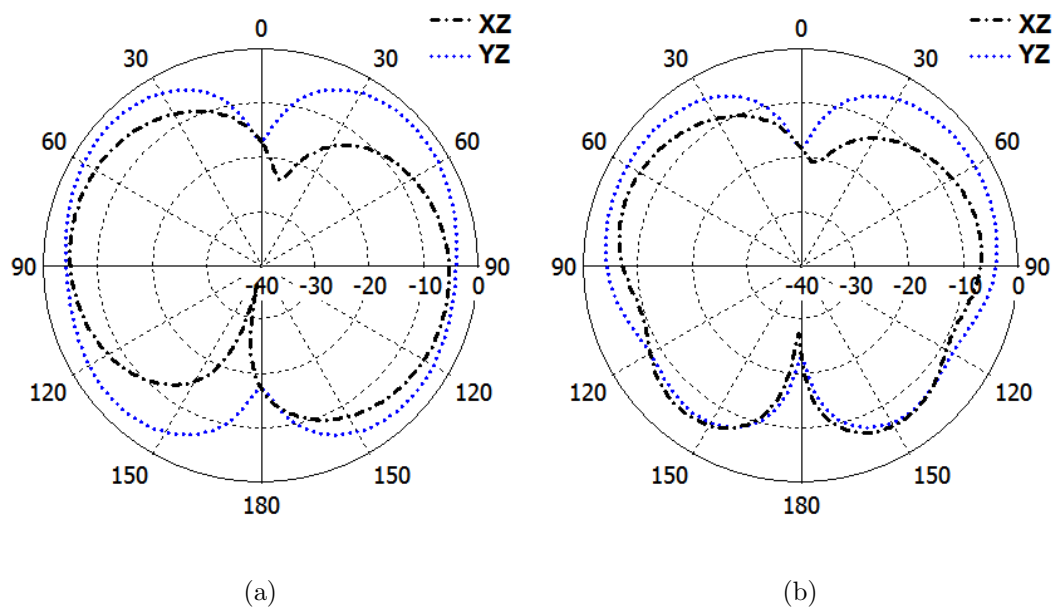
Figure 3.31: Predicted radiation pattern of proposed antenna bent over a cylindrical surface with radius (r=40mm) in the plane perpendicular to the human body (a) in free space (b) near the human body.

Now we will extend this design to a flexible substrate as we have analyzed that this design with modified feed provide an omni-directional radiation pattern under bending condition to provide maximum coverage along the body surface. Impedance matching by tuning stub, feed and the gap parameters has been investigated. Variation in bending curvature of the antenna and presence of the human body slightly affects the return loss and the bandwidth. Omni-directional radiation pattern along the body surface and compact width of antennas makes it a suitable candidate for on-body wearable devices.
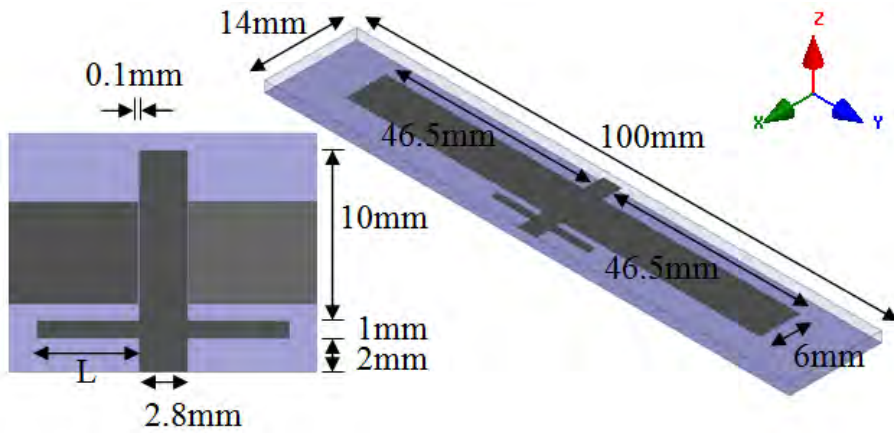
Figure 3.32: Geometry of the proposed antenna with stub loading on flexible substrate.

3.3.3 Antenna Design with Flexible Substrate

Fig. 3.32 shows the geometry of the proposed antenna with dimensions. The antenna is designed for a 14mm x 100mm flexible substrate (Arlon IsoClad 933) with a dielectric constant of 2.33 and a thickness of 1.6 mm. This antenna consists of two electromagnetically coupled radiating elements and a full ground plane. Ground plane size is 14mm x 100mm. This full ground plane helps in reducing the radiation toward the body that can be potentially harmful. Each radiating rectangular strip has a length of 46.5mm and a width of 6mm. Using two gaps each 0.1mm wide, these strips are electromagnetically coupled to a 50 ω microstrip transmission line feed with dimensions of 13mm x 2.8mm.

Table 3.3: PROPERTIES OF THE FOUR-LAYER HUMAN ARM TISSUE MODEL AT 2.45GHz.

Tissues	ε_r	$\sigma\,(S/m)$	$\tan\delta$
Skin	38	1.46	0.283
Fat	5.28	0.105	0.145
Muscle	52.73	1.739	0.242
Bone	11.38	1.394	0.254

A pair of stubs each 1mm wide and 25mm long ($L = 25mm$) is incorporated to achieve impedance matching. This combination of feed and stub also helps to improve null filling as compared to the design presented in Section 3.1.
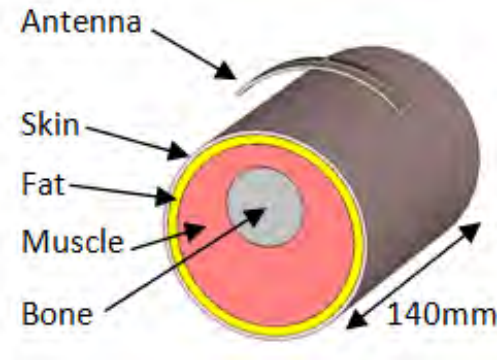
Figure 3.33: Simplified elliptical human arm model (radius=46 mm) with four tissue layers and the conformally bent antenna above the arm.

3.3.4 Results with Human Arm Model

Simulations of the proposed antenna have been carried out using CST Microwave Studio. After designing the antenna for free space, its performance was assessed in the near-body environment and also under bending conditions in close proximity to the human arm
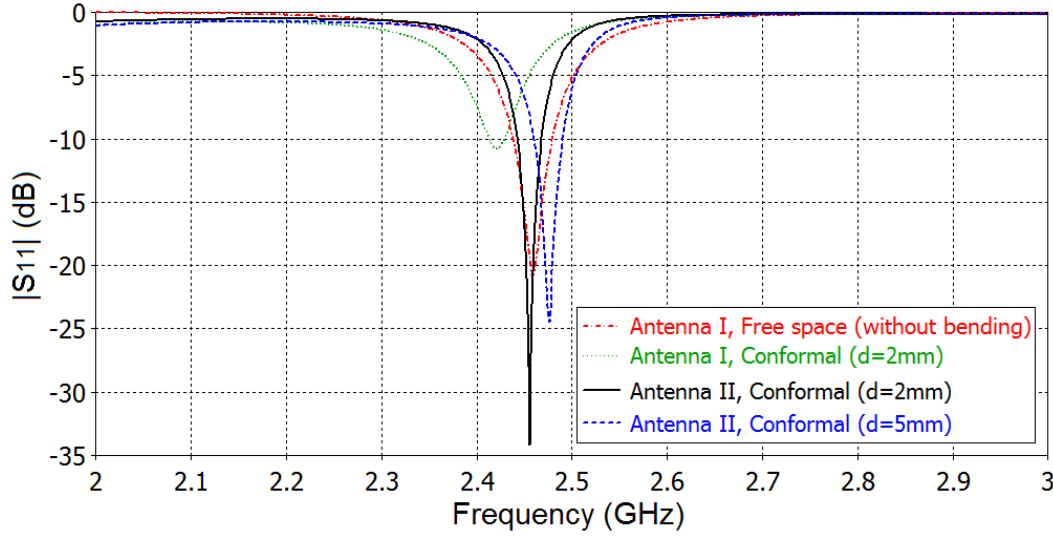
Figure 3.34: Predicted $|S_{11}|$ without bending in free space and near the human body. Stub length (L) is 18.6mm.

model. The simplified elliptical human arm model with four tissue layers 3.33 is used in simulation. The average thicknesses of skin (2mm), fat (4mm), muscle (min. 10mm, max. 35mm) and bone (35mm) tissues were included while modeling a human arm model [42]. The properties of the four tissues are given in Table 3.3 [15].

A. ***Return Loss***

Fig. 3.34 shows the computed reflection coefficients of the proposed antenna in free space and near-body scenarios. In free space, this Antenna I provides a 10dB return loss bandwidth of 50MHz ($2.43-2.48$GHz). Usually, detuning occurs when an antenna is placed closed to a human arm. This detuning is reduced in the proposed design by using a full ground plane but due to the small size of the ground plane slight detuning is noted. Simulations are carried out to investigate antenna performance under conformal bending conditions near the human arm model. When Antenna I is bent over human arm leaving a gap of 2mm between them, and the corresponding return loss is illustrated in Fig. 3.34. Some shifting of the resonance frequency is

observed due to this bending over human arm. To achieve good impedance matching at 2.45 GHz under bending around the human arm, antenna parameters were retuned (stub length changed to 23mm and antenna arms' length to 47.5mm). The retuned Antenna II provides a 10dB return loss bandwidth of 30MHz ($2.44-2.47$ GHz) with a peak return loss of about 34dB at 2.45GHz as shown in Fig. 3.34. The change of resonance frequency due to practical variations in the conformal gap (d) between the arm and Antenna II is very small (0.85% at d=5mm)..

B. ***Radiation Characteristics***

Fig. 3 presents the computed radiation patterns of the proposed antenna at 2.45GHz for free space and near-body scenarios. They show that near the body the antenna beam becomes wider especially in the plane tangential to the body (xy-plane) and the nulls along the x-axis are partially filled to provide a better coverage.

A wearable printed antenna, which has a wide beam under conformal bending around a human arm, is proposed to provide better coverage along the body surface. Antenna performance under different bending scenarios has been investigated. Due to the full ground plane, this antenna performance is very insensitive to the conformal separation between the antenna and the human arm. For example, an increase of this gap from 2mm to 5mm changes the antenna resonance frequency only by 0.85% and its effect on the radiation pattern is not noticeable. Small width of the antenna makes it a suitable candidate for on-body wearable devices.
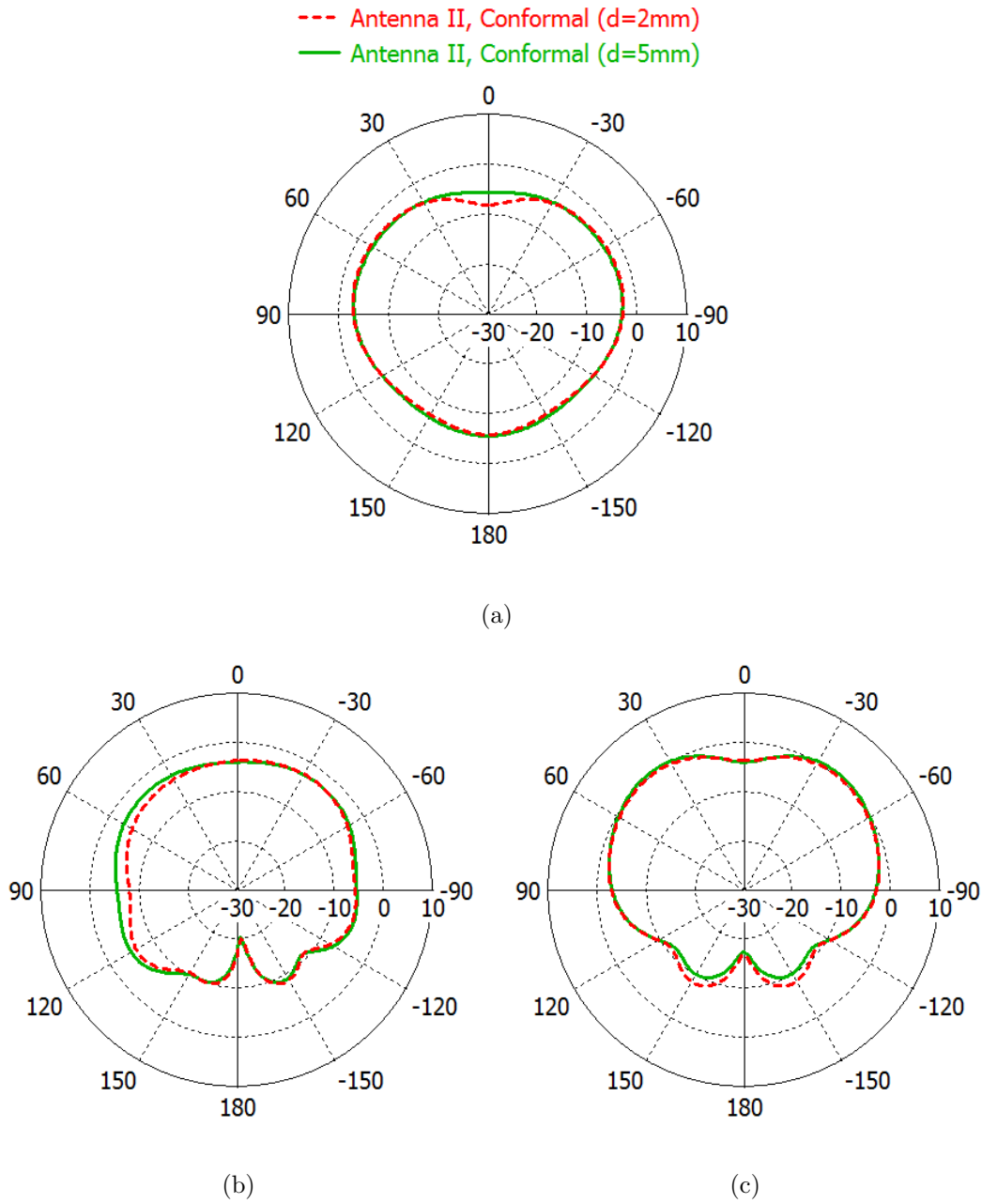
Figure 3.35: Predicted radiation patterns (gain) of proposed antenna in (a) xy-plane (b) xz-plane (c) yz-plane.

3.4 Antenna Sensitivity in Close Proximity to Human Arm

This section presents sensitivity analysis of printed antenna discussed in section 3.3. Antenna input impedance and radiation characteristics are presented along with the parametric analyses. Antenna performance is investigated in free space and in close proximity to various human arm models (i.e. flat, rectangular and elliptical). The full ground plane makes the antenna highly insensitive to the gap between the antenna and the arm in addition to reducing electromagnetic radiation absorption in the arm. Small width (14mm) of the antenna makes it feasible to position along the length of a human arm without bending, which causes shift in resonant frequency. Parametric analyses are carried out to observe the affect of gap variation considering different arm models (i.e. flat, rectangular and elliptical) and antenna placement configurations (i.e. across and along the length of human arm).
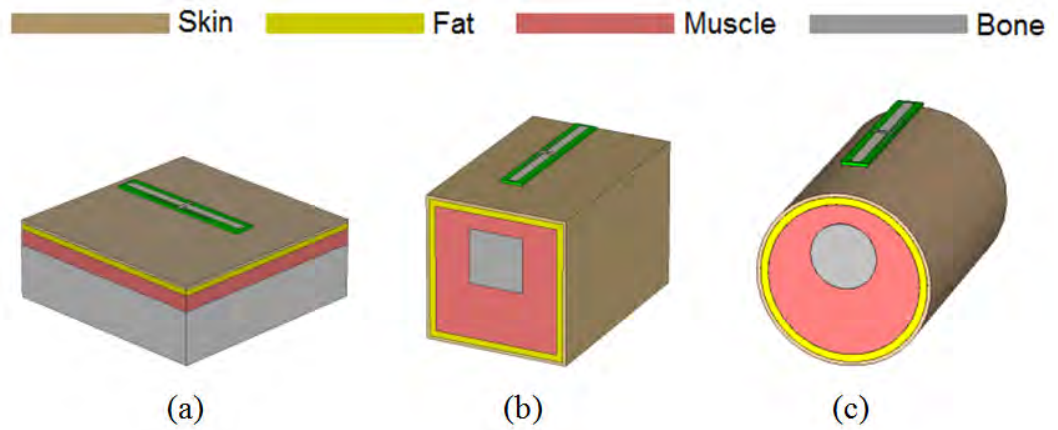
Figure 3.36: Antenna placed over simplified models of human arm section with four tissue layers (a) flat (b) rectangular and (c) elliptical human arm model (radius=46 mm).
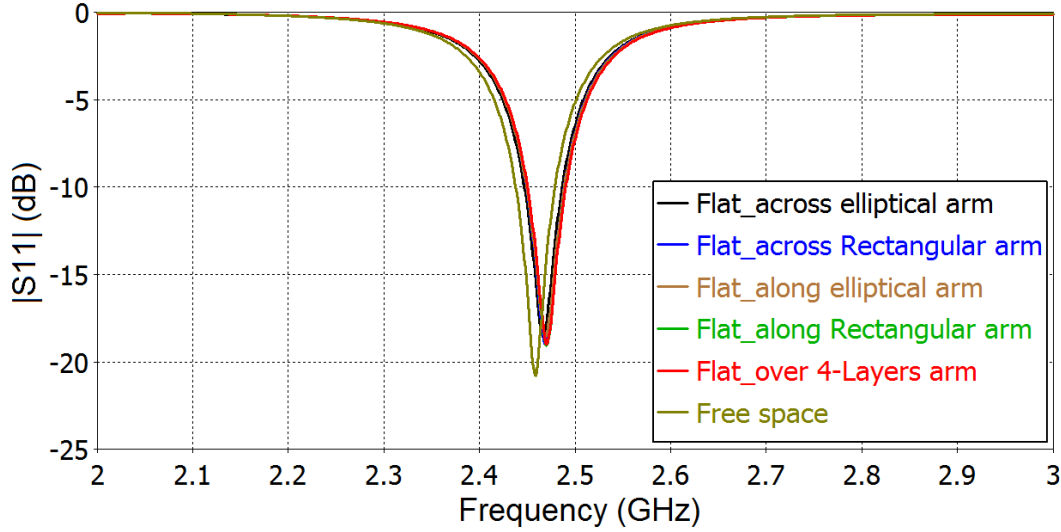
Figure 3.37: $|S_{11}|$ of the proposed antenna in free space and near human arm scenarios. (gap between the arm and the antenna is 5 mm).

3.4.1 Antenna and Near-body Scenarios

Simplified models of human arm section with four tissue layers considered for this research are shown in Fig. 3.36. These are simplified flat, rectangular and elliptical human arm models. The average thicknesses of skin (2mm), fat (4mm), muscle (min. 10mm, max. 35mm) and bone (35mm) tissues are included while modeling a human arm model [2]. The properties of the four tissues are given in Table 3.3.

3.4.2 Results and Analysis

Simulations of the proposed antenna are carried out using CST Microwave Studio. After designing the antenna for free space, its performance was assessed in the near-body environment in close proximity to the human arm models.

A. **Return Loss**

Fig. 3.37 shows the computed reflection coefficients of the proposed antenna in free space and near-body scenarios. In free space, it provides a 10dB return loss bandwidth
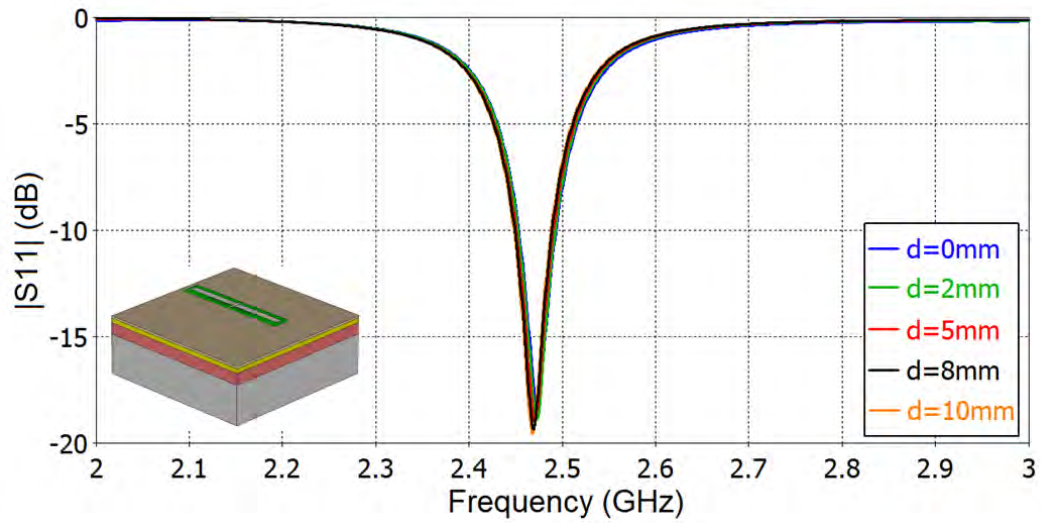
Figure 3.38: Sensitivity of gap (d) between the antenna and the flat human arm model.

of 50MHz (2.43−2.48 GHz). Usually, detuning occurs when an antenna is placed closed to a human arm. This detuning is reduced in the proposed design by using a full ground plane but due to the small size of the ground plane slight detuning is noted. A shift of about 10MHz is noted when antenna is placed near the human arm models. Simulations have been carried out to investigate antenna performance under the gap variation between the antenna and human arm model. When antenna is placed in close proximity to flat human arm negligible variation in resonance frequency is observed, and the corresponding return loss is illustrated in Fig. 3.38.

Antenna is also place over rectangular human arm model considering two scenarios; i) when antenna is placed across the length of rectangular arm model, ii) when antenna is place along the length of human arm model. Negligible shifting of the resonance frequency is observed when gap between the antenna and the rectangular human arm mode is varied for both scenarios (i.e. across and along the length of human arm), and the corresponding return loss is shown in Fig. 3.39 and Fig. 3.40.
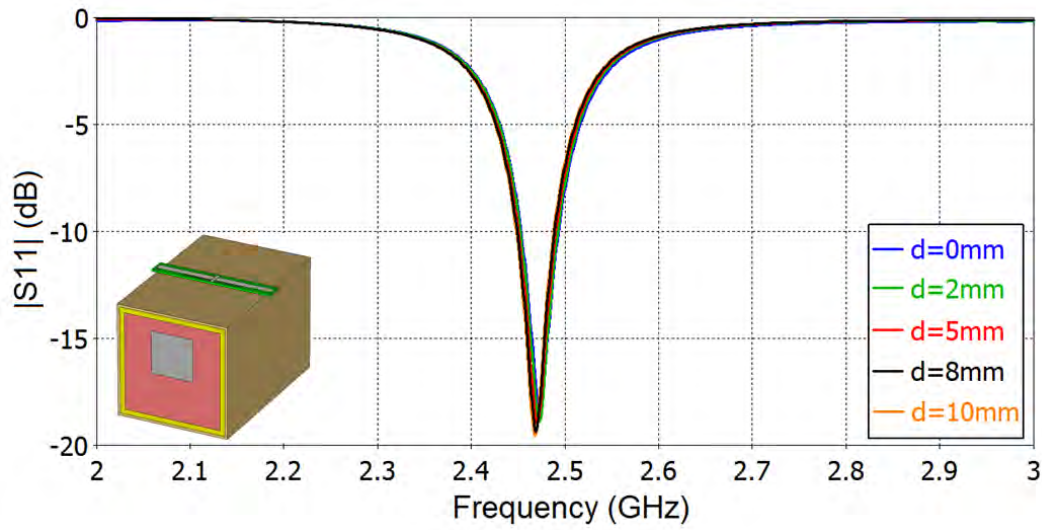
Figure 3.39: Sensitivity of gap (d) between the antenna and the rectangular human arm model when antenna is place across the arm length.
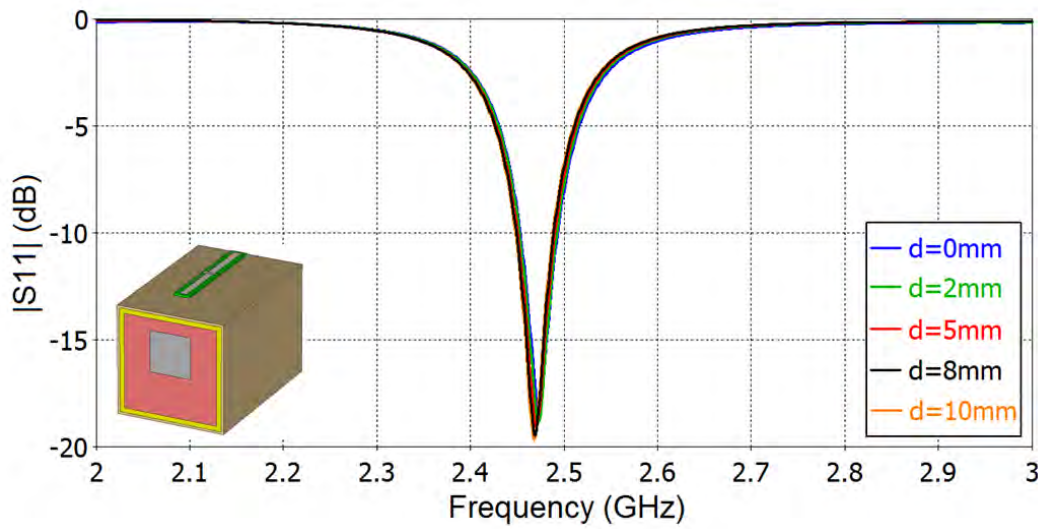
Figure 3.40: Sensitivity of gap (d) between the antenna and the rectangular human arm model when antenna is place along the arm length.

Similarly, antenna performance is also investigated near the elliptical human arm model, when antenna is placed, i) across and ii) along, the length of human arm and

corresponding results are shown in Fig. 3.42 and Fig. **??**. No significant shifting of resonance frequency by varying the gap between the antenna and the elliptical human arm is observed for both scenarios.
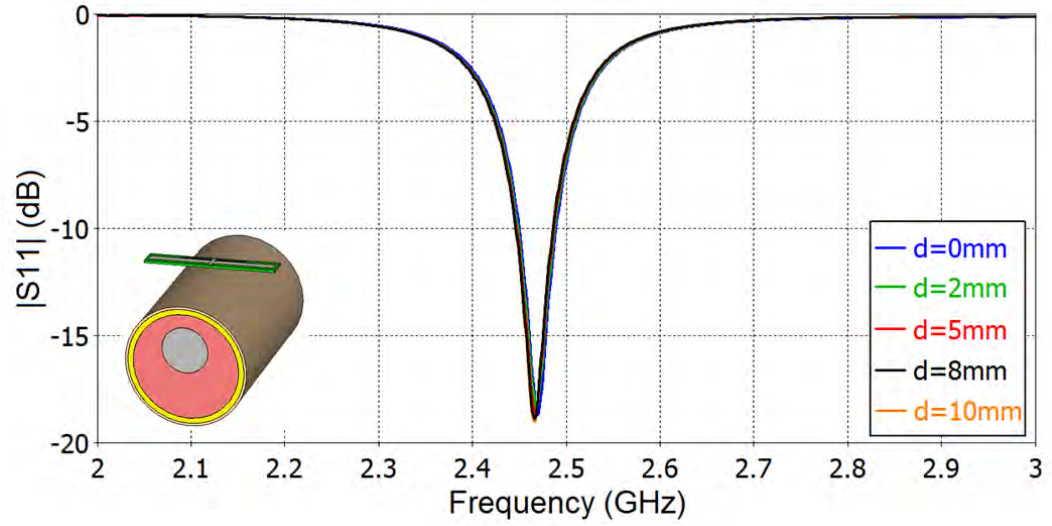
Figure 3.41: Sensitivity of gap (d) between the antenna and the elliptical human arm model when antenna is place across the arm length.
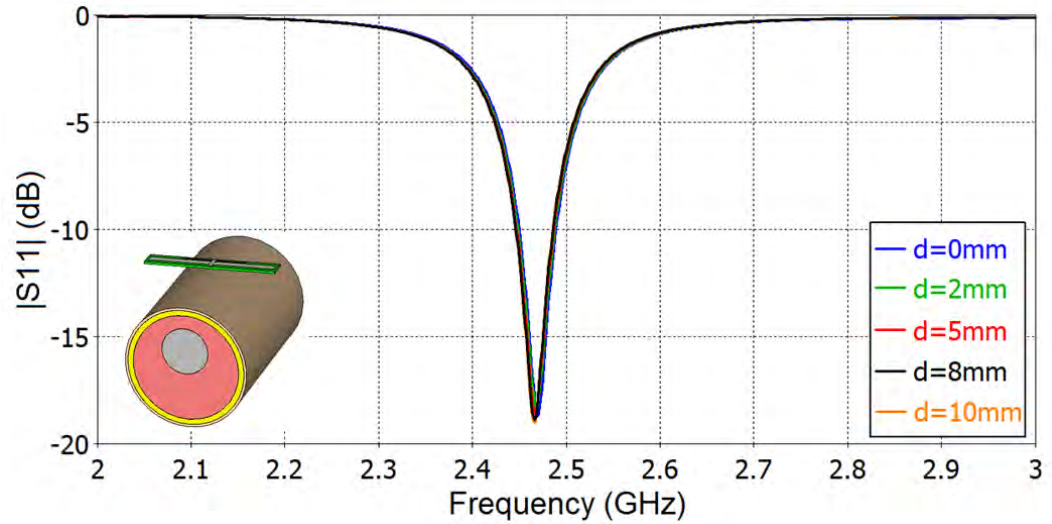
Figure 3.42: Sensitivity of gap (d) between the antenna and the elliptical human arm model when antenna is place along the arm length.

B. *Radiation Characteristics*

Fig. 3.43 - 3.45 presents the computed directivity patterns of the proposed antenna at 2.465GHz for the near-body scenarios. They show that near the body the antenna beam becomes wider especially in the plane tangential to the body (xy-plane) and the nulls along the feed axis are partially filled to provide a better coverage. Slight variation in peak values is observed. The antenna radiation efficiency is about 10% when it is placed closer to the body.
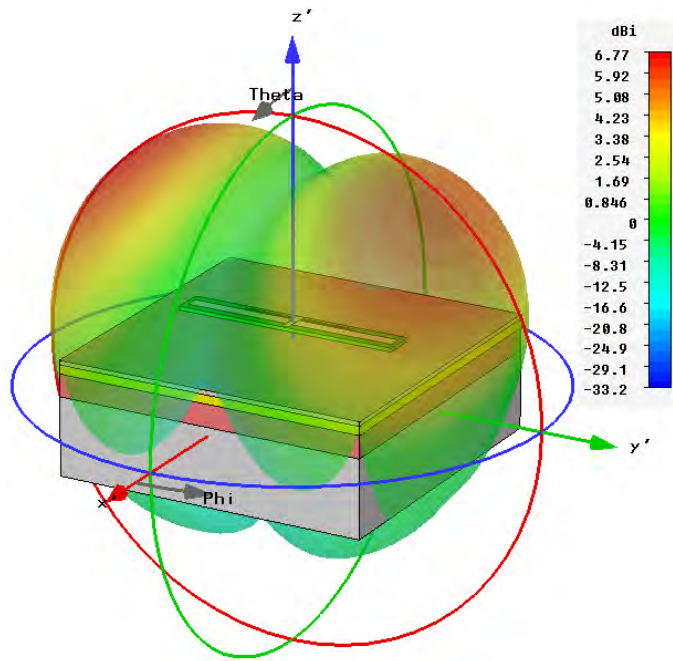
Figure 3.43: Computed radiation patterns (directivity) of proposed antenna in close proximity to flat human arm model.
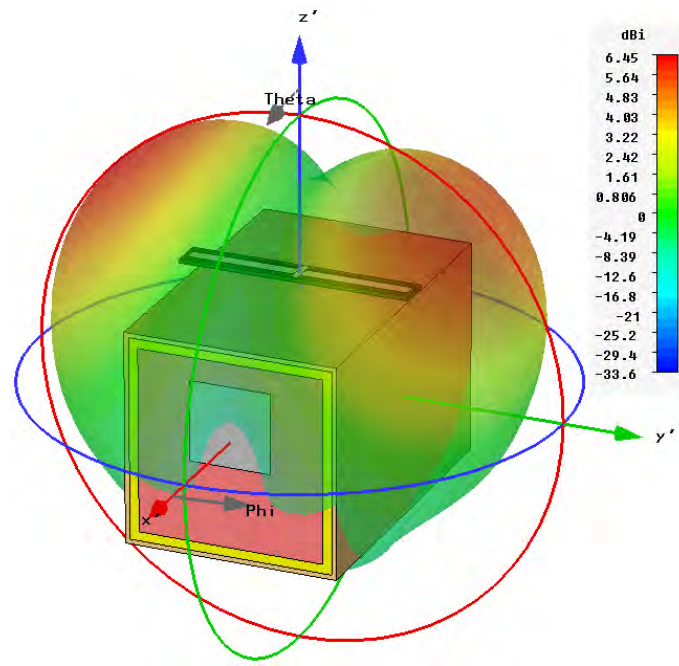
(a)
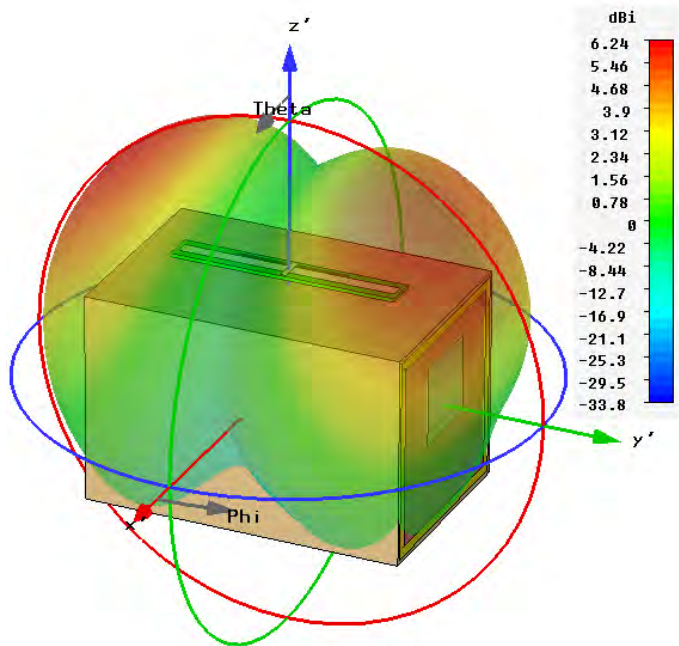
(b)

Figure 3.44: Computed radiation patterns (directivity) of proposed antenna in close proximity to human arm models (a) rectangular (across the arm length) (b) rectangular (along the arm length).
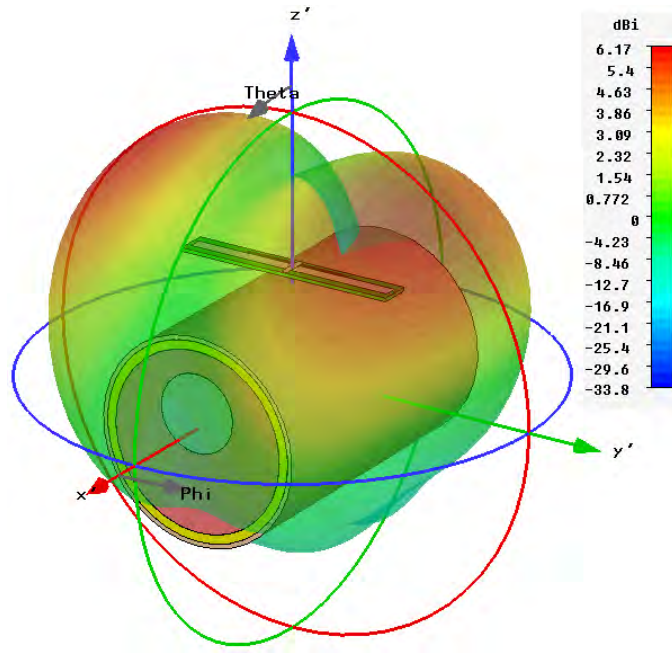
(a)
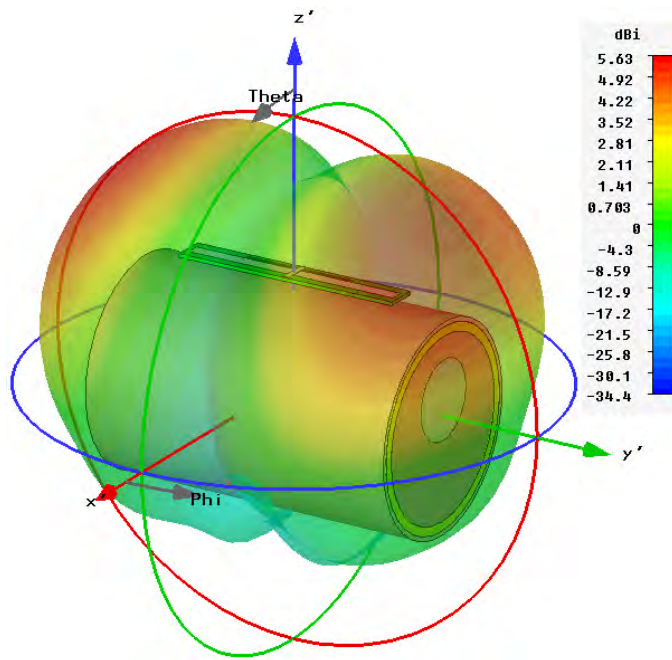
(b)

Figure 3.45: Computed radiation patterns (directivity) of proposed antenna in close proximity to human arm models (a) elliptical (across the arm length) (b) elliptical (along the arm length).

In this section we have discussed sensitivity of wearable printed antenna presented in section 3.3, which has a wide beam and is highly insensitive to the gap between the human arm and provide better coverage along the body surface. Antenna performance under different scenarios has been investigated. Due to the full ground plane, this antenna performance is very insensitive to the separation between the antenna and the human arm. For example, an increase of this gap from 0mm to 10mm has negligible effect on antenna resonance frequency and its effect on the radiation pattern is also not noticeable. Small width of the antenna makes it a suitable candidate for on-body wearable devices and its placement along the arm length can avoid bending and hence possible detuning.

3.5   Performance over Human Body Phantom

To analyze the performance of designed antennas, three layer human tissue body model is considered for simulations. For measurements, gels equivalent to human body tissues are used. The gels were prepared at Electro Science Lab at Ohio State University, USA, and measurements were also performed there. Table 3.4 presents the theoretical and measured properties of skin, fat and muscle tissues. These gels consist of gelatin A, polyethylene glycol mono phenyl ether (Triton X-100), sodium chloride, de-ionizing water, vegetable oil, soap and food colouring. Four different cases were considered and the communication between the antennas shown in Fig. 3.46 is observed. Fig. 3.47 illustrates the female phantom filled with muscle equivalent gel, and layers of skin and fat equivalent gels.

(a)
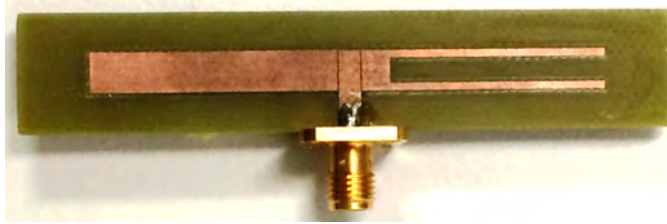
(b)
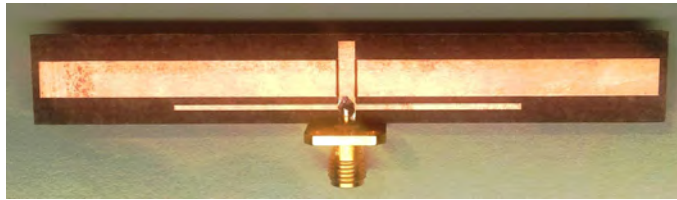
(c)

Figure 3.46: Antennas considered for measurement over phantom (a) Antenna-I (b) Antenna-II (c) Antenna-III.

CASE-I:

When Antenna-I and Antenna-III are placed over abdomen as shown in Fig. 3.48. The corresponding reflection and transmission behaviors are shown in Fig. 3.49. In this case both antennas are having partially filled nulls facing each other (i.e. partially filled nulls are present in direction opposite to feed).

Table 3.4: MEASURED PROPERTIES OF GEL EQUIVALENT TISSUE MODEL AT 2.45GHz.

	Skin ε_r (2mm)	Fat ε_r (10mm)	Muscle ε_r (Phantom)
Theoretical	$38.01 + i * 10.74$	$5.28 + i * 0.77$	$52.73 + i * 12.76$
Measured	$38.09 + i * 2.65$	$7.95 - i * 1.88$	$69.88 + i * 15.80$
	Measured using Agilent 85070b Dielectric Probe Kit	Measured using Agilent E4991A Kit	Measured using Agilent 85070b Dielectric Probe Kit
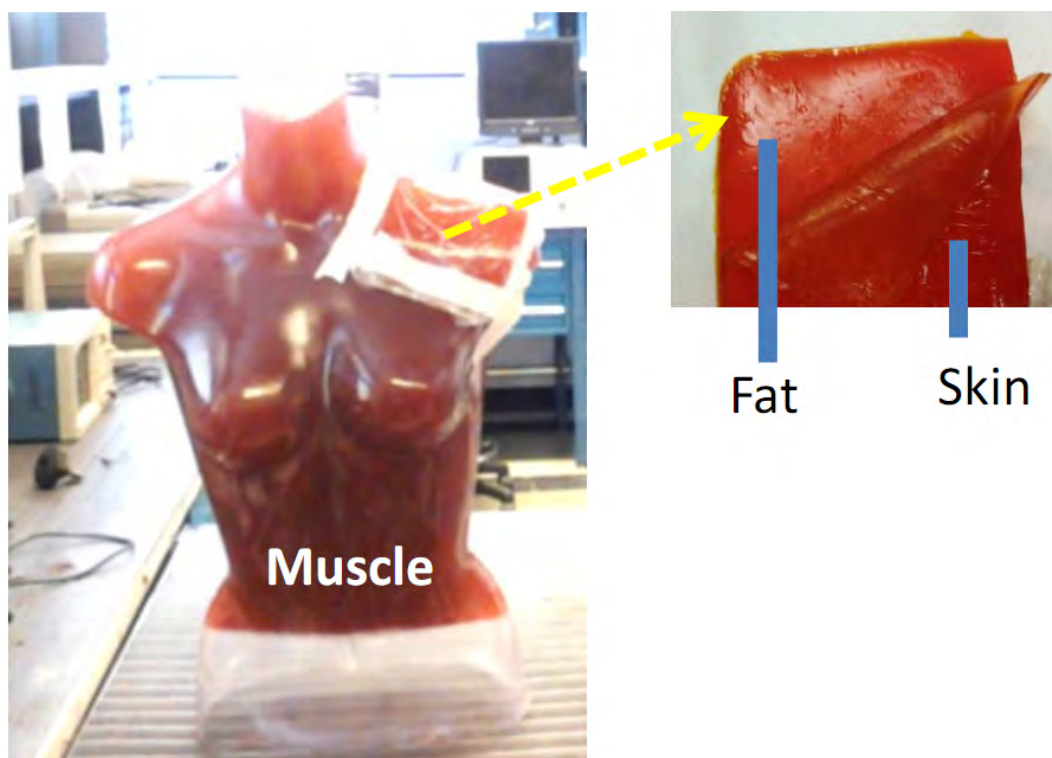
Figure 3.47: Female body phantom (muscle) with skin and fat layers.

Figure 3.48: Placement of antennas over phantom for Case-I.
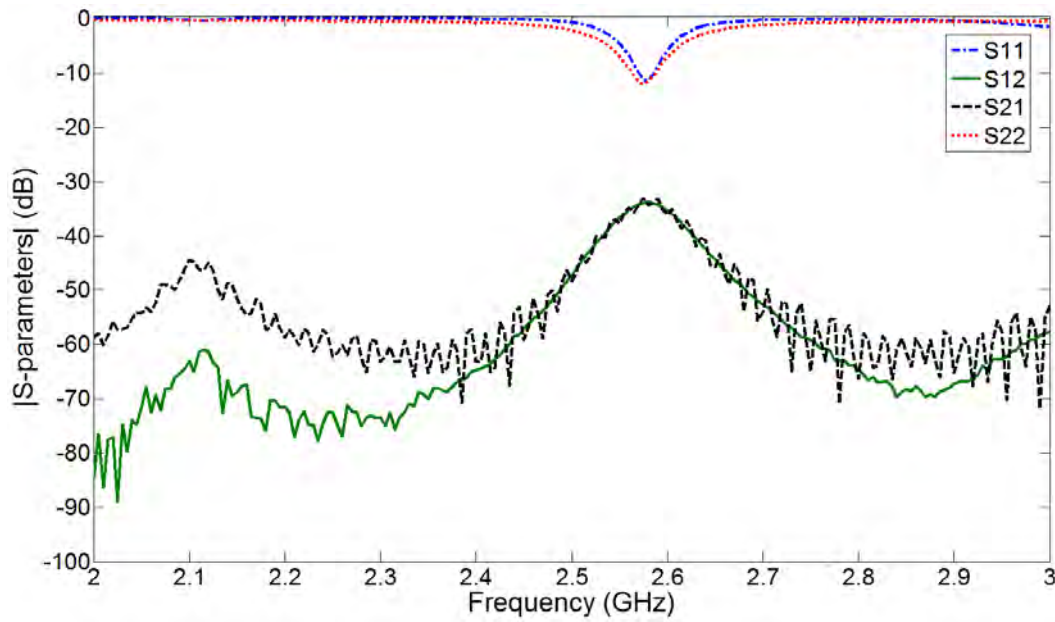
Figure 3.49: Measured S-parameters corresponding to Case-I.
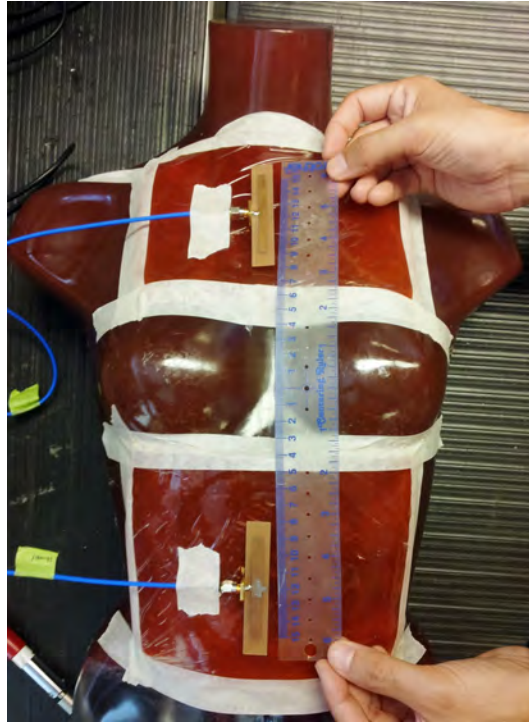
Figure 3.50: Placement of antennas over phantom for Case-II.
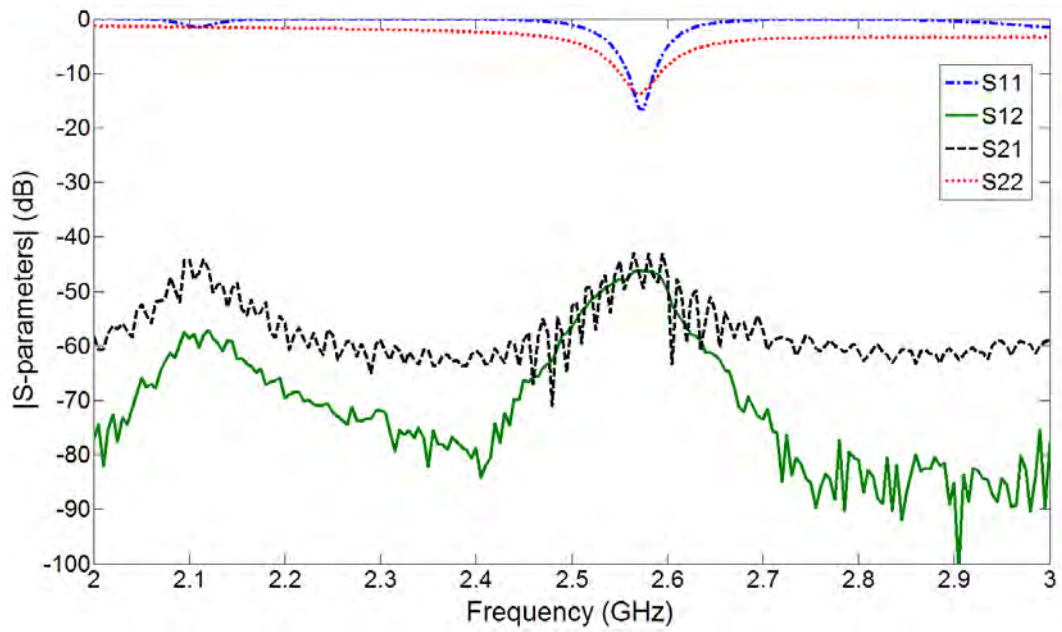
Figure 3.51: Measured S-parameters corresponding to Case-II.

Figure 3.52: Placement of antennas over phantom for Case-III.
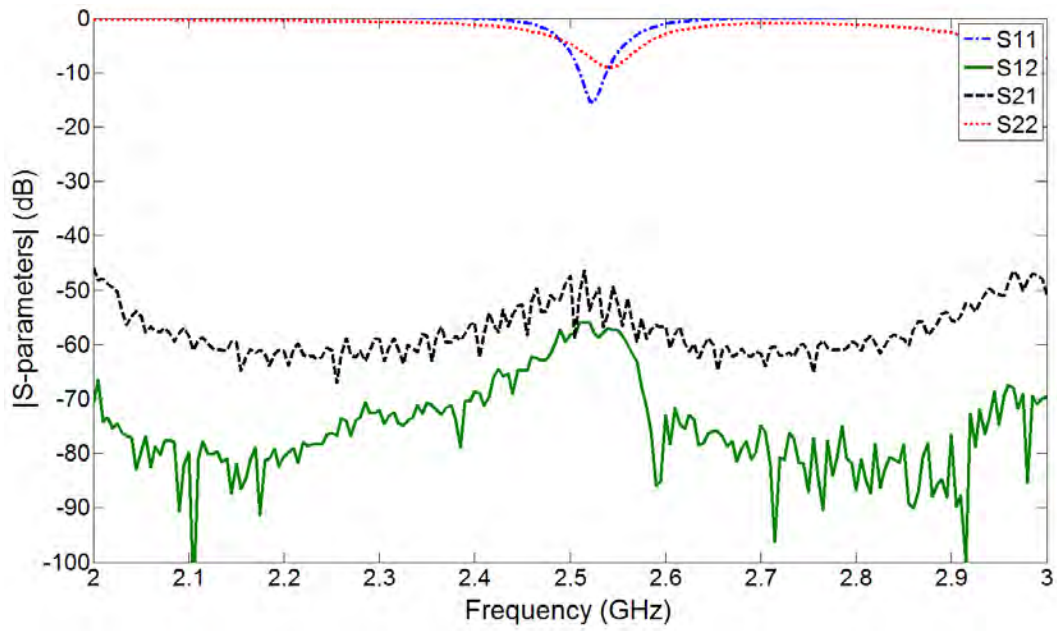
Figure 3.53: Measured S-parameters corresponding to Case-III.

Figure 3.54: Placement of antennas over phantom for Case-IV.

CASE-II:

When Antenna-I and Antenna-III are placed over chest and abdomen, respectively, as shown in Fig. 3.50. The corresponding reflection and transmission behaviors are shown in Fig. 3.51. In this case both antennas are having lobes facing each other ((i.e. lobes are present along the antenna's length)).

CASE-III:

When Antenna-I and Antenna-III are placed over chest and abdomen, respectively, as shown in Fig. 3.52. The corresponding reflection and transmission behaviors are shown in Fig. 3.53. In this case, Antennas-I has radiation beam facing Antenna-III which is placed over chest and has partially filled null towards Antenna-I.

CASE-IV:

When Antenna-I and Antenna-II are placed over shoulders as shown in Fig. 3.54. The corresponding reflection and transmission behaviors are shown in Fig. 3.55. In this case, both antennas have radiation beams facing each other from sides.
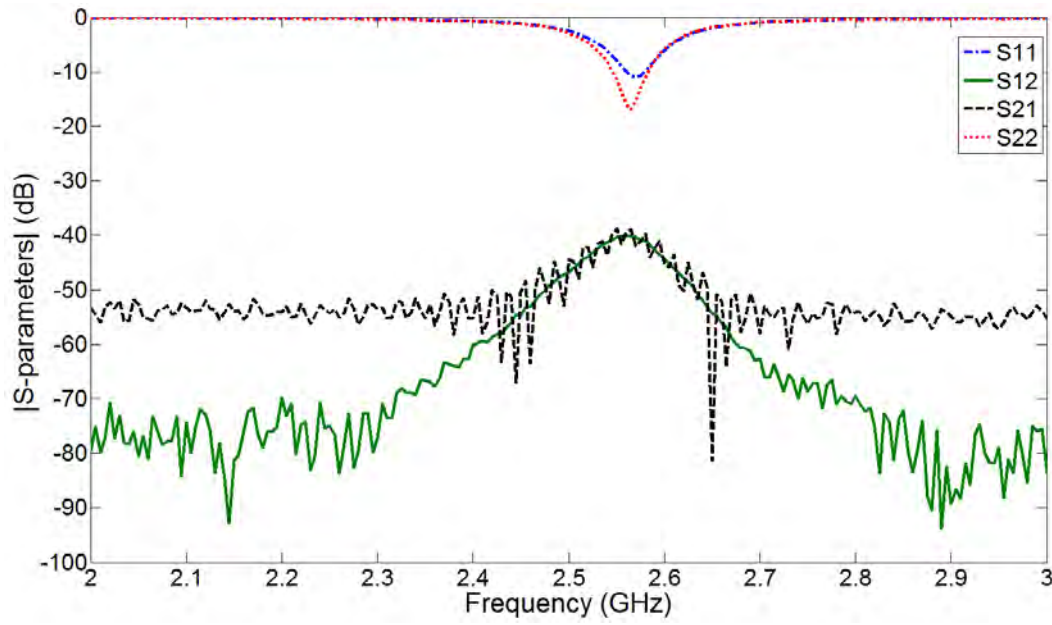
Figure 3.55: Measured S-parameters corresponding to Case-IV.

Figure 3.56: Antenna size comparison with a wrist watch.

3.6 Applications

The antennas presented in this chapter has signification advantage of narrow width in addition to wide-beam for coverage, less sensitivity to gap variation, placement and con-

formal bending. In applications involving body motion/movements, the gap between the antenna and body is continuously changing. The stable performance of proposed designs with the changing gap between the antenna and the body will be highly beneficial. Fig. 3.56 show a size comparison of designed antenna with a wrist watch. Due to these advantages they are suitable for arm- and wrist-band application as shown in Fig. 3.57.

(a)

(b)

Figure 3.57: Wrist band type applications.[1]

---

[1]http://www.fitbit.com

3.7   Conclusion

In this chapter we have discussed novel narrow band antennas. Single- and dual-band antennas are presented for wireless body area network devices operating in the industrial, scientific, and medical (ISM) band at 2.45GHz and 4.9GHz public safety Wireless Local Area Networks (WLAN) band. Performance of the designed antennas has been analyzed for near body scenarios and in close proximity to the human arm models. These antennas have significant advantages of compactness (only 14mm wide), full ground plane to minimize radiation towards the body, a wide radiation pattern over the body surface to provide maximum coverage, and less sensitivity to the variation of the gap between the antenna and the human body. These advantages make them suitable for on-body communications and wearable applications.

Chapter 4

Wide Band Antennas

In this chapter, a flexible embroidered antenna on Polydimethylsiloxane (PDMS) composite is presented. The radiating parts of antenna are embroidered using conductive fibers. The proposed flexible antenna exhibits an ultra-wide return-loss bandwidth and gain bandwidth. A comparison between embroidered antenna on PDMS substrate and an antenna fabricated using copper on Rogers substrate has been carried out to investigate their behavior. The embroidered antenna on PDMS is compact, flexible, easy to integrate with clothing, semi-transparent and is suitable for wearable applications.

4.1 Ultra Wideband Antenna

Wireless body area networks (WBAN) have attracted the attention of antenna researchers over the past years, as they find promising applications in healthcare, monitoring, defence, sports, rescue and public safety [14]. Wearable systems for these applications are expected to use antennas that are light weight, integratable in clothing, conformal and flexible for ease of mobility. Traditionally, antennas are made using copper wires or by etching metal patterns on rigid substrates [1]. These rigid antennas become permanently deformed or break when stretched, folded or twisted. Additionally, when are large they are not

convenient for mobility. Rigid antennas are not a suitable choice for wearable applications as they may require antennas to be bendable and flexible. In literature, several flexible antennas have been reported using copper tape [6] and conductive ink [23, 24] on flexible substrates. Copper tape and conductive inks have durability issues for operating over longer period of time as the tape peels off the substrate easily and the inks erase off. In past, we have demonstrated reliable fabrication and excellent performance of antennas [8], RFID tags [2] and transmission line samples [25] with conductive E-fibers on flexible substrates using embroidery technique [1].

Several embroidered antennas and wearable sensors have been reported in literature using conductive fibers on textiles and polymer composite substrates [1, 3–5, 7, 8]. Embroidered wearable, flexible and stretchable antennas on textile and polymer composites have been reported earlier [1, 2, 26]. The performance of these antennas has been investigated which shows comparable results to the standard flexible copper antennas. Though significant research has been carried out on embroidered antennas which are designed for lower frequencies or to provide narrow band operation, more investigation is needed to analyze their behavior when designed for broad band or ultra-wide band operation.

Here, we present two UWB antennas. One antenna is fabricated on Rogers substrate with copper (i.e. Antenna-I) and the other is embroidered on PDMS composite substrate using conductive fibers (i.e. Antenna-II). Measured results are compared with the aim to analyze behavior of embroidered polymer composite antenna when designed for wideband applications. Antenna configuration and the fabrication of embroidered antenna using conductive fibers on PDMS composite substrate is demonstrated. Results are also discussed.
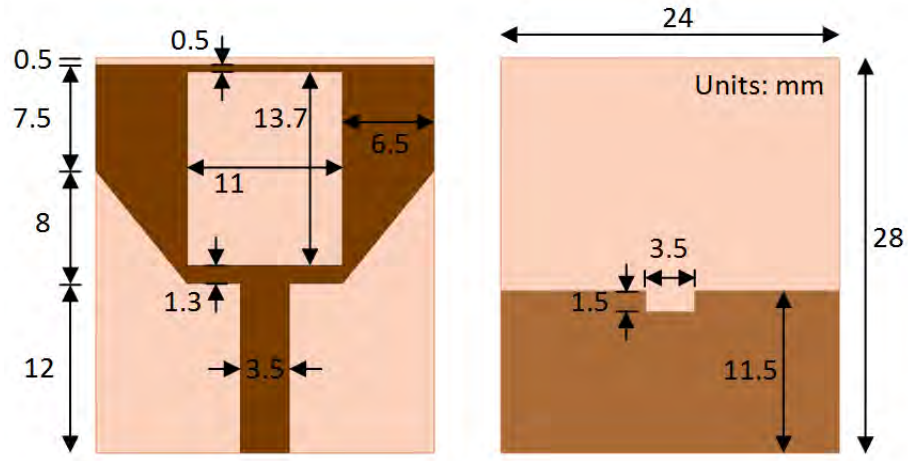
Figure 4.1: Geometry of the antenna.

4.2 Antenna Design

Fig. 4.1 shows the geometry of the printed UWB antenna. It was designed using ANSYS High Frequency Structural Simulator (HFSS). Initially, it was fabricated on a $24 \times 28mm^2$ RO3003 substrate coated with copper and later embroidered using conductive fibers on a PDMS composite. The RO3003 substrate has a dielectric constant of 3, loss tangent of 0.001 and thickness of 1.524mm. The PDMS composite substrate also has a dielectric constant of 3 and thickness of 1.524mm, but its loss tangent is 0.01 that differs by a factor of 10. Motivated from [60], the antenna consists of a monopole radiator and a partial ground plane. The monopole radiator, that is a patch chamfered at its lower corners and having a rectangular slot of $11 \times 13.7mm^2$, is fed by a 50Ω microstrip line, which is 12mm long and 3.5mm wide. The partial ground plane has dimensions of $11.5 \times 24mm^2$ and has a slit beneath the feed line, that helps in impedance matching [60, 62]. The proposed antenna has overall dimensions of $24 \times 28mm^2$ and covers the UWB frequency range.
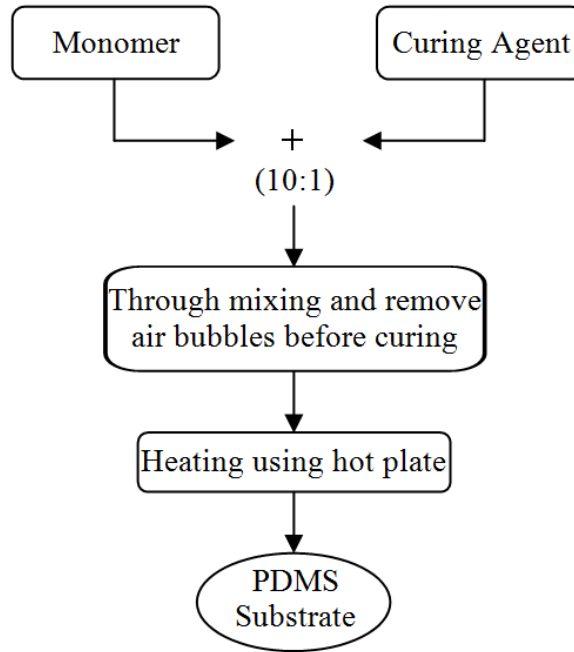
Figure 4.2: PDMS composite substrate making process.

4.3   Fabrication

This section presents the process of making PDMS composite substrate and the proposed flexible antenna using embroidery technique.

4.3.1   Process for Making PDMS Composite Substrate

We have used Sylgard 184 (Dow Corning Corp.) PDMS to make the flexible substrate using the procedure described in [86]. It is chosen as substrate due to its mechanical flexibility, water resistance and inherent chemical stability [87]. It is made manually by thoroughly mixing the monomer and the curing agent in 10:1. The air bubbles are removed before curing and the desired substrate thickness (i.e. 1.524mm) is set. Then the mixture is heated and dried using a hot plate. During substrate making, we tried our best to achieve a uniform thickness of substrate, however due to manual process there is a possibility that thickness may vary slightly.
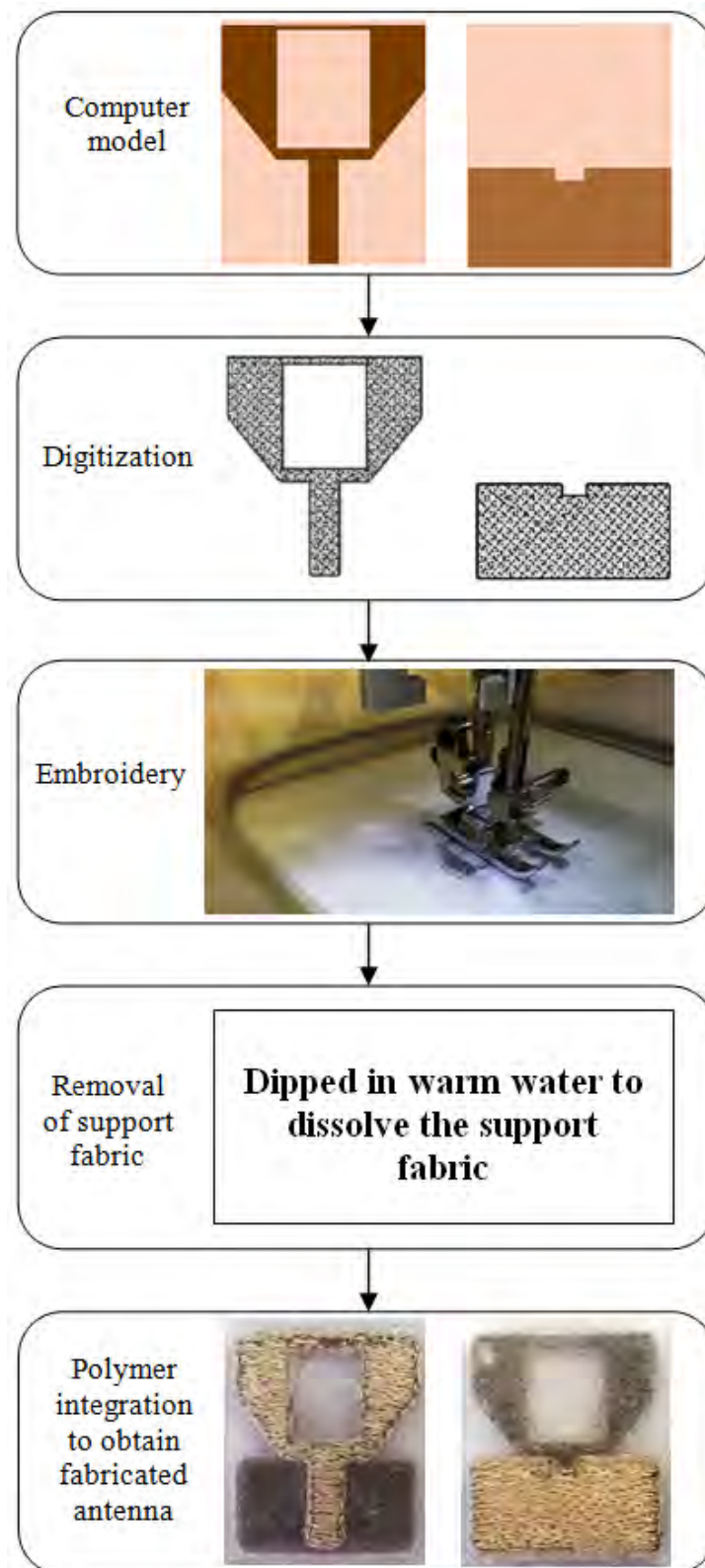
Figure 4.3: Embroidered antenna fabrication process.
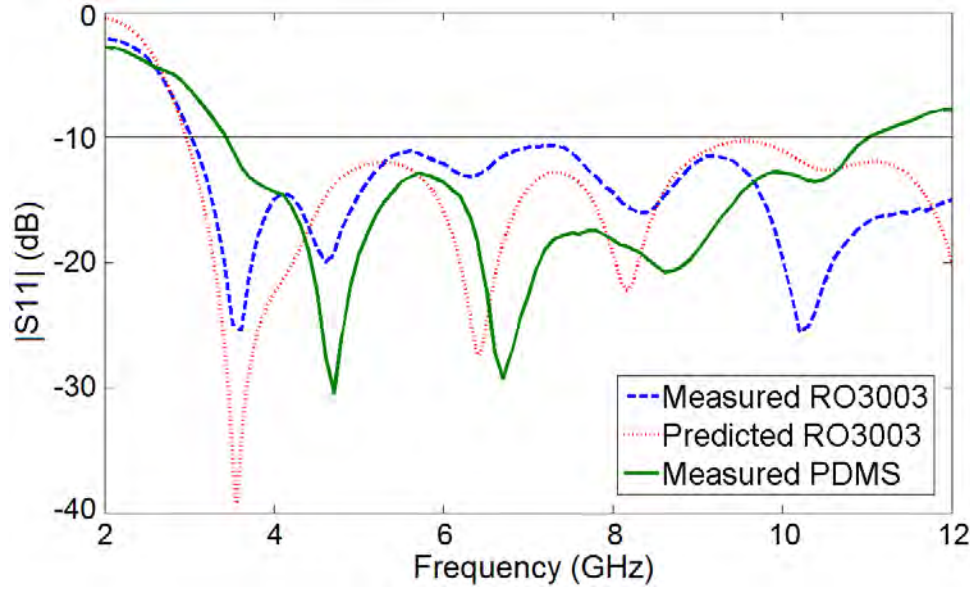
Figure 4.4: Measured and predicted reflection coefficients of the two antennas fabricated using Rogers and PDMS substrates.

4.3.2   Embroidered Antenna Fabrication

The radiating parts of the proposed design are embroidered using Liberator[TM] 20 conductive fibers. This conductive fiber has a DC resistance of 2 Ω/ft. It consists of 20 filaments and is coated with silver. The 2-layer embroidery method [8] is used with a stitching density of 7 lines/mm. This 2-layer embroidery model helps to provide better conductivity [25]. Fig. 4.3 shows the antenna fabrication process from the simulated computer design model to embroidered antenna integrated with PDMS composite substrate. The computer design model is digitized for stitching purpose and computerized embroidery procedure is used. A non-stretchable support fabric is used during embroidery process to have better stitching accuracy. This support fabric is later removed from the embroidered parts as it gets dissolved when dipped into the warm water. The embroidered parts are aligned and integrated with PDMS composite substrate to get the embroidered antenna prototype.
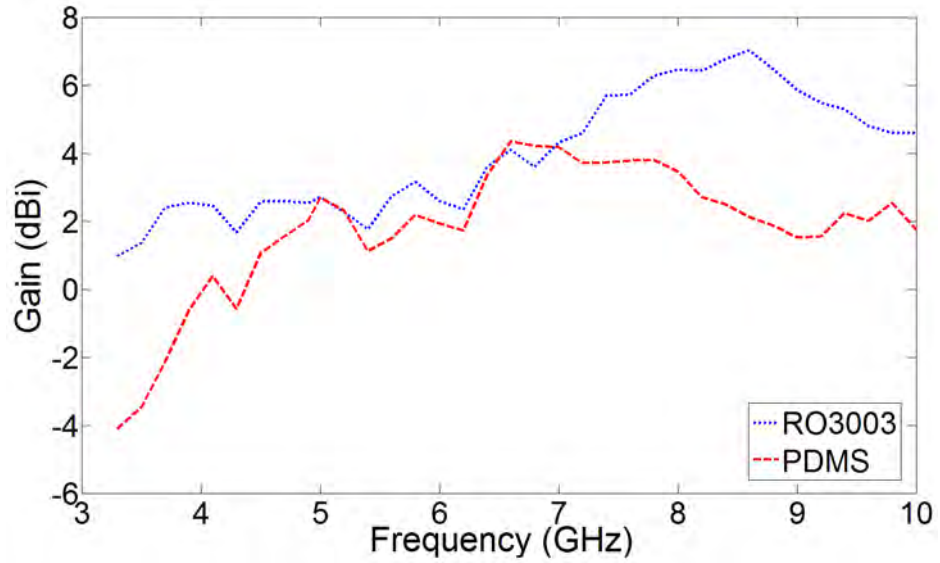
Figure 4.5: Measured gain of the two antennas fabricated using Rogers and PDMS substrates.

4.4 Results and Discussion

Simulations of proposed design shown in Fig. 4.1 were carried out using HFSS. Both prototypes were measured and the corresponding results for the reflection coefficient are presented in Fig. 4.4. It is noted the Antenna-I provides measured 10dB return-loss bandwidth covering the entire FCC ultra-wide band (3.1−10.6GHz). Antenna-II offers a measured 10dB bandwidth of 102% covering the frequency range of 3.43−11.1GHz. The embroidered antenna observes an impedance mismatch at lower frequencies. This can be due to the multiple layer embroidery process. As the multiple layers are stitched perpendicular to each other, the corners cannot be precisely defined as compared to the Rogers board. Another reason for frequency mismatch could be the integration of the antenna with its ground plane. Care has to be taken to align the slit in the ground plane. Since the antenna and the ground plane were integrated manually, a misalignment of slit in the ground plane with the antenna is possible which causes impedance mismatch.

Moreover, the two substrates, Rogers and PDMS, have different dielectric loss tangents. The resistance of conductive fiber can also contribute towards slight variation of results.

Fig. 4.5 presents the measured gain of both antennas. It is noted that Antenna-I has a gain variation in the rage of 1−7dBi whereas Antenna-II has less variation (i.e. 1−4dBi) in the frequency range corresponding to 10dB return-loss bandwidth. Measured radiation patterns of both antennas at different frequencies (i.e. 3.5, 5, 7 and 10GHz) are shown in Fig. 4.6 and are found to be in reasonable agreement. Although some variations in the radiation patterns are noted, it can be possibly due to the fabrication inaccuracy explained earlier.

4.5   Conclusion

A flexible embroidered antenna having an ultra-wide bandwidth, fabricated on poly-dimethylsiloxane (PDMS) composite substrate using conductive fibers, is presented. Another antenna was fabricated using Rogers material and copper, and is compared with embroidered version of the same design fabricated using conductive fibers on PDMS composite. Measured results show the similarity between the two prototypes. The embroidered antenna fabricated using conductive fibers on PDMS composite substrate also provides ultra-wide band operation. It is water resistant, flexible, compact, semi-transparent and is easy to integrate in clothing without being prominent. These traits make it suitable for wearable systems.

Figure 4.6: Measured radiation patterns (a) $\phi = 0°$ (b) $\phi = 90°$ at 3.5GHz, (c) $\phi = 0°$ (d) $\phi = 90°$ at 5GHz, (e) $\phi = 0°$ (f) $\phi = 90°$ at 7GHz, and (g) $\phi = 0°$ (h) $\phi = 90°$ at 10GHz of the two antennas fabricated using Rogers and PDMS substrates.

Chapter 5

Ultra Wideband Antenna with Band Notching

In this chapter, a simple ultra wideband printed monopole antenna with high band rejection and wide radiation patterns is discussed. The designed antenna has strong notch-band rejections (measured VSWR up to 26), and the notch band can be moved over a wide frequency range from 3.55GHz to 6.8GHz. It has wide radiation patterns and yields a measured 10dB return-loss bandwidth from 3GHz to 10.5GHz. This chapter also presents an analytical expression to predict initial design parameters of these antennas and to avoid excessive numerical computations required otherwise.

5.1 Introduction

UWB printed antenna designers often face challenges such as meeting space constraints, achieving a wide impedance bandwidth and wide radiation patterns. In addition, the antenna may need to reject effectively potential interference from the existing narrowband systems operating at higher power levels. This particular requirement becomes more stringent as many wireless systems including 3.6GHz IEEE 802.11y Wireless Local Area

Networks (WLAN) (3.6575−3.69GHz), 4.9GHz public safety WLAN (4.94−4.99GHz) and 5GHz IEEE 802.11a/h/j/n WLAN (5.15−5.35GHz, 5.25−5.35GHz, 5.47−5.725GHz, 5.725−5.825GHz) are operating within the FCC UWB band of 3.1−10.6GHz.

Several designs of planar printed UWB antennas incorporating a notch-band have been proposed to minimize this interference. The most commonly used method is inserting various shapes of slots in the radiating elements or in the ground plane [44–50]. Parasitic elements, electromagnetic-band gap (EBG) structures [51], integrated stopband filters [52], defected ground structures (DGS) [53, 54] and frequency selective surfaces (FSS) positioned above the antennas [55] have also been used to achieve band rejection.

Another popular method is to use a resonator on the other side of the substrate, such as a split ring resonator (SRR), square ring resonator [56], CPW resonator [48], composite right/left-handed (CRLH) resonator [57], capacitive loaded loop (CLL) resonator, open-loop resonator [58, 59] or a dual-gap open-loop resonator. However, only a few of these antennas have strong band rejections with VSWR above 15 [48, 51, 56, 60]. We still need more compact antennas with high band rejections and wide radiation patterns across the UWB band.

In this chapter, we propose a simple and more compact printed monopole antenna with high rejection (VSWR> 25) and wide radiation patterns up to 10GHz. The rejection band could be tuned between 3.55GHz and 6.8GHz to suppress inference. We present the design and a parametric study of the proposed antenna. The experimental results are given to validate the design, along with the design parameters set to mitigate interference caused by specific narrowband systems, as examples, to highlight its practical applications. The performance of the proposed antenna is compared with several previous designs.
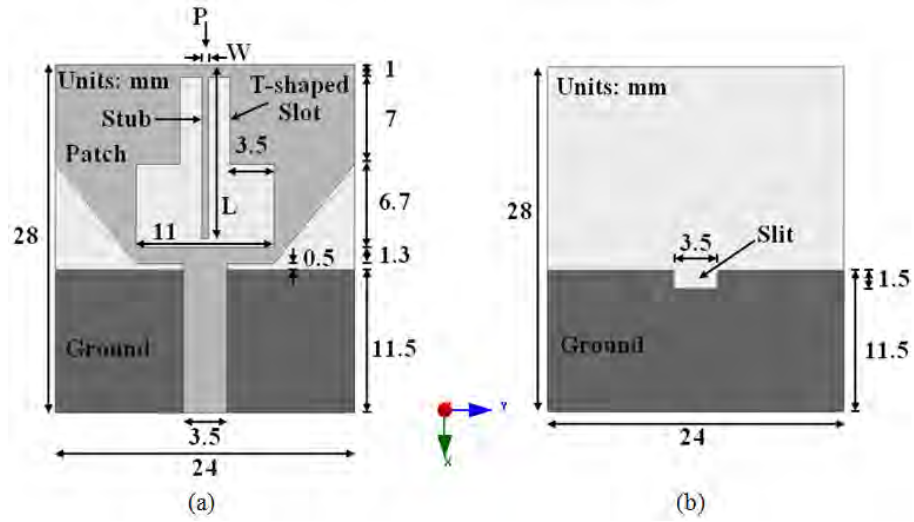
Figure 5.1: Geometry of the proposed UWB antenna with a notch band (a) Front view (b) Back view.

5.2   Antenna Design

Fig. 5.1 shows the geometry of the proposed printed UWB antenna. The antenna was designed using ANSYS High Frequency Structural Simulator (HFSS) and CST microwave studio. It was fabricated on a $28 \times 24mm^2$ RO4003TM substrate with dielectric constant of 3.38 and a thickness of 1.524mm. The design started with a rectangular monopole ($16 \times 24mm^2$) fed by a 50 microstrip line, which is 3.5mm wide and 12mm long. Next the patch was chamfered at the bottom edges and a slit $1.5 \times 3.5mm^2$ was created in the ground plane to improve matching [60]. The ground plane has dimensions of $11.5 \times 24mm^2$. A T-shaped slot in the radiating patch further helps in achieving better impedance match over UWB. Fig. 5.2 shows the impedance matching evolution of the proposed UWB antenna without notch-band. The T-shaped slot shown in Fig. 5.2 is beneficial in achieving antenna compactness as it increases the current path length in the radiating patch. Fig. 5.3(a) shows the matching behavior on a Smith chart at three stages of antenna development.
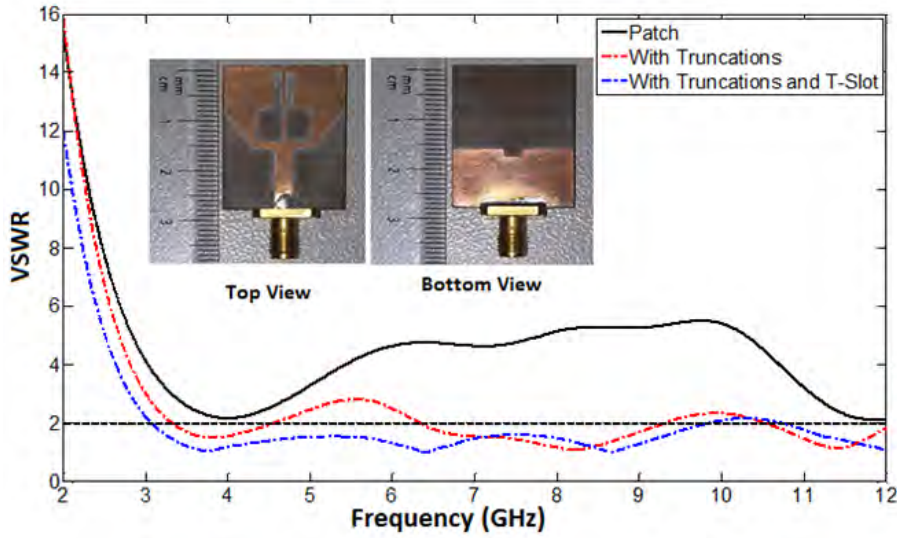
Figure 5.2: VSWR corresponding to three initial design stages of the reference UWB antenna without notch band. Inserts are photographs of the band-notched UWB antenna prototype.

Finally a stub within the T-shaped slot, shown in Fig. 5.1(a), was added to create a rejection notch within the bandwidth of the antenna. Its careful tuning provided high rejection over a narrow range of frequencies. Fig. 5.3(b) compares antenna S_{11} with and without the notch band. Un-normalized radiation patterns shown in Fig. 5.4(a) are consistently wide and stable at lower frequencies. They become more directional around 7GHz but are still reasonably wide. Efficiency of the proposed antenna, shown in Fig. 5.4(b), highlights the dramatic drop in antenna efficiency (by more than 80%) at the notch frequency. A complete parametric study of this notch feature is given in the next section.
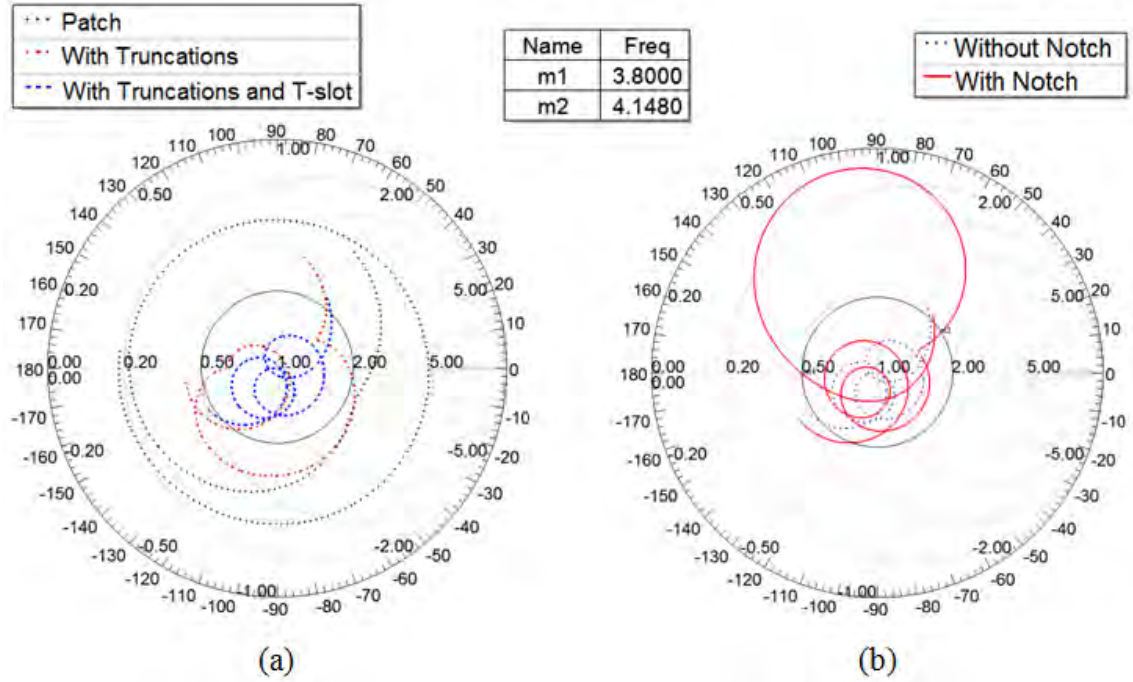
Figure 5.3: (a) Input reflection coefficient (S_{11}) at the three design stages mentioned in Fig. 5.2 (b) S_{11} of the antenna with and without the notch function (notch band is 3.8GHz−4.148GHz).

5.3 Parametric Study of Band Rejection

The centre frequency of the notch band, along with peak VSWR, is controlled by the length, width and position of the stub, as described below.

5.3.1 Effects of Stub Length Variation

By varying the length (L) of the stub from 8 to 14mm, rejection band is tuned. Fig. 5.5 shows the variation in the notch frequency from 3.59GHz to 6.25GHz when the stub length (L) is changed in this range. The stub width is 0.5mm. The 14mm stub provides a maximum VSWR of about 30. It comes down to 5 at 6.25GHz when the stub is shortened to 8mm. In brief, 0.5mm−wide and similar narrow, long stubs are suitable to create strong

(a)

(b)
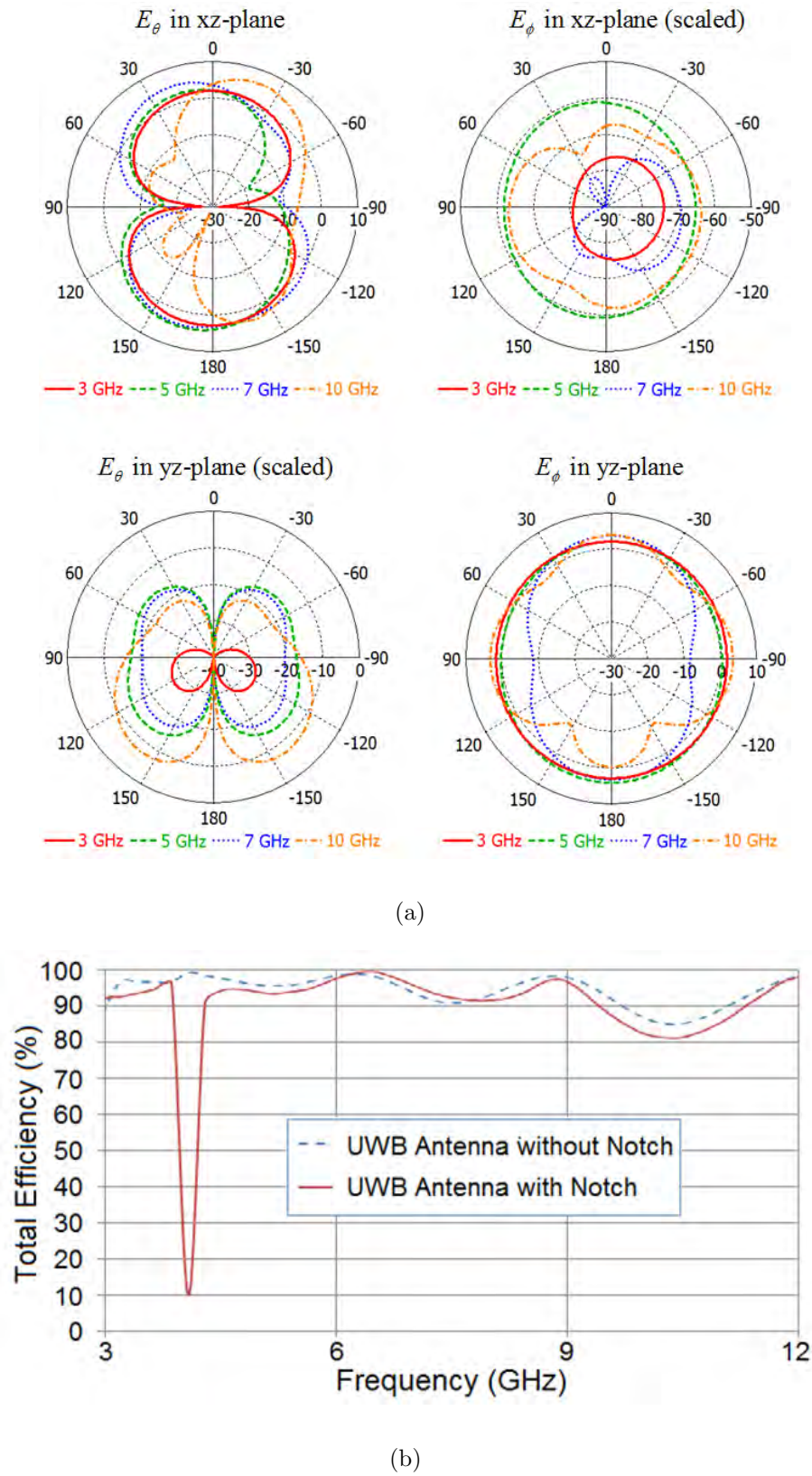
Figure 5.4: (a) Computed radiation patterns of the notched antenna on xz-plane and yz-plane at 3, 5, 7, 10 GHz (b) Antenna efficiency with and without notch.

notches at lower frequencies. When the stub length is 15mm, it touches the transmission line section. This is discussed later as a special case.
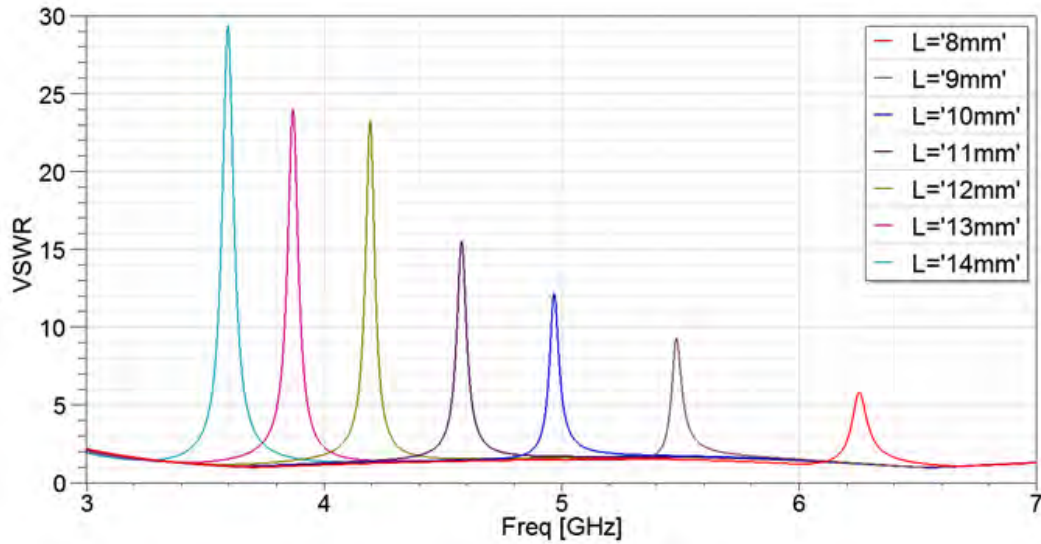
Figure 5.5: The effect of stub length variation on VSWR and notch band (stub width = 0.5mm).

5.3.2   Effects of Stub Width Variation

Fig. 5.6 shows the variation of the notch frequency from 3.55GHz to 4.07GHz, when the width of the stub is changed from 0.1mm to 4mm. The stub length is maintained at 14mm. The increase in the width increases the notch frequency. It is important to note that even at a higher frequency above 4GHz, peak VSWR value as high as 34 can be obtained with thick stub. Such a high VSWR is not possible above 4GHz using narrow (0.5mm) stubs considered in section 5.3.1; thick stubs are suitable for such applications. Thus a judicious choice of length and width is essential to get a notch band with high rejection. At 4mm width, the stub touches the side of T-shape slot. This is also discussed later as a special case.
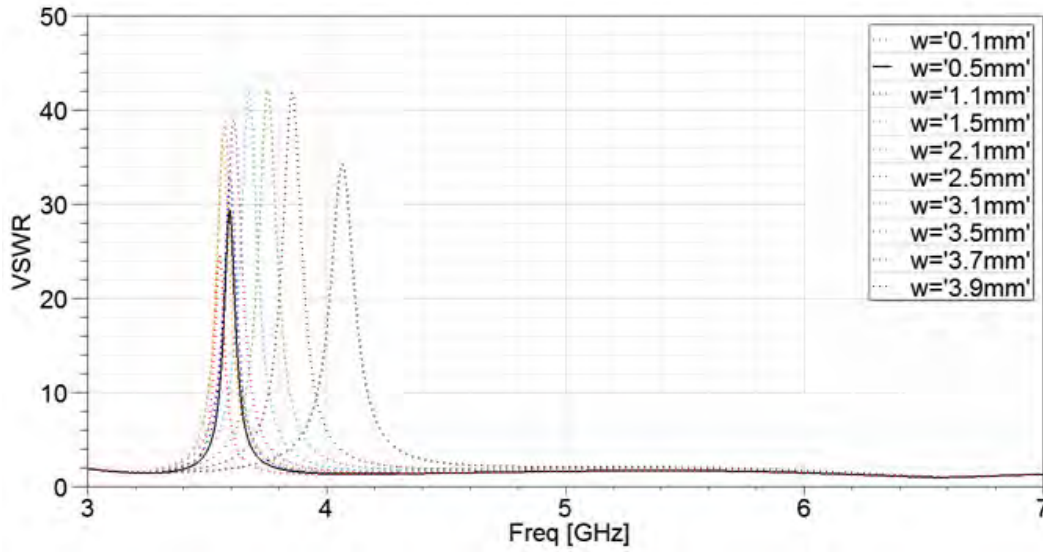
Figure 5.6: VSWR corresponding to stub widths from 0.1mm to 3.9mm (stub length = 14mm). Peak VSWR variation is between 22 to 42.

5.3.3   Effects of Stub Position Variation

The notch frequency can also be fine tuned by changing the position of the stub, making the antenna non-symmetrical. Let p be the offset between the centre line of the stub and the centre line of the patch. Fig. 5.7 illustrates the effect of stub offset on VSWR. For w=0.5mm, when p=1.75mm, the stub touches the patch. When p=2mm, the stub overlaps with the patch. Results illustrate that when moving the stub closer to a slot edge, the rejection band shifts towards higher frequencies and rejection also becomes weaker with a decrease in the peak VSWR. In brief, symmetrical antennas with p=0 have the best rejection.

5.3.4   Special Cases

When the stub is 15mm long, it touches the metal at the other end, completely separating the slot into two parts. Fig. 5.8 shows that a 15mm long and 0.5mm wide stub provides
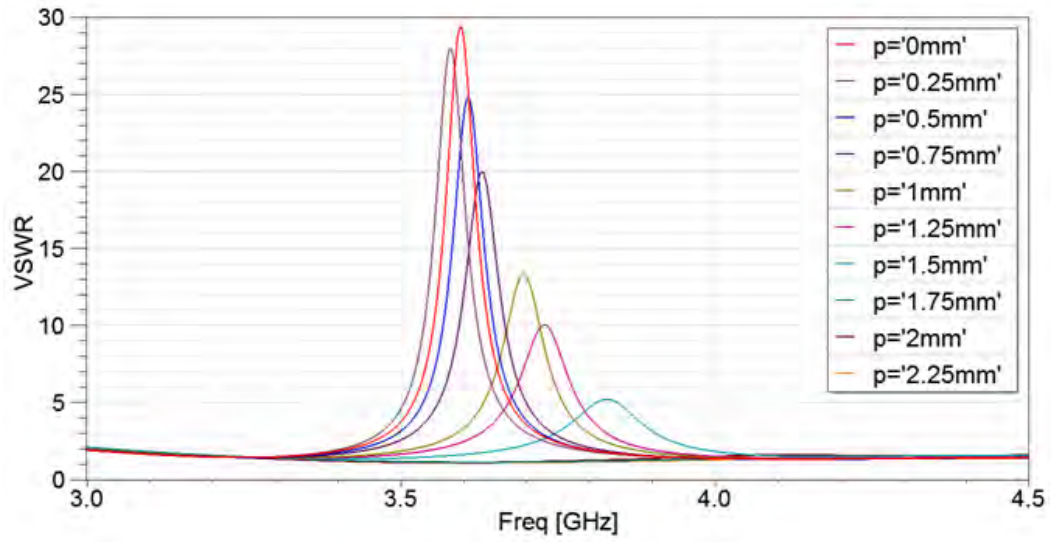
Figure 5.7: VSWR corresponding to several stub positions (stub length = 14mm, stub width = 0.5mm).

a rejection band from 6.46GHz to 7.15GHz at VSWR > 2 with a peak VSWR > 12 at 6.71GHz. For 15mm long and 0.1mm wide stub, rejection band is from 6.52GHz to 7.16GHz with a peak VSWR > 12 at 6.8GHz. Likewise, the maximum stub width is 4mm when it touches sides of the T-shaped slot. A 12mm long and 4mm wide stub provides a rejection band from 6.06GHz to 7.24GHz with a peak VSWR > 11 at 6.56GHz. These three special cases are useful to create notches with VSWR > 10 at higher frequencies (>6.5GHz), which is otherwise very difficult. For 14mm long and 4mm wide stub, rejection band is from 4.09GHz to 6.47GHz with a peak VSWR > 29 at 4.68GHz. This special case is practically not useful due to extremely wide notch.

Based on the parametric studies presented in this section, the following parameters have been selected for prototyping using available fabrication facilities, with the intention of demonstrating a peak VSWR > 20: L=12.75mm, w=0.5mm and p=0.

Table 5.1: COMPARISON OF THE PROPOSED ANTENNA WITH SEVERAL EX-
ISTING DESIGNS.

#	Dimensions (mm^2)	Rejection Band	Peak VSWR
[44]	32×26.8	WLAN 5.8GHz	9
[45]	30×35	WALN around 5.5GHz	14
[46]	28×32	$5.0 - 5.6$GHz	14
[47]	28×30	$5.15 - 5.825$GHz	9
[48]	32×35	$3.26 - 3.75$ & $5.02 - 5.9$GHz	19
[49]	30×39.3	$5.15 - 5.825$GHz	10
[50]	20.4×64	WLAN 5GHz	19.3
[51]	38×40	$3.57 - 6.71$GHz	26
[56]	30×29	$5.2 - 5.95$GHz	17
[58]	35×30	WLAN	9
[59]	40×31	At 5.15GHz	15
[60]	24×36	$5.09 - 5.84$GHz	16
[88]	34×27	$3.23 - 5.93$GHz	14
[89]	40×31	4.13 & 5.244GHz	15
[90]	24×35	$4.5 - 6.5$GHz	–
[91]	30×30	$4.72 - 6.56$GHz	8
[92]	25×28	$4.9 - 5.9$GHz	9
[93]	34×34	WLAN 5GHz	9
[94]	49×53	$5.05 - 6.17$GHz	> 10
Proposed	28×24	Tunable between $3.55 - 6.8$GHz	up to 26 *(measured)**

*For the fabricated antennas used in Fig. 5.9
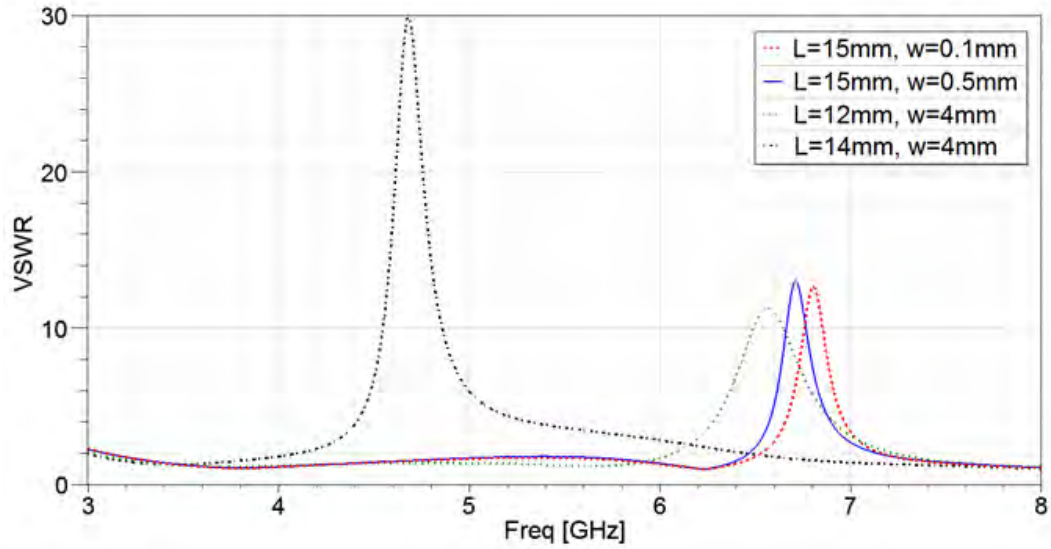
Figure 5.8: VSWR corresponding to two special cases of maximum possible stub length and stub width.

5.4 Experimental Results

The antenna prototype, fabricated and tested to validate the design method, is shown in the inset of Fig. 5.2. Fig. 5.9 compares its measured and predicted VSWR with good agreement. The measured rejection peak has a VSWR > 25. Fig. 5.10 illustrates the variation of the measured peak gain with frequency. Peak gain direction can change with frequency. A 10 dB drop in peak gain is noted in the notch-band. Antenna efficiency without notch is greater than 80 % for all frequencies up to 9.5GHz in the passband and it drops to 10 % at 4.06GHz when a notch is introduced at this frequency. The antenna gain varies from 2 dBi to 6 dBi. Fig. 5.11 shows that the proposed antenna with high notch-band rejection also provides wide radiation patterns in pass bands between 3−10GHz. Some discrepancies can be observed between measured and computed radiation patterns due to connector cables and misalignments. Table 5.1 compares the new antenna against the other reported antennas with notch-band characteristics. We note that only a few
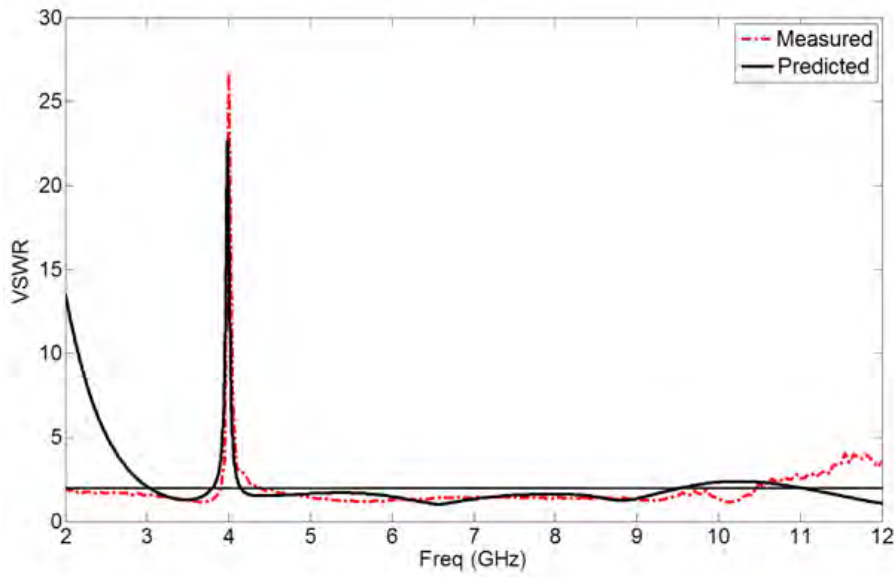
Figure 5.9: Measured and predicted VSWR of the fabricated antenna (notch band is 3.8GHz−4.148GHz).

reported antennas have peak VSWR values greater than 15 and they have lesser control of the notch frequency. With the proposed method, VSWR values as high as 26 can be obtained at the lower notch bands. For higher notch bands close to 6.8GHz, the special cases provide VSWR as high as 12.

5.5 Stub Design and Band Rejection

In this section, stub parameters are changed to demonstrate practical value of the presented antenna concept when it is required to reject signals from 3.6GHz IEEE 802.11y, 4.9GHz IEEE 802.11y and 5GHz IEEE 802.11a/h/j/n systems. To estimate the stub length for a given application, we first derived the following piece-wise analytical expressions for the normalized stub length (L_N), which are independent of substrate dielectric constant, by curve fitting to full-wave simulation results:
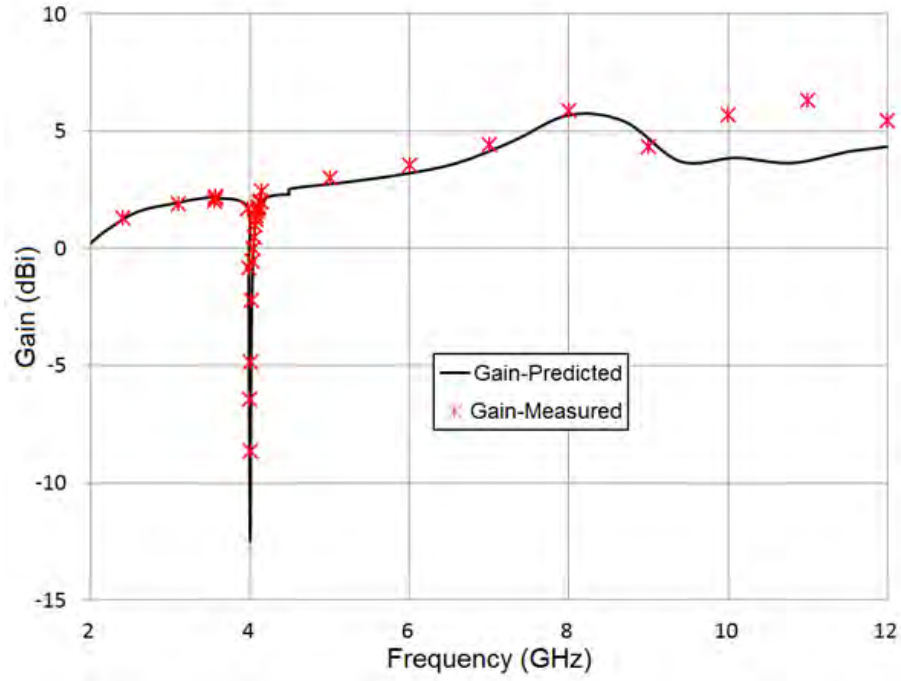
Figure 5.10: Measured and predicted gain for the fabricated antenna (notch frequency is 4.06GHz).

$$
L_N =
\begin{cases}
-1.593 \times 10^{-30} f_o^3 + 2.028 \times 10^{-20} f_o^2 \\
-8.522 \times 10^{-11} f_o + 4.268 \times 10^{-1}; f_o \leq 4.6 GHz \\
\\
-1.909 \times 10^{-31} f_o^3 + 1.027 \times 10^{-20} f_o^2 \\
-9.574 \times 10^{-11} f_o + 6.201 \times 10^{-1}; f_o > 4.6 GHz
\end{cases}
\tag{5.1}
$$

where

L_N is normalized stub length w.r.t. $\lambda_g = \lambda_o \big/ \sqrt{\varepsilon_r}$

f_o is the central notch frequency

The stub length (L) can be obtained for given substrate from

$$
L = L_N \lambda_g = \frac{L_N \times c}{f_o \times \sqrt{\varepsilon_r}}
\tag{5.2}
$$
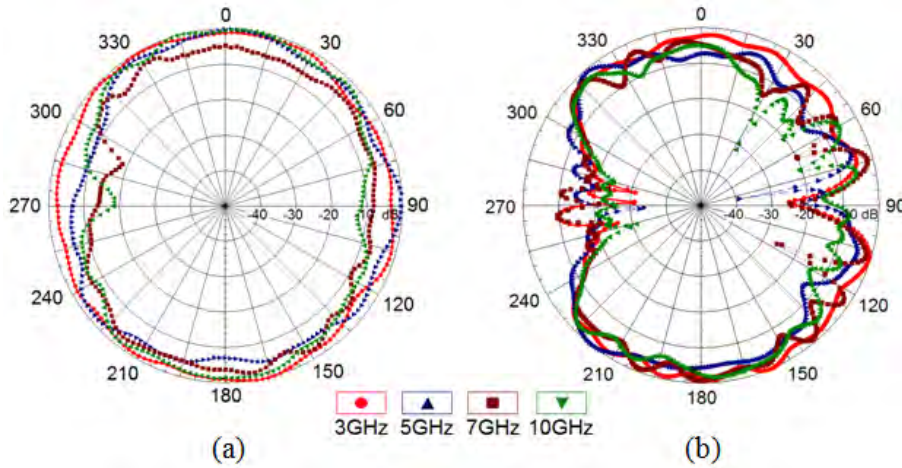
Figure 5.11: Measured overall radiation patterns at 3, 5, 7, 10 GHz in (a) H-Plane (i.e. yz-plane) (b) E-Plane (i.e. xz-plane).

To reject interference caused by IEEE 802.11y ($3.6575-3.69$GHz) systems, the initial stub dimensions were estimated to be L_N =0.3084 and L=13.7mm using (5.1) and (5.2), at the centre frequency of 3.67375GHz. The antenna is to be fabricated on a $28 \times 24mm^2$ RO4003TM substrate with dielectric constant of 3.38. Then stub dimensions (length and width) were fine tuned using HFSS full-wave simulations to maximize the peak VSWR at the centre frequency. Thus results in final stub dimensions of L=13.75mm and w=0.5mm.

Similarly, to mitigate interference caused by 4.9GHz IEEE 802.11y and 5GHz IEEE 802.11a/h/j/n, the initial stub lengths on the same substrate, from (5.1) and (5.2), were L_N =0.3727 and L=11.3mm. The parameters were further fine-tuned to L=11.3mm and w=3.8mm. Fig. 5.12 illustrates the band rejections obtained from HFSS full-wave simulations for these two cases.
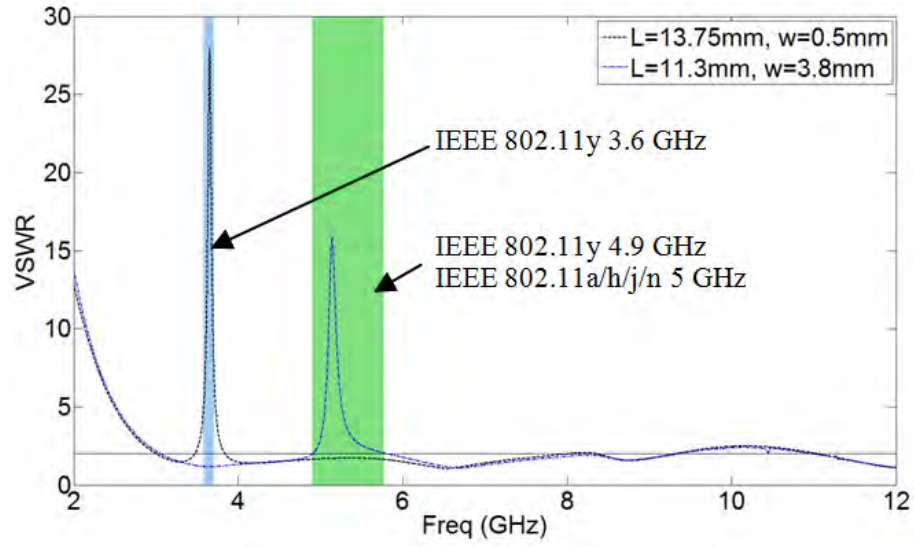
Figure 5.12: Band rejections after ne tuning the stub dimensions. Notch bands are 3.474−3.84GHz and 4.9−5.8GHz.

5.6 Conclusion

A compact UWB printed monopole antenna with high band rejection (up to VSWR > 25), tunable over a broad range of frequencies from 3.55GHz to 6.8GHz, is presented. The piece-wise analytical expressions give sufficiently accurate first estimate of the required stub length, avoiding excessive trail-and-error full-wave simulations. The new antenna has additional advantages of smaller size and wide radiation patterns.

Chapter 6

Antennas with Reflectors

In this chapter, a present use of frequency selective surfaces (FSSs) and high impedance surfaces (HISs) with antennas to achieve desired radiation patterns. To achieve a uni-directional radiation pattern, an ultra-wideband FSS is utilized as reflector with a UWB antenna which has bi-directional radiation pattern. Similarly, to achieve omni-directional and steerable patterns, printed microstrip HIS is used. In this chapter, we also present control of the dispersion characteristic, mainly in the position of the band-gap, for printed microstrip HIS that operate at lower frequencies.

6.1 Ultra Wideband Antenna with Wideband FSS Reflector

In this section, a low profile coplanar waveguide (CPW) fed printed semicircular slot antenna (PSSA) loaded with multilayer frequency selective surface (FSS) is presented. The slot antenna is placed over a closely spaced FSS reflector, which helps in achieving a stable uni-directional pattern over a broad bandwidth. The FSS reflector consists up of two layers; each layer contains a combination of slots and dipoles and yields a ultra-wide stop

bandwidth (UWSB) of 133%. Theoretical and measured analysis of the FSS is presented before proceeding toward the incorporation of FSS screen as a reflector underneath a slot antenna. The dual-layer FSS provides an appropriate reflection phase to act as a reflector and is able to provide uni-directional patterns. Measurement shows a linear phase response from 3.5GHz to 12GHz that is sufficient for an ultra wideband operation. The composite antenna has a theoretical average gain of 8.5dBi and a very small maximum gain variation of ± 1.5dB over the 3.5 to 10GHz frequency range. Experimental results for the final antenna design (with a size of $30 \times 60 \times .0787 mm^3$), mounted on a back plate (with a size of $330 \times 480 \times 1.6 mm^3$), exhibit a 115% impedance bandwidth, the peak gain reach up to a maximum of 9.8dBi, low cross-polarization, and a front-to-back ratio with FSS reflector (no electric conductor backing) reached up to 27dB at 6.5GHz and better that 15dB over the whole impedance bandwidth. The results are improved in terms of radiation pattern i.e. uni-directional with stable beam over a wide bandwidth as compared to our earlier reported slot structure [95]. Its compact configuration provides flexibility for mounting the reflector close to the slot antenna and makes it more suitable for modern communication systems.

6.1.1 Unidirectional Slot Radiators

A printed slot antenna with cavity-back for wireless local area network (WLAN) access points (base stations) was presented in [96]. The antenna is wideband with frequency-stable unidirectional radiation pattern, low cross polarization, and high front-to-back ratio and which allows very close packing to form a compact array with low mutual coupling. Measured front-to-back ratio (f/b) ranges between 11 and 20dB within the operating bandwidth from 2.5 up to 5.5GHz with gain increases with frequency from 5.5 to 8dBi. The dimensions are $57 \times 57 \times 27 mm^3$ ($0.48\lambda \times 0.48\lambda \times 0.18\lambda$) at the lower operating frequency of 2.5GHz. A circular polarized cavity-backed antenna excited by crossed triangular bowtie
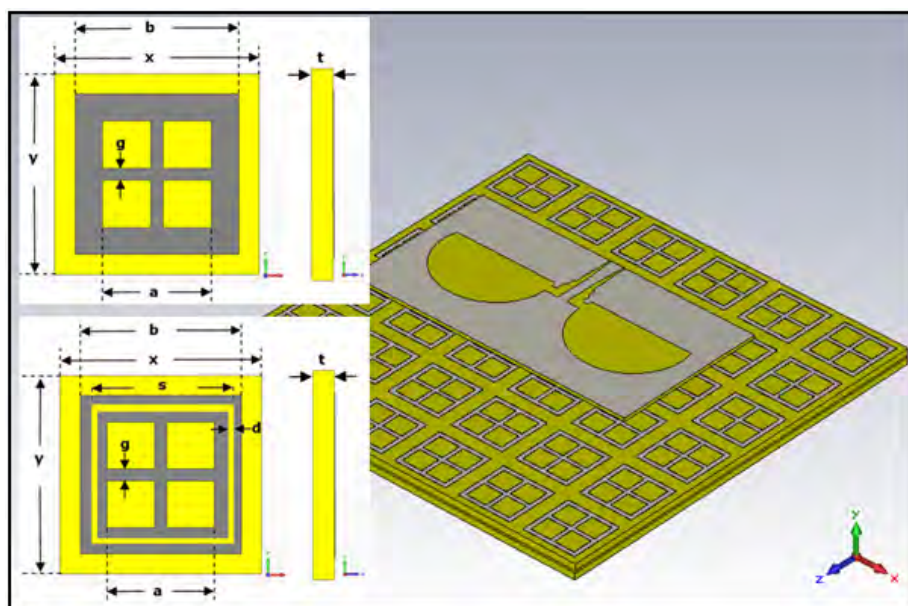
(a)
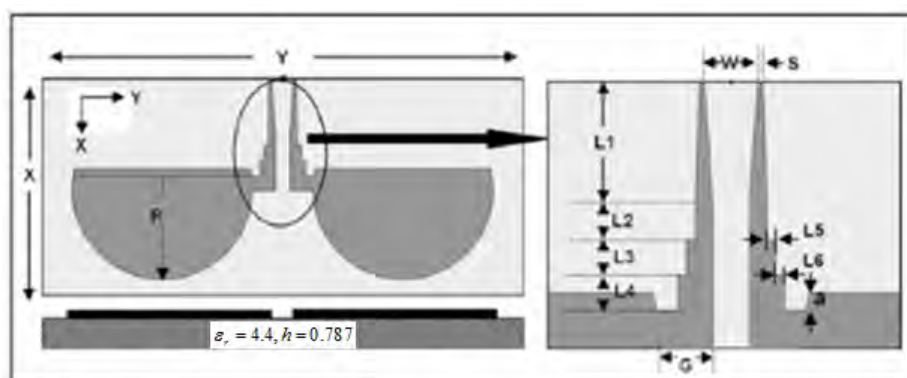
CPW-fed SSA

X=30, Y=60, W=3, S=0.3, G=2.5, L1=7, L2=L3=L4=2, L5=L6=0.5, a=1 and R=12
(All dimensions are in mm)

(b)

Figure 6.1: (a) SSA over the dual-layer FSS reflector. The unit cell geometry is shown in the inset. First layer of FSS unit cell: x=y=15, b=12, g=0.9, t=1.6; Second layer of FSS unit cell that has dual band behavior and has all dimensions same as in layer 1 except d=1.0 mm; Gray areas have metal coating. (b) CPW fed semicircular slot antenna [13].

dipoles was presented in [97]. Antenna achieved an impedance bandwidth of over 57.6% with broadside gain of 8 to 10.7dBi; this large gain is because of increasing aperture of tapered cavity (1.028λ) while the overall height if the cavity is 0.257λ. A CPW-fed log-periodic slot antenna with unidirectional back cavity has been proposed and investigated in [98]. The use of multiple cavities makes this structure more complicated but compact, the cavity resonating at lowest frequency is placed at $\lambda/8$ however the log periodic nature of the feed make this antenna less favorable for several pulse applications. Most of these cavities structures are made of hard metal and produce added mechanical fabrication and mounting needs with added bulk to the structure. AMC/EBG or FSS provide a low mounting of slot radiators close to the metallic structure and inherent phase property and easy fabrication over substrate make them more favorable candidates. The reflection phase of the AMC reflectorat the centre frequency it should ideally be $0°$ and minimum variation as function of frequency will ensure optimum bandwidth of the antenna. Back in 1999, Shumpert et al. [99] published results of a conductor-backed folded slot (fed with a coaxial transmission line) with an EBG structure. The gain of the antenna was found to be approximately 3.7 ± 0.2dB, yielding an estimated efficiency of between 80% 90%. Elek et al. [100] present a slot antenna with use of modified mushroom EBG with a front-to-back ratio of 21 ± 3dB at broadside. The gain improvement at broadside in both the E and H planes was experimentally measured to be between 2.5 and 2.9dB over the frequency range spanning from 3.8 to 4.0GHz, indicating radiation efficiency between 89% and 98%. Park et al. [101] presented a compact cavity-backed (with open sides) slot antenna (offset-fed with a microstrip line) with an etched or so-called "uni-planar compact photonic band-gap" (UC-PBG) reflector. The gain of this antenna and the reference antenna are 3.47dB and 2.47dB, respectively, which is 1dB improvement over reference antenna. The front-to-back ratio is 8.83dB for the E-plane and 12.67dB for the H-plane. The cross-polarization level is lower than 11dB for the E-plane and 12.5dB for the H-

plane. In another reported design, FSS has been used as a backing reflector for extending the frequency range of usability [102]. FSSs have been sandwiched between the antenna and the ground plane, providing an additional reflecting plane for the most critical higher frequency band. In most of these designs, the operation of the FSS has been limited to a narrow frequency band [103], although dual- and wide-band operation has been considered in a recent publication [104], exploiting the potential offered by the association of two different elements over a single unit cell, namely a square loop and a crossed dipole. The demonstrated structures show a bandwidth of 52%. We recently come with an idea of a stacked two-layer FSS that can be used as a reflector for a UWB antenna placed above the FSS. The antenna composite has a theoretical impedance bandwidth of 132%, and the FSS provides reflection-phase coherence (at the antenna plane) over an ultra-wide bandwidth, however the results only limited to theoretical validations of a small 6×6 array of unit cells embedded with a asymmetrical feed line [105] and conductor backing. In this work, we extend our study with experimental verification of theoretical results obtained from FSS used in [13] and further demonstrate experimentally with effectiveness of reflector a compact CPW fed symmetrical feed slot antenna backed by metal ground plane.

6.1.2   Antenna Design with Dual Layer Reflector

We choose one of our previous designs [13] of a compact CPW-fed SSA with a simple CPW-to-CPW transition as the reference antenna. A detailed investigation on improving gain of SSA while maintaining impedance bandwidth is carried out in our current research.

In this antenna, better matching to the resonant modes of the semicircular slot is obtained by integrating step and taper transitions to the CPW feed line. The impedance bandwidth of the designed antenna, defined by the 10dB return loss, extends from 3.0GHz to 11.6GHz (i.e. a percentage bandwidth of 118%). Fig. 1 shows the design of CPW-fed
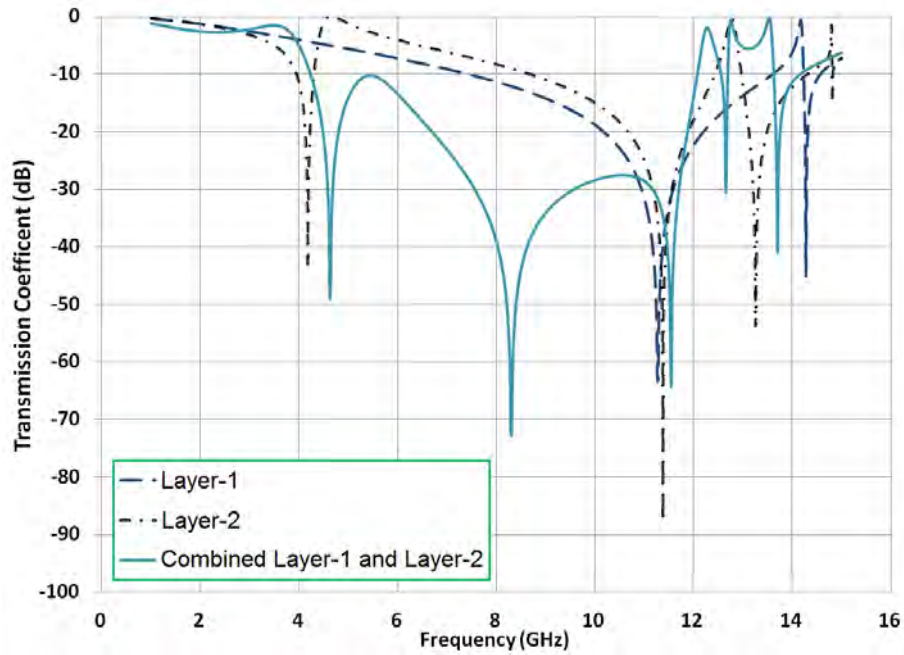
(a)
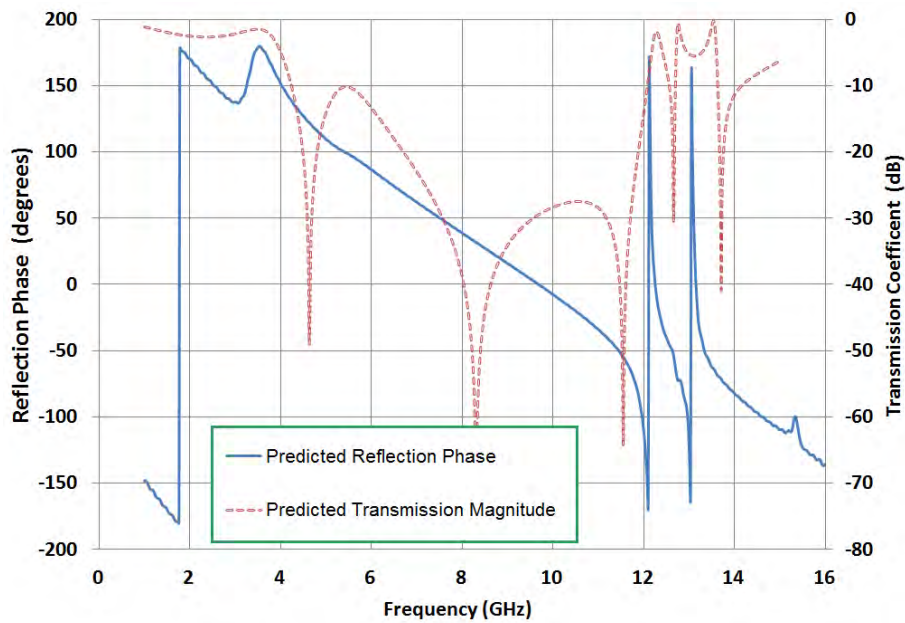
(b)

Figure 6.2: (a) Comparison of transmission through Layer 1, Layer 2 and combined dual-layer FSS (Layer 1 and 2) (b) Predicted reflection phase and transmission coefficient of the dual-layer FSS.
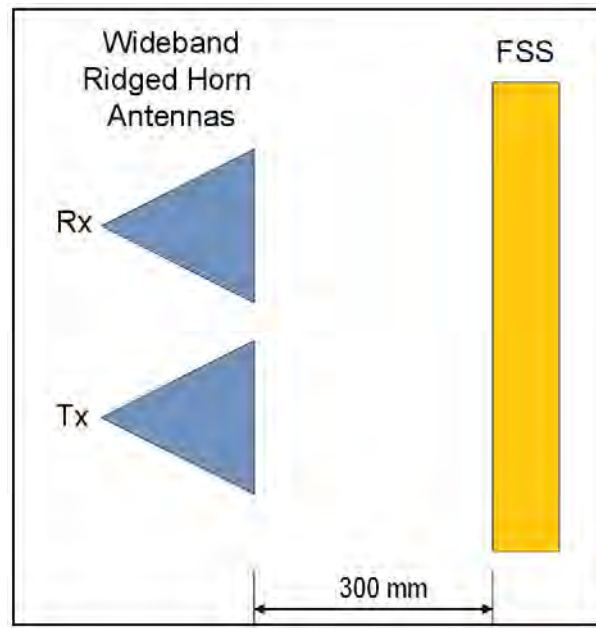
(a)
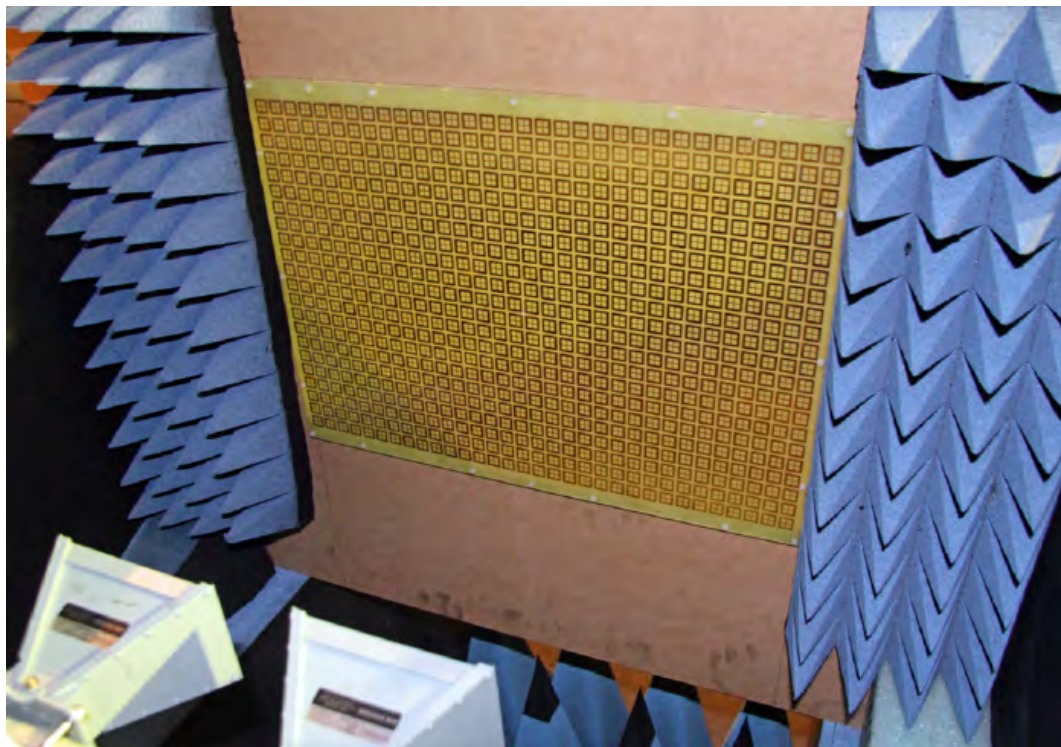
(b)

Figure 6.3: (a) Schematic of the setup for reflection phase measurement (b) Stacked layer of FSS prototypes and measurement setup for reflection phase.
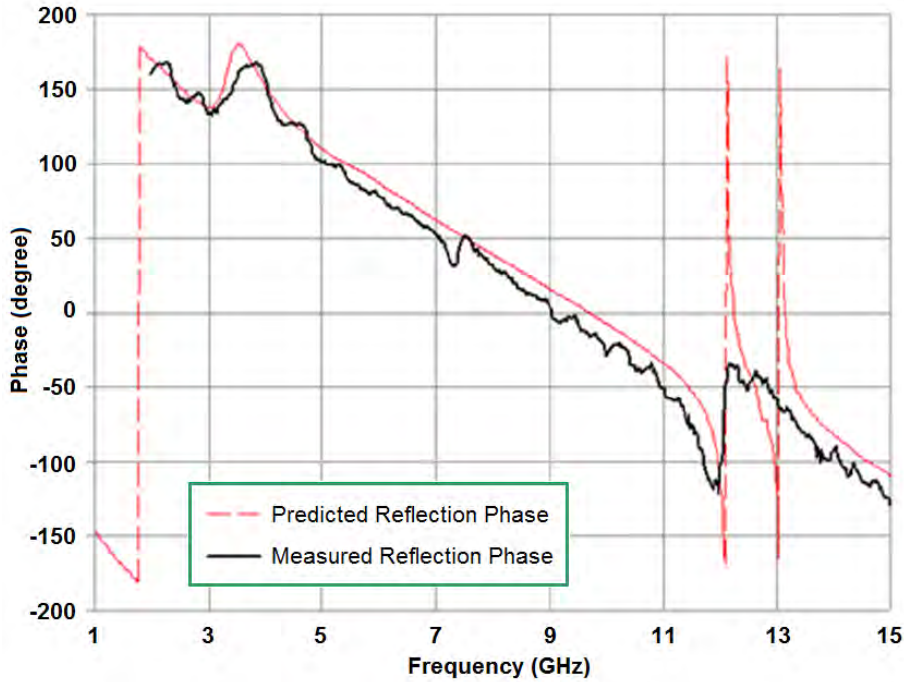
Figure 6.4: Predicted and measured reflection phase of the dual-layer FSS screen.

SSA and the geometry of FSS reflector unit cell. The FSS unit cells play a critical role in the design of the reflector. The first layer of the FSS combines cross dipole and square loop elements and the second layer consist of similar unit cell with an additional slot in the square loop. Simultaneous optimization of both layers yielded a stop band from 3.5 to 11.5GHz. Moreover, the reflection phase is almost linear across the whole band. A complete parametric study of this FSS is available in [13]. Fig. 2 shows the transmission coefficients of individual and combined layers, and the reflection phase of the dual-layer FSS reflector.

6.1.3 Measured Results of Frequency Selective Surface

A FSS prototype consisting of 32×22 unit cells has been fabricated on 1.6mm thick FR-4 dielectric substrate with $\varepsilon_r = 4.4$. To find magnitude and the reflection phase of the FSS, two dual-ridge H-1498 horns from BAE Systems were used in the measurement setup as
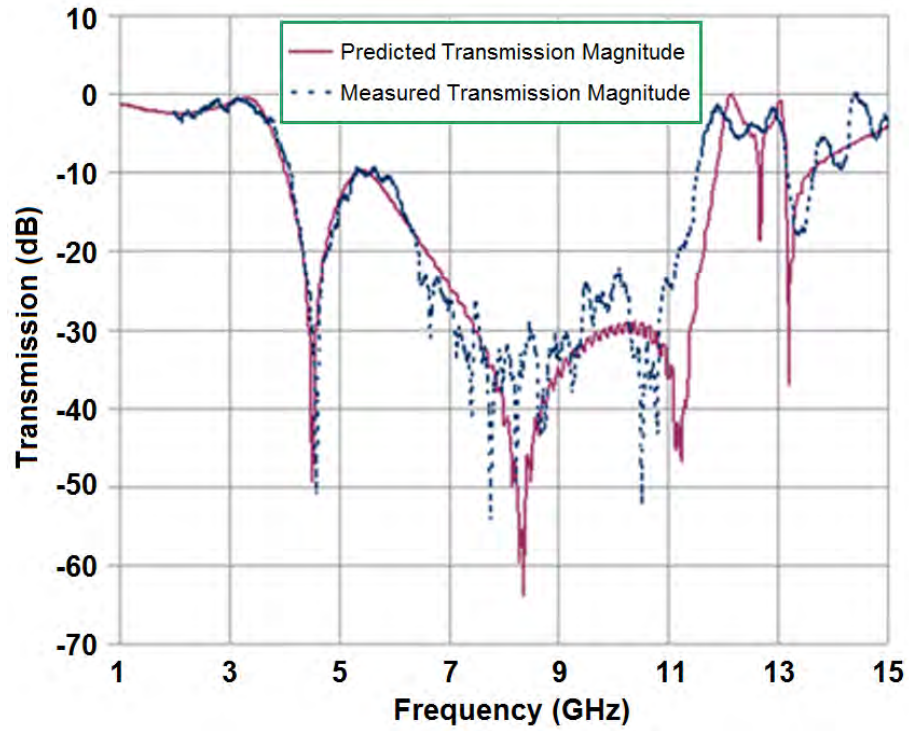
Figure 6.5: Predicted and measured transmission coefficient magnitude ($|S_{21}|$) of the dual-layer FSS Screen.

shown in Fig. 3. They have an operating bandwidth from 2GHz to 18GHz. The entire setup was measured in an anechoic chamber. To minimize reflections from the support structure a wooden frame was used and additional grooves for mounting provided good support for the dual-layer structure. To analyse the reflection coefficient at a distance of 9.5mm in front of the FSS, the electrical delay for the FSS measurement was set to -19mm (i.e. $2 \times 9.5mm$). Phase has been unwrapped from the measured data for comparison with the simulation. The FSS screen is 300mm away from the horn antennas. To ensure the exact spacing between the two layers, Nylon spacers of fixed thickness were specially manufactured. A comparison of predicted and measured reflection phase is shown in Fig. 4.

Transmission magnitude measurements were carried out with a setup similar to that
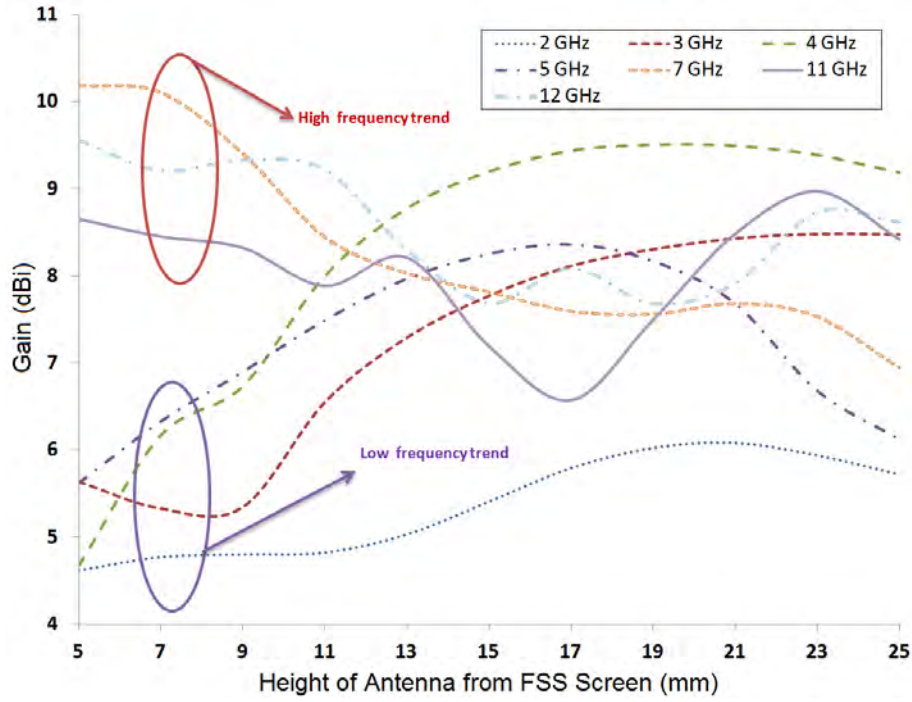
Figure 6.6: Theoretical gain trends at various frequencies with respect to the height of antenna over FSS reflector.

used for reflection phase measurements, apart for the location of horns. The measured and predicted transmission coefficients are compared in Fig. 5. The measured -10dB transmission bandwidth of 122% (3.85GHz to 11.23GHz) agrees well with the predicted bandwidth of 133% (3.5GHz to 11.45GHz). The performance of a UWB slot antenna integrated to a 6×6 version of the same FSS has been presented in [105].

6.1.4 Placement of Antenna over FSS and Measured Results with Discussion

The predicted results were obtained using waveguide simulation technique in CST Microwave Studio. The layer-1 reflects higher frequencies while layer-2 resonates at lower frequencies in addition to a stop band produced by layer-1. The combined effects of layer-
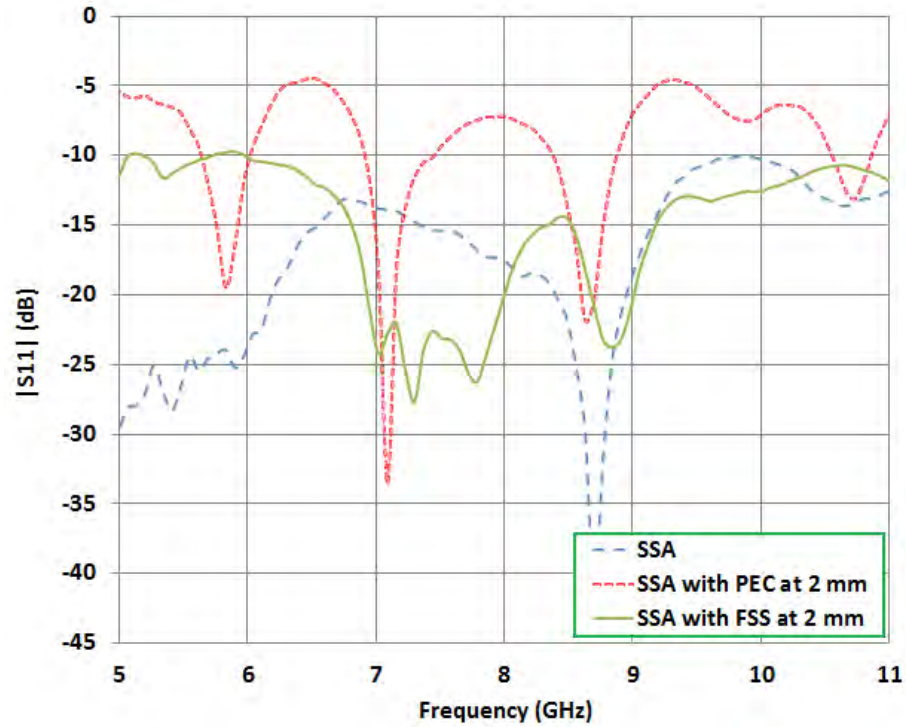
Figure 6.7: Measured input reflection coefficient of the SSA with and without the reflector and perfect electric conductor at 2mm spacing.

1 and layer-2 yields an ultra-wide stop band and also fulfill the linear phase requirement explained in [95]. Once the transmission magnitude and reflection phase of the FSS were optimized, an array of unit cells combined together with the SSA was considered. The placement of the antenna over the reflector is critical. Fig. 6 shows the optimization of the height of the antenna over the reflector screen. The gap between the reflector and the antenna has been varied from 0mm to 16mm. Following the parametric study, the optimum height of 10mm has been chosen, which yields a comfortable response in the entire FCC UWB bandwidth and even beyond. With the use of a dual-layer FSS reflector the gain increases over the entire frequency band. The performance enhancement due to the FSS-based reflector is evaluated with the UWB semicircular slot antenna shown in Fig. 1. The predicted input reflection coefficient and gain are shown in Fig. 7 and Fig.
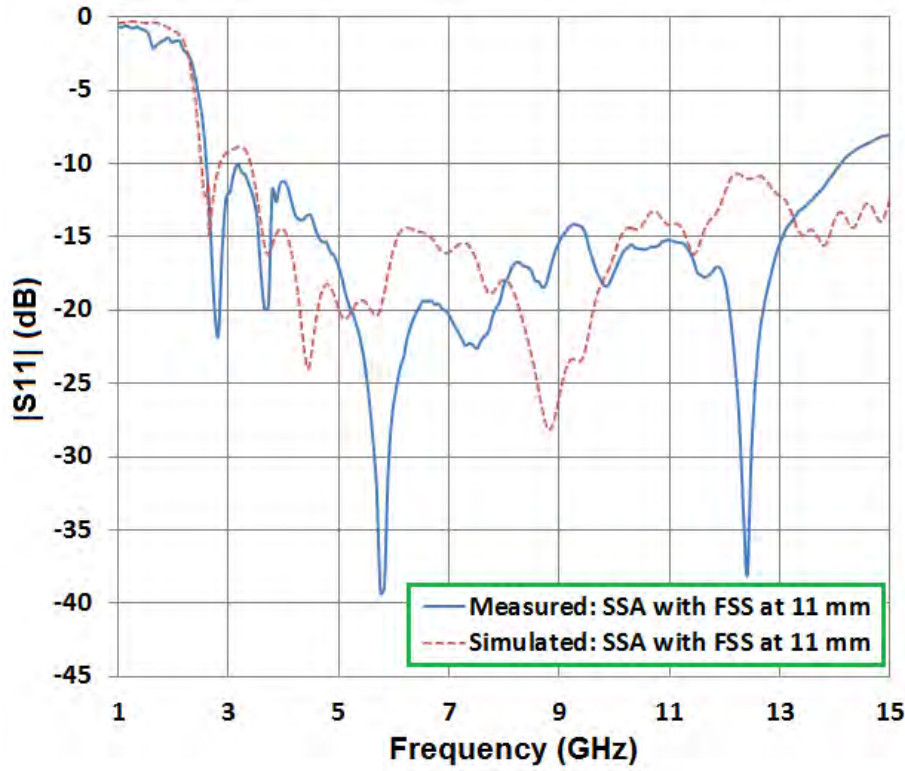
Figure 6.8: Measured input reflection coefficient of the SSA with and without the reflector.

8, respectively. The reflector does not affect the antenna return loss significantly. More importantly, the antenna with the reflector maintains a good impedance match (return loss > 9 dB) over the entire FCC UWB band from 3.1 to 10.6GHz. The gain enhancement due to the reflector is observed across the entire band. The minimum gain enhancement is about 2.5dB, at the lower end of the UWB band, and the maximum gain enhancement is about 4dB at 4.2GHz.
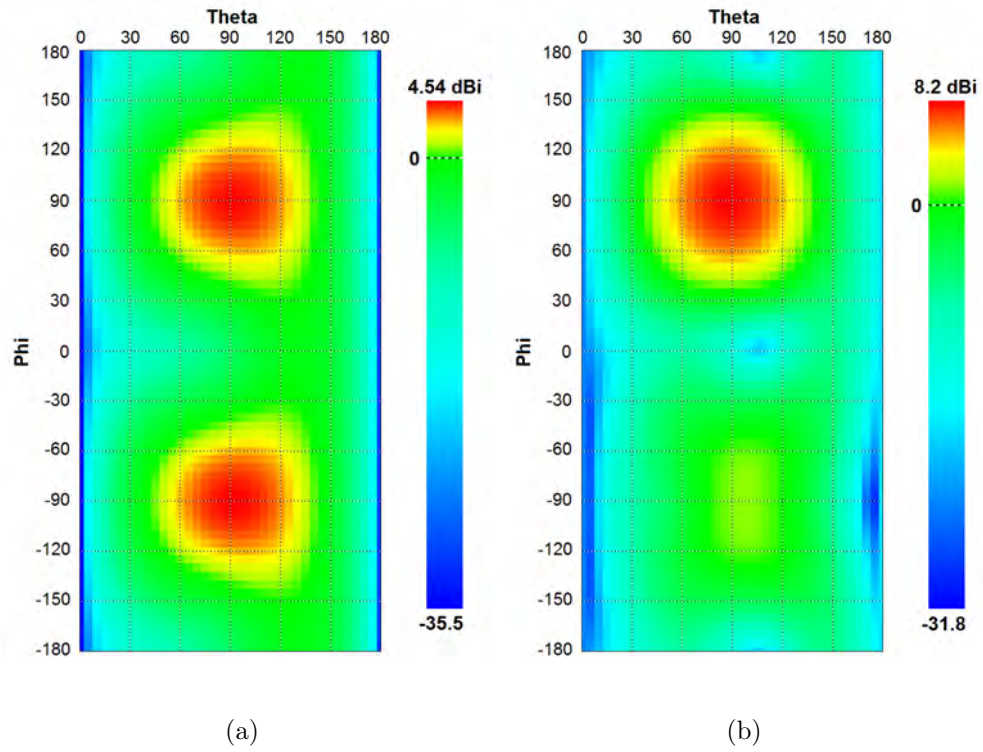
Figure 6.9: Theoretical 2D radiation patterns of the SSA and the SSA with the reflector. (a) SSA radiation pattern (without the reflector) at 3GHz; (b) SSA pattern with the FSS reflector at 3GHz.

The maximum gain is 9.5dBi at 4.2GHz. The gain variation is ±1.5dB from 3GHz to 10GHz. Antenna radiation patterns with and without the reflector screen are plotted in Fig. 9. The predicted 2D radiation pattern shown in Fig. 9(a) corresponds to the CPW-fed SSA without FSS reflector at 3GHz. The antenna has typical radiation patterns of a slot antenna with bidirectional radiation and beams are towards the ±900 directions. With the addition of the reflector the patterns become uni-directional as illustrated in Fig. 9(b). At lower frequencies the beam is strongly directional but with the increase of frequency the beam starts splitting. This beam splitting is not due to the reflector but an inherent property of this slot antenna at higher frequencies. One can use an antenna with a more stable radiation, with this reflector, to get a more directive beam at higher

frequencies.
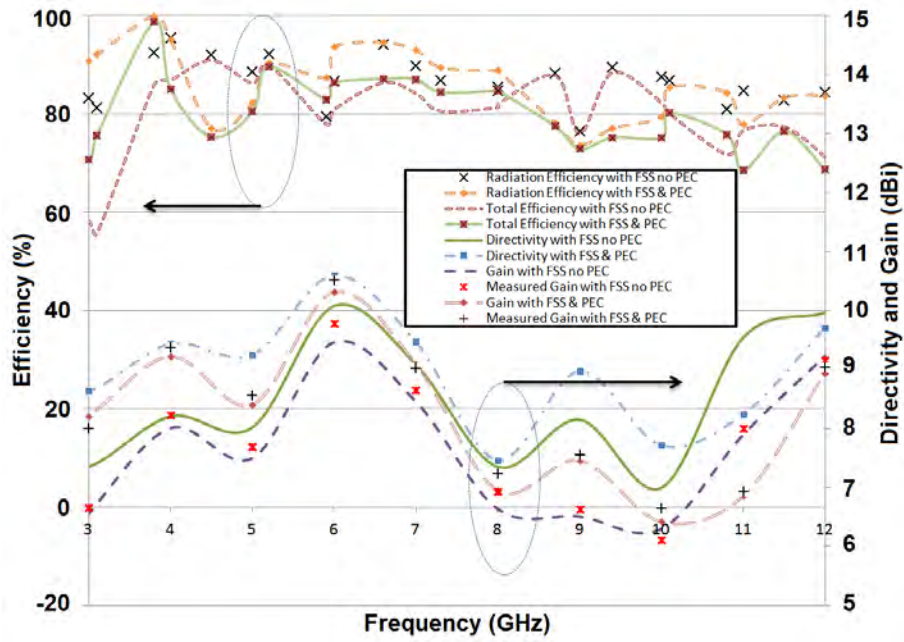
Figure 6.10: Theoretical and measured gain of the SSA with and without the reflector.

Fig. 10 presents the gain, directivity and efficiency of SSA with and without reflector under various conditions. The effect of introducing a PEC with FSS is also analyzed.

Measured radiation patterns of SSA antenna with reflector at different frequencies (i.e. at 3, 4, 5, 6, 7 and 10GHz) are shown in Fig. 11. It is noted that the antenna with reflector provides a stable directional pattern over a broad bandwidth.

(a)

(b)

(c)

(d)

(e)

(f)
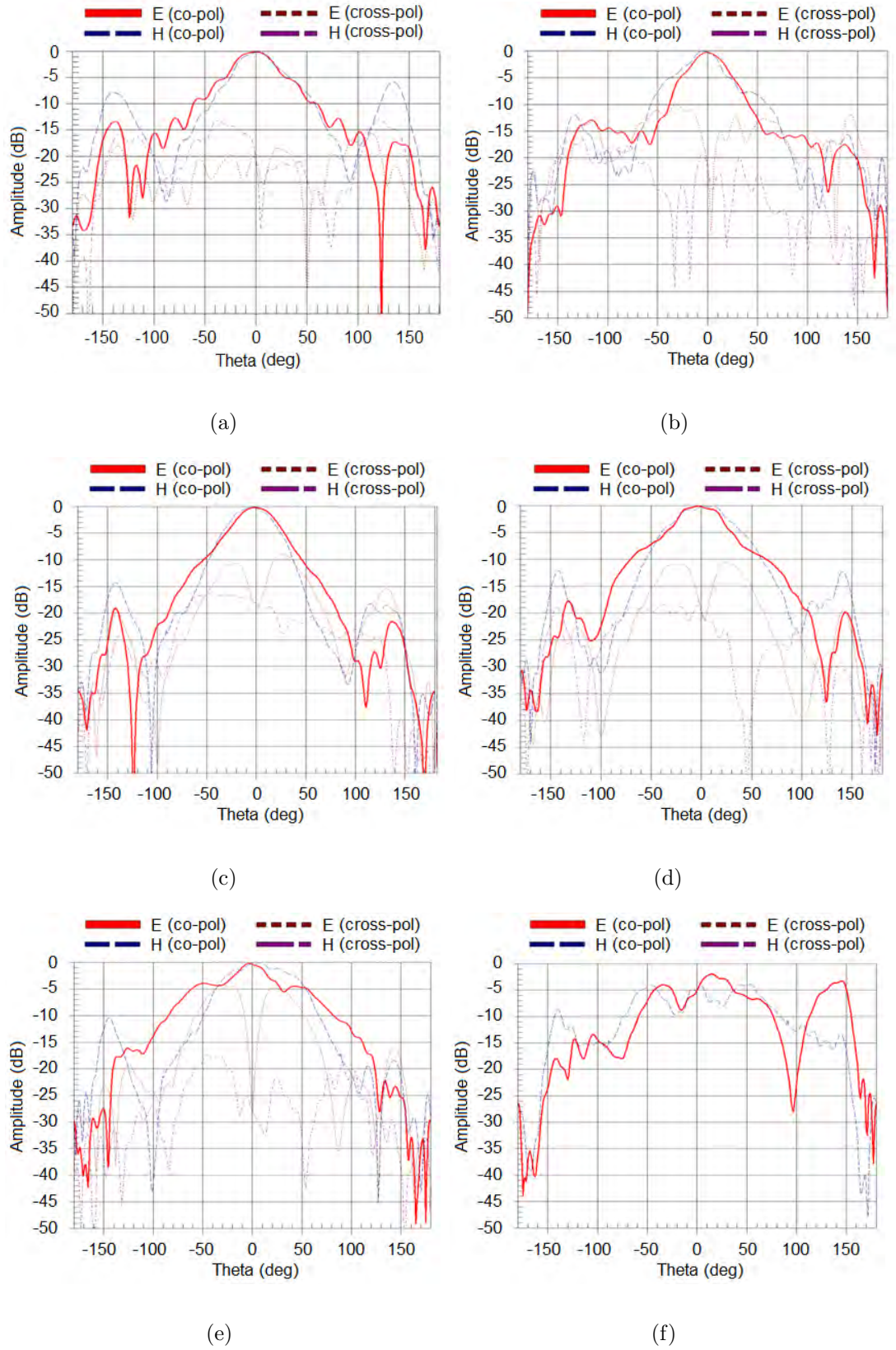
Figure 6.11: Measured radiation patterns of SSA with reflector at (a) 3GHz (b) 4GHz (c) 5GHz (d) 6GHz (e) 7GHz (d) 10GHz.

6.2 Antennas with High Impedance Surfaces

In this section, we present a novel type of printed microstrip High Impedance Surface (HIS) focusing on control of the dispersion characteristic, mainly in the position of the band-gap. Later, in this chapter we will use it to achieve desired radiation pattern. The HIS consists of a periodic arrangement of macro unit cells, which in turn are formed by sequential arrangement of similar elementary unit cells, each of them exhibiting analytically known dispersion diagram. The band-gap of the macro unit cell is positioned at lower frequencies that of the different unit cells that have their own band-gap at higher frequency range. Analyses of different sequences are presented, and it is demonstrated that the order of the arrangement allows controlling of the position of the band-gap while for different combinations of same order band-gap shift is negligible. The macro unit cell, a quasi-periodic arrangement of similar unit cells, consisting of three width modulated microstrip lines will be considered. The structure is completely printable on the substrates and no vias are required. The geometry of the unit cell with a width modulated microstrip line structure has been introduced in [106], and the idea of quasi periodic arrangement has been discussed in [107]. First we present the shifting the band gap of single unit cells (i.e. combination of different width modulated microstrip lines) to lower frequency range.

6.2.1 Width Modulated Line Based HIS

The geometry of unit cells [106] used in this paper is shown in Fig. 1. The variation of the line-width along the unit cell guarantees a sinusoidal variation of the effective dielectric constant around the average value ε_{avg} according to (6.1):

$$\varepsilon_{eff}\left(u\right) = \varepsilon_{avg}\left[1 + M_u \sin\left(2\pi \frac{u}{D_u}\right)\right] \tag{6.1}$$

here D_u indicates the length of the unit cell along the longitudinal direction u, and
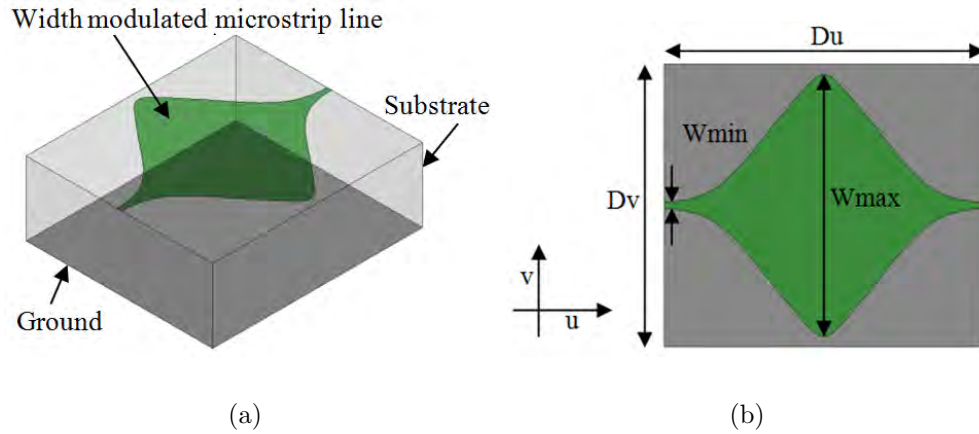
Figure 6.12: Geometry of unit cell with single width modulated microstrip line (a) side view (b) top view.

M_u is the modulation constant ($\in (0,1)$).

In order to avoid discontinuities at the cell-to-cell transitions, the minimum width in each unit cell has been maintained constant, and only the maximum widths have been varied. The DD for transverse electric (TE) polarisation can be analytically computed by the method described in [106,107]. The limits of the band-gaps depend on the modulation parameter M_u of the microstrip line. In the first band-gap, below the light-line (LL), the incident field will be completely reflected making the structure suitable for reflectarray type of applications. As frequency goes higher and the dispersion curves cross the light line, fields are no more bounded and radiation of surface wave occurs.

6.2.2 Band-Gap Shifting using Combination of Different Width Modulated Microstrip Lines M_u with-in the Unit Cell

Unit cell is considered using Rogers RO3210 substrate having dielectric constant of 10.2 and height of 1.58mm. Size of unit cell with single width modulated transmission line, shown in Fig. 1 is $4.5mm \times 4mm$. where D_u is along x-axis and D_v is along y-axis.
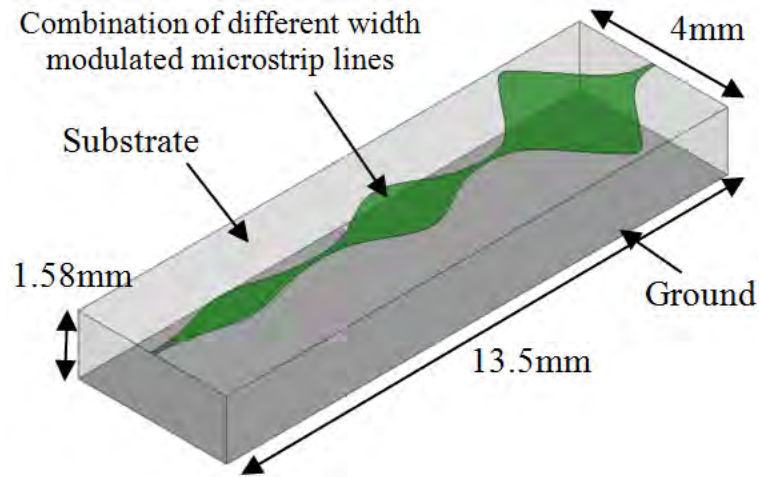
(a)
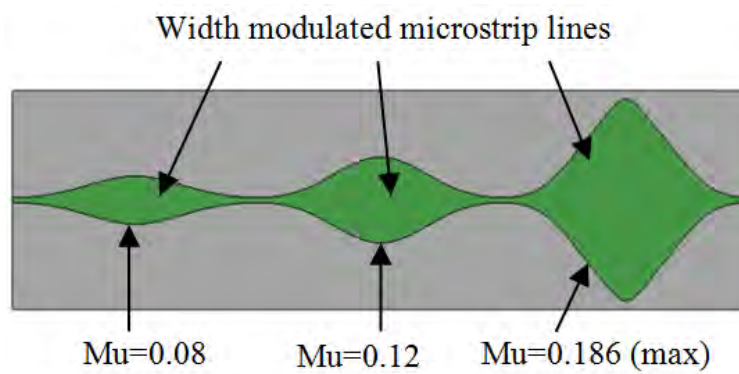
(b)

Figure 6.13: Geometry of unit cell with three different width modulated microstrip lines (a) side view (b) top view.
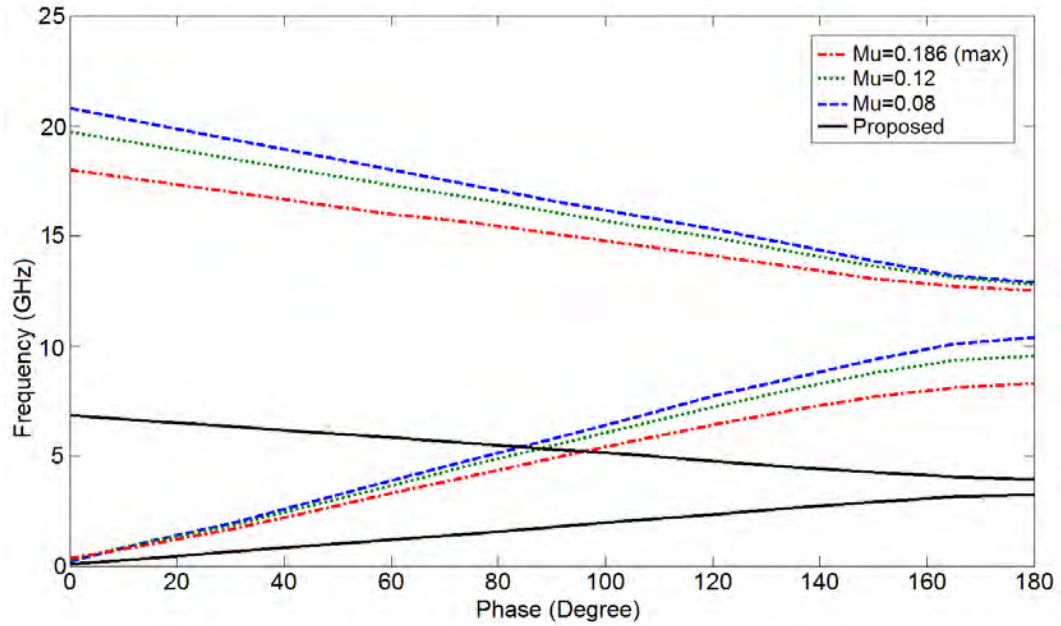
Figure 6.14: Band-gap comparison of unit cell with single width modulated microstrip line and band-gap of geometry of macro unit cell shown in Fig. 6.13(b) with three different width modulated microstrip lines.

Geometry of the proposed unit cell with three width modulated microstrip lines is shown in Fig. 2 and it has dimension as $13.5mm \times 4mm$.

The DD for unit cells with single width modulated microstrip line having modulation parameter M_u equal to 0.186, 0.12 and 0.08 respectively are shown in Fig. 3. It illustrates that the band-gaps are in the range of 8-14GHz. Fig. 3 also report the band-gap of the proposed macro unit cell that has a combination of three different width modulated microstrip lines. It is clearly observed from the figure that the band-gap of the proposed unit cell is at lower frequency range of 3GHz to 4GHz.

Further investigations were carried out to check the effect of rearranging the width modulated lines in the proposed design framework, where M_u=0.08 will be called as 8, M_u=0.12 as 12 and M_u=0.186 as max. Three combinations of these unit cells are proposed as follows: 8-12-max, 8-max-12 and max-8-12 and shown in Fig. 4. The corresponding
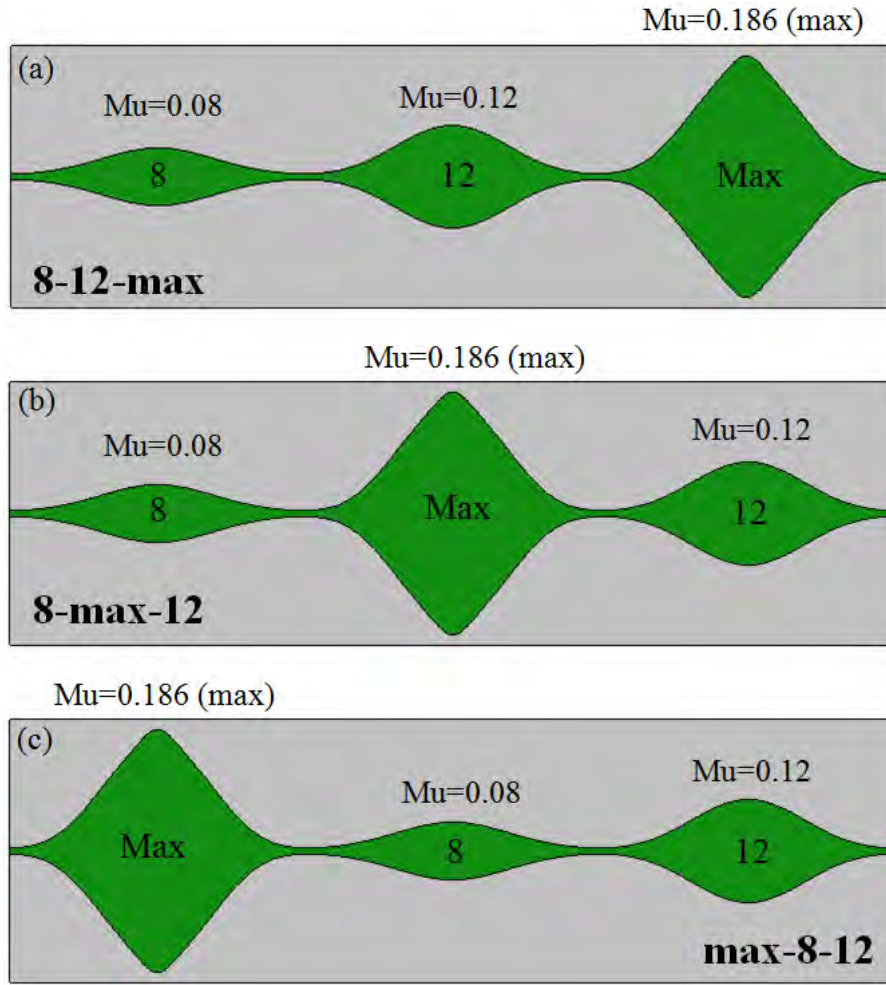
Figure 6.15: Combinations of proposed unit cell with three different width modulated microstrip lines (a) 8-12-max, (b) 8-max-12, (c) max-8-12.

results are presented in Table 1 and presented in Fig. 5.

As expected, the 8-12-max and max-8-12 sequences present identical responses, which is slightly different with respect to the response of the 8-max-12 sequence. This allows to (i) rearrange the sequence based on other requirements, and also to (ii) realize a fine tuning of the band-limits. From the results in the last two rows in the table, it can also be noticed, that as expected, the reduction in frequency of the position of the band-gap is mainly determined by the number of the unit cells within the macro cell, but it also
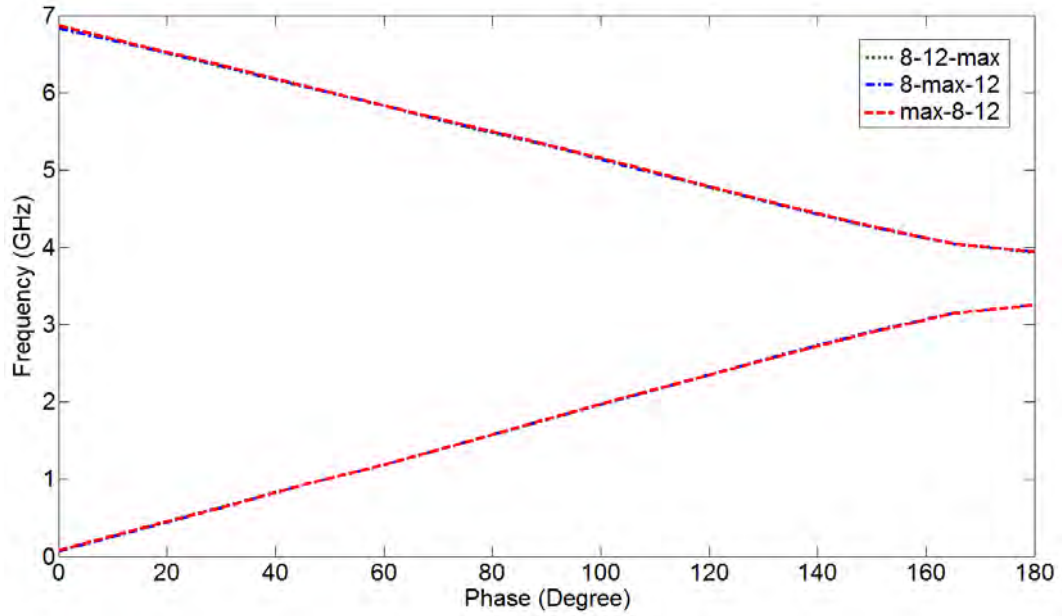
Figure 6.16: Comparison of dispersion diagram of macro unit cells with three different sequences of the same width modulated microstrip lines.

depends on the characteristics of the single unit cells.

6.2.3 Periodic HIS Based Antenna

Sequences of periodic modulated line HIS is placed in a cylindrical shape and is fed using a dipole from inside the cylinder. An omni-directional pattern is observed in the plane that is perpendicular to the height of the cylinder, when modulated lines with higher width are used. Fig. 6.17 shows the width modulated line cells with equal width in a cylindrical shape. Return loss and the radiation pattern from the top view to highlight its omni-directional pattern are shown in Fig. 6.18 and Fig. 6.19 respectively.

Figure 6.17: Periodic HIS based cylindrical antenna.
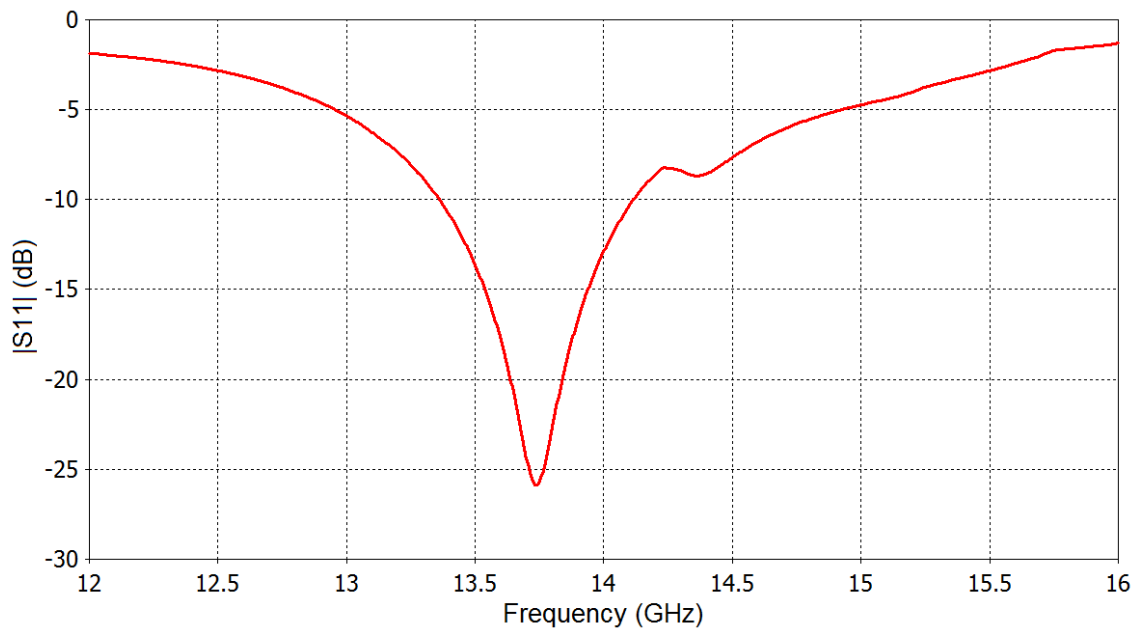
Figure 6.18: Predicted $|S_{11}|$ corresponding to periodic HIS with equal width.
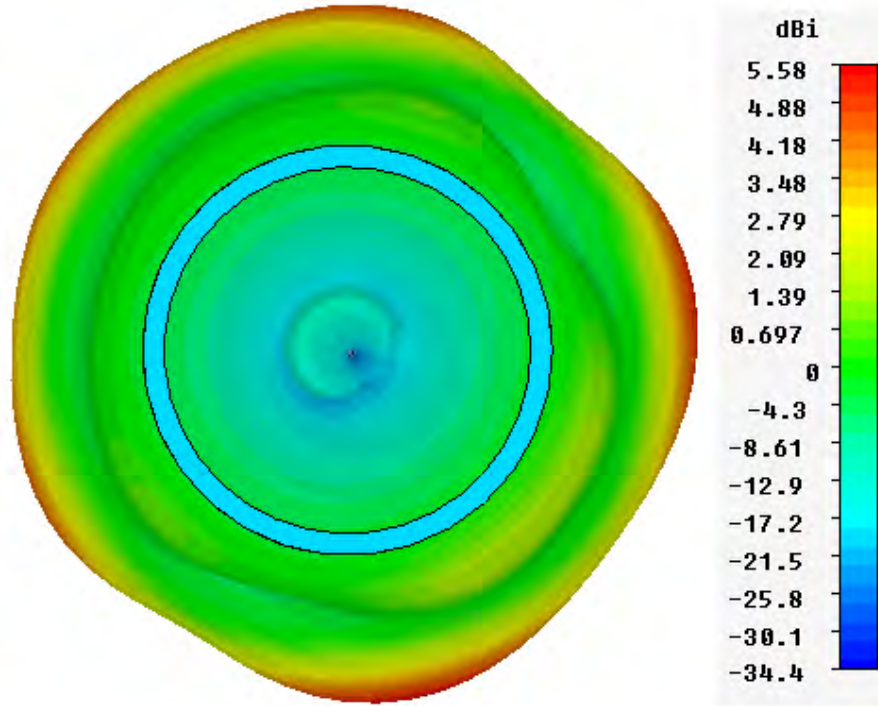
Figure 6.19: Radiation pattern of periodic HIS based cylindrical antenna at 13.8GHz.

6.2.4 Quasi-Periodic HIS based cylindrical antenna.

Similarly, when modulated lines with different modulation widths are used in cylindrical shape (as shown in Fig. 6.20) and are fed using a dipole. It is observed that modulated lines with higher modulation width acts as pass-band while modulated lines with small modulation width behaves as stop-band.are used. By appropriate selection of widths for the modulation lines, the radiation pattern can be controlled as the beam can be steered as well. Fig. 6.21 and Fig. 6.22 shows the corresponding return loss and the radiation pattern, respectively. Here, we present selected preliminary results for both periodic and quasi-periodic cylindrical configuration. Investigation on impedance has been carried out for the considered unit cells as well.

Figure 6.20: Quasi-periodic HIS based cylindrical antenna.
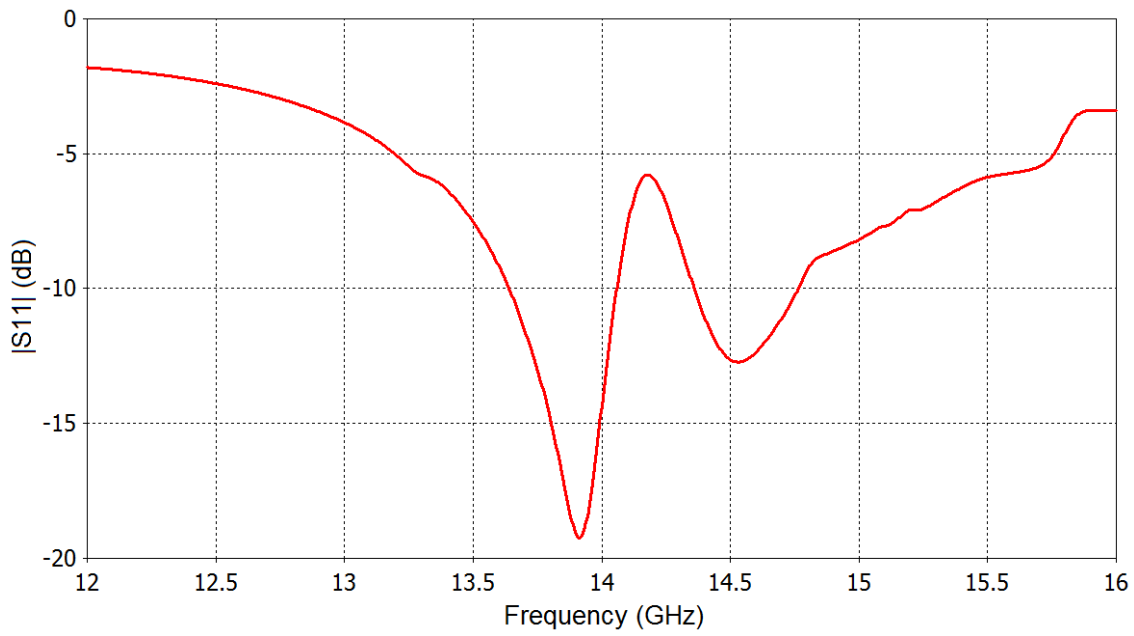
Figure 6.21: Predicted $|S_{11}|$ corresponding to quasi-periodic HIS with different widths.
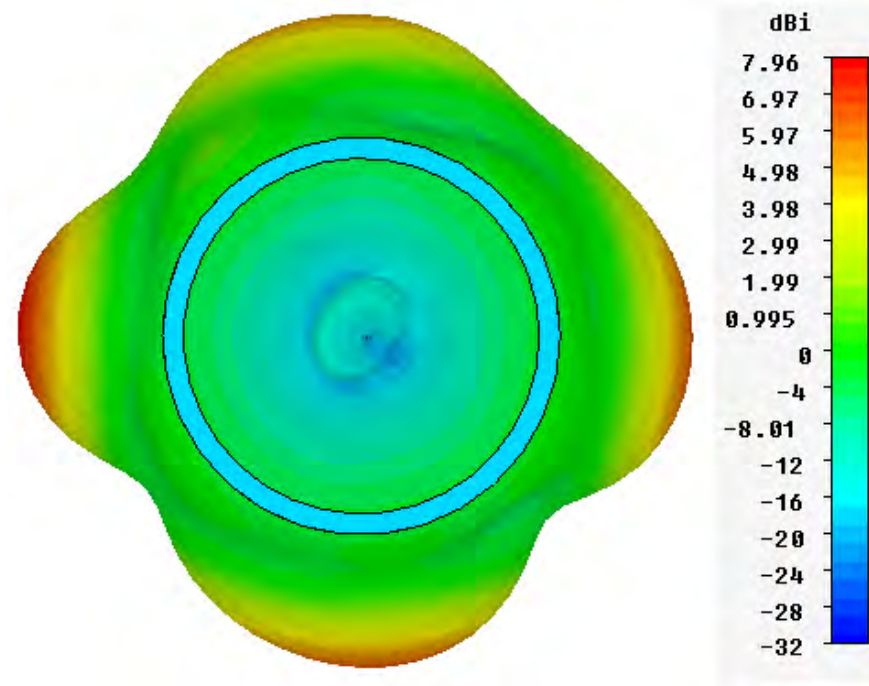
Figure 6.22: Radiation pattern of quasi-periodic HIS based cylindrical antenna at 13.8GHz.

6.3   Conclusion

The use of wideband FSS to obtain uni-directional radiations is presented. By use of in-phase reflection over a wideband, the backward radiation are reduced and a stable radiation pattern with higher gain is obtained. Investigation focusing on control of dispersion characteristics mainly in the band-gap region are presented for novel printed microstrip HIS. By placing these HIS in a cylindrical shape and feeding it using a dipole from inside, omni-directional or controled radiations can be obtained depending upon selected modulated width for the HIS.

Chapter 7

Reconfigurable Antennas

With the increasing demand of communication at higher data rates, the compactness of devices is also desired. Most of the communication devices support multi-frequency operation. In common practice, separate antennas are used for different frequency bands. That consumes a lot of space and restricts the compactness of device. Single antenna supporting multiple frequency bands can significantly contribute towards size reduction in wireless communication systems. Reconfigurable and switchable antennas can offer multi-frequency operation through electronic tunability by means of switches. These antenna can be precisely tuned to desired frequency by changing the switch configuration. Several techniques have been reported to make the antennas reconfigurable by using electrical or electromechanical switches. Considerable development has been reported by incorporating switches like PIN diodes, RF microelectromechanical systems (MEMS) , varactors, field-effect transistors (FETs) and optical switches. RF MEMS have the advantages of low loss and high linearity but need complex fabrication process. On the other hand antennas with simple choices of switches are more cost effective. PIN diodes offer the advantage of very low driving voltage, reasonable linearity, comparatively high power-handling capability, and are relatively low cost. In this chapter, we will focus on reconfigurable antennas to
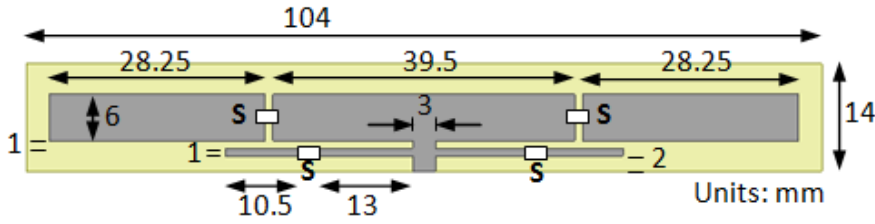
Figure 7.1: Geometry of the proposed antenna and location of switches.

provide narrow band operation for the 2.45GHz ISM and 5GHz WLAN band. We will also present a reconfigurable antenna, providing narrow band operation in one mode for long-range communications and in another mode providing UWB operation for short-range communications.

7.1 Narrow Band Reconfigurable Antennas

In this section, a narrow band reconfigurable antenna is presented for WBAN applications in healthcare, public safety and defense [14]. In earlier chapters we have discussed narrow band antennas with full ground planes and electromagnetically coupled feeds, designed for body area network devices operating in the ISM band at 2.45GHz, have been reported previously [17, 18]. An electromagnetically coupled feed was used to partially fill a null that was otherwise present towards the direction opposite to the feed. In [18] stub loading has been used to achieve better impedance matching. A dual-band antenna with a full ground plane and an electromagnetically coupled feed, operating in both the ISM band at 2.45GHz and 4.9GHz public safety Wireless Local Area Networks (WLAN) band (4.940 − 4.990 GHz) has also been reported [19]. A printed antenna described in [20] is suitable for a flexible substrate. With full ground plane and electromagnetically feed, it is suitable for arm-band wearable applications in the 2.45GHz ISM band. These antennas exhibit wide radiation patterns along the body surface to provide wider coverage. The narrow

Table 7.1: ELECTRICAL PROPERTIES OF THREE-LAYER HUMAN TISSUES MODEL AT 2.45GHz.

Tissues	ε_r	$\sigma\,(S/m)$	$\tan\delta$
Skin	38	1.464	0.2826
Fat	5.28	0.1045	0.1452
Muscle	52.73	1.7388	0.2419

gap required in these antennas to achieve electromagnetically coupled feed is difficult to fabricate. The proposed antenna design does not require such a small gap and is easy to fabricate. It also exhibits a wide radiation pattern along the body surface to provide wide coverage. By introducing switching in the design the operating band can be selected as 2.45GHz or 5GHz. Here we will describe the antenna design along with the results and analysis.

7.1.1 Antenna Design

Fig. 7.1 shows the geometry of the proposed antenna with dimensions. It is to be fabricated on a 14mm x 104mm Arlon Iso clad 933 substrate with a dielectric constant of 2.33 and a thickness of 1.6mm. Its full ground plane is considered to reduce radiation towards the body, which can possibly harm the human tissues. Radiating element consists of rectangular strips fed using a 50 ohm microstrip transmission line. Four switches, shown in Fig. 7.1, are used to shift the operating frequency between 2.45GHz or 5GHz depending upon the ON/OFF state of the switches. The dielectric constants, conductivity and loss tangent of different body tissues have been considered when modeling the antenna operation near a human body [15].

Table 7.2: ELECTRICAL PROPERTIES OF THREE-LAYER HUMAN TISSUE MODEL AT 5.2GHz.

Tissues	ε_r	$\sigma\,(S/m)$	$\tan\delta$
Skin	35.61	3.2185	0.3124
Fat	5.01	0.2547	0.1757
Muscle	49.28	4.2669	0.2993

7.1.2   Results and Analysis

Simulations of the proposed antenna have been carried out using CST Microwave Studio. After designing the antenna in free space, its performance was investigated in near-body environment. The average thicknesses of skin, muscle and fat tissues were considered while modeling a sample phantom for near-body simulation [6, 15, 17–19, 85]. The tissue layers are shown in Fig. 7.2. The properties of the three tissues at 2.45GHz and 5.2GHz are given in Table 7.1 and Table 7.2, respectively. The properties of the tissues normally change with frequency and thickness of the tissues [85].
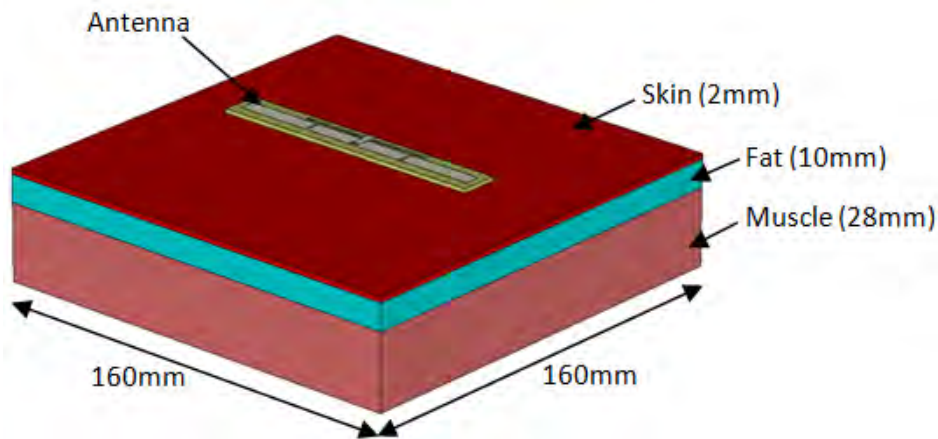
Figure 7.2: Simplified body model with three tissue layers.
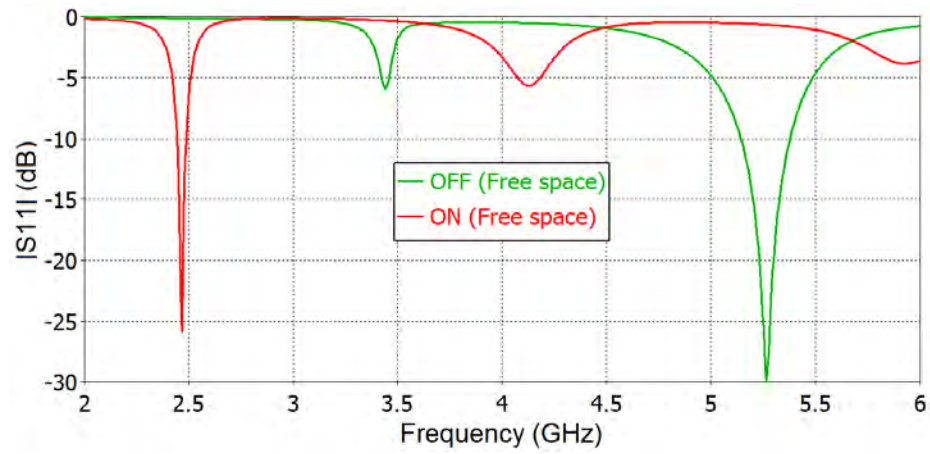
Figure 7.3: Predicted $|S_{11}|$ in free space (i.e. without body) when all switches are ON and when all switches are OFF.
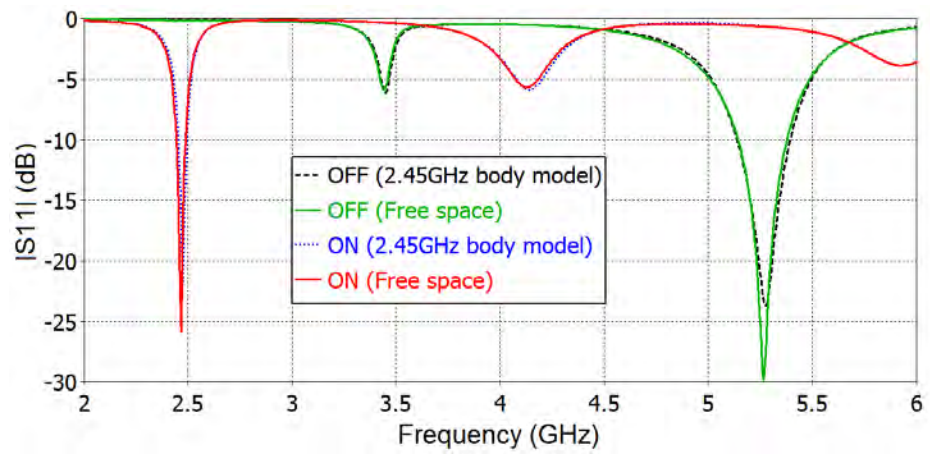
Figure 7.4: Predicted $|S_{11}|$ corresponding to switches configuration when antenna is placed near 2.45GHz human body model.
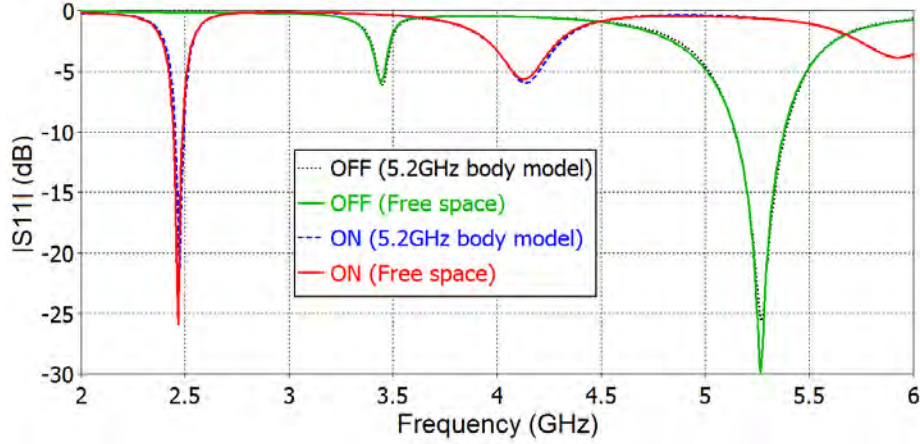
Figure 7.5: Predicted $|S_{11}|$ corresponding to switches configuration when antenna is placed near 5.2GHz human body model.

A. ***Return Loss***

Fig. 7.3 shows the predicted $|S_{11}|$ of the proposed antenna in free space. When all switches are in ON state, the antenna operates in the ISM band at 2.45GHz, which is suitable for body centric wireless communication and provides a bandwidth of 44MHz $(2.444 - 2.488 \text{ GHz})$. When all switches are in OFF state it provides a bandwidth of 235MHz $(5.144 - 5.379 \text{ GHz})$ that is suitable for devices operating in 5GHz IEEE 802.11 WLAN band $(5.15 - 5.35 \text{ GHz}, 5.25 - 5.35 \text{ GHz})$. To investigate its performance for WBAN applications, the same antenna has been simulated in close proximity to the human body (i.e. at distance of 5mm) and the corresponding return loss is shown in Fig. 7.4 and Fig. 7.5, respectively, for 2.45GHz and 5.2GHz body models. Results show that there is negligible variation in resonance frequency and bandwidth as compared to free space when antenna is placed in close proximity to human body. A variation of about 8MHz is noted in resonance frequency when the antenna is placed near the human body models.
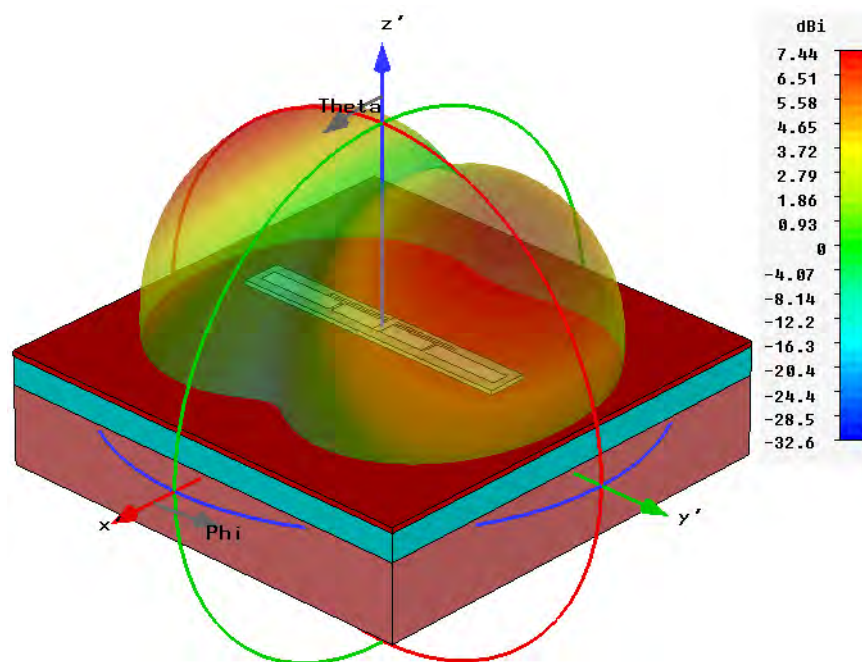
Figure 7.6: Predicted radiation pattern at 2.476GHz when all switches are in ON state.
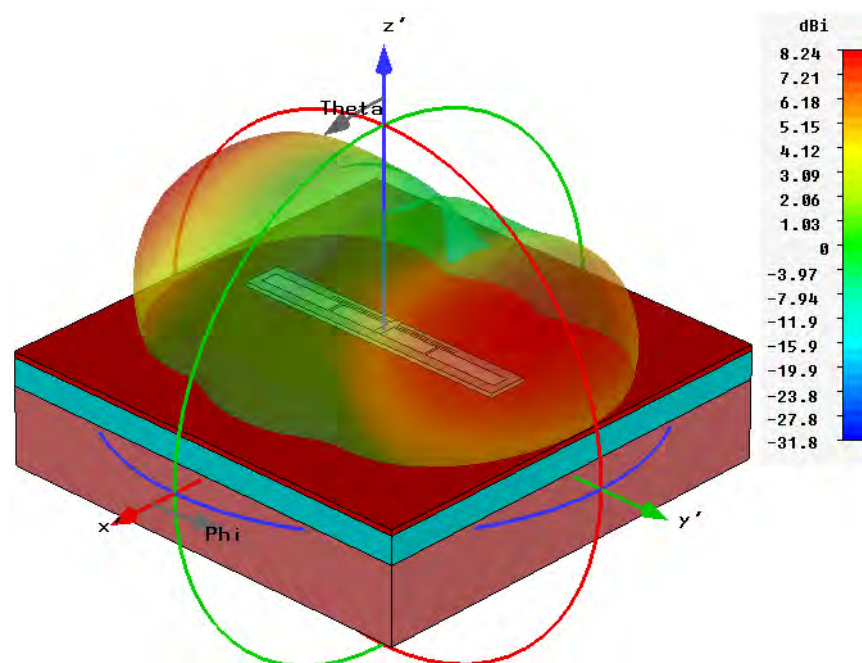
Figure 7.7: Predicted radiation pattern at 5.272GHz when all switches are in OFF state.

B. ***Radiation Characteristics***

Fig. 7.6 and Fig. 7.7 presents the simulated 3D radiation patterns of the proposed antenna at 2.476GHz and 5.272GHz for near-body scenarios, with 2.45GHz and 5.2GHz body models, respectively. They show that near the body the antenna beam becomes wider especially in the plane of the body (x-y plane) and the null along the negative x-axis is partially filled to provide a better coverage.

A switchable printed antenna with a wide-beam radiation pattern, to provide a wide coverage along the body surface, has been proposed. The operating bands can be switched between 2.45GHz and 5GHz by turning the switches ON or OFF. Antenna performance characteristics near the human body models has been investigated. When the antenna is placed near a human body (5mm away from the body), the resulting shift in its resonance frequencies is negligible (less than 10MHz). This antenna also has a narrow width that makes it a suitable candidate for wearable devices.

7.2   Narrow Band and Wide Band Reconfigurable Antennas

In this section, a simple printed coplanar strip-fed frequency reconfigurable antenna is presented for wireless medical body area applications. It has several key advantages over the other recently designed reconfigurable antenna, for example; it has a 10.6GHz ultra-wide bandwidth in one state and another state of operation covers narrow ISM band. In addition its complete printed single layer geometry allows simplification of bias networks and eliminations of any vias to the ground. The connecting pads helps to provide ease of integration. Moreover, this multifunctional operation with the compact configuration ultimately saves a must needed comprehensive amount of space for wearable electronic

Figure 7.8: Antenna configuration. X=40, Y=50, R=12, L=10, L1=15, L2=23. S=0.5, g=0.2, each pad is $2 \times 2mm^2$. (All dimensions are in mm)

devices. The Narrowband mode shows a 1.5GHz to 2.98GHz -10dB impedance bandwidth, while the Ultra-wideband mode yields a 121% impedance bandwidth.

(a)   (b)

Figure 7.10: (a) Equivalent circuit models of diodes in OFF and ON state (b) Configuration of diodes and bias circuit.
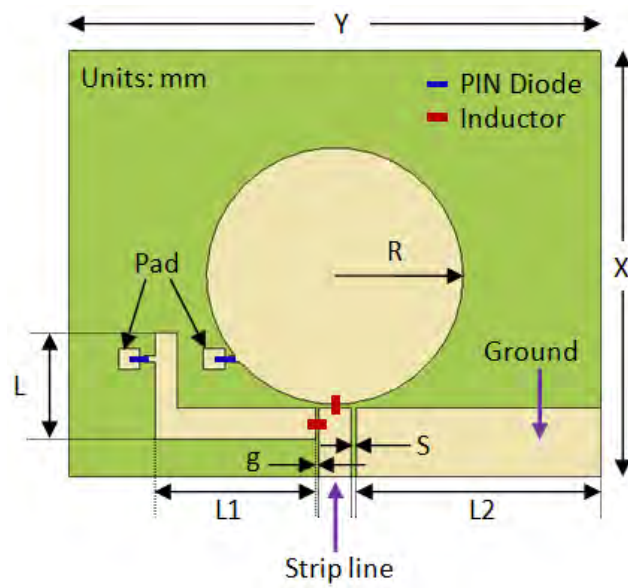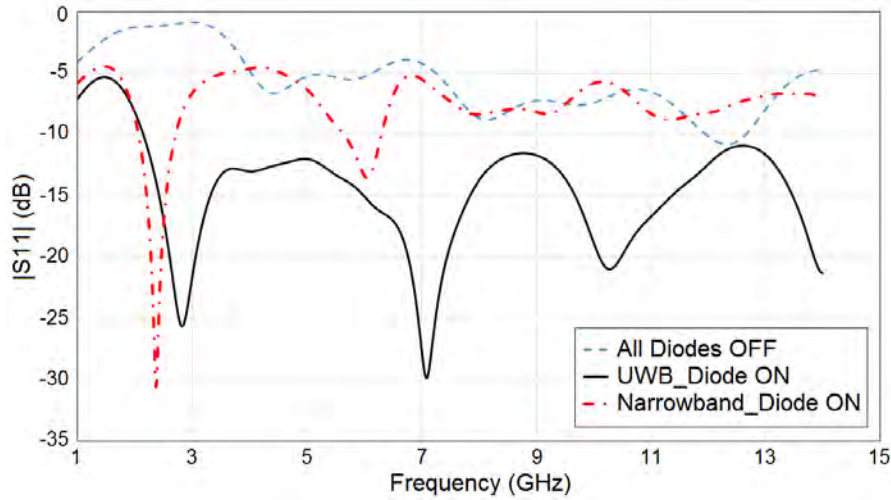
Figure 7.9: Input reflection coefficients under various operation states ((dashed line) both diodes OFF, (dot-dashed line) diode connected to L-arm is ON and the other diode is OFF, and (solid line) diode connected to circular patch is ON and the other diode is OFF.

7.2.1   Antenna Configuration and Bias Network

Fig. 7.8 shows the antenna configuration, which consists of a circular metal patch pattern etched on the top surface of a standard 1.6mm FR4 substrate. An L-shaped arm operating as a monopole is also printed on the same substrate along with a ground plane. The overall dimensions of the antenna is $40 \times 50mm^2$. The simulations of the proposed antenna are carried out using CST Microwave Studio.

The two radiating elements (circular patch and L-arm) are connected to strip feed through MACOM (MA4FCP300) PIN diodes. Following the PIN diode datasheet [108], each diode is modeled as a 4 resistor for the ON state and a parallel circuit consisting of a 0.04pF capacitor and a 20K resistor for the OFF state in CST Microwave Studio simulations. The diodes shown in Fig. 7.8 are mounted in opposite polarities, which enables the use of only one DC biasing voltage to control both diodes. Voltage is applied to the diodes and through the metallization of the strip feed. This DC biasing voltage and the RF signal are simultaneously fed through the coaxial probe by using a bias tee.
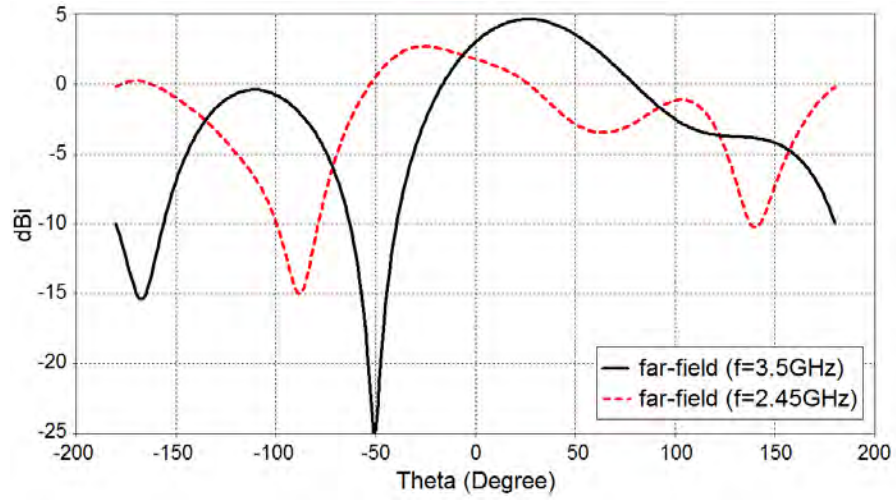
Figure 7.11: Predicted E-plane radiation patterns at 2.45GHz for Narrowband Mode (dotted line) and at 3GHz for ultra-wideband (solid line).

Two inductors (68nH) are used to create a DC closed circuit for diodes while blocking the RF signal.

Due to the orientation of the PIN diodes, when the bias voltage is negative, the diode connected to the L-arm is switched ON and the diode connected to circular patch is switched OFF, and vice versa for opposite polarity. In order to mitigate the effects of the bias line and simplify the antenna design, two small pads are created as the DC grounds next to the radiating elements. Initial performance of antenna is evaluated without the effect of any parasitic of lumped components and bias networks.

Fig. 7.9 shows the predicted performance for three operation states. In State I when both diodes are OFF the antenna is not matched in the frequency range from 1 to 15GHz. In State II, the diode connected to L-shaped arm is ON and the other diode is OFF. In this mode, the antenna has a narrow bandwidth and operates in the 2.45GHz ISM band. State III represents the ultra-wideband mode of the antenna. In this state, diode connected to circular patch is ON and the other diode is OFF. The final antenna was optimized using a more accurate spice model. Fig. 7.10(a) shows the equivalent circuit models of
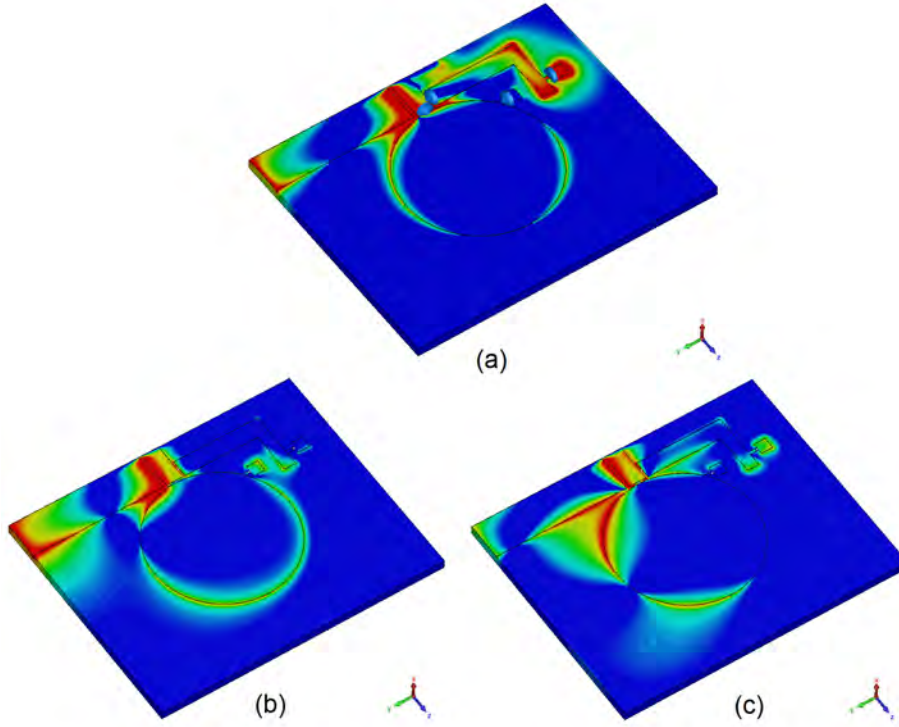
Figure 7.12: A comparison of electric-field distributions (a) Narrowband mode at 2.45GHz (b) UWB mode at 3GHz (c) UWB mode at 6GHz.

diodes in ON and OFF state while Fig. 7.10(b) shows the complete configuration of bias arrangements.

Fig. 7.11 shows the initial predicted radiation patterns at 2.45GHz and 3GHz, which correspond to the resonance frequency of the Narrowband mode and lower cut-off frequency of the UWB mode. In the Narrowband mode, beam is tilted at -300 due to the asymmetrical nature of the antenna geometry. However in case of the UWB mode, beam at 3GHz is tilted toward +300 because of the dominant nature of the ground which makes effective contribution in radiated fields. Initial predicted results in Fig. 7.9 and Fig. 7.11 show some variation compare to the actual results that will be shown later in the next section because of the ideal component used in simulation with no biasing network.

To gain more insights in the operation mechanism, field distributions in the two modes

<div align="center">(a)   (b)</div>
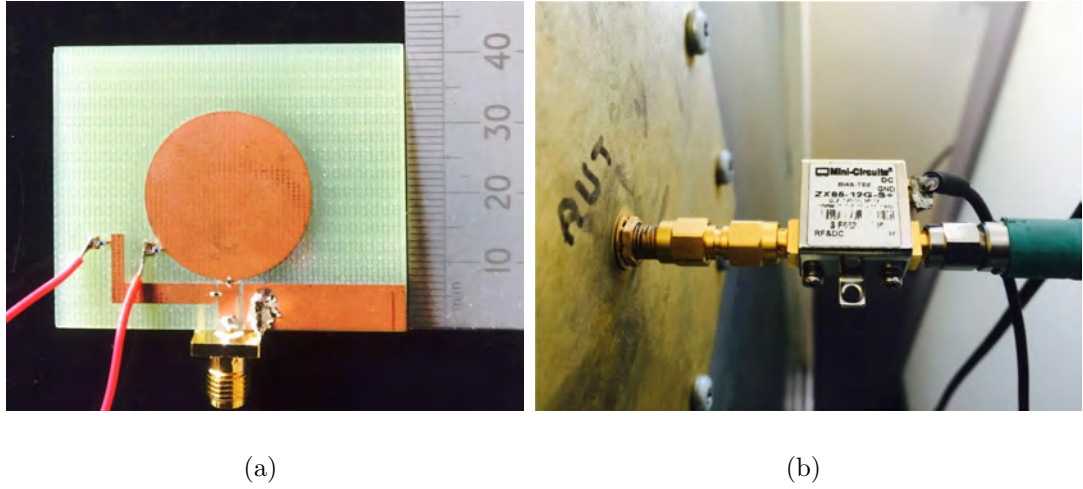
Figure 7.13: (a) Antenna prototype (b) Bias tee outside the anechoic chamber for supplying RF and DC bias.

are plotted in Fig. 7.12. Fig. 7.12(a) represents the Narrowband mode in which the L-arm resonates at 2.45GHz and some of the energy is coupled to the circular patch. However, when only the diode connected to circular patch is turned ON, most of the energy is coupled through to the circular patch and a much wider impedance is achieved. Figs. 7.11(b) and 7.11(c) show the field distributions of the UWB mode at 3 and 6GHz, respectively.

7.2.2   Results And Discussion

Fig. 7.13(a) shows a prototype of the antenna, tested in a NSI-2000 Near-Field Range with a bias tee and an RF feed through the mini circuit shown in Fig. 7.13(b). The PIN diodes are attached to the antenna using electrically conductive silver epoxy.

Figs. 7.14(a) and (b) show the predicted and measured input reflection coefficients versus frequency for the Narrowband and UWB modes of the antenna, respectively. The predicted results have taken the lumped elements and the entire biasing network into account. The predicted 10dB return loss bandwidth for Narrowband mode is as shown in

Fig. 7.14(a) is from 1.56GHz to 2.56GHz, while the measured bandwidth is from 1.5GHz to 2.98GHz. It can be noted that there is another resonant around 7GHz. In practice, this will be filtered out to avoid the out-of-band radiation. In the UWB mode, the predicted response shows a 119% impedance bandwidth ($2.79-11.1$GHz) while the measured results show a bandwidth of 121% from 3.0GHz to 12.2GHz. Most of the discrepancies can be attributed to the inaccuracies in the fabrication process and the uncertainties in the discrete component parameters given in the manufacturers datasheet.

Far-field radiation patterns of the proposed antenna were measured for both Narrowband and UWB modes using a spherical near-field (SNF) antenna measurement system NSI-700S-50 at Australian Antenna Measurement Facility (AusAMF). A NSI-RF-WR340 open-ended rectangular waveguide probe was used as the transmitting antenna for Narrowband mode; NSI-RF-WR229, 159 and 112 probes were used for the UWB mode. As seen from Fig. 7.15, the measured main beam for Narrowband mode is pointing at -300 at around 2.45GHz. Radiation patterns shown in Fig. 7.16 were measured over a broad range of frequencies from 3 to 10 GHz for the UWB mode. It can be seen that a broad beam coverage is realized, however, as frequency goes higher more null predominately appears in the patterns because of typical natures of dipole antennas.

The predicted and measured realized gains are compared in Fig. 7.17 for the Narrowband and UWB modes of the antenna. The measured realized gain for the Narrowband mode varies between 2 to 2.8dBi between 2.4 and 2.6GHz. In the UWB mode, gain varies between 3.5 and 5.5dBi. It is noticed that the gain variation is 1dB from 3 to 12GHz band. This may be an important feature for some UWB applications. Some slight variations in the measured gains is observed compare to the simulated ones. This can be mainly attributed to the inaccuracy of the modelling of the loss of the PIN diodes due to a lack of available data for the PIN diode operating above 5 GHz and uncertainties in the losses of other discrete elements.
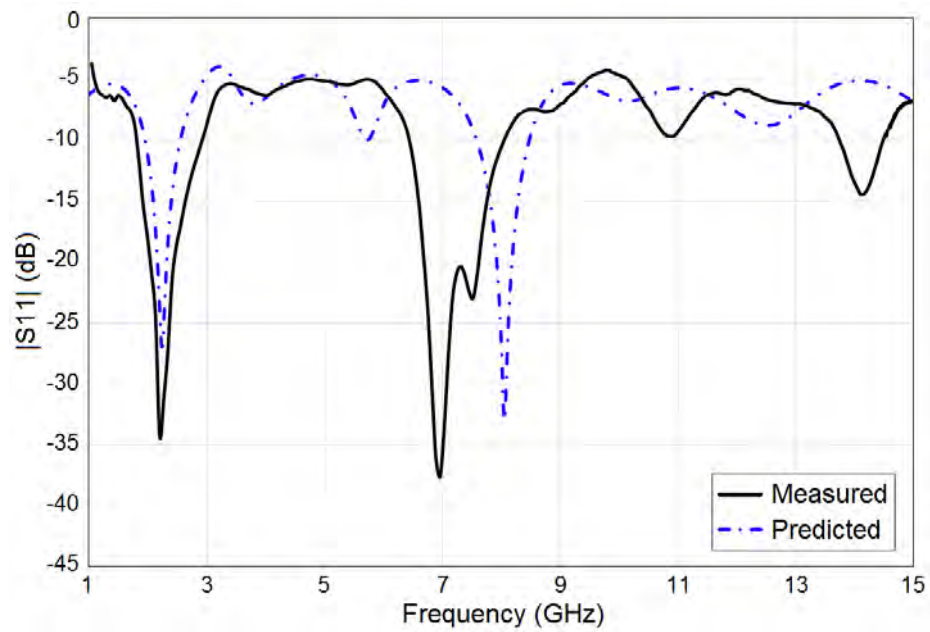
(a)
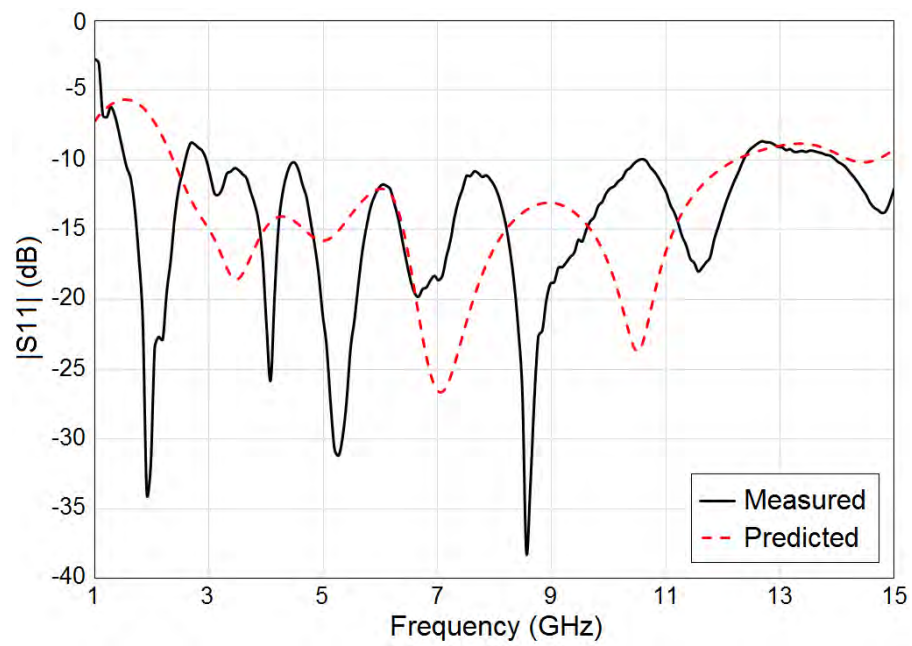
(b)

Figure 7.14: Predicted and measured input reflection coefficients for two modes (a) Narrowband mode and (b) Ultra-wideband mode.
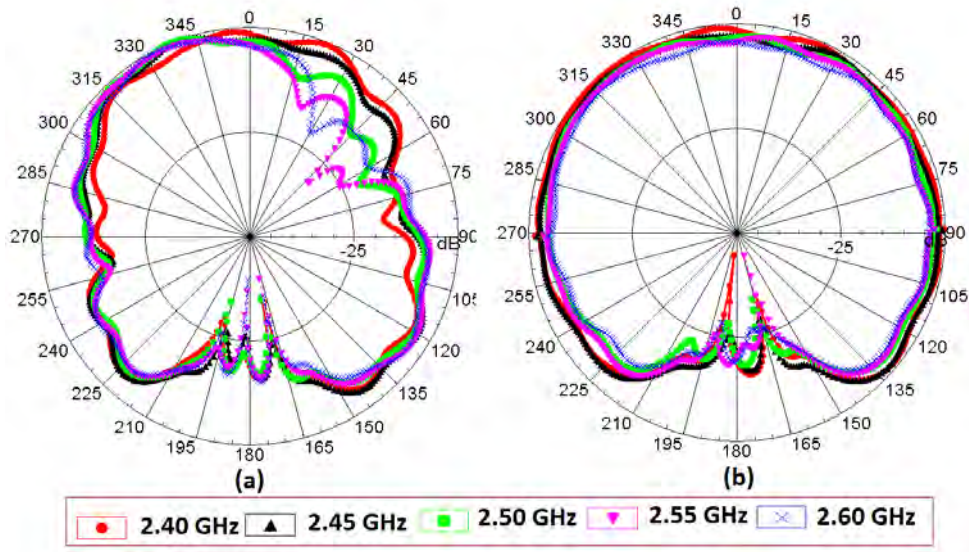
Figure 7.15: Measured radiation patterns in Narrowband mode (a) H-Plane (b) E-Plane.
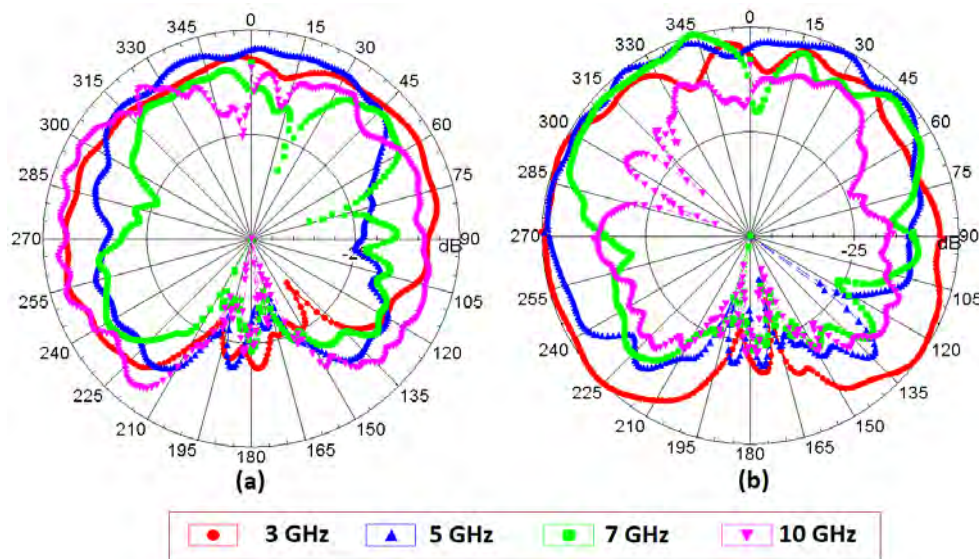
Figure 7.16: Measured radiation patterns in UWB mode (a) H-Plane (b) E-Plane.
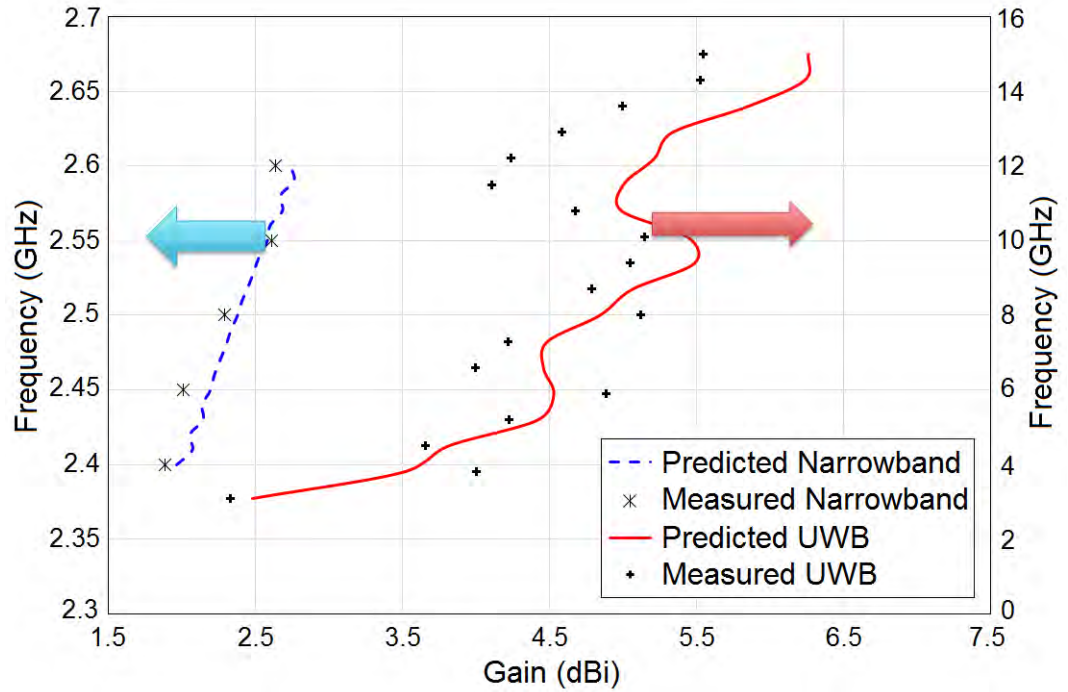
Figure 7.17: Predicted and measured gain in Narrowband and UWB modes.

A co-planar-strip-fed printed antenna for frequency reconfigurable application was presented. It has several key features including; a wide 120% bandwidth for short range on body applications or 2.45GHz ISM band operation for trans-receiver communication over longer ranges of wearable devices across WiFi range. The design shows good agreement between theoretical and measured performance.

7.3   Conclusion

Reconfigurable antenna with narrow band operations focusing on ISM band at 2.45GHz and WLAN band at 5GHz is presented. The design has narrow width which makes it feasible for integration in wearable applications. Detailed discussion about such narrow band antennas has been carried out in chapter 3. Another design that operates in ISM band at 2.45GHz in one mode and in another mode it provides UWB operation has been

presented. This antenna has simple design with single side printed geometry and provides low-cost solution.

Chapter 8

Carbon NanoTubes Yarns

Carbon Nanotube (CNT) yarns are novel CNT-based materials that extend the advantages of CNT from the nano-scale to macro-scale applications. In this chapter, we model CNT yarns as potential data transmission lines. Test structures have been designed to measure electrical properties of CNT yarns, which are attached to these test structures using gold paste. DC testing and microwave S-parameter measurements have been conducted for characterization. The observed frequency independent resistive behavior of the CNT yarn is a very promising indicator that this material, with its added values of mechanical resilience and thermal conductivity, could be invaluable for a range of applications such as Body Area Networks (BAN). A model is developed for a CNT yarn, which fits the measured data collected and agrees in general with similar data for non-yarn CNTs. Electrical characterization of CNT yarns is available for DC, whereas it was not investigated at RF/microwave frequencies particularly for the range of $0.5-20$GHz. This work is a highly significant contribution to fill this gap and reports the RF/microwave electrical characterization of CNT yarns from 50MHz to 20GHz with the goal of incorporating them in several roles in UWB WBAN. In this chapter, an overview on CNT yarn fabrication and their fixturing on developed test structures is also provided. Measurement

procedure, circuit modeling and results are presented.

8.1   Introduction

Carbon Nanotubes (CNTs) have emerged as potential candidates for replacement of conventional metals due to their significant mechanical, electrical and thermal properties and non-oxidizing abilities [9–11,109]. CNTs have been of interest in nanoelectronics and nanoantenna applications [110–114] since the density of CNT composites is about one fifth of that of copper and around half of that of aluminium. Also their thermal conductivity is about ten times that of copper. Electrical conductivity of CNT composites depends on the properties and loading of CNTs, the aspect ratio of the CNTs and the characteristics of the conductive network.

CNTs hold great promises in a number of related medical applications because of their remarkable physical properties. CNT has been used, for example, as the basic underlying material for an artificial muscle [115] due to their incredible strength-to-weight ratio. Electrically, as they are more conductive than copper in nano scales [116, 117], their potential use in in-body integrated-circuit-based ultra-wideband (UWB) wireless body area networks (WBAN) would go beyond the artificial muscle to RF/microwave dielectrics, conductors and sensors [118], suitable for EMI/EMC applications [119] to transistors [120].

Underlying any attempt to integrate CNT into such applications is establishing its properties in suitable fabrication technologies using compound semiconductor or CMOS. Recently, the investigation of the RF/microwave material properties of CNT bundles (on the order of tens of microns long) in single- and multi-walled configurations have been the subject of many studies with somewhat conflicting results [121]. While CNT bundles are the underlying building block for many applications, CNT yarns comprised

of woven, individual nanotubes, can be made to be tens of millimeters in length and as such are suitable for MEMs, tunable dielectrics, and related electrical structures at UWB frequencies. Establishing the RF/microwave material properties of CNT yarns is an essential first step to their use in hybrid manufacturing technologies.

8.2   CNT Yarn Fabrication

The Multi Walled Carbon Nanotube (MWCNT) forest was synthesized by Catalytic Chemical Vapor Deposition (CCVD) using acetylene gas as the carbon source [122]. Carbon nanotubes, in the 300-μm-tall forest, typically had diameters of about 10nm. The yarns were drawn from the forest by pulling and twisting as described in [83, 123]. CNT composite yarns can be obtained using dry spinning process [84]. Processing them using volatile liquids (like ethanol and methanol) will reduce the manufacturing irregularities and make them smooth [12, 124].

A Leica Stereoscan 440 Scanning Electron Microscope (SEM) was used for morphological studies of the fibers. SEM micrographs of the pristine CNT yarns (Fig. 8.1) show that the nanotubes are uniform, and predominantly oriented with a helix angle $(\alpha) \sim 25°$. The CNT yarns in our experiments were drawn into 12- and 100-μm diameters. The twist is characterized by the helix angle (α), which depends directly upon the degree of twist and inversely on the yarn diameter. The number of twists is typically 20000 turns per meter. Earlier, Miao [125] has investigated electrical conductivity of CNT yarns, specifically relationships between number of CNT-to-CNT contact points, yarn surface twist angle and porosity, effects of yarn porosity on electrical conductivity and resistivity of pure CNT yarns.
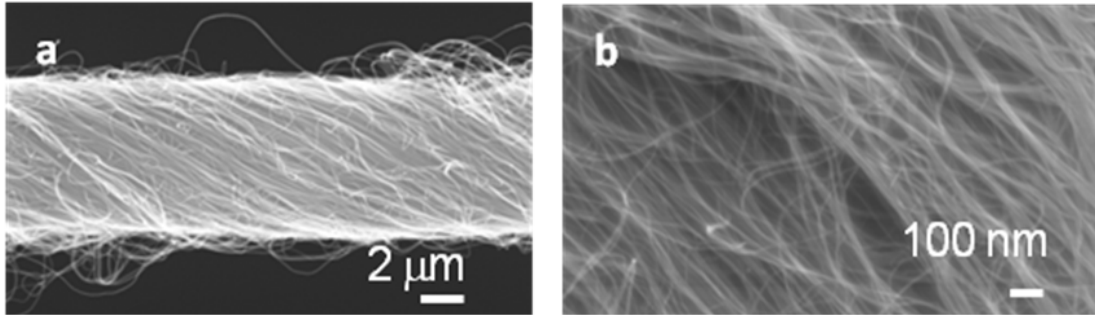
(a) (b)

Figure 8.1: SEM micrographs of pristine CNT yarn at (a) low and (b) higher magnification.

8.3 CNT Yarn Fixturing

Prepared yarns of diameter 12- and 100-μm were attached using a two-step procedure. First, the ends were prepared so as to have a planar face by carefully cleaving them perpendicularly to the major axis of the yarn. Secondly, each yarn was electrically and mechanically connected to two launches of a test structure (described in Section 8.4) using gold paste. Since CNTs, as the building blocks of CNT yarn, are quasi-one dimensional conductors, special care was taken to insure that the ends of each yarn had a continuous coating of gold from the end to the test structure launch. Confirmation of the repeatable of the coating was evidenced by consistency in DC resistance (described in Section 8.5).

A second test structure was prepared as a control for the attachment method and as a potential modeling guide. An enamel-coated wire, approximately $100\mu m$ in diameter, was prepared in the same manner as the CNT yarns and fixed to this test structure.

(a)   (b)
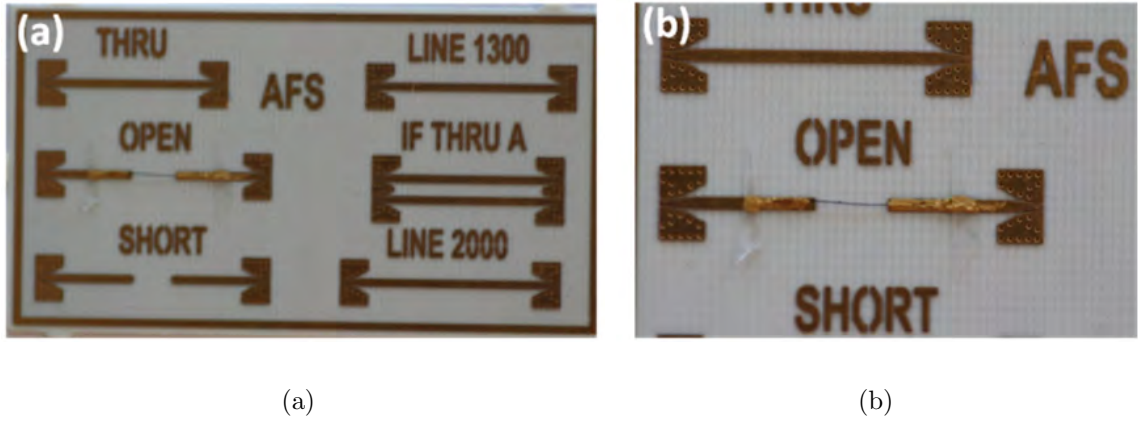
Figure 8.2: (a) Photo of the test structure with calibration structures; (b) Close up of a sample attached to golden pads using gold paste.

8.4   Test Structures and Measurement Procedure

In order to get an indication of the distributed behavior of the CNT yarns, a test structure is needed that is a substantial fraction of a wavelength. To this end, test structures supporting yarn lengths of $3500\mu m$ and $4500\mu m$ were fabricated on 10-mil-thick Rogers 4350 ($\varepsilon_r = 3.66$ and $\delta = 0.0037$) substrates, patterned with various metal structures, which were previously fabricated and used to characterize the Rogers-based material system. A nominal 50Ω line in this system is more than one-tenth of a wavelength long for frequencies above 5GHz for the 3500-μm-long test structure.

In addition to the test structure to support yarn attachment, calibration structures were included on each test vehicle for short, open, and thru calibration in both microstrip and coplanar waveguide configurations. The entire test coupon is shown in Fig. 8.2(a). Yarn samples were attached as shown in Fig. 8.2(b). Electrical connection was made to the test structure through ground-signal-ground pads at the end. While both coplanar and microstrip structures are available on the test coupon, its reuse for this application was limited to the microstrip structures only.

Table 8.1: YARNS MEASURED DATA FOR DC

Diameter (μm)	Samples' Resistance			Average Resistance (Ω)
	I	*II*	*III*	
100	186	167	158	170
12	2599	2570	2465	2545

Measurements were performed from 50MHz to 20GHz using an HP 8510C. Prior to measurements, a TRL calibration was performed using the calibration structures on the test coupon.

8.5   Measurement Results

Testing was done in two phases. First, DC testing was done to characterize the quality and repeatability of the attachment and to get a measure of contact resistance. Second, the actual microwave measurements were performed. So as to eliminate any potential effects of gold paste diffusion into the CNT yarns, testing was done right after the preparation of the samples and both tests were performed consecutively.

Three samples of 12- and three samples of 100-μm yarns were tested. Three samples of the enamel-coated wire were also tested.

8.5.1   DC Measurements and Analysis

Test results are shown in Table 8.1. The DC resistance of the thru line of the calibration structure was approximately 2Ω, which compared to the samples' resistances is negligible. The average measured resistance of the 12- and 100-μm yarns are 2.55$K\Omega$ and 170Ω, respectively. Taking the ratio of the length (l) to diameter (d) as proportional to an equivalent sheet carrying current along the yarn, the 12-μm sample is approximately 375-

units long and the 100-μm sample is 35 units. The sheet resistance then for the 12-μm yarn is 6.8 Ω/square and the 100-μm sample is 4.9 Ω/square.

It would be expected that equivalent CNT densities in the yarns would yield equivalent sheet resistivities (R_s). However, contact resistance (R_c) in CNTs is known to be high [126] and should scale approximately with the contact area. If the total resistance is taken as the sum of a contact resistance (R_c) that is inversely proportional to the contact area (or to the square of the yarn diameter so that thicker yarns have lower a contact resistance) and a sheet resistance that is directly proportional to the length of the yarn and inversely proportional to the sheet width (or yarn diameter so that thicker yarns give lower resistance and longer yarns give higher resistance), then an approximate contact resistance and sheet resistivity can be calculated using (8.1) and (8.2):

$$R \approx R_c + R_s \tag{8.1}$$

$$R \approx \frac{4r_c}{\pi d^2} + \frac{lr_s}{d} \tag{8.2}$$

The substitution of the DC resistance values gives 855 and 12.3 $\Omega \cdot m^2$ as r_c of the 12-μm and 100-μm yarns, respectively. The r_s is a constant 4.5 Ω/square for both yarn lengths.

8.5.2 Microwave Measurements

Scattering parameters of all samples were measured from 50MHz to 20GHz. Measured S_{21} is shown on the Smith chart in Figs. 8.3 - 8.5 for the 12-μm yarn, 100-μm yarn and enamel-coated wire, respectively.
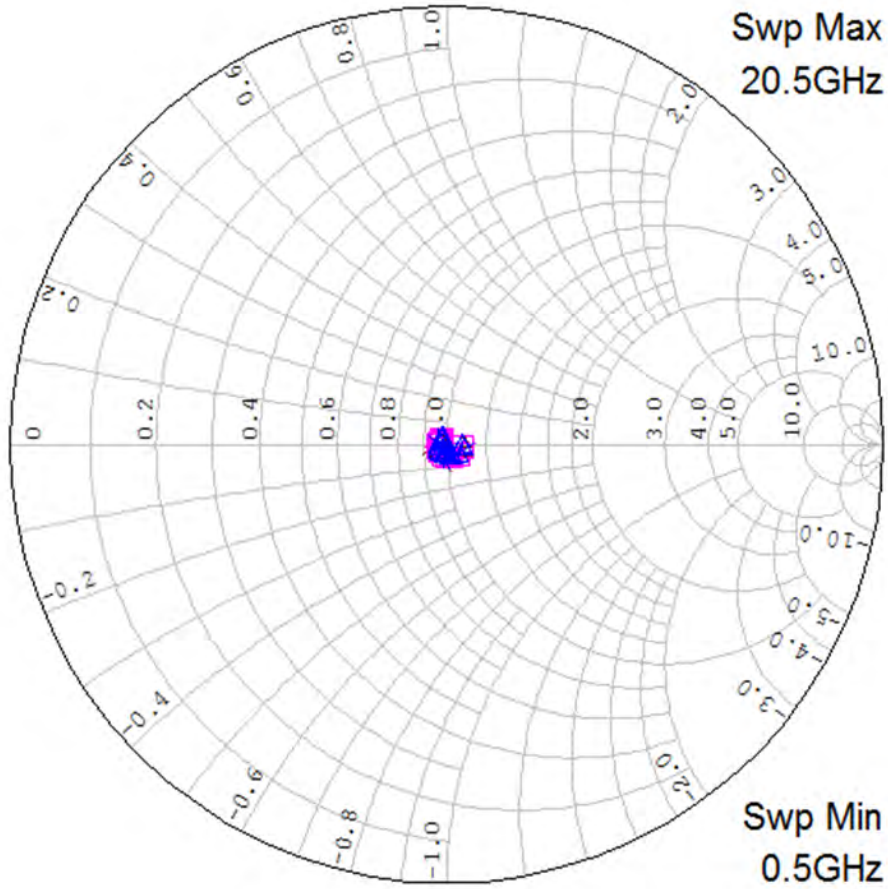
Figure 8.3: Measured S21 of the three $12\mu m$ yarn samples on $4500\mu m$ substrates showing very high absorption in transmission and resistance at DC.

8.6   Modeling

Distributed circuit modeling was performed to ascertain an understanding of the material characteristics from the test structure configuration. Previous models have been developed from first principles for single or bundled CNTs [127, 128], which are not directly applicable to CNT yarns as they are complex structures made out of CNTs. Therefore, phenomenological models are used here for CNT yarns here to identify their functional performance suitable for circuit design.

Several factors need to be addressed in the model to represent non-idealities in the test
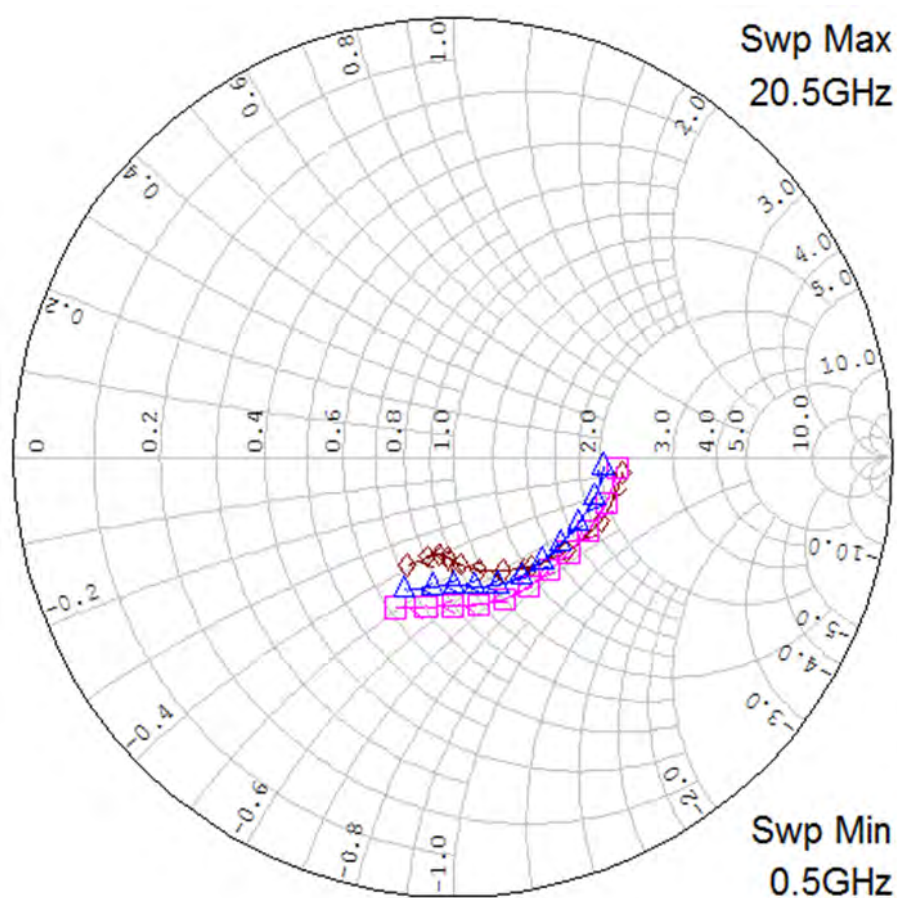
Figure 8.4: Measured S21 for the three $100\mu m$ yarn samples on $3500\mu m$ substrates showing moderate absorption in transmission and resistance at DC.

structure in the electrical model. First, the planar nature of the test structure launch does not provide any facility for repeatable positioning of the yarn or wire in the longitudinal dimension. As such, there is a potential error induced in the effective length of the line which can be corrected by introducing a series inductance or by lengthening the transmission line. Second, while the transmission structure is clearly a conductor over a ground plane, it is not truly microstrip since the conductor is circular and no physical means of adhesion between the conductor and the dielectric substrate is provided directly by the attachment technique beyond yarn/wire tension and gravity. This causes variability
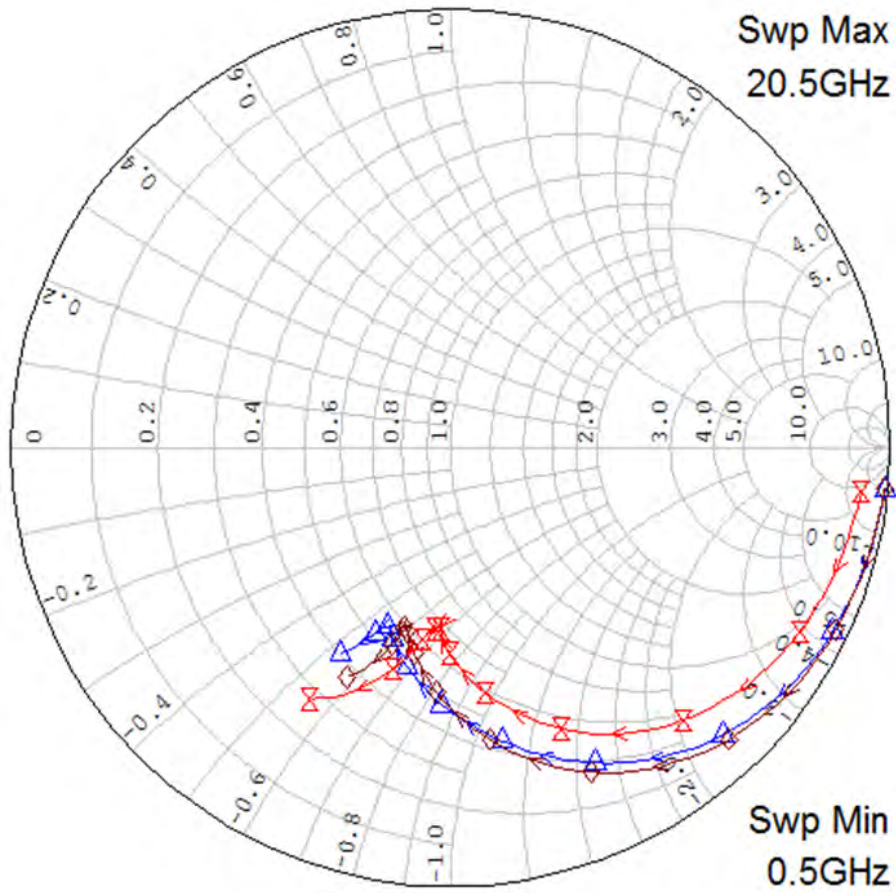
Figure 8.5: Measured S21 for the three $100\mu m$ enamel-coated wires samples on $3500\mu m$ substrates showing low absorption in transmission and negligible DC resistance.

in the characteristic impedance. Third, the high contact resistance of the CNT must be accounted for with a fixed resistance, R_c. Finally, the gold paste on the narrow launch potentially adds a parasitic series inductance, L_p, and a shunt capacitance, C_p, or makes at least one of the ports appear to be complex relative to the calibration.

As a method of extracting reasonable material and circuit parameters from these measurements, two circuit-based models using lumped and distributed elements, representing the effects mentioned above, were developed using AWR Microwave Office [129]. The model topologies are shown in Fig. 8.6. The $RLGC$ distributed model assumes that dielectric losses in the Rogers material are negligible and so a shunt conductance per me-

(a)

(b)
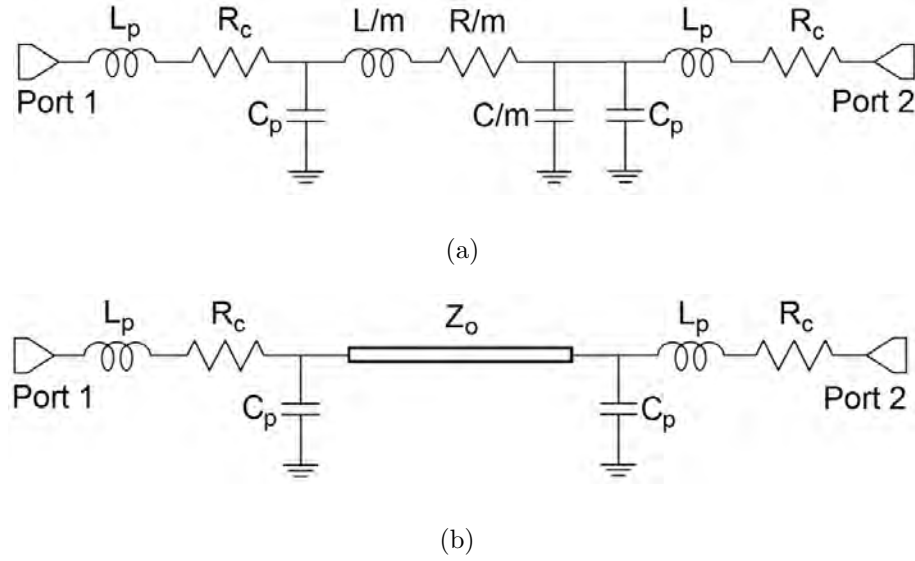
Figure 8.6: Yarn and wire models of a transmission line with parasitic resistors, capacitor, and inductor for non-ideal attachment (a) RLGC transmission line (b) TLINP transmission line.

ter, G, is not included in the $RLGC$ modeling of the transmission line. In comparison, the $TLINP$ distributed model [129] extracts the characteristic impedance Z_o, electrical length and attenuation.

The measured data was extracted also using the distributed model parameters for the enamel-coated wire. Its agreement with the measured data is shown in Fig. 8.7, showing excellent agreement up to approximately 15GHz. This model of the wire (Table 8.2) represents a characteristic impedance of approximately 128Ω which correlates well to the expected value, not taking into account the enamel, as shown in Fig. 8.7 when compared to an electromagnetic (EM)-based WIRES models [129] using the finite-elements method (FEM). The enamel-coated wire provides a control for the fixturing procedure and the use of quasi-TEM modeling for a cylinder-over-ground-plane configuration rather than the traditional microstrip line-over-ground-plane.

Using the same models shown in Fig. 8.6(b), the 100-μm yarn was modeled. The
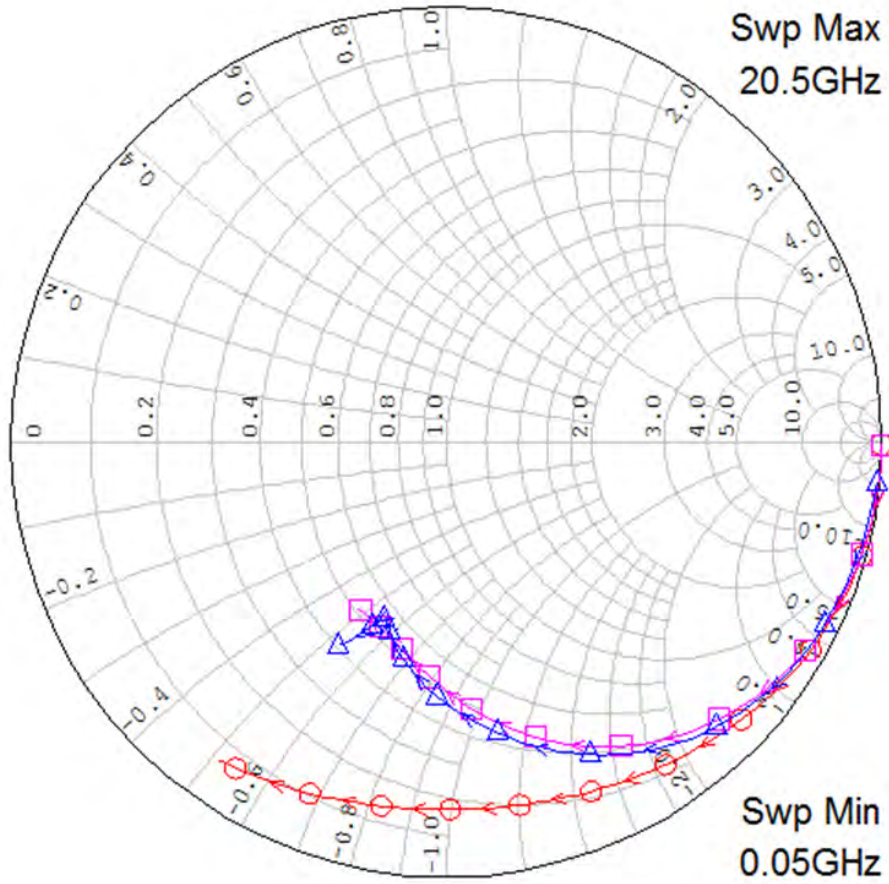
Figure 8.7: Enamel-coated wires S21: measured (blue triangle) vs. modeled (pink square) vs. ideal FEM analysis (red circle).

results for this are shown in Fig. 8.8 comparing the measured S_{21} data to the two models from 0.05GHz to 20.5GHz. A least squares fit of the complete set of S-parameters for both reflection and transmission corresponding to this model as compared to the measured data was calculated and the worst case error between the measured and the Fig. 8.6(b) model results is better than 0.25 %.

As the 12-μm yarn is exceedingly lossy for WBAN applications, the analysis focuses on 100-μm model. The value of the each inductor in the models (in Fig. 8.6) is 0.025 nH. This inductor models the extra line length from the calibration reference plane to the CNT yarn (modeled as the transmission line). The value of each R_c is 15 Ω plus a
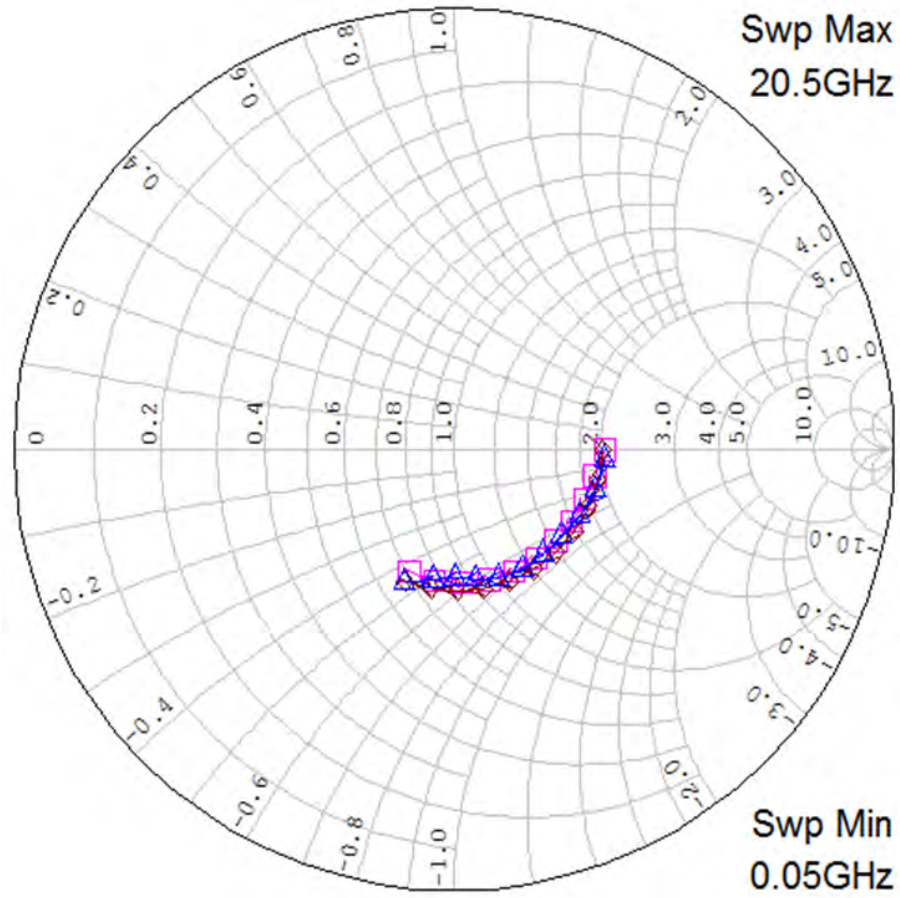
Figure 8.8: 100 m yarns S21: measured (blue triangle) vs. distributed model (brown diamond) vs. lumped model (pink square).

small frequency-dependent portion that is proportional to $\sqrt{f}$ to model the skin depth of the conductive paste connecting the CNT yarn to the reference plane. The value of each shunt capacitor that takes into account the extra parasitic capacitance from the paste to ground and fringing capacitance of the discontinuity at the start/termination of the CNT yarn has a value of 0.1 fF. We also added a small frequency-dependent series reactive part (Z_p) to the 50Ω termination at port 2 to model any asymmetry in the paste and CNT yarn placement. However, the (Z_p) is only about 0.5 and contributes only 2 % at 10GHz to the magnitude of the load impedance 50Ω; it only improves the fit to the measured data marginally. De-embedding these from the measured data leaves the $TLINP$ transmission

Table 8.2: CNT YARN AND COPPER WIRE COMPARISON AT 5GHz USING TLINP TRANSMISSION LINE MODEL

Diameter & Type	Transmission Properties			Parasitic		
	$(Z_0$ (Ω)	Phase (Deg)	Attenuation α (dB/m)	R_c (Ω)	L_p (nH)	C_p (pF)
$100\mu m$ copper wire $3500\mu m$ long (measured)	128	38	4.8	0.001	0.025	0.001
$100\mu m$ yarn $3500\mu m$ long (measured)	124	29	22	15	0.025	0.001
$12\mu m$ ideal copper wire $4500\mu m$ long (simulated)	206	45	8.0	0.001	0.025	0.001
$12\mu m$ yarn $4500\mu m$ long (measured)	206	35	28	855	0.025	0.001

line to have a characteristic impedance of 124 Ω and an electrical length of 29° at 5GHz.

Next, using the $RLGC$ transmission-line model in Fig. 8.6(a) for the transmission line and taking the calculated contact resistance from the DC values used in $TLINP$ transmission line model extractions, parameters were fit for the measured data. The per unit length values for the 100-μm-diameter and 3500-μm-long yarn are given in Table 8.3.

The model extracted for the CNT yarn, after taking into account the non-idealities mentioned above, shows transmission line characteristic impedance to be nearly identical to the wires of similar diameter (Table 8.2) at 5GHz. The difference in phase is partially due to the systematic error in this sensitive measurement and in the attachment procedure but this alone cannot account for the difference. The longer electrical length for the yarns as compared to the copper wire is consistent with CNT yarn conduction theories, which show that the longitudinal conduction mechanism includes hopping from one CNT

Table 8.3: CNT YARN AND COPPER WIRE COMPARISON AT 5GHz USING RLGC TRANSMISSION LINE MODEL

Diameter & Type	Lumped Properties			Parasitic		
	R/m	L/m	C/m	R_c	L_p	C_p
	(Ω/m)	(nH/m)	(pF/m)	(Ω)	(nH)	(pF)
$100\mu m$ copper wire $3500\mu m$ long (measured)	29	720	38	0.001	0.025	0.001
$100\mu m$ yarn $3500\mu m$ long (measured)	$45K$	390	27	12.3	0.025	0.001
$12\mu m$ yarn $4500\mu m$ long (measured)	$200K$	900	24	855	0.025	0.001

filament to another along the yarn axis [9]. Accurate extraction of this phase becomes problematic for the thinner yarns where the resistance is very high. The yarn models (both $RLGC$ and $TLINP$) differ significantly from the wire model with a very high loss for each of the models. The combined effect of the R_c and transmission line ($RLGC$ or $TLINP$) losses account for the entire measured DC resistance and it is fixed, with no significant frequency-dependent contribution over the measured frequencies. The lack of a strong frequency dependent resistance in the yarn is consistent with that found elsewhere [121].

8.7 Performance Limitations

Higher resistivity of CNT limits it performance in some applications, while it is beneficial in others. Similarly, conductivity also plays a significant role in consideration of their usage. Electrical conductivity of CNT composites depends on the properties and loading of CNTs, the aspect ratio of the CNTs and the characteristics of the conductive network.

New CNT preparation techniques which include a dopant have been shown to further reduce the resistivity which may open up additional applications [130].

8.8   Conclusions

CNT yarns were measured at RF/microwave frequencies in a microstrip configuration to ascertain their material properties for UWB WBAN system components as EM surfaces, dielectrics, and conductors. In this first such test for CNT yarns, the data suggests that the CNT yarn performs very much like the underlying multi-walled CNT bundles. Contact resistance is relatively high, but good conduction is found within the yarn itself. After accounting for the contact and an effective sheet resistance, the yarn presents a characteristic impedance that is well approximated through measurement and modeling by a copper wire of similar diameter and attachment method. These models for the CNT yarn give very good agreement to both the transmitted and reflected S-parameters. The observed frequency-independent resistive behavior of the CNT yarn is a very promising indicator that when the conductivity is improved as a result of ongoing research, this material, with its added values of mechanical resilience and thermal conductivity, could be invaluable for a range of applications such as body area network (BAN).

These results suggest that the CNT yarn can be used in microwave applications in a manner similar to resistive materials, such as NiCr or doped polysilicon. In this configuration, the CNT yarn could act as a probe or conductive structure that is acceptable to biological tissue. New CNT preparation techniques which include a dopant have been shown to further reduce the resistivity which may open up additional applications [130].

Work continues in this area and is focusing on more accurate measurements and varying yarn construction factors. To remove variability in the attachment method, the test structure launch is being redesigned to cradle the yarn in the transverse and longitudi-

nal dimensions. This will have the additional benefit of better fixing the yarn lengths. Different length yarns will be tested as well to get better understanding of phase characteristics. Finally, denser and looser yarns will be tested along with doped yarns which have improved DC conductivity.

Chapter 9

Conclusions and Future Work

9.1 Conclusions

This thesis presents the research work carried out to develop novel antennas and components for modern communication systems, including wireless body area networks.

We have discussed novel narrow band antennas. Single- and dual-band antennas are presented for wireless body area network devices operating in the industrial, scientific, and medical (ISM) band at 2.45GHz and 4.9GHz public safety Wireless Local Area Networks (WLAN) band. Performance of the designed antennas has been analyzed for near body scenarios and in close proximity to the human arm models. These antennas have significant advantages of compactness (only 14mm wide), full ground plane to minimize radiation towards the body, a wide radiation pattern over the body surface to provide maximum coverage, and less sensitivity to the variation of the gap between the antenna and the human body. These advantages make them suitable for on-body communications and wearable applications. Furthermore, performance of these antennas has been analyzed in close proximity of different body models. To assess their real-time performance, they have been evaluated with gel based tissue equivalent layer models and over a female body

175

phantom. They show good performance and are suitable for on-body communications.

A flexible embroidered antenna having an ultra-wide bandwidth, fabricated on poly-dimethylsiloxane (PDMS) composite substrate using conductive fibers, is presented. Another antenna was fabricated using Rogers material and copper, and is compared with embroidered version of the same design fabricated using conductive fibers on PDMS composite. Measured results show the similarity between the two prototypes. The embroidered antenna fabricated using conductive fibers on PDMS composite substrate also provides ultra-wide band operation. It is water resistant, flexible, compact, semi-transparent and is easy to integrate in clothing without being prominent. These traits make it suitable for wearable systems.

A compact UWB printed monopole antenna with high band rejection (up to VSWR > 25), tunable over a broad range of frequencies from 3.55GHz to 6.8GHz, is presented. The piece-wise analytical expressions give sufficiently accurate first estimate of the required stub length, avoiding excessive trail-and-error full-wave simulations. The new antenna has additional advantages of smaller size and wide radiation patterns. To demonstrate its practical usage, as examples, design parameters are presented to reject two different interfering frequency bands.

The use of wideband FSS to obtain uni-directional radiations is presented. By use of in-phase reflection over a wideband, the backward radiation are reduced and a stable radiation pattern with higher gain is obtained. Moreover, investigation focusing on control of dispersion characteristics mainly in the band-gap region are presented for novel printed microstrip HIS. By placing these HIS in a cylindrical shape and feeding it using a dipole from inside, omni-directional or controlled radiations can be obtained depending upon selected modulated width for the HIS.

Reconfigurable antenna with narrow band operations focusing on ISM band at 2.45GHz and WLAN band at 5GHz is presented. The design has narrow width which makes it

feasible for integration in wearable applications. Another design that operates in ISM band at 2.45GHz in one mode and in another mode it provides UWB operation has been presented. This antenna has simple design with single side printed geometry and provides low-cost solution.

Theoretical and experimental characterization of Carbon Nanotubes (CNT) yarns is a valuable contribution that opens new paths of research related to CNT. Electrical properties on CNT yarns were known for Direct Current (DC), however they were not available at RF and microwave frequencies. CNT yarns are modelled as transmission lines and are characterized. They were measured at RF/microwave frequencies in a microstrip configuration to ascertain their material properties for UWB WBAN system components as EM surfaces, dielectrics, and conductors. In this first such test for CNT yarns, the data suggests that the CNT yarn performs very much like the underlying multi-walled CNT bundles. Contact resistance is relatively high, but good conduction is found within the yarn itself. After accounting for the contact and an effective sheet resistance, the yarn presents a characteristic impedance that is well approximated through measurement and modeling by a copper wire of similar diameter and attachment method. These models for the CNT yarn give very good agreement to both the transmitted and reflected S-parameters. The observed frequency-independent resistive behavior of the CNT yarn is a very promising indicator that when the conductivity is improved as a result of ongoing research, this material, with its added values of mechanical resilience and thermal conductivity, could be invaluable for a range of applications such as body area network (BAN). These results suggest that the CNT yarn can be used in microwave applications in a manner similar to resistive materials, such as NiCr or doped polysilicon. In this configuration, the CNT yarn could act as a probe or conductive structure that is acceptable to biological tissue.

9.2 Future Work

- For the narrow band antennas presented in chapter 3, bandwidth enhancement can be explored and radiation efficiency can be improved.

- Using better and more fine embroidery techniques antennas with better performance can be achieved. Antenna pulse performance can be investigated for the design presented in chapter 4.

- For the design presented in chapter 5, additional band rejections can be added to the current design. In addition to making it reconfigurable, size reduction and better controlled radiation can also be explored.

- Investigation for better phase control of FSS can lead to more stable directive patterns. Similarly, further investigations can be carried out to obtain controlled radiations by using high impedance surfaces.

- Reconfigurable antennas presented in chapter 7 can further to investigated to obtain deigns with better performance.

- CNT yarns can be used in microwave and antenna applications that need radiating elements by be flexible, highly conductive, and resistive to temperature and rusting problems.

Bibliography

[1] A. Kiourti and J. Volakis, "Stretchable and flexible E-fiber wire antennas embedded in polymer," *IEEE Antennas and Wireless Propagation Letters*, vol. 13, pp. 1381–1384, 2014.

[2] S. Shao, A. Kiourti, R. Burkholder, and J. Volakis, "Broadband and flexible textile RFID tags for tires," in *IEEE International Symposium on Antennas and Propagation*, July 2014, pp. 1507–1507.

[3] K. Koski, E. Moradi, A. Babar, T. Bjorninen, L. Sydanheimo, L. Ukkonen, and Y. Rahmat-Samii, "Durability of embroidered antennas in wireless body-centric healthcare applications," in *7th European Conference on Antennas and Propagation*, April 2013, pp. 565–569.

[4] L. Zhang, Z. Wang, and J. Volakis, "Textile antennas and sensors for body-worn applications," *IEEE Antennas and Wireless Propagation Letters*, vol. 11, pp. 1690–1693, 2012.

[5] S. Amendola, E. Moradi, K. Koski, T. Bjorninen, L. Sydanheimo, L. Ukkonen, J. Rabaey, and Y. Rahmat-Samii, "Design and optimization of mm-size implantable and wearable on-body antennas for biomedical systems," in *8th European Conference on Antennas and Propagation*, April 2014, pp. 520–524.

[6] S. Shahid, M. Rizwan, M. A. B. Abbasi, H. Zahra, S. M. Abbas, and M. A. Tarar, "Textile antenna for body centric WiMAX and WLAN applications," in *International Conference on Emerging Technologies (ICET)*, 2012, pp. 1–5.

[7] S. Morris, Y. Bayram, L. Zhang, Z. Wang, M. Shtein, and J. Volakis, "High-strength, metalized fibers for conformal load bearing antenna applications," *IEEE Transactions on Antennas and Propagation*, vol. 59, no. 9, pp. 3458–3462, Sep. 2011.

[8] Z. Wang, L. Zhang, Y. Bayram, and J. Volakis, "Embroidered conductive fibers on polymer composite for conformal antennas," *IEEE Transactions on Antennas and Propagation*, vol. 60, no. 9, pp. 4141–4147, Sep. 2012.

[9] Z. Yijun, Y. Bayram, D. Feng, D. Liming, and J. L. Volakis, "Polymer-carbon nanotube sheets for conformal load bearing antennas," *IEEE Transactions on Antennas and Propagation*, vol. 58, no. 7, pp. 2169–2175, Jul. 2010.

[10] A. Mehdipour, I. D. Rosca, A. R. Sebak, C. W. Trueman, and S. V. Hoa, "Full-composite fractal antenna using carbon nanotubes for multiband wireless applications," *IEEE Antennas and Wireless Propagation Letters*, vol. 9, pp. 891–894, 2010.

[11] ——, "Carbon nanotube composites for wideband millimeter-wave antenna applications," *IEEE Transactions onAntennas and Propagation*, vol. 59, no. 10, pp. 3572–3578, Oct. 2011.

[12] S. Fan, "CNT Research: from academic wonder to industrial exploration," in *13th International Workshop on Computational Electronics*, 2009, pp. 1–4.

[13] Y. Ranga, L. Matekovits, A. R. Weily, and K. P. Esselle, "A low-profile dual-layer ultra-wideband frequency selective surface reflector," *Microwave and Optical Technology Letters*, vol. 55, no. 6, pp. 1223–1227, 2013.

[14] P. S. Hall and Y. Hao, *Antennas and propagation for body-centric wireless communications.* Artech House, 2006.

[15] "Dielectric properties of body tissues." available: http://niremf.ifac.cnr.it/tissprop/.

[16] A. Brizzi, A. Pellegrini, and Y. Hao, "Design of a cylindrical resonant cavity antenna for ban applications at V-band," in *IEEE International Workshop on Antenna Technology (iWAT)*, 2012, pp. 152–155.

[17] S. M. Abbas, Y. Ranga, and K. P. Esselle, "A printed antenna with a ground plane and electromagnetically coupled feed for 2.45GHz body area networks," in *IEEE International Symposium on Antennas and Propagation*, 2013, pp. 2143–2144.

[18] S. Abbas, Y. Ranga, and K. Esselle, "Stub-loaded printed antenna with a ground plane and electromagnetically coupled feed for 2.45GHz body area networks," in *IEEE MTT-S International Microwave Workshop Series on RF and Wireless Technologies for Biomedical and Healthcare Applications (IMWS-Bio 2013)*, 2013.

[19] S. M. Abbas, K. P. Esselle, and Y. Ranga, "A printed dual band antenna with a ground plane and electromagnetically-coupled feed for wireless body area networks," in *IEEE International Workshop on Antenna Technology (iWAT)*, March 4-6 2014.

[20] S. Abbas and K. Ranga, Y.and Esselle, "An armband-wearable printed antenna with a full ground plane for body area networks," in *IEEE International Symposium on Antennas and Propagation*, July 2014, pp. 318–319.

[21] S. M. Abbas, Y. Ranga, and K. P. Esselle, "A switchable printed antenna with a ground plane for 2.45/5 GHz wireless body area networks," in *IEEE International Workshop on Antenna Technology (iWAT)*, March 4-6 2015.

[22] ——, "Reconfigurable antenna options for 2.45/5 GHz wireless body area networks in healthcare applications," in *37th Annual International Conference of the IEEE Engineering in Medicine and Biology Society (EMBC)*, August 25-29 2015.

[23] A. Rida, L. Yang, R. Vyas, and M. Tentzeris, "Conductive inkjet-printed antennas on flexible low-cost paper-based substrates for RFID and WSN applications," *IEEE Antennas and Propagation Magazine*, vol. 51, no. 3, pp. 13–23, Jun. 2009.

[24] P. Nikitin, S. Lam, and K. Rao, "Low cost silver ink RFID tag antennas," in *IEEE International Symposium on Antennas and Propagation*, vol. 2B, July 2005, pp. 353–356.

[25] L. Zhang, Z. Wang, and J. Volakis, "Embroidered textile circuits for microwave devices," in *IEEE International Symposium on Antennas and Propagation*, July 2012, pp. 1–2.

[26] E. Moradi, K. Koski, L. Ukkonen, Y. Rahmat-Samii, T. Bjorninen, and L. Sydanheimo, "Embroidered RFID tags in body-centric communication," in *International Workshop on Antenna Technology (iWAT)*, March 2013, pp. 367–370.

[27] D. Porcino and W. Hirt, "Ultra-wideband radio technology: potential and challenges ahead," *IEEE Communications Magazine*, vol. 41, no. 7, pp. 66–74, 2003.

[28] K. Siwiak, "Ultra-wide band radio: introducing a new technology," in *IEEE VTS 53rd Vehicular Technology Conference*, vol. 2, 2001, pp. 1088–1093.

[29] Y. Dong, P. R. Runkle, L. Carin, R. Damarla, A. Sullivan, M. A. Ressler, and J. Sichina, "Multi-aspect detection of surface and shallow-buried unexploded ordnance via ultra-wideband synthetic aperture radar," *IEEE Transactions on Geoscience and Remote Sensing*, vol. 39, no. 6, pp. 1259–1270, 2001.

[30] C. Chi-Chih, M. B. Higgins, K. O'Neill, and R. Detsch, "Ultrawide-bandwidth fully-polarimetric ground penetrating radar classification of subsurface unexploded ordnance," *IEEE Transactions on Geoscience and Remote Sensing*, vol. 39, no. 6, pp. 1221–1230, 2001.

[31] S. Colson and H. Hoff, "Ultra-wideband technology for defence applications," in *IEEE International Conference on Ultra-Wideband*, 2005, pp. 615–620.

[32] Z. Zhu, Z. Xiao, L. Hao, L. Guohua, J. Xijing, and W. Jianqi, "Human-target detection and surrounding structure estimation under a simulated rubble via UWB radar," *IEEE Geoscience and Remote Sensing Letters*, vol. 10, no. 2, pp. 328–331, 2013.

[33] L. Jeong Soo, N. Cam, and T. Scullion, "A novel, compact, low-cost, impulse ground-penetrating radar for nondestructive evaluation of pavements," *IEEE Transactions on Instrumentation and Measurement*, vol. 53, no. 6, pp. 1502–1509, 2004.

[34] G. Adamiuk, T. Zwick, and W. Wiesbeck, "UWB antennas for communication systems," *Proceedings of the IEEE*, vol. 100, no. 7, pp. 2308–2321, 2012.

[35] X. Chen, J. Liang, S. Wang, Z. Wang, and C. Parini, "Small ultra wideband antennas for medical imaging," in *Loughborough Antennas and Propagation Conference (LAPC)*, 2008, pp. 28–31.

[36] K. E. Browne, R. J. Burkholder, and J. L. Volakis, "Through-wall radar imaging system utilizing a light-weight low-profile printed array," in *4th European Conference on Antennas and Propagation (EuCAP)*, 2010, pp. 1–5.

[37] W. Yifan, A. M. Abbosh, B. Henin, and N. Phong Thanh, "Synthetic bandwidth radar for ultra-wideband microwave imaging systems," *IEEE Transactions on Antennas and Propagation*, vol. 62, no. 2, pp. 698–705, 2014.

[38] K. Ono, Y. Noguchi, Y. Nakahata, I. Matsunam, and A. Kajiwara, "UWB-IR-based home security sensor with directional antenna," in *International Symposium on Information Theory and its Applications (ISITA)*, 2008, pp. 1–5.

[39] Z. Xiaodong and A. G. Yarovoy, "A sparse aperture MIMO-SAR-based UWB imaging system for concealed weapon detection," *IEEE Transactions on Geoscience and Remote Sensing*, vol. 49, no. 1, pp. 509–518, 2011.

[40] R. Chavez-Santiago, K. E. Nolan, O. Holland, L. De Nardis, J. M. Ferro, N. Barroca, L. M. Borges, F. J. Velez, V. Goncalves, and I. Balasingham, "Cognitive radio for medical body area networks using ultra wideband," *IEEE Wireless Communications*, vol. 19, no. 4, pp. 74–81, 2012.

[41] N. Chahat, M. Zhadobov, R. Sauleau, and K. Ito, "A compact UWB antenna for on-body applications," *IEEE Transactions on Antennas and Propagation*, vol. 59, no. 4, pp. 1123–1131, 2011.

[42] M. Koohestani, N. Pires, A. K. Skrivervik, and A. A. Moreira, "Performance study of a UWB antenna in proximity to a human arm," *IEEE Antennas and Wireless Propagation Letters*, vol. 12, pp. 555–558, 2013.

[43] S. M. Abbas, O. Sevimli, M. C. Heimlich, K. P. Esselle, B. Kimiaghalam, J. Foroughi, and F. Safaei, "Microwave characterization of carbon nanotube yarns for UWB medical wireless body area networks," *IEEE Transactions on Microwave Theory and Techniques*, vol. 61, no. 10, pp. 3625–3631, 2013.

[44] S. Nikolaou, K. Boyon, Y. S. Kim, J. Papapolymerou, and M. M. Tentzeris, "CPW-fed ultra wideband (UWB) monopoles with band rejection characteristic on ultra thin organic substrate," in *Asia-Pacific Microwave Conference*, 2006, pp. 2010–2013.

[45] E. Pancera, D. Modotto, A. Locatelli, F. M. Pigozzo, and C. De Angelis, "Novel design of UWB antenna with band-notch capability," in *European Conference on Wireless Technologies*, 2007, pp. 48–50.

[46] J. B. Jiang, Z. H. Yan, and C. Wang, "A novel compact UWB notch-filter antenna with a dual-Y-shaped slot," *Progress In Electromagnetics Research Letters*, vol. 14, pp. 165–170, 2010.

[47] X. L. Bao and M. J. Ammann, "Printed band-rejection UWB antenna with H-shaped slot," in *International Workshop on Antenna Technology: Small and Smart Antennas Metamaterials and Applications (iWAT)*, 2007, pp. 319–322.

[48] Y. F. Weng, S. W. Cheung, and T. I. Yuk, "Ultrawideband antenna using CPW resonators for dual-band notched characteristic," in *International Conference on Wireless Communications and Signal Processing*, 2009, pp. 1–4.

[49] Y. F. Weng, W. J. Lu, S. W. Cheung, and T. I. Yuk, "UWB antenna with single or dual band-notched characteristic for WLAN band using meandered ground stubs," in *Loughborough Antennas and Propagation Conference (LAPC)*, 2009, pp. 757–760.

[50] S. Barbarino and F. Consoli, "UWB circular slot antenna provided with an inverted-L notch filter for the 5GHz WLAN band," *Progress In Electromagnetics Research*, vol. 104, pp. 1–13, 2010.

[51] P. Lin and R. Cheng-Li, "UWB band-notched monopole antenna design using electromagnetic-bandgap structures," *IEEE Transactions on Microwave Theory and Techniques*, vol. 59, no. 4, pp. 1074–1081, 2011.

[52] Z. H. S. Hu, R. J. Kelly, P. S. Hall, and P. Gardner, "Wideband conical monopole antenna with integrated stopband filter," *Progress In Electromagnetics Research C*, vol. 27, pp. 223–238, 2012.

[53] A. Nouri and G. R. Dadashzadeh, "A compact UWB band-notched printed monopole antenna with defected ground structure," *IEEE Antennas and Wireless Propagation Letters*, vol. 10, pp. 1178–1181, 2011.

[54] J. J. Liu, K. P. Esselle, S. G. Hay, and S. S. Zhong, "Planar ultra-wideband antenna with five notched stop bands," *Electronics Letters*, vol. 49, no. 9, 2013.

[55] J. Yeo and R. Mittra, "A novel wideband antenna package design with a compact spatial-notch filter for wireless applications," *Microwave and Optical Technology Letters*, vol. 35, no. 6, pp. 455–460, 2002.

[56] L. Wen-jun, C. Chong-hu, and Z. Hong-bo, "Improved frequency notched ultrawideband slot antenna using square ring resonator," *IEEE Transactions on Antennas and Propagation*, vol. 55, no. 9, pp. 2445–2450, 2007.

[57] W. Feng, W. Qiu Yi, S. Xiao Wei, and C. Li, "Compact UWB bandpass filter with dual notched bands based on SCRLH resonator," *IEEE Microwave and Wireless Components Letters*, vol. 21, no. 1, pp. 28–30, 2011.

[58] W. Sung-Jung, K. Cheng-Hung, C. Keng-Hsien, and T. Jenn-Hwan, "Study of an ultrawideband monopole antenna with a band-notched open-looped resonator," *IEEE Transactions on Antennas and Propagation*, vol. 58, no. 6, pp. 1890–1897, 2010.

[59] J. R. Kelly, P. S. Hall, and P. Gardner, "Band-notched UWB antenna incorporating a microstrip open-loop resonator," *IEEE Transactions on Antennas and Propagation*, vol. 59, no. 8, pp. 3045–3048, 2011.

[60] K. S. Ryu and A. A. Kishk, "UWB antenna with single or dual band-notches for lower WLAN band and upper WLAN band," *IEEE Transactions on Antennas and Propagation*, vol. 57, no. 12, pp. 3942–3950, 2009.

[61] E. Lim, Z. Wang, C. Lei, Y. Wang, and K. Man, "Ultra wideband antennas: past and present," *IAENG International Journal of Computer Science*, vol. 37, no. 3, pp. 304–314, 2010.

[62] S. Abbas, Y. Ranga, A. Verma, and K. Esselle, "A simple ultra wideband printed monopole antenna with high band rejection and wide radiation patterns," *IEEE Transactions on Antennas and Propagation*, vol. 62, no. 9, pp. 4816–4820, 2014.

[63] Y. Ranga and K. P. Esselle, "CPW-fed semicircular slot antenna for UWB PCB applications," in *IEEE International Symposium on Antennas and Propagation*, 2009, pp. 1–4.

[64] Y. Ranga, K. P. Esselle, A. R. Weily, and A. K. Verma, "A compact antenna with high gain for ultra wide band systems," in *European Microwave Conference (EuMC)*, 2009, pp. 85–88.

[65] J. Y. Siddiqui, C. Saha, and Y. M. M. Antar, "A novel ultrawideband (UWB) printed antenna with a dual complementary characteristic," *IEEE Antennas and Wireless Propagation Letters*, vol. 14, pp. 974–977, 2015.

[66] R. L. Haupt and M. Lanagan, "Reconfigurable antennas," *IEEE Antennas and Propagation Magazine*, vol. 55, no. 1, pp. 49–61, 2013.

[67] N. Haider, D. Caratelli, and A. G. Yarovoy, "Recent developments in reconfigurable and multiband antenna technology," *International Journal of Antennas and Propagation*, vol. 2013, p. 14, 2013.

[68] P.-Y. Qin, Y. Guo, and C. Ding, "A dual-band polarization reconfigurable antenna for WLAN systems," *IEEE Transactions on Antennas and Propagation*, vol. 61, no. 11, pp. 5706–5713, Nov. 2013.

[69] S. Genovesi, A. Di Candia, and A. Monorchio, "Compact and low profile frequency agile antenna for multistandard wireless communication systems," *IEEE Transactions on Antennas and Propagation*, vol. 62, no. 3, pp. 1019–1026, March 2014.

[70] P. Bhartia and I. Bahl, "A frequency agile microstrip antenna," in *International Symposium on Antennas and Propagation*, vol. 20, May 1982, pp. 304–307.

[71] S.-J. Wu and T.-G. Ma, "A wideband slotted bow-tie antenna with reconfigurable CPW-to-slotline transition for pattern diversity," *IEEE Transactions on Antennas and Propagation*, vol. 56, no. 2, pp. 327–334, Feb 2008.

[72] Y. Cai, Y. Guo, and T. Bird, "A frequency reconfigurable printed Yagi-Uda dipole antenna for cognitive radio applications," *IEEE Transactions on Antennas and Propagation*, vol. 60, no. 6, pp. 2905–2912, June 2012.

[73] H. Rajagopalan, J. Kovitz, and Y. Rahmat-Samii, "MEMS reconfigurable optimized E-shaped patch antenna design for cognitive radio," *IEEE Transactions on Antennas and Propagation*, vol. 62, no. 3, pp. 1056–1064, March 2014.

[74] T. Aboufoul, A. Alomainy, and C. Parini, "Reconfiguring UWB monopole antenna for cognitive radio applications using GaAs FET switches," *IEEE Antennas and Wireless Propagation Letters*, vol. 11, pp. 392–394, 2012.

[75] C. Panagamuwa, A. Chauraya, and J. Vardaxoglou, "Frequency and beam reconfigurable antenna using photoconducting switches," *IEEE Transactions on Antennas and Propagation*, vol. 54, no. 2, pp. 449–454, Feb 2006.

[76] A. Mansoul, F. Ghanem, M. Hamid, and M. Trabelsi, "A selective frequency-reconfigurable antenna for cognitive radio applications," *IEEE Antennas and Wireless Propagation Letters*, vol. 13, pp. 515–518, 2014.

[77] L. Pazin and Y. Leviatan, "Reconfigurable rotated-T slot antenna for cognitive radio systems," *IEEE Transactions on Antennas and Propagation*, vol. 62, no. 5, pp. 2382–2387, May 2014.

[78] T. Aboufoul, X. Chen, C. Parini, and A. Alomainy, "Multiple-parameter reconfiguration in a single planar ultra-wideband antenna for advanced wireless communication systems," *IET Microwaves, Antennas Propagation*, vol. 8, no. 11, pp. 849–857, August 2014.

[79] C. Balanis, *Antenna Theory: Analysis and Design.* John Wiley, 2005.

[80] P. V. Nikitin, S. Lam, and K. V. S. Rao, "Low cost silver ink RFID tag antennas," in *IEEE International Symposium on Antennas and Propagation Society*, vol. 2B, 2005, pp. 353–356.

[81] M. M. Tentzeris, "Novel paper-based inkjet-printed antennas and wireless sensor modules," in *IEEE International Conference on Microwaves, Communications, Antennas and Electronic Systems*, 2008, pp. 1–8.

[82] H. Rmili, J.-L. Miane, H. Zangar, and T. Olinga, "Design of microstrip-fed proximity-coupled conducting-polymer patch antenna," *Microwave and Optical Technology Letters*, vol. 48, no. 4, pp. 655–660, 2006.

[83] M. Zhang, K. R. Atkinson, and R. H. Baughman, "Multifunctional carbon nanotube yarns by downsizing an ancient technology," *Science*, vol. 306, no. 5700, pp. 1358–1361, 2004.

[84] T. Canh-Dung, S. M. Smith, G. Higgerson, B. Anh, L. K. Randeniya, and T.-C. Thanh, "Spinning CNT based composite yarns using a dry spinning process," in *International Conference on Nanoscience and Nanotechnology (ICONN)*, 2010, pp. 17–20.

[85] D. Ma and W. X. Zhang, "A dual-band dual-polarized antenna for body area network," in *Proceedings of the Fourth European Conference on Antennas and Propagation (EuCAP)*, 2010, pp. 1–5.

[86] J. C. McDonald and G. M. Whitesides, "Poly(dimethylsiloxane) as a material for fabricating microfluidic devices," *Accounts of Chemical Research*, vol. 35, no. 7, pp. 491–499, 2002, pMID: 12118988. [Online]. Available: http://dx.doi.org/10.1021/ar010110q

[87] S. Koulouridis, G. Kiziltas, Y. Zhou, D. Hansford, and J. Volakis, "Polymer-ceramic composites for microwave applications: Fabrication and performance assessment," *IEEE Transactions on Microwave Theory and Techniques*, vol. 54, no. 12, pp. 4202–4208, Dec. 2006.

[88] L. Chia-Ching, J. Peng, and R. W. Ziolkowski, "Single, dual and tri-band-notched ultrawideband (UWB) antennas using capacitively loaded loop (CLL) resonators," *IEEE Transactions on Antennas and Propagation*, vol. 60, no. 1, pp. 102–109, 2012.

[89] J. R. Kelly, P. S. Hall, and P. Gardner, "Planar band-notched UWB antenna," in *3rd European Conference on Antennas and Propagation (EuCAP)*, 2009, pp. 1636–1639.

[90] H. Chong-Yu, L. Ching-Wei, I. Y. Tarn, and C. Shyh-Jong, "Design of a planar ultrawideband antenna with a new band-notch structure," *IEEE Transactions on Antennas and Propagation*, vol. 55, no. 12, pp. 3391–3397, 2007.

[91] T. Dissanayake and K. P. Esselle, "Prediction of the notch frequency of slot loaded printed UWB antennas," *IEEE Transactions on Antennas and Propagation*, vol. 55, no. 11, pp. 3320–3325, 2007.

[92] R. Eshtiaghi, J. Nourinia, and C. Ghobadi, "Electromagnetically coupled band-notched elliptical monopole antenna for UWB applications," *IEEE Transactions on Antennas and Propagation*, vol. 58, no. 4, pp. 1397–1402, 2010.

[93] M. Tzyh-Ghuang, H. Ren-Ching, and C. Chin-Feng, "Design of a multiresonator loaded band-rejected ultrawideband planar monopole antenna with controllable notched bandwidth," *IEEE Transactions on Antennas and Propagation*, vol. 56, no. 9, pp. 2875–2883, 2008.

[94] J. Joon-Won and H. Hee-Yong, "An improved band-rejection UWB antenna with resonant patches and a slot," *IEEE Antennas and Wireless Propagation Letters*, vol. 8, pp. 299–302, 2009.

[95] Y. Ranga, L. Matekovits, K. P. Esselle, and A. R. Weily, "Multioctave frequency selective surface reflector for ultrawideband antennas," *IEEE Antennas and Wireless Propagation Letters*, vol. 10, pp. 219–222, 2011.

[96] C. R. Medeiros, E. B. Lima, J. R. Costa, and C. A. Fernandes, "Wideband slot antenna for WLAN access points," *IEEE Antennas and Wireless Propagation Letters*, vol. 9, pp. 79–82, 2010.

[97] Q. Shi-Wei, C. Chi Hou, and X. Quan, "Wideband and high-gain composite cavity-backed crossed triangular bowtie dipoles for circularly polarized radiation," *IEEE Transactions on Antennas and Propagation*, vol. 58, no. 10, pp. 3157–3164, 2010.

[98] J. O. Yang, S. Bo, J. Zhang, and F. Yang, "A low-profile unidirectional cavity-backed log-periodic slot antenna," *Progress In Electromagnetics Research*, vol. 119, pp. 423–433, 2011.

[99] J. D. Shumpert, W. J. Chappell, and L. P. B. Katehi, "Parallel-plate mode reduction in conductor-backed slots using electromagnetic bandgap substrates," *IEEE*

Transactions on Microwave Theory and Techniques, vol. 47, no. 11, pp. 2099–2104, 1999.

[100] F. Elek, R. Abhari, and G. V. Eleftheriades, "A uni-directional ring-slot antenna achieved by using an electromagnetic band-gap surface," *IEEE Transactions on Antennas and Propagation*, vol. 53, no. 1, pp. 181–190, 2005.

[101] J. Y. Park, C. C. Chang, Y. Qian, and T. Itoh, "An improved low-profile cavity-backed slot antenna loaded with 2D UC-PBG reflector," in *IEEE International Symposium on Antennas and Propagation*, vol. 4, 2001, pp. 194–197.

[102] M. Pasian, S. Monni, A. Neto, M. Ettorre, and G. Gerini, "Frequency selective surfaces for extended bandwidth backing reflector functions," *IEEE Transactions on Antennas and Propagation*, vol. 58, no. 1, pp. 43–50, 2010.

[103] G. I. Kiani, A. R. Weily, and K. P. Esselle, "A novel absorb/transmit FSS for secure indoor wireless networks with reduced multipath fading," *IEEE Microwave and Wireless Components Letters*, vol. 16, no. 6, pp. 378–380, 2006.

[104] R. M. S. Cruz, A. G. D'Assuncao, and P. H. F. da Silva, "A new FSS design proposal for UWB applications," in *International Workshop on Antenna Technology (iWAT)*, 2010, pp. 1–4.

[105] Y. Ranga, K. P. Esselle, L. Matekovits, and S. G. Hay, "Increasing the gain of a semicircular slot UWB antenna using an FSS reflector," in *IEEE-APS Topical Conference on Antennas and Propagation in Wireless Communications (APWC)*, 2012, pp. 478–481.

[106] L. Matekovits, G. Colome, and M. Orefice, "Controlling the bandlimits of TE-surface wave propagation along a modulated microstrip-line-based high impedance

surface," *IEEE Transactions on Antennas and Propagation*, vol. 56, no. 8, pp. 2555–2562, Aug. 2008.

[107] L. Matekovits, "Analytically expressed dispersion diagram of unit cells for a novel type of holographic surface," *IEEE Antennas and Wireless Propagation Letters*, vol. 9, pp. 1251–1254, 2010.

[108] "MACOM," Available: http://cdn.macom.com/datasheets/MA4FCP300.pdf.

[109] A. Mehdipour, A. Sebak, C. Trueman, I. Rosca, and S. Hoa, "Reinforced continuous carbon-fiber composites using multi-wall carbon nanotubes for wideband antenna applications," *IEEE Transactions on Antennas and Propagation*, vol. 58, no. 7, pp. 2451–2456, July 2010.

[110] N. Srivastava, H. Li, F. Kreupl, and K. Banerjee, "On the applicability of single-walled carbon nanotubes as VLSI interconnects," *IEEE Transactions on Nanotechnology*, vol. 8, no. 4, pp. 542–559, July 2009.

[111] G. Hanson, "Current on an infinitely-long carbon nanotube antenna excited by a gap generator," *IEEE Transactions on Antennas and Propagation*, vol. 54, no. 1, pp. 76–81, Jan 2006.

[112] G. W. Hanson, "Fundamental transmitting properties of carbon nanotube antennas," *IEEE Transactions on Antennas and Propagation*, vol. 53, no. 11, pp. 3426–3435, 2005.

[113] L. Hoseon, G. Shaker, K. Naishadham, S. Xiaojuan, M. McKinley, B. Wagner, and M. Tentzeris, "Carbon-nanotube loaded antenna-based ammonia gas sensor," *IEEE Transactions on Microwave Theory and Techniques*, vol. 59, no. 10, pp. 2665–2673, 2011.

[114] R. De Paolis, S. Pacchini, F. Coccetti, G. Monti, L. Tarricone, M. M. Tentzeris, and R. Plana, "Circuit model of carbon-nanotube inks for microelectronic and microwave tunable devices," in *IEEE MTT-S International Microwave Symposium Digest*, 2011, pp. 1–4.

[115] T. Mirfakhrai, J. Oh, M. Kozlov, S. Fang, M. Zhang, R. H. Baughman, and J. D. W. Madden, "Carbon nanotube yarn actuators: An electrochemical impedance model," *Journal of the Electrochemical Society*, vol. 156, no. 6, pp. K97–K103, 2009.

[116] Y. Zhou, S. Sreekala1, Ajayan, and S. K. Nayak, "Resistance of copper nanowires and comparison with carbon nanotube bundles for interconnect applications using first principles calculations," *Journal of Physics: Condensed Matter*, vol. 20, no. 9, pp. 1–5, 2008.

[117] H. J. Li, W. G. Lu, J. J. Li, X. D. Bai, and C. Z. Gu, "Multichannel ballistic transport in multiwall carbon nanotubes," *Physics Review Letters*, vol. 95, p. 086601, Aug 2005. [Online]. Available: http://link.aps.org/doi/10.1103/PhysRevLett.95.086601

[118] T. Mirfakhrai, O. Jiyoung, M. E. Kozlov, F. Shaoli, Z. Mei, R. H. Baughman, and J. D. W. Madden, "Mechanoelectrical force sensors using twisted yarns of carbon nanotubes," *IEEE/ASME Transactions on Mechatronics*, vol. 16, no. 1, pp. 90–97, 2011.

[119] K.-Y. Park, S.-E. Lee, C.-G. Kim, and J.-H. Han, "Application of MWNT-added glass fabric/epoxy composites to electromagnetic wave shielding enclosures," *Composite Structures*, vol. 81, no. 3, pp. 401–406, 2007.

[120] P. J. Burke, "AC performance of nanoelectronics: towards a ballistic THz nanotube transistor," *Solid-State Electronics*, vol. 48, no. 10-11, pp. 1981–1986, 2004.

[121] Y. Yang, C. Y. Tan, W. Q. Sun, W. Li, C. K. Ong, Y. Liu, Y. Li, and S. Y. Xu, "High frequency resistance of single-walled and multiwalled carbon nanotubes," *Applied Physics Letters*, vol. 98, no. 9, pp. 093 107–3, 2011.

[122] A. E. Aliev, C. Guthy, M. Zhang, S. Fang, A. A. Zakhidov, J. E. Fischer, and R. H. Baughman, "Thermal transport in MWCNT sheets and yarns," *Carbon*, vol. 45, no. 15, pp. 2880–2888, 2007.

[123] K. R. Atkinson, S. C. Hawkins, C. Huynh, C. Skourtis, J. Dai, M. Zhang, S. Fang, A. A. Zakhidov, S. B. Lee, A. E. Aliev, C. D. Williams, and R. H. Baughman, "Multifunctional carbon nanotube yarns and transparent sheets: Fabrication, properties, and applications," *Physica B: Condensed Matter*, vol. 394, no. 2, pp. 339–343, 2007.

[124] T. Iijima, Y. Hayashi, U. B. Suryavanshi, A. Hayashi, M. Tanemura, and H. Oshima, "Electrical property of carbon nanotube fiber spun from vertically aligned carbon nanotube forest," in *IEEE 4th International Nanoelectronics Conference (INEC)*, 2011, pp. 1–2.

[125] M. Miao, "Electrical conductivity of pure carbon nanotube yarns," *Carbon*, vol. 49, no. 12, pp. 3755–3761, 2011.

[126] D. Fathi and B. Forouzandeh, *Interconnect Challenges and Carbon Nanotube as Interconnect in Nano VLSI Circuits.* InTech, 2010.

[127] P. J. Burke, "An RF circuit model for carbon nanotubes," *IEEE Transactions on Nanotechnology*, vol. 2, no. 1, pp. 55–58, 2003.

[128] G. Y. Slepyan, S. A. Maksimenko, A. Lakhtakia, O. Yevtushenko, and A. V. Gusakov, "Electrodynamics of carbon nanotubes: Dynamic conductivity, impedance boundary conditions, and surface wave propagation," *Physical Review B*, vol. 60, no. 24, p. 17136, 1999.

[129] "Microwave office," . AWR Corporation, El Segundo, CA, USA,
Available: http://www.awrcorp.com/Usa/Products/Microwave-Office/.

[130] Q. W. Li, Y. Li, X. F. Zhang, S. B. Chikkannanavar, Y. H. Zhao, A. M. Dangelewicz,
L. X. Zheng, S. K. Doorn, Q. X. Jia, D. E. Peterson, P. N. Arendt, and Y. T. Zhu,
"Structure-dependent electrical properties of carbon nanotube fibers," *Advanced
Materials*, vol. 19, no. 20, pp. 3358–3363, 2007.